OPTICAL SPECTROSCOPIC PROPERTIES OF ACTIVE NANO-CRYSTAL DOPED TRANSPARENT GLASS COMPOSITES

by

THANDAR MYINT

A dissertation submitted to the Graduate Faculty in Engineering in partial fulfillment of the requirements for the degree of Doctor of Philiosophy. The City University of New York

2010

#approval

This manuscript has been read and accepted for the
Graduate Faculty in Engineering in satisfaction of the
dissertation requirement for the degree of Doctor of Philosophy.

Prof. Robert R. Alfano

Date

Chair of Examining Committee

Prof. Mumtaz K. Kassir

Date

Executive Officer

Prof. Roger Dorsinville

Prof. Anshel Gorokhovsky

Dr. Mikhail Sharonov

Dr. Wubao Wang

Supervisory Committee

THE CITY UNIVERSITY OF NEW YORK

Abstract

OPTICAL SPECTROSCOPIC PROPERTIES OF ACTIVE NANO-CRYSTAL DOPED TRANSPARENT GLASS COMPOSITES

by

Thandar Myint

Adviser: Professor Robert R. Alfano

Cr^{4+} and some Cr^{3+} ions doped tunable laser media operate in optical telecommunication bands. The tunability of some Cr^{3+} doped media cover the telecom O,E,S,C and L bands while Er doped glass, widely used in optical amplifiers, covers only C bands. If the telecom utilizes Cr doped materials as the amplified media in fiber lasers and amplifiers, it can revolutionize the optical communications. But making Cr doped crystal in fiber form is difficult and expensive while the glass is the best material to make the fiber form. One solution to solve this problem is to synthesize the glass composites which have the good mechanical properties of glasses and perfect optical properties of bulk single crystals. In this thesis, synthesis and optical properties of chromium doped transparent glass-ceramics with the chemical composition similar to Cunyite(Cr^{4+}:Ca_2GeO_4) laser crystal are presented. Broadband structureless fluorescence and high quantum efficiency of new glass-ceramic make it the promising medium for fiber lasers and amplifiers. One barrier in synthesizing the glass ceramics is controlling the size of the nanocrystals inside the glass matrix. Since the glass composite is a two-phase (glass and crystal phase) system, the size of nano-crystals must be small to reduce the scattering and consequently produce the transparent sample. In order to produce smaller nano-crystals inside the glass matrix, porous glass with pore size of 4nm is also investigated. The optical properties of synthesized porous-glass show the crystal having a few lattice parameters in size can be grown inside the pore network.

This thesis is dedicated to
my parents and sister, KAYTHI OO.

Acknowledgements

First and foremost, I would like to thank my thesis adviser, Distinguished Professor Robert R. Alfano for giving me a chance to work in IUSL. I'm really surprised to see how passionate he is about science, how vast his knowledge is and how fast his reading speed is. He is a fun person to work with even though he is a larger than life figure in optics. I'm always thankful to him for giving me financial security and for showing me how to do the research properly.

I'm extremely thankful to Dr. Mikhail Yu. Sharonov for mentoring throughout my doctoral years in IUSL. Without him, this thesis may not even exist. He is a very competent scientist (both experimentally and theoretically) and I truly feel lucky that I have a chance to work with him. Because of him, I became to like the physics of laser crystals even though initially I see the subject as a boring one. Now it becomes my career and I owe him a great deal for having a career path. He'll always be my teacher.

I'm truly thankful to Prof. Vladimir Petricevic for mentoring me during my second exam and reminding me that "Everything takes time and it will come to you gradually". Every time I have trouble understanding the theory, these words help me a lot.

I would like to thank Dr. Alexei Bykov for creating such unparallel samples. We can all agree that he is the source person who made all great discoveries (LIGO, LISO & CUNYite crystals) possible.

I'm particularly thankful to Dr. Wabao Wang for giving me inspiration everyday

and for showing me how a respectful and organized scientist should be. He always encourages me and gives me advices whenever I need them.

I'm really thankful to Dr. Shengkun Zhang for showing me the way how I can find a job effectively and giving me encouragement during my downtime.

Especially, I'm thankful to Dr. Xiaohui Ni for helping me during the dissertation writing period. I have to acknowledge that he guides me through the last year at IUSL.

Dr. Kestutis Sutkus is really a kind person. I'm thankful to him for his kind treatment throughout my years at IUSL.

I would like to express my gratitude to Prof. Swapan Gayen for always asking me about my progress and my country(BURMA) and giving me kind support.

I'm especially thankful to Prof. Roger Dorsinville and Prof. Anshel Gorokhovsky for serving on the examination committee.

I would like to thank Cindy for introducing me to Prof. Alfano and giving me her room when she graduated.

I'm truly thankful to Joan and Lauren for helping me with the administrative issues during my five years studies at IUSL. Particularly I thank Joan for giving me a big smile on my thesis defense day.

I would like to thank Sasha for helping me whenever I need help with the experiments.

I'm truly thankful to Mrs. Liu for measuring Raman lines of LISO crystals and for giving me smile whenever I see her on the hallway.

I also want to thank Mr. Michelet Jeanty for helping me to improve my oral presentation.

I want to thank all my friends giving me support during my exciting years at IUSL. I'm truly grateful to them.

Finally, I would like to thank myself for contribution of these publications[1, 2, 3,

4, 5] to the science community.

Contents

List of Figures

List of Tables

Chapter 1

Introduction

Discovering the first Cr^{4+}laser by Alfano's group[19, 20, 14] opens the whole new era of Cr^{4+}tunable lasers lasing in near infrared region. Since the major applications such as optical communications, remote sensing use the near infrared region, Cr^{4+}lasers are ever valuable tools for wide-range of applications. Since the past decade, our institute has been constantly looking for the new more efficient Cr-doped laser materials. Since the non-radiative relaxation is a major loss channel for Cr^{4+}doped crystals, understanding the non-radiative process in these materials is crucial important for finding a new efficient material. Our group's thorough understanding in growing Cr doped material and pioneer work on the nonradiative mechanism in Cr^{4+}:forsterite(Mg_2SiO_4) [21, 22] helps find more-efficient(wide tunability and high quantum efficiency) Cr-doped tunable lasers. Development of new solid state laser based on Ca_2GeO_4 crystal[23, 24, 25], which is tunable in eye safe "1.3 - 1.5μm" range, is one of the major accomplishments. This crystal is named CUNYite to honor CUNY (The City University of New York).Raman measurement shows that there is only one significant local mode in this crystal[26] and consequently the non-radiative decay rate in CUNYite(Cr^{4+}:Ca_2GeO_4) is much less than that in Cr^{4+}:forsterite(Mg_2SiO_4) . The measured quantum efficiency of CUNYite(Cr^{4+}:Ca_2GeO_4) is about 50% compared to 10% in Cr^{4+}:forsterite(Mg_2SiO_4) . Surprisingly enough, this effort produces three more laser crystals, namely, Cr^{3+}:$LiScGeO_4$[27], Cr^{3+}:$LiInGeO_4$and Cr^{3+}:$LiInSiO_4$[28,

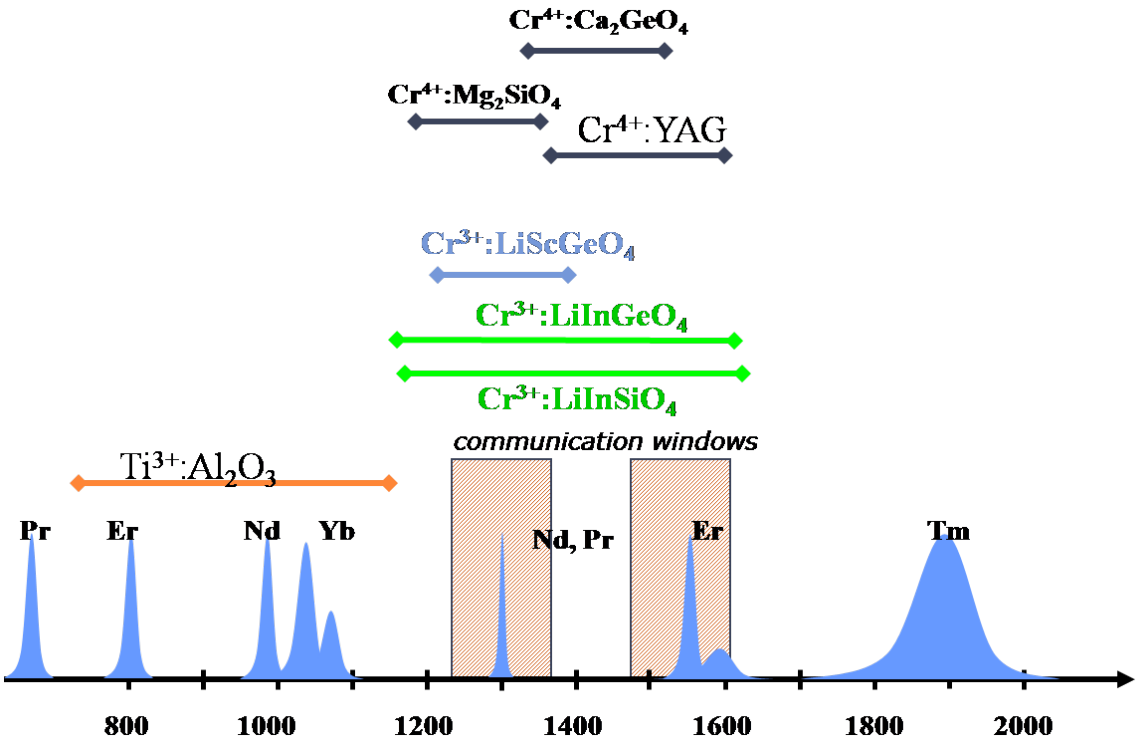

Figure 1.1: Tunable range of Cr^{3+} and Cr^{4+} doped olivine crystals and the optical telecommunication bands

29, 30]. The more surprising result of these crystals is the lasing center is not Cr^{4+}ions, but Cr^{3+}ions[12]. Historically, the lasing center of the first Ruby laser[31] is Cr^{3+}ions and the famous R line is located at "694.3 nm", and the famous Alexandrite (Cr^{3+}:$BeAl_2O_4$)[32] was the first Cr^{3+}-doped tunable laser with range of operation in "700 - 820 nm". Before development of Cr^{3+}:$LiInGeO_4$& Cr^{3+}:$LiInSiO_4$, known Cr^{3+}laser materials never lase in near-infrared region. They also have ultra-wide tunability. Ultra-wide range of tunability and high quantum efficiency make these crystals the very promising media for optical lasers, amplifiers and ultra short pulse generation in the near-infrared range of spectrum.

Figure.1.1 shows the tunable range of $Cr^{3+}$and Cr^{4+}activated olivine crystals and table.1.1 shows the optical communication bands. Optical communication bands have to be categorized depending on the available sources, the available detectors and the

Optical Communications band	Symbol	Wavelength range (nm)
Original	O	1260-1360
Extended	E	1360-1460
Short λ Band	S	1460-1530
Conventional Band	C	1530-1565
Long λ Band	L	1565-1625
Ultralong λ Band	U	1625-1675

Table 1.1: Optical communication bands

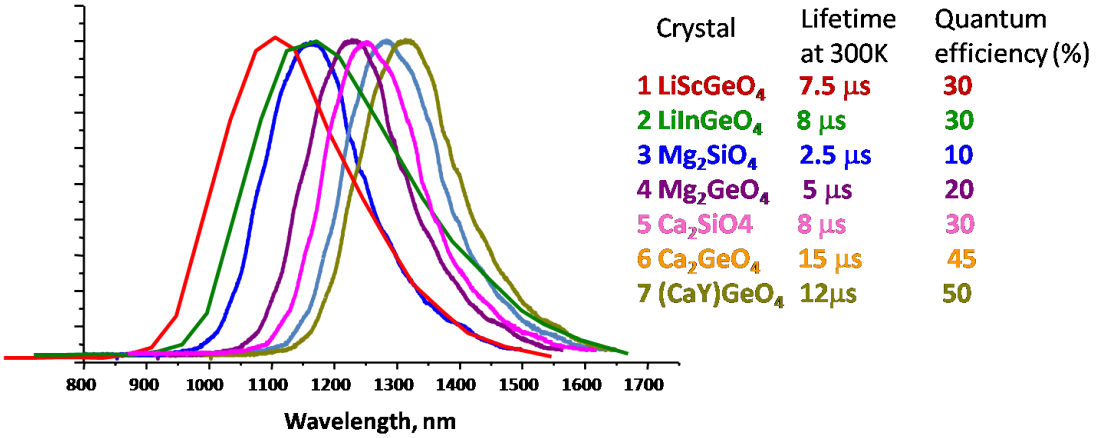

Figure 1.2: Emission spectrum of chromium doped various olivine crystals

available amplifiers. The active ions used in the sources and amplifiers of the optical telecommunication are the rare-earth ions. As shown in the figure.1.1, the tunable range of rare-earth ions is only tens of nm width. In contrast to the tunable bandwidth of rare-earth ions doped crystals, that of Cr doped olivine crystals such as LIGO and LISO wides 460nm. Since the tunable range of these crystals are so wide that it covers all the optical communication bands except U (Ultralong wavelength) band. If we can use these crystals in the optical communications, we can revolutionize the optical communications.

But the problem is the optical properties of transition metal ions such as titanium and chromium ions are very sensitive to the local environment. As shown in the figure.1.2, the emission peak is shifted up to 400nm by changing the host crystal

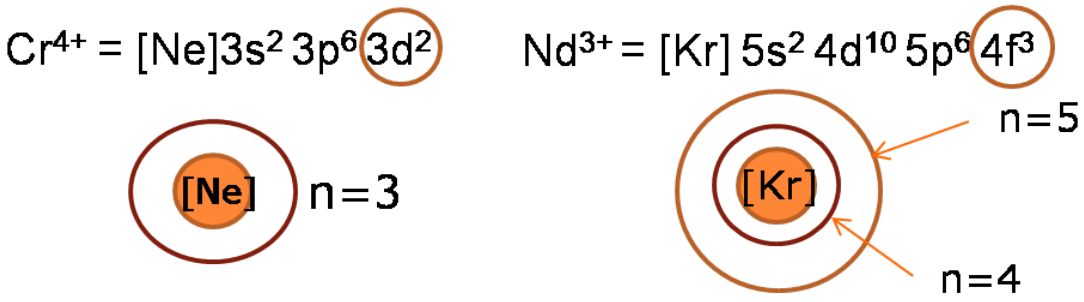

Figure 1.3: Energy level diagram of $Cr^{4+}$and Nd^{3+} ions

composition from $LiScGeO_4$ to $(CaY)GeO_4$. On the other hand, the optical properties of rare-earth ions do not change significantly with the local environment.

The explanation for this reason lies on the electronic structure of each ion. The optical properties of Cr^{4+}ions are determined by 3d electrons while the optical properties of Nd^{3+} ions are determined by 4f electrons. In Cr^{4+}ions, since the outmost electron cloud is 3d electron cloud, the electronic energy is strongly affected by surrounding ligands. On the other hand, in Nd^{3+} ions, the optical properties are determined by 4f electrons and but the outermost electron cloud is 5s and 5p, not 4f. Because of not being the outermost layer spatially, the 4f electronic cloud is minimally affected by the surrounding ligands. Because of that reason, the crystal field split energy of Cr^{4+}ions is about 10,000 cm^{-1} while the crystal field split energy of Nd^{3+} ions is 100 cm^{-1}. If chromium is doped in the glass, the optical properties of Cr doped glass change dramatically and the emission disappears because of wide distribution of changes in local surrounding. On the other hand, the optical properties are maintained in rare-earth ions because of shielding effect. The problem here is we cannot dope chromium directly into the glass while the glass is the best material to make the fiber form. Although Nd-doped, Er-doped glass are the materials of choice to use in fiber lasers and amplifiers, their operation bandwidth is too narrow.

To solve this problem, one solution seems to be to synthesize the glass composite

materials which have the good optical properties of Cr doped single crystal and the good mechanical properties of glass. The desired optical properties of Cr doped olivine single crystal can be maintained by growing the active nano-crystals inside the glass matrix because chromium ions are located in crystalline surrounding. Thus the distribution of local environment changes will be narrower than that in the glass matrix.

In this thesis, I studied the optical center formation in germanate glass ceramics as a function of composition and heat treatment and identified the phase of nanocrystals with array of spectroscopic measurements. This study will help understand the fundamental structure of these composite materials and that in turn will help create the novel laser materials.I'll focus my research on the Cunyite glass ceramics (glass embedded with proven Cr^{4+}:Ca_2GeO_4 laser crystallites) because the spectroscopic properties of Cunyite is well known and only Cr^{4+}valence state can exist in this crystal. Having one valence state greatly reduces the complexity of assignment of emission center.

In this thesis, I also investigated the nanocrystals impregnated porous glass in order to create the glass composite materials. The porous glass gives us the unique way to create the nanocrystals of a few lattice parameters in size.

Chapter 2

Theory of transition metal complexes

When we look at the transition metal complexes, the first thing we notice is their beautiful colors. Where these colors are coming from? Transition metal doped crystals are colorful as shown in fig.(2.1) is due to internal crystal field. In this thesis, since I'm dealing with $Cr^{3+}$and Cr^{4+}ions, I will talk about the theory of first row transition metal ions and the coordination complexes centering these metal ions.

Group#	3	4	5	6	7	8	9	10	11	12
Atomic#	21	22	23	24	25	26	27	28	29	30
	Sc	Ti	V	Cr	Mn	Fe	Co	Ni	Cu	Zn
$[Ar]4s^2$	$3d^1$	$3d^2$	$3d^3$	$4s^1 3d^5$	$3d^5$	$3d^6$	$3d^7$	$3d^8$	$4s^1 3d^{10}$	$3d^{10}$

Table 2.1: First row transition metal ions & their electronic structure

As shown in the table2.1, the valence electronic structure of the first row transition metal is $4s^x 3d^y$. The outermost orbitals having valence electrons are 3d orbitals. Five degenerated d orbitals are $d_{xy}, d_{xz}, d_{yz}, d_{z^2}$ and $d_{x^2-y^2}$. The structure of real function of d orbitals in cartesian coordinate systems is shown in fig.2.2.

Figure 2.1: striking color appearance of transition metal ions doped single crystals[6]

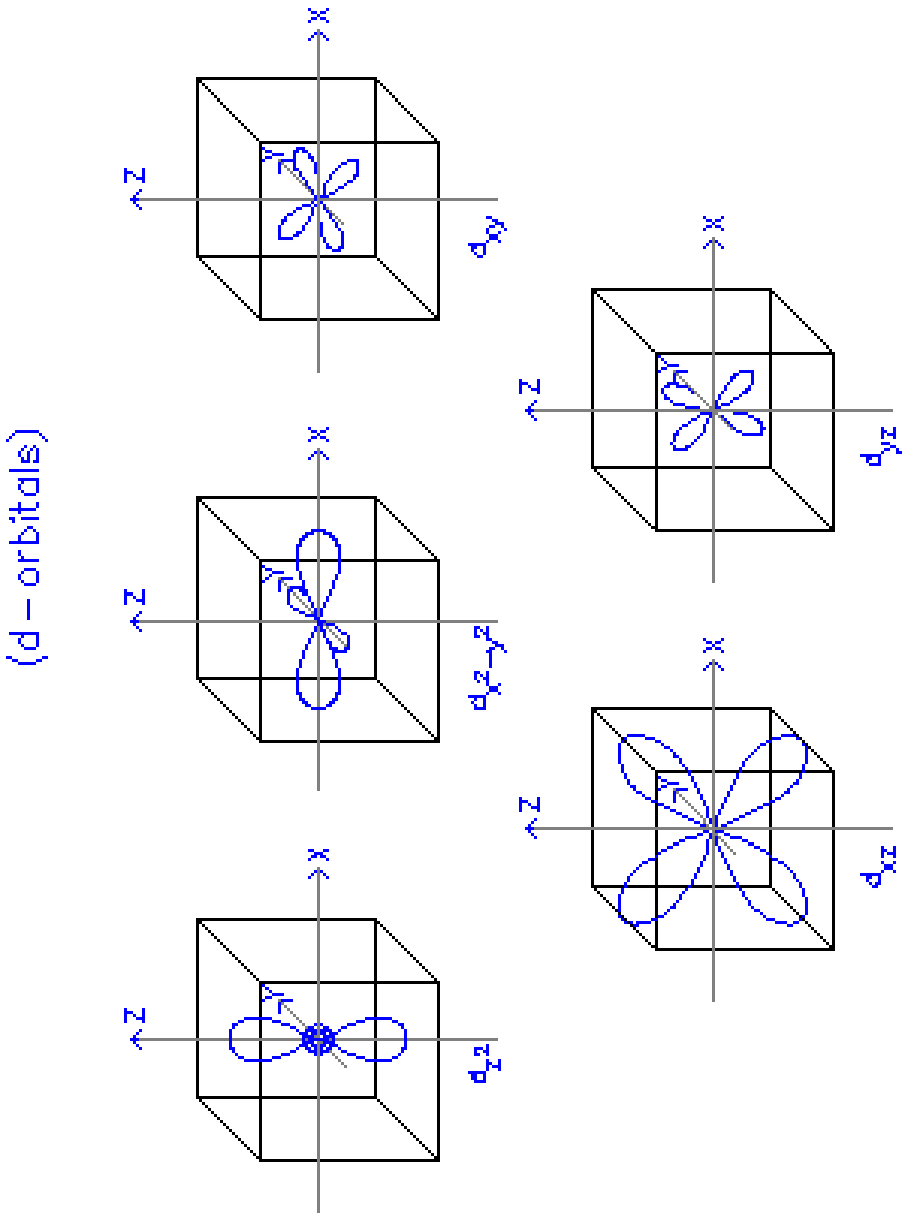

Figure 2.2: Degenerated d orbitals [7]

2.1 One electron system under cubic field (Ti^{3+})

The electronic structure of the titanium ion (Ti^{3+}) is $[Ar]3d^1$. Please refer to table(2.1). There is only one valence electron in the outermost 3d orbitals. Let start to think about the energy level of free (Ti^{3+}) ion.If we think of no free ions can exist in real life, we can think of the metal ions surrounded by the spherical electric crystal field. In the free ions, these degenerated d orbitals have the same energy. Let's say six water molecules are brought in near (Ti^{3+}) free ions and they form the octahedral complex together, $Ti(H_2O)_6^{3+}$. Because of these water ligands, the degeneracy of d orbitals is lifted and they are split into two groups depending on their corresponding energy. I'll talk about how these two groups are split in the octahedral coordination. In the crystal field model, the ligands are treated as the negative point charges and the metal as the positive point charge and the electrostatic interaction between them affects the d orbitals splitting.

As shown in the fig. 2.3, the six ligands are located on the face of the cube and the metal ions are at the center of the cube. The orientation of d_{z^2} orbital directly points to two ligands located on the Z-axis. Also, the orientation of $d_{x^2-y^2}$ orbital directly points to four ligands located on the X and Y-axis. Contrary to d_{z^2} and $d_{x^2-y^2}$, the orientation of d_{xy}, d_{xz}, and d_{yz} orbitals do not directly point to the ligands. Because of this reason, d_{z^2} and $d_{x^2-y^2}$ orbitals are destabilized by $+6Dq_{oct}$ while d_{xy}, d_{xz}, and d_{yz} orbitals are stabilized by $-4Dq_{oct}$. Thus the total crystal field splitting of d orbitals under the octahedral crystal field is $\Delta_{oct} = 10Dq_{oct}$. Here Dq is defined as:

$$Dq = \frac{1}{6}\left[\frac{Ze^2\bar{r^4}}{a^5}\right] \tag{2.1}$$

where,

D: $D = \frac{35Ze}{4a^5}$

q: $q = \frac{2e\bar{r^4}}{105}$

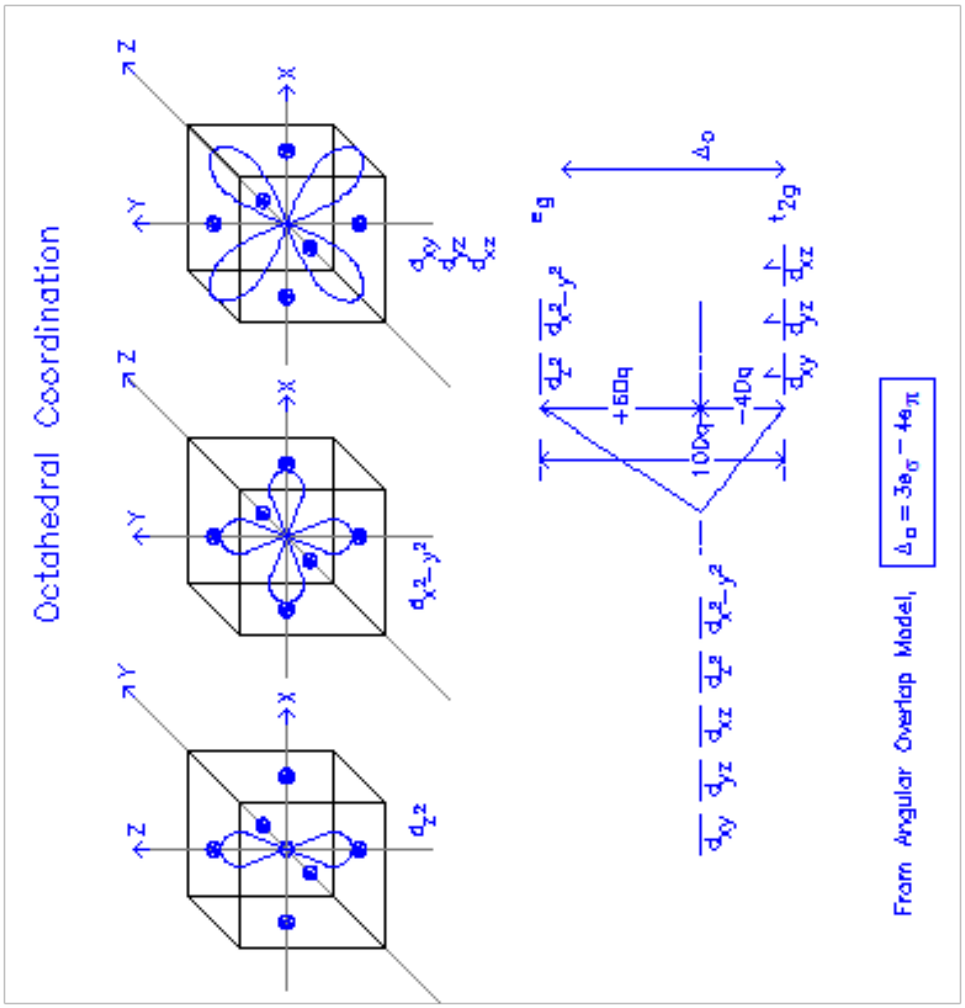

Figure 2.3: Effect of octahedral crystal field on the d orbitals [8]. Explanation of figures: In $[CrO_6]^{9-}$ octahedral complex, the six oxygen ligands are located on the three cartesian axes. As shown in the figure, the electron lobe of d_{z^2} orbital is directly pointed to the oxygen ligands on +z and -z directions. Because of the electrostatic force between ligands and metal electrons is strong, the d_{z^2} orbital is destabilized and its energy is raised related to free ions 3d orbital energy. The same explanation applies to $d_{x^2-y^2}$ orbital. But for d_{xy}, d_{yz} and d_{xz} orbitals, as their orbital lobes are not directly pointed to the oxygen ligands, the energy of these orbitals is decreased relative to free ion 3d orbital.

a: the distance between metal and ligand ions

$\bar{r^4}$**:** the mean fourth power radius of d electrons of the center ion

e: the charge of d electron

Ze: the charge of ligand

.

Usually, Dq parameter is calculated using experimentally measured energy values.

If the coordination of transition metal complex is tetrahedral coordination, the crystal field splitting of d orbitals is weaker than that in octahedral coordination. The reason is as shown in fig.2.4.

Now the four ligands are located at the four edges as shown in the figure and forming the tetrahedron if the ligands are connected. The angle between the two ligands is 109.5 degree. Now if we look at the orientation of d five orbitals with respect to the ligand location, any d orbital doesn't pointed directly to the ligands. This is the main reason why the tetrahedral crystal field is lower than the octahedral crystal field. But compared to d_{z^2} and $d_{x^2-y^2}$ orbitals, d_{xy}, d_{xz}, and d_{yz} orbitals are closer to the ligands and these orbitals are destabilized by $4Dq_{tet}$ and d_{z^2} and $d_{x^2-y^2}$ orbitals are stabilized by $-6Dq_{tet}$. Now the crystal field splitting value is $\Delta_{tet} = 10Dq_{tet}$. The relationship between the octahedral and tetrahedral crystal field strength is $\Delta_{tet} = -\frac{4}{9}\Delta_{oct}$.

One thing to note here is in O_h symmetry (octahedral coordination), d_{z^2} and $d_{x^2-y^2}$ orbitals transform into t_{2g} irreducible representation and d_{xy}, d_{xz}, and d_{yz} orbitals transform into e_g symmetry term. Here, g stands for having the center of symmetry in the complex. Since the octahedral and tetrahedral crystal fields are cubic fields, in T_d symmetry (tetrahedral coordination), d_{z^2} and $d_{x^2-y^2}$ orbitals also transform into t_2 and d_{xy}, d_{xz}, and d_{yz} orbitals transform into e. Here, g is dropped because the tetrahedron doesn't have the center of symmetry. Collectively, we call the two d

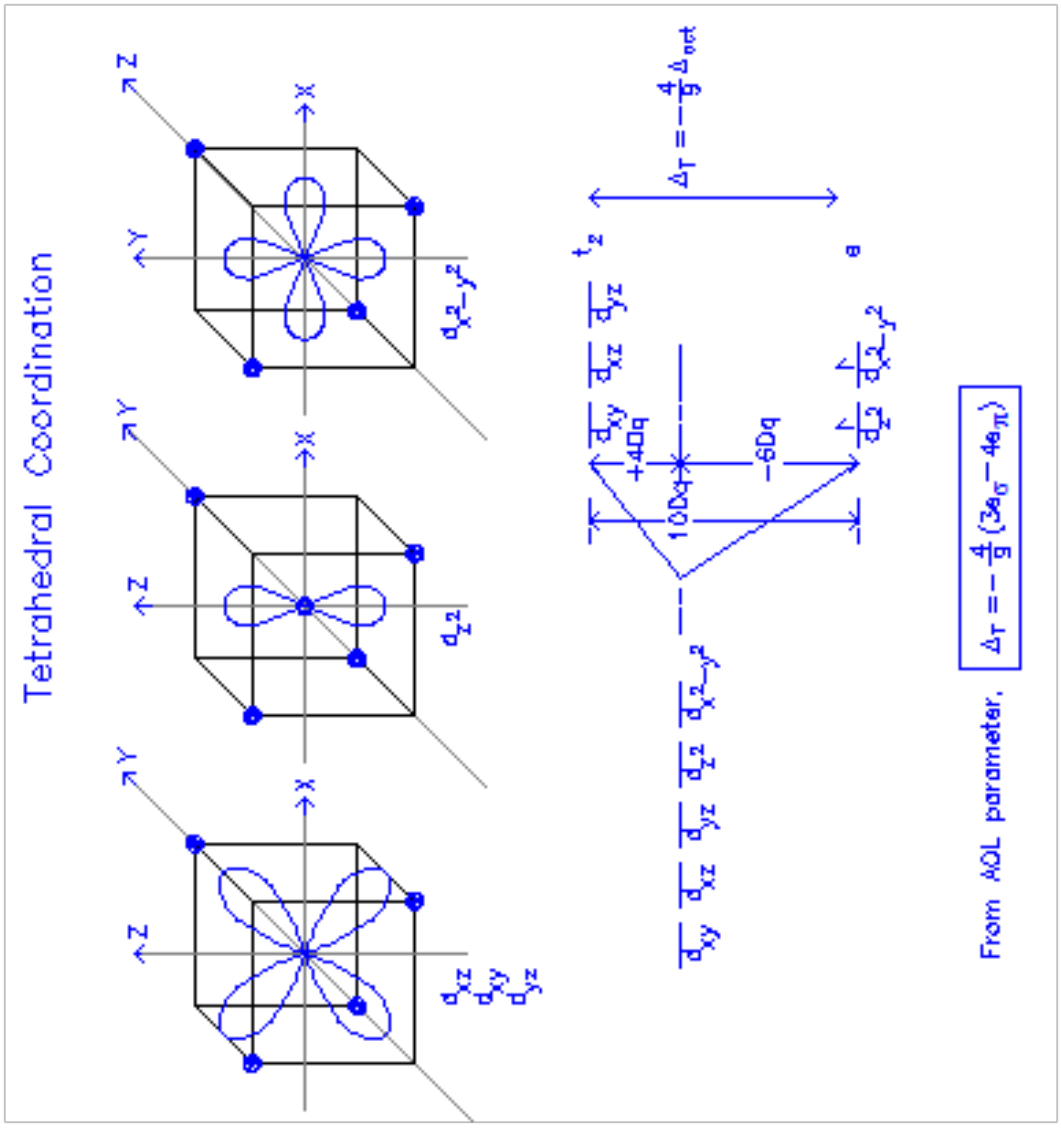

Figure 2.4: Effect of tetrahedral crystal field on d orbitals [8]

orbital groups as t_g orbital having 3 degenerated d orbitals and e_g orbital having 2 degenerated d orbitals. The energy different between the energy of e_g and t_g orbitals is crystal field splitting energy $\Delta_{oct} = 10Dq_{oct}$. This is only true for d^1 and d^9 electron configuration.

In crystal field model, the covalent effect between metal ion and ligands is ignored. In ligand field model, also known as angular overlap model (AOM) considered the covalent effect in addition to the electrostatic interactions between ligand and metal ions. The advantage of using AOM is you need to know only two bonding parameters known as e_σ and e_π to determine the value of crystal field parameter Dq. In the next section, I would like to discuss about the angular overlap model in detail because it is a model of choice for calculating the energy level splitting of d orbitals in transition metal complex with lower symmetry crystal field.

2.1.1 Ti:Al_2O_3 (d^1 System)

The well known Ti:Spphire crystal is an one-electron octahedral coordination system [11, 17]. Because of this reason, its energy level structure is much simpler than other two or three electrons systems. The ground state is t_{2g} and the excited state is e_g. The value of crystal field Δ_{oct} is around 20,000cm^{-1}. According to Jahn-Teller theorem, the nonlinear systems having the orbitally degenerated energy level are not stable and induce the distortion which lifts the orbital degeneracy. Because of this reason, t_{2g} and e_g orbitals are further split and these split energy levels give out the different bands in absorption spectrum.

2.2 Angular overlap model

In angular overlap overlap model, there are two main parameters, e_σ and e_π. e_σ is the sigma bonding energy and e_π is the π bonding energy. When the metal ion interacts

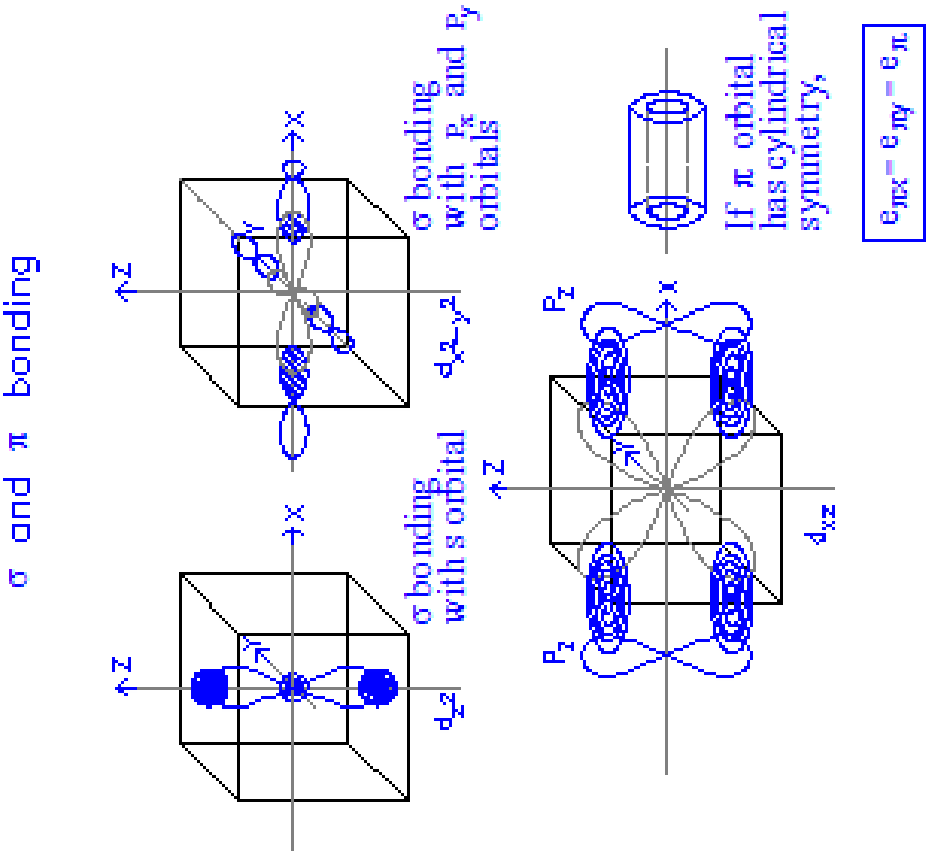

Figure 2.5: σ and π bond formation with d orbitals and ligand orbitals [7]

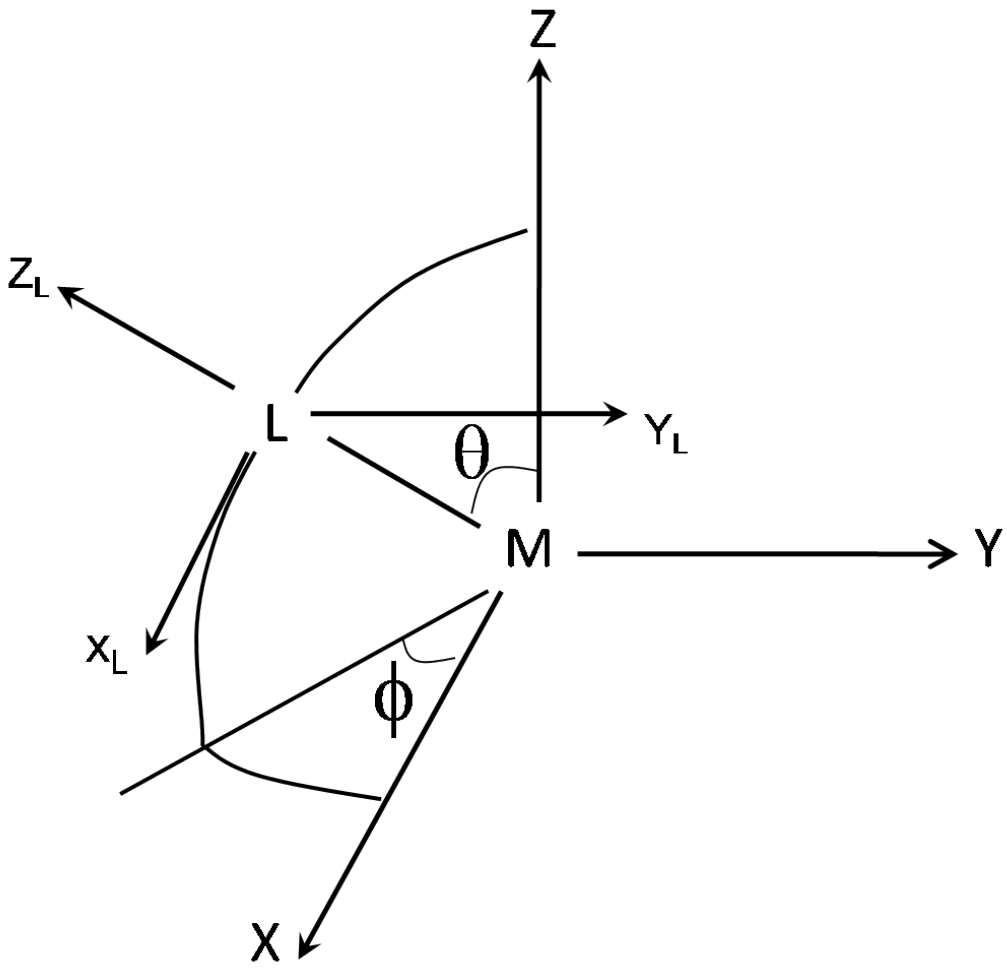

Figure 2.6: Figure showing the metal global coordinate and ligand local coordinate [7]

with the ligands, the energy of d orbital is changed depending on the symmetry of bonding behavior. The illustration of σ and π bond formation with d and ligand orbitals are shown in figure(2.5). In AOM, the effect of all ligands on each d orbitals of metal ions is calculated by using the complex geometry and the location of ligands relative to the metal ions. As shown in fig.2.6, the global coordinate of the metal and local coordinate of ligand is illustrated. The ligand position is defined with three angle parameters. They are:

θ**:** the angle between global Z axis and metal-ligand bond direction

ϕ the angle between global X axis and the projection of metal-ligand bond direction on the global XY plane

ψ**:** the angle between global Z axis and the orientation of ligand XY plane

The table(2.2) defines the angular overlap factors indicating the effect on the d orbitals of the angular rotations θ and ϕ. In other words, these are d orbital wave functions corresponding to σ and ϕ bonding direction.

	F_σ[d,L(θ,ϕ)]	$F_{\pi y}$[d,L(θ,ϕ)]	$F_{\pi x}$[d,L(θ,ϕ)]
$d_{x^2-y^2}$	$(\sqrt{3}/4)\cos 2\phi(1-\cos 2\theta)$	$-\sin 2\phi \sin\theta$	$(1/2)\cos 2\phi \sin 2\theta$
d_{z^2}	$(1/4)(1+3\cos 2\theta)$	0	$-(\sqrt{3}/2)\sin 2\theta$
d_{xy}	$(\sqrt{3}/4)\sin 2\phi(1-\cos 2\theta)$	$\cos 2\phi \sin\theta$	$(1/2)\sin 2\phi \sin 2\theta$
d_{xz}	$(\sqrt{3}/2)\cos\phi \sin 2\theta$	$-\sin\phi\cos\theta$	$\cos\phi\cos 2\theta$
d_{yz}	$(\sqrt{3}/2)\sin\phi \sin 2\theta$	$\cos\phi\cos\theta$	$\sin\phi\cos 2\theta$

Table 2.2: Angular Overlap Factors [7, 17] Indicating the Effect on the d Orbitals of the Angular Rotations θ and ϕ

Here, I would like to show how to calculate the energy levels of d orbitals of metal ions in octahedral coordination (ML_6 system). First, we have to find the matrix

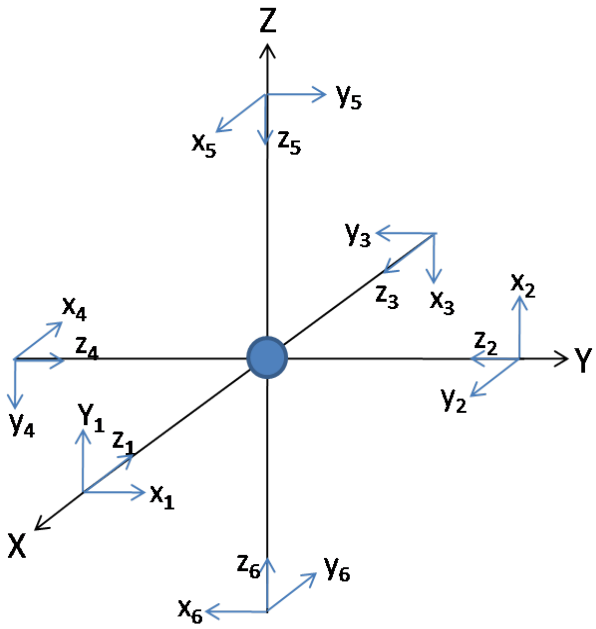

Figure 2.7: Global and Local-Ligand coordinates for ML6 system [7]

elements of octahedral crystal field. The matrix elements can be calculated using eq.2.2.

$$\begin{aligned}\langle \mathrm{d}_i|V_{AOM}|\mathrm{d}_j\rangle = \sum_{k=1}^{n}[&e_\sigma(L_k)F_\sigma(\mathrm{d}_i,\mathrm{L}_k(\theta,\phi))F_\sigma(\mathrm{d}_j,\mathrm{L}_k(\theta,\phi))\\ &+ e_{\pi y}(L_k)F_{\pi y}(\mathrm{d}_i,\mathrm{L}_k(\theta,\phi))F_{\pi y}(\mathrm{d}_j,\mathrm{L}_k(\theta,\phi))\\ &+ e_{\pi x}(L_k)F_{\pi x}(\mathrm{d}_i,\mathrm{L}_k(\theta,\phi))F_{\pi x}(\mathrm{d}_j,\mathrm{L}_k(\theta,\phi))]\end{aligned} \tag{2.2}$$

where, n = total number of ligands.

Global and local ligand coordinates for octahedral (ML_6) system is as shown in fig.2.7. Using this figure, we calculate θ and ϕ of each ligand position in the complex.

Now we starts to calculate the ligand field effect of each ligand on each d orbital, $d_{x^2-y^2}$, d_{z^2}, d_{xy}, d_{xz} and d_{yz}. First, we start to calculate the effect on $d_{x^2-y^2}$ orbital from six ligands, L_1, L_2, L_3, L_4, L_5 and L_6. As illustrated in fig(2.5), $d_{x^2-y^2}$ orbital

	L_1	L_2	L_3	L_4	L_5	L_6
θ°	90	90	90	90	0	180
ϕ°	0	90	180	270	0	0

Table 2.3: The θ and ϕ values of each ligand in ML_6 system

can form only σ bond with four ligands located in X-Y axes in octahedral coordination geometry. Because of this reason, the angular overlap factors indicating π bonding interaction ($F_{\pi x}$ and $F_{\pi y}$) is zero.

From eq.2.2,

$$\langle d_{x^2-y^2}|V_{AOM}|d_{x^2-y^2}\rangle = \frac{3}{4}e_\sigma(L_1) + \frac{3}{4}e_\sigma(L_2) + \frac{3}{4}e_\sigma(L_3) + \frac{3}{4}e_\sigma(L_4) \tag{2.3}$$

Like $d_{x^2-y^2}$ orbital, d_{z^2} orbital also forms σ bonds with ligand orbital. The calculation also shown in the table(2.4).

$$\langle d_{z^2}|V_{AOM}|d_{z^2}\rangle = \frac{1}{4}e_\sigma(L_1) + \frac{1}{4}e_\sigma(L_2) + \frac{1}{4}e_\sigma(L_3) + \frac{1}{4}e_\sigma(L_4) + e_\sigma(L_5) + e_\sigma(L_5) \tag{2.4}$$

As shown in the figure(2.5), d_{xy}, d_{xz} and d_{yz} orbitals bond with ligand orbitals with π symmetry and thus e_σ value is zero for these d orbitals. Depending on the ligand coordinates, d_{xy} has only π bonding in y_L direction and d_{xz} has only π bonding x_L direction while d_{xy} has π bonding in both x_L and y_L directions. The table(2.4) also shows the AOM factors on d_{yz} orbital.

$$\langle d_{yz}|V_{AOM}|d_{yz}\rangle = e_\pi x(L_2) + e_\pi x(L_4) + e_\pi y(L_5) + e_\pi y(L_6) \tag{2.5}$$

By using the table (2.4), Angular Overlap Matrix for the complex is tabulated using eq.2.2.

	F_σ[d,L(θ,ϕ)]	$F_{\pi y}$[d,L(θ,ϕ)]	$F_{\pi x}$[d,L(θ,ϕ)]
For $d_{x^2-y^2}$,			
L_1	$\sqrt{3}/2$	0	0
L_2	-$\sqrt{3}/2$	0	0
L_3	$\sqrt{3}/2$	0	0
L_4	-$\sqrt{3}/2$	0	0
L_5	0	0	0
L_6	0	0	0
For d_{z^2},			
L_1	-0.5	0	0
L_2	-0.5	0	0
L_3	-0.5	0	0
L_4	-0.5	0	0
L_5	1	0	0
L_6	1	0	0
For d_{yz},			
L_1	0	0	0
L_2	0	0	-1
L_3	0	0	0
L_4	0	0	1
L_5	0	1	0
L_6	0	-1	0

Table 2.4: The sample calculation of the effect of each ligand on each d orbitals in ML_6 system

	$d_{x^2-y^2}$	d_{z^2}	d_{xy}	d_{xz}	d_{yz}
$d_{x^2-y^2}$	$0.75e_\sigma(1)+$ $0.75e_\sigma(2)+$ $0.75e_\sigma(3)+$ $0.75e_\sigma(4)$	$-\sqrt{3}/4e_\sigma(1)+$ $\sqrt{3}/4e_\sigma(2)+$ $-\sqrt{3}/4e_\sigma(3)+$ $\sqrt{3}/4e_\sigma(4)$	0	0	0
d_{z^2}	$-\sqrt{3}/4e_\sigma(1)+$ $\sqrt{3}/4e_\sigma(2)+$ $-\sqrt{3}/4e_\sigma(3)+$ $\sqrt{3}/4e_\sigma(4)$	$0.25e_\sigma(1)+$ $0.25e_\sigma(2)+$ $0.25e_\sigma(3)+$ $0.25e_\sigma(4)+$ $e_\sigma(5)+$ $e_\sigma(6)$	0	0	0
d_{xy}	0	0	$e_{\pi x}(1)+$ $e_{\pi y}(2)+$ $e_{\pi y}(3)+$ $e_{\pi x}(4)$	0	0
d_{xz}	0	0	0	$e_{\pi y}(1)+$ $e_{\pi x}(3)+$ $e_{\pi x}(5)+$ $e_{\pi y}(6)$	0
d_{yz}	0	0	0	0	$e_{\pi x}(2)+$ $e_{\pi y}(4)+$ $e_{\pi y}(5)+$ $e_{\pi x}(6)$

Table 2.5: Angular Overlap Matrix of ML_6 system

	$d_{x^2-y^2}$	d_{z^2}	d_{xy}	d_{xz}	d_{yz}
$d_{x^2-y^2}$	$3e_\sigma$	0	0	0	0
d_{z^2}	0	$3e_\sigma$	0	0	0
d_{xy}	0	0	$4e_\pi$	0	0
d_{xz}	0	0	0	$4e_\pi$	0
d_{yz}	0	0	0	0	$4e_\pi$

Table 2.6: Reduced AOM matrix

If all ligands are identical and π bonding have cylindrical symmetry,

$$e_\sigma(1\cdots6) = e_\sigma \tag{2.6}$$

$$e_{\pi x}(1\cdots6) = e_{\pi y}(1\cdots6) = e_\pi \tag{2.7}$$

Then the above AOM matrix reduces into:

$$E(d_{x^2-y^2}) = E(d_{z^2}) = E(t_{2g}) = 3e_\sigma \tag{2.8}$$

$$E(d_{xy}) = E(d_{xz}) = E(d_{yz}) = E(e_g) = 4e_\pi \tag{2.9}$$

Since the energy difference between t_{2g} orbital and e_g orbital is Δ_{oct}, the correlation between the crystal field parameter Dq the angular overlap parameters e_σ and e_π for octahedral coordination and tetrahedral coordination is described in eq(2.10) & eq(2.11) respectively.

$$\Delta_{oct} = 10Dq_{oct} = 3e_\sigma - 4e_\pi \qquad \text{(for octahedral coordination)} \tag{2.10}$$

$$\Delta_{tet} = 10Dq_{tet} = -\frac{4}{9}(3e_\sigma - 4e_\pi) \qquad \text{(for tetrahedral coordination)} \tag{2.11}$$

2.3 Inter-electronic Repulsions: Free ions with two electrons(Cr^{4+})

Up until now, we're only dealing with crystal field effect on one-electron system. If we talk about $Cr^{4+}$and Cr^{3+}ions, Cr^{4+}ion has 2 electrons in 3d orbital while Cr^{3+}ion has 3 electrons in 3d orbital. Now we have to think about the inter-electronic repulsion effect on the energy level splitting in addition to the crystal field splitting. First we only consider the energy level splitting because of inter-electronic repulsion effect without considering crystal field effect. The split energy levels due only to inter-electronic repulsion are called free ions terms.

2.3.1 Free ions terms

As mention in section.2.1, one-electron system has one electron in outermost 3d orbital. Thus there is no inter-electronic interaction in the system and we just need to consider the crystal field effect on five degenerated d orbitals of single existing electron. Now we have two electrons in 3d orbitals and we need to think about the two electrons as one system. To describe the two-electron system, we introduce free ions TERMs. If we only think about one 3d electron, its principle quantum number is $n = 3$, its orbital angular momentum quantum number is $l = 2$, and its spin quantum number is $s = \frac{1}{2}$. The Z-component of l is called magnetic orbital angular momentum quantum number(m_l) and it spans $+l$ to $-l$. If $l = 2$, $m_l = -2, -1, 0, 1, 2$. The Z-component of magnetic spin quantum number is m_s and it spans $+s$ to $-s$. So the energy level of each electron is uniquely defined by using four quantum numbers, n, l, m_l and m_s. Please notice that we use small letter symbol for all quantum numbers for one electron system.

For two-electron systems, we'll use the capital letter for TERM symbol. Free ions TERMs determination is nothing special. Free ion TERMs is one electron system +

M_L	M_S=0	1	-1
4	(2+,2-)		
3	(2±,1∓)	(2+,1+)	(2-,1-)
2	(1+,1-)(2±,0∓)	(2+,0+)	(2-,0-)
1	(1±,0∓)(2±,-1∓)	(1+,0+)(2+,-1+)	(1-,0-)(2-,-1-)
0	(0+,0-)(2±,-2∓)(1±,-1∓)	(2+,-2+)(1+,-1+)	(2-,-2-)(1-,-1-)
-1	(-1±,0∓)(-2±,1∓)	(-1+,0+)(-2+,1+)	(-1-,0-)(-2-,1-)
-2	(-1+,-1-)(-2±,0∓)	(-2+,0+)	(-2-,0-)
-3	(-2±,-1∓)	(-2+,-1+)	(-2-,-1-)
-4	(-2+,-2-)		

Table 2.7: Possible electronic configuration with five d orbitals

electron spin. Now we need to think the spin quantum number in addition to orbital quantum number. Pauli exclusion principle states that no two electrons can have the same quantum numbers. In other word, all other quantum numbers are the same, the electron spin must be different. By using this principle, I'll pair the two electrons in five d orbitals. The degeneracy of d orbitals is m_l=-2,-1,0,1,2 while m_s= $\pm\frac{1}{2}$.

M_L and M_s for two-electron system can be calculated by using eq.(2.12) and eq.(2.13).

$$M_L = m_{l1} + m_{l2} \tag{2.12}$$

$$M_S = m_{s1} + m_{s2} \tag{2.13}$$

As shown in the above table, there are total of 45 components by pairing the two electrons in five d orbitals in every possible ways by using Pauli exclusion principle. Compared to two electrons systems, one electron system has total of 10 wavefunctions: one electron, five d orbitals with spin up and spin down. One thing to note here is we can determine the upper limit of possible energy levels for one electron and two electron systems. The maximum split energy levels you can get from one electron system under the influence of infinite field is 10 while the maximum split energy levels you can get from two-electron system under the influence of infinite field is 45

Quantum #	One-electron	Two-electron
orbital quantum number	l	L
spin quantum number	s	S
magnetic orbital quantum number	$m_l(-l \cdots + l)$	$M_L(-L \cdots + L)$
magnetic spin quantum number	$m_s(-s \cdots + s)$	$M_S(-S \cdots + S)$

Table 2.8: Quantum number notation for one-electron and two-electron systems

because there are total of 45 possible wave functions in two-electron system.

Now I have 45 components in my hand and I'll write down the free ions TERMs for two-electron system. A free ion term is a collection of degenerated wave functions from 45 possible components. The analogy between free ions terms and one electron quantum number is shown in the table(2.8).

From the table(2.7), we can count the number of occurrence of specific M_L and M_S values.

$$\begin{aligned} M_L &= \pm 4 \rightarrow 1 \text{ time} \\ &= \pm 3 \rightarrow 4 \text{ times} \\ &= \pm 2 \rightarrow 5 \text{ times} \\ &= \pm 1 \rightarrow 8 \text{ times} \\ &= 0 \rightarrow 9 \text{ times} \\ M_S &= 0 \rightarrow 25 \text{ times} \\ &= \pm 1 \rightarrow 10 \text{ times} \end{aligned}$$

In one electron system, if you know l and s and you can immediately write down m_l and m_s values. For two-electron system, here we just know M_L and M_S. From the known M_L and M_S occurrence times, the backward calculation has to be made

L =	0	1	2	3	4
X =	S	P	D	F	G

Table 2.9: Two-electron system orbital quantum number definition

S =	0	$\frac{1}{2}$	1	$1\frac{1}{2}$	2	$2\frac{1}{2}$
Term =	Singlet	Doublet	Triplet	Quartet	Quintet	Sextet
2S+1=	1	2	3	4	5	6

Table 2.10: Free ion terms are named according to spin quantum number of two-electron system

to determine two-electron system orbital (L) and spin (S) quantum numbers.

The free ion term is defined as ${}^{2S+1}X$. Here, $2S+1$ is the spin multiplicity and describe the total unpaired electrons present plus one. S is the multi-electron spin quantum number. Terms are named according to the value of S as defined in table(2.10).

The steps to determine the free ions terms of two-electron system are as follows:

Step1: Start with the largest M_L value. Here is $M_L = 4$. $M_L = 4$ corresponds to $L = 4$. $L = 4$ is G orbital. The degeneracy of G orbital is $-4, -3, -2, -1, 0, 1, 2, 3, 4$ (M_L). Since the degeneracy of G orbital is 9, there are total of 9 wave functions. G occurs only one time. Thus the multiplicity of G term is 1. This translates to $S = 0$. Thus the free ion term is ${}^1G$. We need to subtract one time from

each M_L value and 9 times from $M_S = 0$. This reduces to

$$\begin{aligned} M_L &= \pm 3 \rightarrow 3 \text{ times} \\ &= \pm 2 \rightarrow 4 \text{ times} \\ &= \pm 1 \rightarrow 7 \text{ times} \\ &= 0 \rightarrow 8 \text{ times} \\ M_S &= 0 \rightarrow 16 \text{ times} \\ &= \pm 1 \rightarrow 10 \text{ times} \end{aligned}$$

Step2: Choose again the largest M_L value. This time is $M_L = 3$, which corresponds to $L = 3$. $L = 3$ is F orbital. The degeneracy of F orbital is $-3, -2, -1, 0, 1, 2, 3$ (M_L). F occurs 3 times. Thus the multiplicity of F term is 3. This leads to $S = 1$ and the degeneracy of S is $-1, 0, 1$ (M_S). The resulted free ions term is ${}^3F$. Since F occurs 3 times, we need to subtract 3 times from each M_L and 7 times from each M_S. This leads to

$$\begin{aligned} M_L &= \pm 2 \rightarrow 1 \text{ time} \\ &= \pm 1 \rightarrow 4 \text{ times} \\ &= 0 \rightarrow 5 \text{ times} \\ M_S &= 0 \rightarrow 9 \text{ times} \\ &= \pm 1 \rightarrow 3 \text{ times} \end{aligned}$$

Step3: The largest M_L this time is 2, which leads to $L = 2$, which is D orbital. The degeneracy of D orbital is $-2, -1, 0, 1, 2$ (M_L).Since it occurs 1 time, the

multiplicity of D term is 1. Thus S is 0. The free ion term this time is ^1D. We need to subtract one time from each M_L and 5 times from $M_S = 0$. This leads to

$$M_L = \pm 1 \rightarrow 3 \text{ times}$$
$$= 0 \rightarrow 4 \text{ times}$$
$$M_S = 0 \rightarrow 4 \text{ times}$$
$$= \pm 1 \rightarrow 3 \text{ times}$$

Step4: The largest M_L is 1, which is P orbital. The degeneracy of P is $-1, 0, 1$ (M_L). Since it occurs 3 times, the multiplicity is 3, leading to S is 1. The degeneracy of S is $-1, 0, 1$ (M_S). The free ion is ^3P. We need to subtract 3 times from each M_L and 3 times from each $M_S = 0$. This leads to

$$M_L = 0 \rightarrow 1 \text{ time}$$
$$M_S = 0 \rightarrow 1 \text{ time}$$

Step5: Now M_L is 0, which is S orbital occurring 1 time. Thus the last free ion term is ^1S.

Thus the free ions term of d^2 system is ^1G, ^3F, ^1D, ^3P and ^1S. If we count the total orbital degeneracy and spin degeneracy, the total number of wave functions is 45.

The main idea here is we need to accommodate the electrons in 10(orbital+spin) degenerated d orbitals by using Pauli Exclusion Principle and to generate the free ion terms using the same technique described above for the two-electron system.

Configuration	Terms	Total ψ
d^1	^2D(Term) (or) $d_0(\pm\frac{1}{2}), d_{\pm1}(\pm\frac{1}{2}), d_{\pm2}(\pm\frac{1}{2})$(One e^- notation)	10
d^2	^3F, ^3P, ^1G, ^1D and ^1S	45
d^3	^4F, ^4P, ^2H, ^2G, ^2F, ^2D (2 times) and ^2P	120

Table 2.11: The terms that arise from $d^1(Ti^{3+})$, $d^2(Cr^{4+})$ and $d^3(Cr^{3+})$ configuration

If there is one electron in 3d orbital, there are 10 degenerated orbitals. *They all have the same energy.* If another electron brings into the system, these degenerated orbitals transform into the free ion TERMs *which doesn't have the same energy because of the inter-electronic repulsion forces.* The relative energy value of the transformed free ion terms for a two-electron system is $^3F >^3 P >^1 G >^1 D >^1 S$. The ground term of the system is ^3F. The determination of ground term for each electron configuration is determined using Hund's rules. Hund's rule states that

1. Of the terms of a configuration, those with maximum multiplicity tend to the lowest. That means that electron pairing increases the total energy of the system.

2. Of the terms with maximum multiplicity, that with the largest value of L lies lowest.

2.3.2 Racah Parameters describing Electronic Repulsions in a two-electron system

If the d orbital has more than one electron, 10 degenerated d orbitals transforms into free ions terms and these terms doesn't have the same energy value because of inter-electronic repulsions. To describe the energy separation between them, the two parameters (B & C) is used. They describes the strength of electronic repulsion interaction which split the d orbitals. These parameters are called Racah parameters. The energy difference between the free ion terms with the same multiplicity can be

described using only B parameter while the energy difference between the terms with the different multiplicity needs both B and C parameters. Since the electronic transition moment is strong for spin-allowed transition (terms with same multiplicity), B parameter is more important than C. For a two-electron system, the free ions value of B and C/B is $866cm^{-1}$ and 4.42. When the two-electron system is placed under the influence of specific crystal field, the free ions value of B is somewhat reduced because of covalency between d and ligand orbitals. Accordingly, the energy difference between free ions terms changes. Figure(2.8) shows the energy of free ion terms of two-electron system with respect to B and C Racah parameters.

2.4 Crystal field + Inter-Electron Repulsion in a two-electron system

Up until now, we only consider the free ions for two-electron system. We just only think about d orbital splitting because of the inter-electronic repulsions. If the cubic crystal field such as octahedral or tetrahedral crystal field surrounds the two-electron system such as Cr^{4+}ions, now we have to think about how the free ion terms are split because of crystal field.

The d orbitals are split because of both inter-electronic repulsions and surrounding crystal field. The question here is which interaction is stronger between these two. If the inter-electronic repulsions is stronger than the crystal field strength, in calculation the d orbital splitting energy levels, we start with the free ion terms and then make the splitting of free ions terms under the influence of crystal field. This kind of calculation is done in *the weak field model*.

On the other hands, if the crystal field is stronger than the inter-electronic repulsions, we use *the strong field model*. In the strong field model, d orbitals from each electron are split into t_2 and e orbitals. Then these t_2 and e orbitals are split again

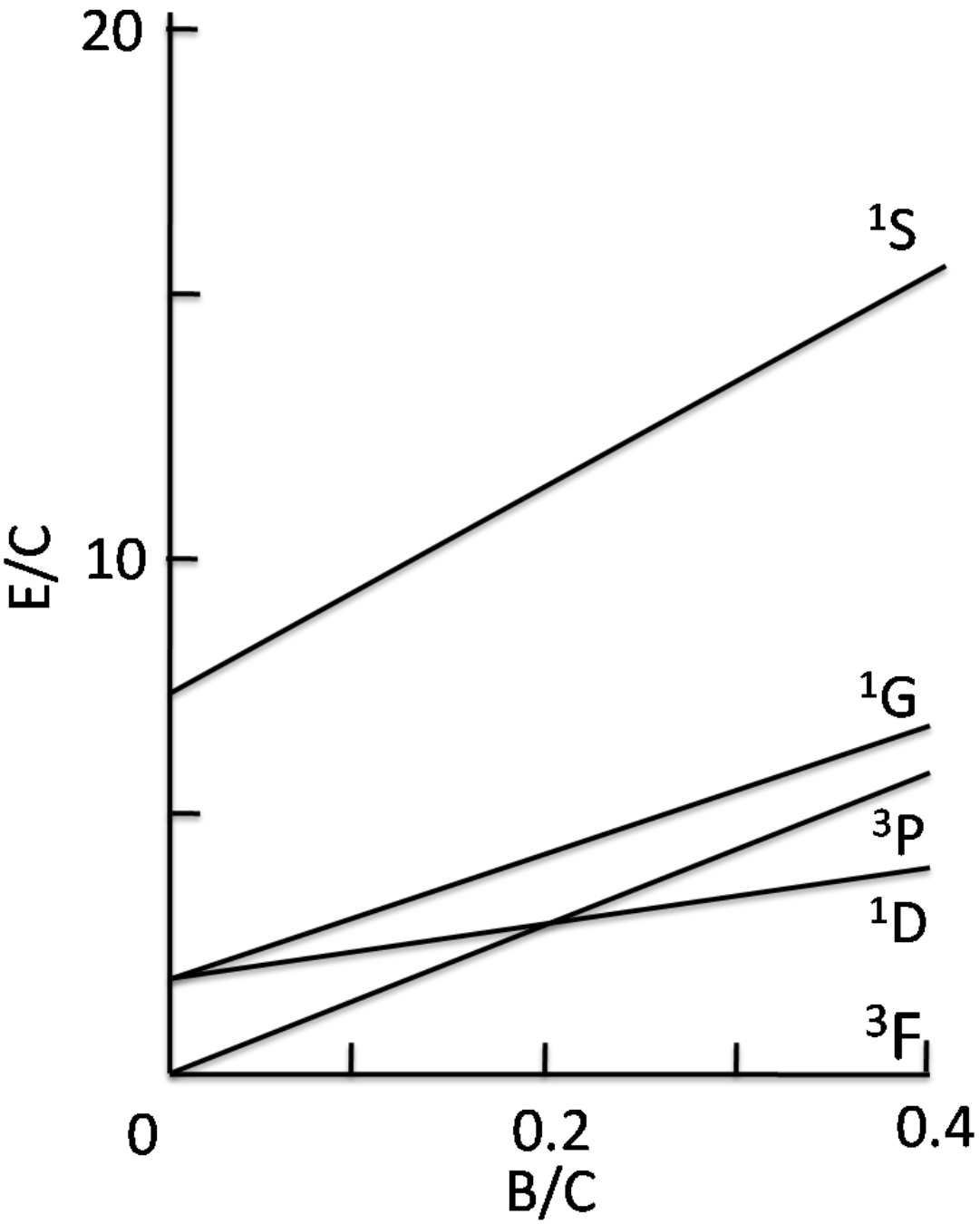

Figure 2.8: Variation of energy of free ion terms with inter-electronic repulsion parameters B & C. The picture is taken from ref.[7].

because of the inter-electronic repulsions.

2.4.1 Weak field model

As mention in section.2.4, in weak field model, the electronic energy levels resulted from d orbital splitting are calculated first from the inter-electronic repulsions and then from crystal field. The resulted energy levels from inter-electronic repulsions are free ion TERMs. **The free ions term of d^2 system is ^1G, ^3F, ^1D, ^3P and ^1S.**

Since the cubic field and the tetrahedral crystal field strength differs from the octahedral crystal field by a numerical factor ($\Delta_{tet} = -\frac{4}{9}\Delta_{oct}$ and $\Delta_{cubic} = -\frac{8}{9}\Delta_{oct}$) , I start with the octahedral crystal field effect on d^2 configuration to examine the cubic field effect on the mulielectron systems. If the two-electron system is placed under the octahedral crystal field, the free ion terms are further split by V_{oct}. One important thing to note here is *the crystal field only lift the orbital degeneracy of the free ion terms. In other words, the crystal field doesn't lift the spin degeneracy.Because of this reason the multiplicity of the terms remain unchange.*

S Term: Since there is no degeneracy in S term, S term is not further split by octahedral crystal field.

P Term: For d^2 and d^3 systems, P term is not split by octahedral crystal field.

D Term: There is one to one correspond between one electron d orbital and two-electron D Term. Since d orbital is split into two groups (t_{2g} and e_g) under the octahedral crystal field, D Term also is split to two groups (T_{2g} and E_g) under V_{oct}. Please notice that for D Term, the capital letter symmetry symbols are used while the small letter symbols are used for one electron system.

F Term: The one electron f orbital is split into t_{1g}, t_{2g}, and a_{1g} under the octahedral crystal field. Thus F term is split into three terms. These are T_{1g}, T_{2g}, and A_{1g}.

${}^1S(1)$	${}^1A_1(1)$
${}^3P(9)$	${}^3T_1(9)$
${}^1D(5)$	${}^1E(2)+{}^1T_2(3)$
${}^3F(21)$	${}^3A_2(3)+{}^3T_1(9)+{}^3T_2(9)$
${}^1G(9)$	${}^1A_1(1)+{}^1E(2)+{}^1T_1(3)+{}^1T_2(3)$

Table 2.12: Under T_d field, further split symmetry-adapted energy levels from free-ion terms. The number in the bracket describes the total number of degenerated orbitals of respective energy terms.

G Term: G Term is split the same manner as one electron g orbital under V_{oct}.

In ref([22]), by using the group theory formalism, how the degeneracy of ${}^3F$, ${}^3P$, ${}^1G$, ${}^1D$ and ${}^1S$ orbitals are lifted under the tetrahedral crystal field into different symmetry terms is shown in detail.*In transforming into the symmetry terms, you can use one electron wave functions because there is one to one correspondence between s,p,d,f,g one-electron orbitals and S,P,D,F and G multi-electron orbitals.*The point symmetry of tetrahedral field is T_d.

2.4.1.1 Quantitative determination of split energy levels of ${}^3F$ term under V_{oct}

In this section, I would like to show an example of how the calculation is done to determine the energy of split terms of free ion ${}^3F$ under V_{oct}. L value of F term is 3. The M_L values of L is $-3, -2, -1, 0, 1, 2, 3$. The total orbitals is 7 since the spin degeneracy is not lifted under V_{oct}. We need to create $7X7$ matrix to find the energy of 7 orbitals. The matrix elements are $\langle\{L, M_L\}|V_{oct}|\{L, M_L\}\rangle$ such as $\langle\{3, \pm3\}|V_{oct}|\{3, \pm3\}\rangle$. Example of matrix elements calculation is $\langle\{3, 0\}|V_{oct}|\{3, 0\}\rangle$ = C_0(0,0)+C_1(-1,-1)+C_2(-2,-2). (0,0) is a wave function specified by M_L with each electron in two electron system having the magnetic quantum number 0. I left out the calculation here and you can find the complete calculation from the book([7]). The calculated matrix element values and the resulted crystal field matrix is shown

$\{L, M_L\}$	$\{3,3\}$	$\{3,2\}$	$\{3,1\}$	$\{3,0\}$	$\{3,-1\}$	$\{3,-2\}$	$\{3,-3\}$
$\{3,3\}$	$-3Dq-E$				$\sqrt{15}Dq$		
$\{3,2\}$		$7Dq-E$				5Dq	
$\{3,1\}$			$-Dq-E$				$\sqrt{15}Dq$
$\{3,0\}$				$-6Dq-E$			
$\{3,-1\}$	$\sqrt{15}Dq$				$-Dq-E$		
$\{3,-2\}$		5Dq				$-7Dq-E$	
$\{3,-3\}$			$\sqrt{15}Dq$				$-3Dq-E$

Table 2.13: Crystal field matrix of two-electron system under octahedral crystal field.

E=-6Dq	${}^3T_{1g}$	$\frac{1}{\sqrt{24}}[\sqrt{15}\{3,3\}-3\{3,-1\}]$ $\{3,0\}$ $\frac{1}{\sqrt{24}}[\sqrt{15}\{3,-3\}-3\{3,1\}]$
E=2Dq	${}^3T_{2g}$	$\frac{1}{\sqrt{24}}[3\{3,3\}+\sqrt{15}\{3,-1\}]$ $\frac{1}{\sqrt{2}}[\{3,2\}-\{3,-2\}]$ $\frac{1}{\sqrt{24}}[3\{3,-3\}+\sqrt{15}\{3,1\}]$
E=12Dq	${}^3A_{1g}$	$\frac{1}{\sqrt{2}}[\{3,2\}+\{3,-2\}]$

Table 2.14: Under V_{oct} crystal field, the corresponding 7 wave functions associated with the energy value $-6Dq$, $2Dq$ and $12Dq$.

in table(2.13).

The solutions of the above matrix are: $E=-6Dq$ occurring 3 times, $E=2Dq$ occurring 3 times and $E=12Dq$ occurring 1 times. As described in section.2.4.1, split energy levels of ${}^3F$ term under V_{oct} are ${}^3T_{1g}$, ${}^3T_{2g}$, and ${}^3A_{1g}$. The calculation of wave functions shows that ${}^3T_{1g}$ is stabilized by $-6Dq$, while ${}^3T_{2g}$ and ${}^3A_{1g}$ are destabilized by $2Dq$ and $12Dq$ respectively under octahedral crystal field. The ascending order of energy level in octahedral crystal field is ${}^3T_{1g} < {}^3T_{2g} < {}^3A_{1g}$. Since $\Delta_{tet} = -\frac{4}{9}\Delta_{oct}$, in the tetrahedral crystal field, ${}^3T_1$ is destabilized by $6Dq$, while ${}^3T_2$ and ${}^3A_1$ are stabilized by $-2Dq$ and $-12Dq$ respectively. Thus the ascending order of energy level in tetrahedral crystal field is ${}^3A_1 < {}^3T_2 < {}^3T_1$.

For V_{oct}, using the energy value $-6Dq$, $2Dq$ and $12Dq$, the corresponding 7 wave functions can be generated. They are tabulated in table(2.14).

Thus the free ion degenerated orbitals of ${}^3F$ term is $\{3,\pm3\}$, $\{3,\pm2\}$, $\{3,\pm1\}$

and $\{3, 0\}$. Under the octahedral crystal field, some orbitals are mixed if the V_{oct} matrix has off-diagonal terms and the new 7 orbitals are formed. These new 7 orbital wavefunctions are described in table(2.14).

2.4.2 Strong field model

If the crystal field is stronger than the inter-electronic repulsions, the strong field model should be used. In the strong field model, the energy splitting is determined first by the crystal field and the split terms are determined without the effect of inter-electronic repulsions. If there is no inter-electronic repulsion, we can treat a two-electron system as an one-electron system in the crystal field. Thus in the octahedral crystal field, the d orbitals are split into t_{2g} and e_g orbital groups. Now we will bring in the inter-electronic repulsion into the consideration. To determine orbital splitting because of inter-electronic repulsion, we need to think the possible electronic configuration. On important thing not to confuse here is *small symmetry letters are used for one-electron system while Capital symmetry letters are used for two (or) more electron system.*In the octahedral crystal field, t_{2g} orbitals are stabilized by $-4Dq$ while e_g orbitals are destabilized by $6Dq$. What are the possible electronic configurations for the two-electron system?

As shown in fig.2.9, the two electrons are placed only in t_{2g} bonding orbitals and t_{2g}^2 configuration are formed. Since both electrons are in bonding orbitals, the energy of orbitals of t_{2g}^2 configuration is lowest among possible configuration. If one electron is in t_{2g} (bonding orbital) and another in e_g (anti-bonding orbital), the configuration $(t_{2g}^1 e_g^1)$ is formed. Electron configuration e_g^2 is formed if both electrons are in e_g anti-bonding orbitals. It is understandable that the energy of orbitals of $t_{2g}^1 e_g^1$ configuration is lower than these of e_g^2. The energy difference between each consecutive configuration is Δ_{oct}.

The degeneracy of t_{2g} and e_g orbitals are lifted depending on the electronic con-

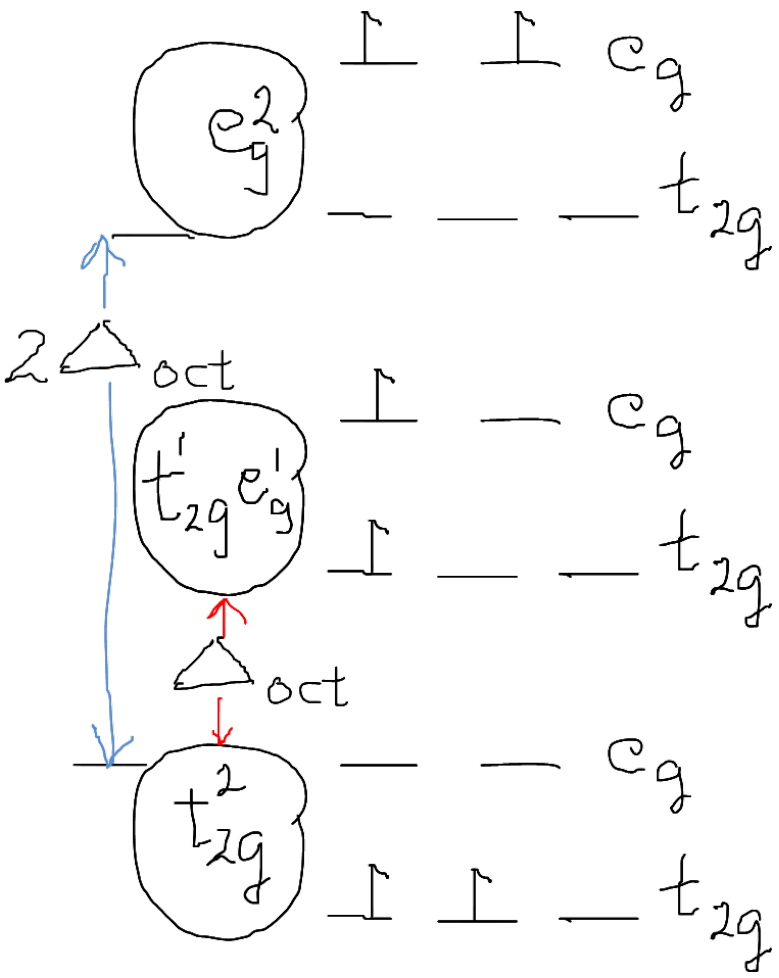

Figure 2.9: Possible electron configurations of a two-electron system in octahedral crystal field

electron configuration	generated terms
t_{2g}^2	$T_{1g}^3 + T_{2g}^1 + E_g^1 + A_{1g}^1$
$t_{2g}^1 e_g^1$	$T_{1g}^1 + T_{2g}^1 + T_{1g}^3 + T_{2g}^3$
e_g^2	$A_{2g}^3 + E_g^1 + A_{1g}^1$

Table 2.15: Split energy levels for each electronic configuration in strong field model.

figurations described above. The split terms can be generated by finding the direct product of symmetry label(t_{2g} or e_g) of d orbitals each electron occupies. The split levels of each configuration are tabulated in table(2.15).

How the energy terms are generated by direct product of one-electron orbitals are shown in the next section in detail. Calculating the multiplicity in strong field model is a little bit complicated and I'm not showing here.

2.4.2.1 Calculating the energy levels of transition metal complex under cubic field using strong field model

In practice, the strong field model is a model of choice to calculate the energy terms of a complex. The Sugano-Tanabe diagrams are drawn using strong field calculation. In strong field model, you first need to find the wavefunctions of cubic field terms of one electron system using 5 (d) orbital wavefunctions. Then by using the wavefunctions of cubic field terms, you can calculate the energy eigenvalues by building the inter-electronic repulsion interaction matrix. If the complex symmetry is high, there will be little interaction among the different terms and only the diagonal matrix elements are resulted. If the complex symmetry is low, the off-diagonal matrix elements will be non-zero value, the wavefunctions of the final orbital terms and calculation will be complex because of coupling between t_{2g} and e_g orbital wavefunctions.

2.4.2.2 Group Theory - Reducible and Irreducible Representations

In the study of coordination complex, the optical and magnetic properties varies dramatically with the symmetry of the complex. If the complex's symmetry is reduced from cubic field, these properties are quite different from the ones with cubic field. That's why understanding the symmetry of the complex, orbitals and bonding, etc.., is very important to understand the material properties of the transition metal complexes. Because of this reason, the application of group theory to understand the properties of the transition metal complexes are quite successful. That's why the split energy level is labeled according to the irreducible representation of a particular point group where the complex belongs.

2.4.2.2.1 Formula used to find the irreducible representations from reducible representation For any reducible representation Γ

$$\Gamma = \sum_j a_j \Gamma_j$$

where, a_j = the integer coefficient of irreducible representation

Γ_j = the irreducible representation such as

$A_1, A_2, E, T_1$and T_2 in T_d symmetry

$$a_j = \frac{1}{n} \sum_i \chi_{\mathbf{R}}(\Gamma_{total}) \times \chi_{\mathbf{R}}(\Gamma_i) \times m$$

where, n = the order of a specific group

or the total number of possible symmetric operations

$\chi_{\mathbf{R}}(\Gamma_{total})$ = the character of a reducible representation Γ_{total}

for a symmetric operation $\mathbf{R}$

$\chi_{\mathbf{R}}(\Gamma_i)$ = the character of an irreducible representation Γ_i

for a symmetric operation $\mathbf{R}$

m = the multiplicity of a symmetric operation $\mathbf{R}$

$\mathbf{R} = E(identity), C_2, C_3, C_4, etc.(rotation), \sigma_v, \sigma_h, etc.(reflection)$

(2.14)

2.4.2.2.2 Direct Product Table If you use the strong field model, the inter-electronic repulsion terms are generated by calculating the direct product of the irreducible representation of the orbital each electron localizes. Then you need to know how to generate the irreducible representation of a group from the reducible

$O \otimes O$	A_1	A_2	E	T_1	T_2
A_1	A_1	A_2	E	T_1	T_2
A_2	A_2	A_1	E	T_2	T_1
E	E	E	$A_1 + A_2 + E$	$T_1 + T_2$	$T_1 + T_2$
T_1	T_1	T_2	$T_1 + T_2$	$A_1 + E + T_1 + T_2$	$A_2 + E + T_1 + T_2$
T_2	T_2	T_1	$T_1 + T_2$	$A_2 + E + T_1 + T_2$	$A_1 + E + T_1 + T_2$

Table 2.16: The direct product table of the pure rotation group having octahedral symmetry.

	A	B	C	D	E	F	G
	$\Gamma_{E\otimes E}$	order	A_1	A_2	E	T_1	T_2
1	4	1	1	1	2	3	3
2	1	8	1	1	-1	0	0
3	4	3	1	1	2	-1	-1
4	0	6	1	-1	0	1	-1
5	0	6	1	-1	0	-1	1
6		24	24	24	24		
7			1	1	1		

Table 2.17: Sample calculation of direct product table.

terms resulted from the direct product. The following is one example how to generate the direct product table of 'O' group.

As an example, Let's find $E \otimes E$. To get the direct product table, we should use Microsoft excel.

Step1: Using character table of group 'O', find the product of character of E representation and place the result in column A.

Step2: Place the order of each symmetry element (E, C_3, C_2, C_4, C_2') in column B.

Step3: Place the character of each representation in column C, D, E, F, and G.

Step4: Do the calculation for each column C, D, E, F, and G by using the formula $\sum_{i=1}^{5}(A_i \times B_i \times C_i^*)$. In place of C, replace respective column letter for each calculation

Step5: Find the total number of order in cell B6 and divide cell C6,D6,E6,F6 and G6 by B6.

Step6: Since only A_1, A_2 and E has non-zero value, the result is $E \otimes E = A_1 + A_2 + E$.

2.5 Correlation between weak field model and strong field model

In practice, the energy of split orbitals of multi-electron systems under cubic field can be calculated using both weak field or strong field model. The beauty of science is it will give you the same result either you start with free ion terms or cubic field split d orbitals (t_{2g} and e_g).

Figure.2.10 shows the correlation diagram for free ion terms with strong-field configurations for $d^2(Cr^{4+})$ in T_d symmetry. The figure shows the energy level with the same multiplicity in red color. We're only interested in spin-allowed transitions.

The left side of fig.2.10 shows the energy diagram of weak field crystals and the right side shows that of strong field crystals. Both the weak field and strong field systems, the ground level doesn't change. It still $^3A_2$.

The first excited state in weak field crystal is $^3T_2$ while the first excited state is strong field crystal is ^1E. Thus, in weak field crystal, the emission is broad and strong because of inter-configurational($e_g^2 \rightarrow t_{2g}^1 e_g^1$) and spin-allowed transition. But, in strong field crystal, the emission is sharp and weak because of intra-configuration ($e_g^1 \rightarrow e_g^1$) and spin-forbidden transition.

It is also interesting to see that $^3T_2$ level is stronger in energy than that of $^3T_1$ in strong crystal field.

There is a so-called Sugano-Tanabe Diagrams, which shows the continuous variation of energy levels of d^n configurations in cubic field with crystal field strength.

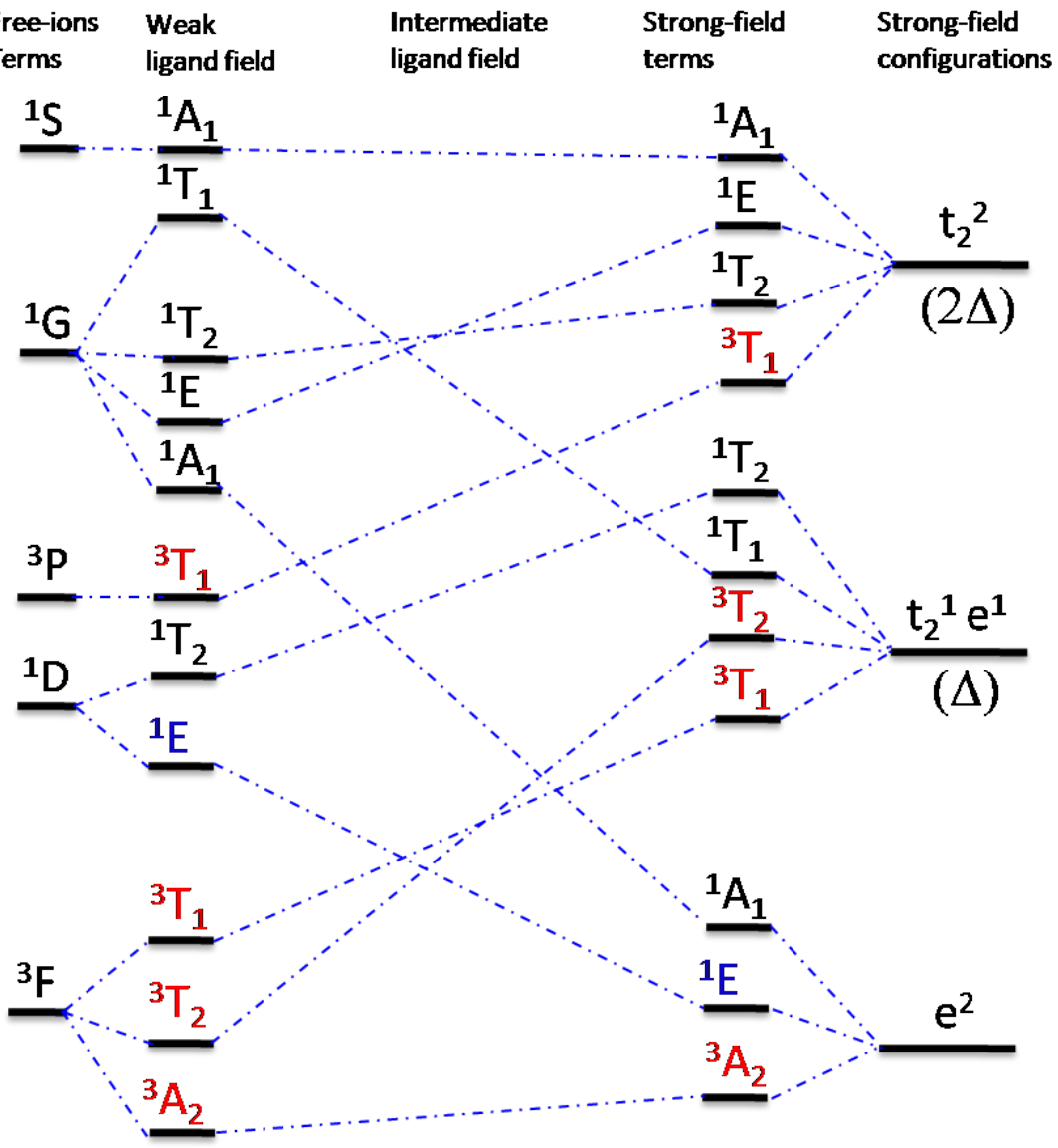

Figure 2.10: Correlation diagram between weak field model and strong field model[7]

Ligands	$I < Br < Cl$ weak field ligands Δ is small High spin	$F < OH^{-1} < H_2O$	$NH_3 < CO < CN$ strong field ligands Δ is large Low spin
Complexes Absorb	Low energy photons long wavelength (λ)		High energy photons short wavelength (λ)
Complexes Transmit	Complementary of Absorption violet blue green		Complementary of Absorption yellow orange red

Table 2.18: The effect of weak field and strong field ligands on the color appearance of transition metal complexes.

The next section will explain these diagrams in detail. Table(2.18) summarizes the weak and strong field effect on the color appearance of transition metal complexes.

2.6 Sugano-Tanabe Diagram

Calculating the energy levels of a multi-electronic system under cubic field is a laborious job and demands the computing power and calculating time. Sugano and Tanabe make this task much easier by calculating energy of different split terms of different electron configuration under perfect cubic field.This so-called Sugano-Tanabe diagram shows the calculated energy of different electronic terms split under cubic field with variable field strength. Since they draw these diagram by assuming under the perfect cubic crystal field, this diagram cannot be used for the lower symmetry crystal field. But you can still use them if you're only interested the average energy of lifted degenerated orbitals of cubic terms under low-symmetry field. The figure.2.11 shows (E/B Vs Δ/B) of two-electron system under tetrahedral crystal field. The X-axis shows the cubic field strength divided by free ion inter-electronic repulsion parameter B. The Y-axis of the diagram shows the energy value of electronic terms divided by free-ion value B. The diagram is drawn using C/B ratio of 4.71.

2.6.1 Understanding Sugano-Tanabe Diagram

To understand the Sugano-Tanabe Diagram qualitatively, we look at the figure.2.11 as well as correlation figure.2.10.

- In figure.2.11, ^1E and $^1A_1$ levels are almost FLAT with the crystal field strength. This is because these levels have the same electronic-configuration(e^2) with ground state $^3A_2$, see figure.2.10.

- There is inter-configurational interaction among different electronic-configurations if they have the energy levels with the same symmetric representation. For example, $^3T_1(^3F)(t_2^1e^1)$ and $^3T_1(^3P)(t_2^2)$ can interact because they have the same symmetric character. Because of the non-crossing rule, they will never cross in any cubic field strength. Because of this reason,$^3T_1(^3P)$ level have curvature

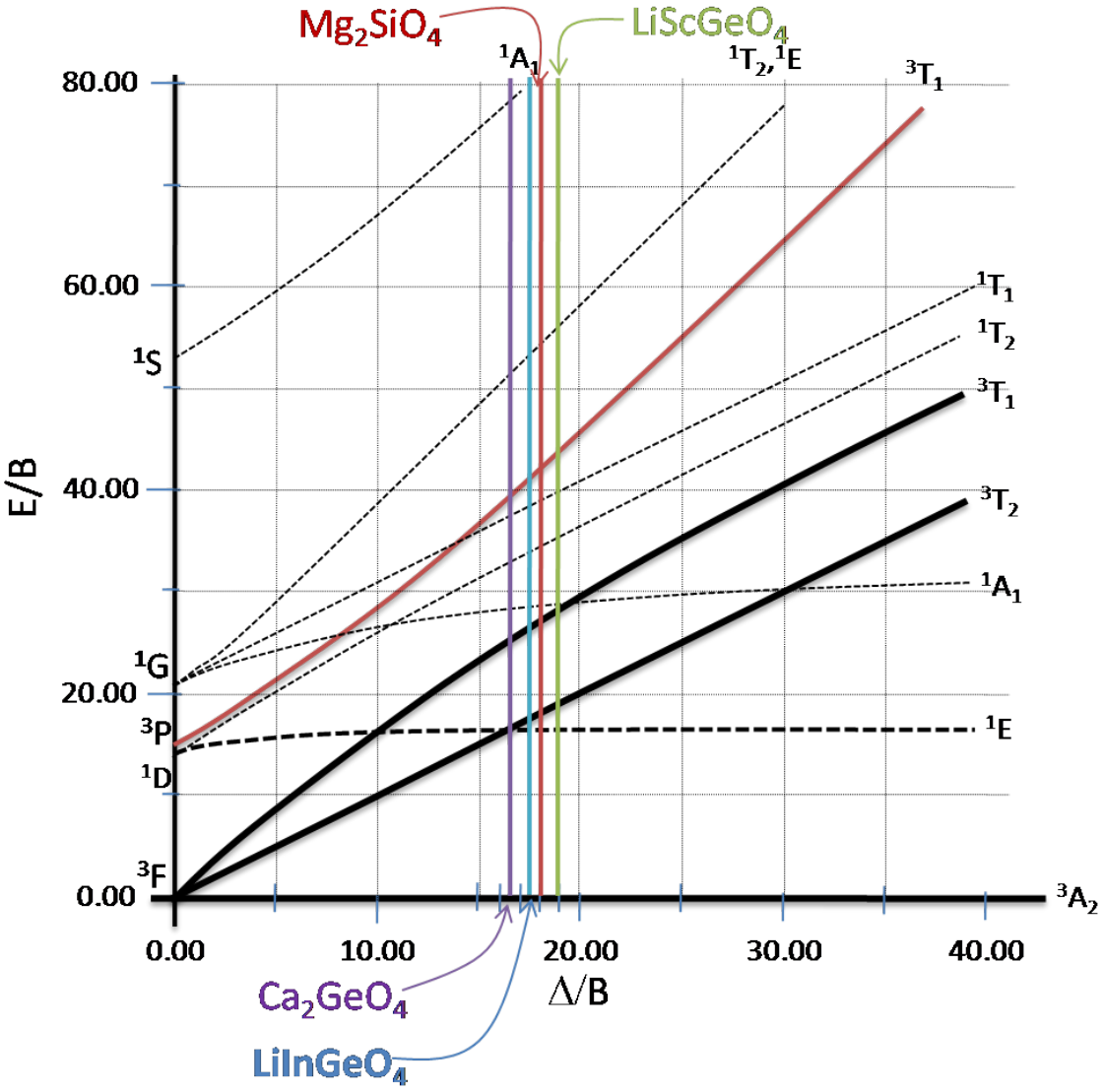

Figure 2.11: Sugano-Tanabe Diagram of d^2 configuration in tetrahedral crystal field,[7, 9, 10, 11, 12]

which goes upward while ${}^3T_1({}^3F)$ level also have curvature which goes downward.

- If the energy level doesn't involve in inter-configurational interaction, it varies linearly with cubic field strength. In other words, they appear straight line in Sugano-Tanabe diagram. Example of such levels is ${}^3T_2({}^3F)$ and ${}^1T_1({}^1G)$.

2.6.2 Finding $\Delta(10Dq)$, B & C parameters from Sugano-Tanabe Diagram

If we have the absorption spectrum of transition metal complexes, we can determine the ligand field parameters from the ST-diagram.

Step1: First, we have to choose two spin-allowed transitions, which have dynamic changes with crystal field strength. For Cr^{4+}ions in cunyite crystal, first let's forget about the splitting related to low-symmetry crystal field. The two spin-allowed transitions in visible range are ${}^3A_2 \rightarrow {}^3T_2$ and ${}^3A_2 \rightarrow {}^3T_1$. The approximate center of gravity of these two transition from the absorption spectrum is $8500cm^{-1}$ and $14000cm^{-1}$ respectively.

Step2: Find the ratio of these two transition and fit this value in Sugano-Tanabe diagram of d^2 in tetrahedral crystal field. Here is the ratio is: $({}^3A_2 \rightarrow {}^3T_1 / {}^3A_2 \rightarrow {}^3T_2)$ $= 1.65$.

Step3: Find Δ/B from fitting the ST diagram. The fitting value of ratio 1.65 is $\Delta/B = 16$. Since Sugano-Tanabe diagrams start from free ion terms, the energy difference between the ground state and the first excited state is Δ, which is $8500cm^{-1}$.

Step4: Find the Racah parameter B from $\Delta/B = 16$ and $\Delta = 8500cm^{-1}$. The resulted B value is $530cm^{-1}$ and C value is $2350cm^{-1}$. Since the free-ions value

Crystal	$e_\sigma(cm^{-1})$	$e_\pi(cm^{-1})$	$\Delta_{tet}(cm^{-1})$	$B_{complex}(cm^{-1})$	$\frac{\Delta}{B}$
Mg_2SiO_4	9735	1623	10100	560	18
Ca_2GeO_4	8629	1438	8950	540	16.5
$LiScGeO_4$	9578	1596	9933	526	19
$LiInGeO_4$	9440	1573	9790	557	17.5

Table 2.19: The ligand field parameters of Cr^{4+}tetrahedral complex of different olivine laser crystals[9, 10, 11, 12]

Crystal	$e_\sigma(cm^{-1})$	$e_\pi(cm^{-1})$	$\Delta_{tet}(cm^{-1})$	$B_{complex}(cm^{-1})$	$\frac{\Delta}{B}$
Mg_2SiO_4					
$LiScGeO_4$	6670	1110	15570	738	21
$LiInGeO_4$	6530	1088	15238	746	20.5

Table 2.20: The ligand field parameters of Cr^{3+}octahedral complex of different laser crystals[12]

of inter-electronic repulsion parameter B is $1042cm^{-1}$, B of complex is only 50% of free ion value. Thus the inter-electronic repulsion effect is reduced in tetrahedral complex because covalent bonding between the metal and ligand electrons.

Summary: Thus the crystal field parameters of cunyite crystal is:

$$\begin{aligned} \Delta &\quad 8500cm^{-1} \\ B &\quad 530cm^{-1} \\ C &\quad 2500cm^{-1} \end{aligned}$$

The energy levels of Cr^{4+}ions in Mg_2SiO_4, Ca_2GeO_4, $LiScGeO_4$ and $LiInGeO_4$ laser level are shown on Sugano-Tanabe diagram, see fig.2.11 of d^2 tetrahedral complex and the energy levels of Cr^{3+}ions in $LiScGeO_4$ and $LiInGeO_4$ are shown on Sugano-Tanabe diagram, see fig.2.12 of d^3 octahedral complex.

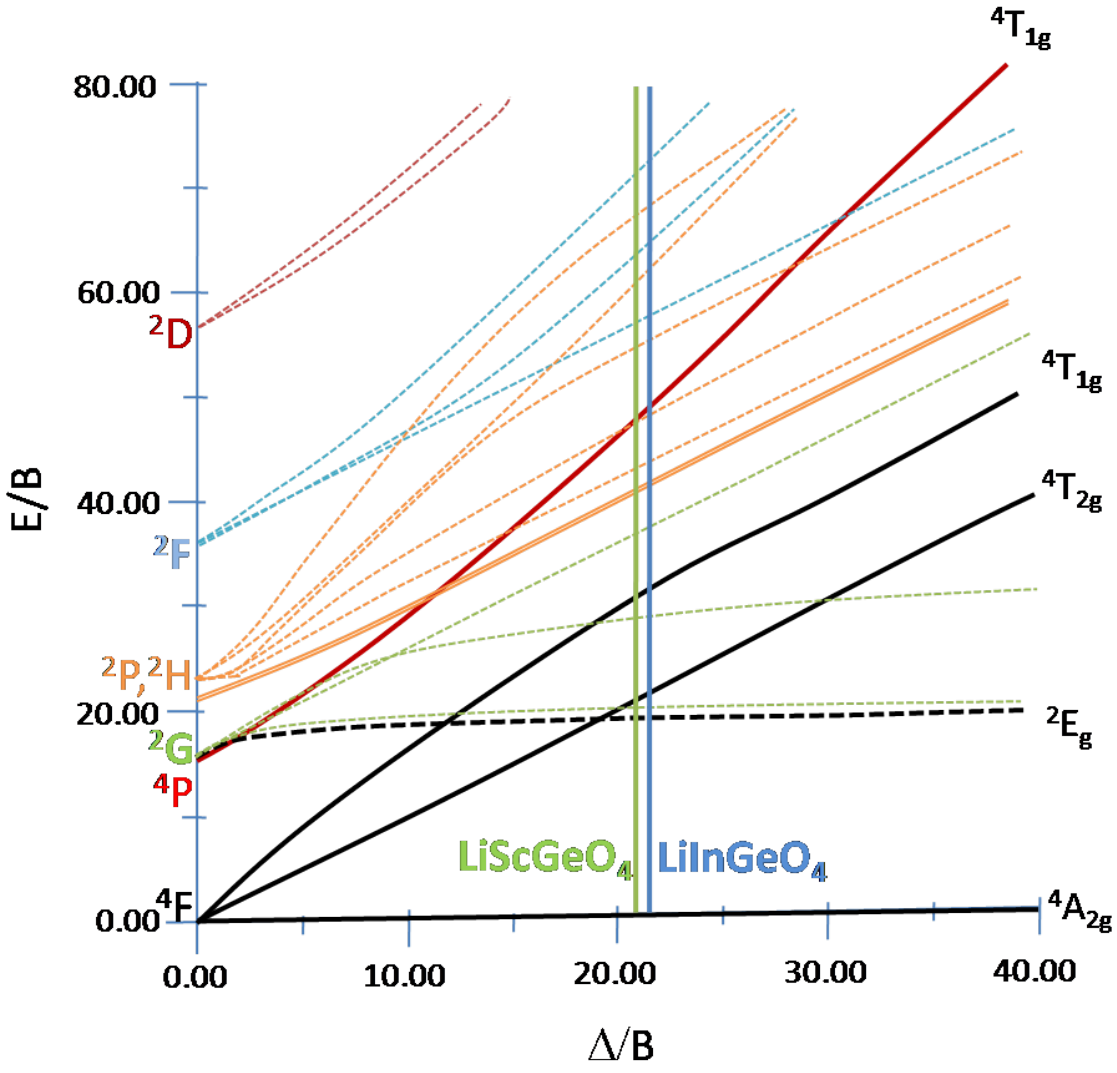

Figure 2.12: Sugano-Tanabe Diagram of d^3 configuration in octahedral crystal field,[7, 12]

2.7 Band splitting due to low symmetry crystal field

As you can see from figures.2.11, since the crystal field strength ($\frac{\Delta}{B}$) of Cr^{4+}activated Mg_2SiO_4 and Ca_2GeO_4 is around '17' in cubic symmetry, the first excited state should be ^1E and not the spin-allowed transition $^3T_2$. According to crystal field theorem, since the ground state $^3A_2$ and ^1E excited state have the same electronic configuration, the equilibrium position of the ground and excited state aligns and the sharp transition is observed as there is no vibronic progression in this transition. But in reality, the first excited state of these crystals is $^3T_2$, not ^1E and broadband transitions are observed. This is because when the crystal is doped with chromium ions, SiO_4 or GeO_4 tetrahedron is distorted and the complex symmetry is reduced from 'T_d' to 'C_s' point symmetry. In other words, the crystal field is no longer cubic field and the actual energy levels cannot be calculated from Sugano-Tanabe diagram because the diagram is drawn for cubic field. The calculated crystal file strengths Δ I have shown in the table(2.19) are the mean value of non-degenerated split levels of $^3T_2$ cubic field term. Since we're only interested in the visible and near-infrared range of electromagnetic spectrum, the cubic split terms $^3A_2$, $^3T_2$, $^3T_1$ of ^3F and $^3T_1$ of ^3P free ions terms are enough to understand the absorption and emission spectrum of Cr^{4+}ions doped tetrahedral complexes. Since the crystal field symmetry is reduced from cubic field, the orbital degeneracy of T(orbital degeneracy =3) and E(orbital degeneracy =2) cubic terms are lifted. The figure.2.13(a) shows how the cubic field terms are split under C_{3v} and C_s site symmetry by removing the orbital degeneracy. The figure.2.13(b) shows the experimentally observed energy of split levels under C_s local symmetry. From the observed energy values, e_σ and e_π values are calculated and these values are correlated with the crystal field parameters (10Dq and B). By using these crystal field parameters, the mean energy levels of cunyite crystal are found

using Sugano-Tanabe diagram. That's why you can see that the energy reading from Sugano-Tanabe diagram doesn't represent real observed data because the real symmetry of local enviroment is not cubic symmetry. There are the important things to note here is:

For d^2 configuration in tetrahedral complex,

- The energy difference between the cubic terms is around (10Dq) 10,000 cm^{-1}.
- The energy difference between the split levels of cubic term is around (Dq) 1000 cm^{-1}.
- Sometimes the split energy due to low symmetry crystal field is so large (around 3000 cm^{-1}) that the energy position of two cubic terms cannot be easily distinguished from the absorption spectrum.

The olivine crystal have two distinct sites. one is tetrahedral site for Cr^{4+}ions substitution and another one is octahedral sites for Cr^{3+}ions substitution. Figure.2.13(c) shows the illustration of how the orbital degeneracy are lifted when the symmetry of octahedral complex is reduced to C_s from O_h symmetry through D_{2h} because of Cr^{3+}substitution to magnesium ions in forsterite laser crystal. Why do we need the energy level of D_{2h} symmetry? The energy level calculation of low symmetry is so complex that the energy splitting of real C_s symmetry can be estimated from the energy of D_{2h} higher symmetry because as shown in the figure.2.13(c), the observed energy is not very far from the energy level of D_{2h} higher symmetry.

For d^3 electronic configuration in octahedral site,

- The energy difference between the cubic terms is about (10 Dq) 15500 cm^{-1}.
- *The energy difference between the non-degenerated split levels under C_s symmetry is smaller than that of tetrahedral complex. Compared to 1000 cm^{-1}*

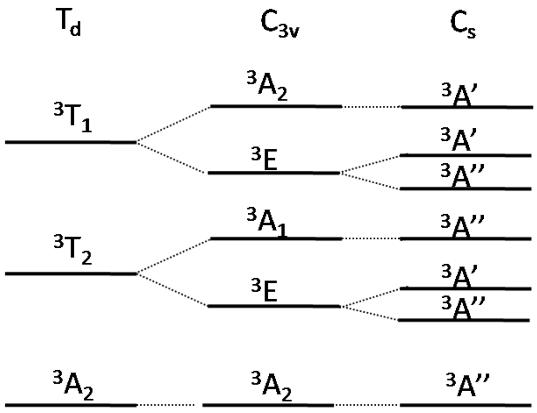

(a) Illustration of lifting of orbital degeneracy of cubic terms in CrO_4^{4-} tetrahedral complex when the complex symmetry is reduced to C_s from T_d through C_{3v}.

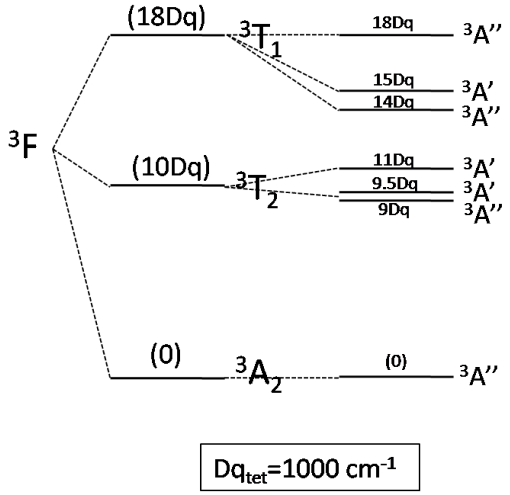

(b) Quantitative comparison between the cubic terms(mean value) and experimentally observed data for Cr^{4+}ions activated cunyite crystal

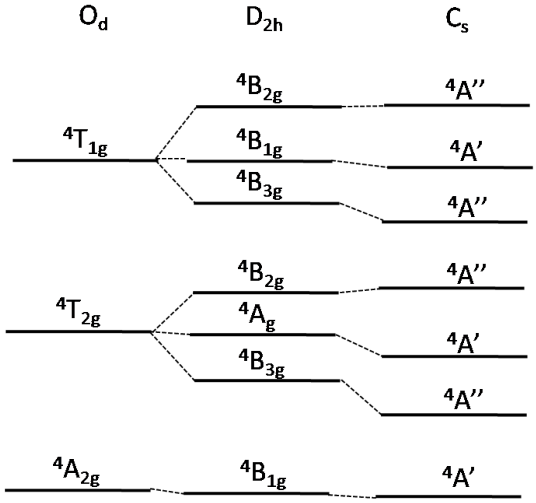

(c) Illustration of lifting of orbital degeneracy of cubic terms in CrO_6^{9-} octahedral complex when the complex symmetry is reduced to C_s from O_h through D_{2h}.

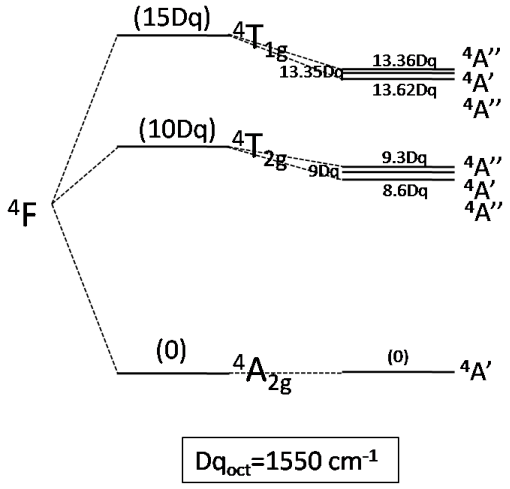

(d) Quantitative comparison between the cubic terms(mean value) and experimentally observed data for Cr^{3+}ions activated $LiScGeO_4$ crystal

Figure 2.13: Typical energy level diagram of Cr^{4+}ions in tetrahedral site and Cr^{3+}ions in octahedral site of olivine crystal structure.

in tetrahedral complex, the observed energy in octahedral complex is about 500 cm^{-1}.

- Since the energy difference between the split levels of Cr^{3+}ions in octahedral complex is so small that the energy position of cubic terms are clearly visible in absorption spectrum of octahedral complexes.

The possible causes of reducing the complex symmetry from cubic,

- **Crystal structure distortion**; The site symmetry is not cubic because of crystal structure distortion due to active ion doping.
- **Complex having different ligands**; it is possible that the impurity ions replace the oxygen ions in CrO_4^{4-}
- **Crystal packing forces**; the crystal forces must change if the host is doped with chromium in order to reduce the overall energy of the system
- **Jahn-Teller effect**; Jan-Teller theorem states that the nonlinear molecule having the terms with orbital degeneracy is stable and induces the distortion which can lift the orbital degeneracy.

2.8 Electronic transition in transition metal complexes

2.8.1 Transition moment integral

When a photon is absorbed, the electron jumps from the ground state to the excited state. The strength of this electronic transition is described by the square of transition moment integral. The transition moment integral is defined as:

$$Q =< \psi_1|\mathbf{r}|\psi_2 > \tag{2.15}$$

where, $\mathbf{r}$ = electric-dipole operator.

2.8.2 Selection Rules

Understanding the selection rules is very important in assigning the electronic transitions from the measured absorption spectrum. The ground state and excited states wave functions is a product of orbital, spin and vibrational waves functions.

$$\psi = \psi_{orbital} \cdot \psi_{spin} \cdot \psi_{vibration} \tag{2.16}$$

2.8.2.1 Spin-Selection Rule

The calculation shows that the transition moment integral $Q =< \psi_1|\mathbf{r}|\psi_2 >$ is non-zero only if S_{ψ_1} and S_{ψ_1} is the same. In other words, the electronic transitions are only allowed (spin-allowed transition) between the states with the same multiplicity. The transitions are forbidden (spin-forbidden transition) between the states with different multiplicity. **The optical density (A) of the spin-allowed transition is two to three order of magnitude (100 to 10,000 times) stronger than that of spin-forbidden transition.**

2.8.2.2 Parity selection rule (Laporte Rule)

Parity selection rule deals with the orbital part of the wave function. The transition moment integral is zero if the integrand is antisymmetric to the inversion through the center of system. In other words, the integrand cannot have "u" symmetric character. The transition moment integral is only non-zero if the integrand is symmetric to inversion. Thus the integrand needs "g" symmetric character.

The electric dipole operator($\mathbf{r}$) is antisymmetric to the inversion and thus it has "u" symmetric character. The application of group theory in execution the parity selection rule is a big help in determining the allowed and forbidden transitions in transition metal complexes.

In octahedral crystal field, the d orbitals transform into t_{2g} and e_g irreducible representations of O_h group. All 5 d orbitals have "g" character in O_h group where the molecule belongs. The transition moment integrals of "d-d" transition in O_h group is zero since the resulted integrand $\psi_{d1} \cdot \mathbf{r} \cdot \psi_{d2}$ is antisymmetric to the inversion through center. Thus "d-d" transition in octahedral crystal field is forbidden.

In reality, in any crystal field, the "d-d" transition is forbidden because d wave functions are centrosymmetric functions and but the mixing of "3d" and "4p" orbitals relaxes this parity selection rules in non-centrosymmetric complexes such as tetrahedral coordination because "p" orbitals have "u" character. But in centrosymmetric complexes such as octahedral ones, the mixing effects are canceled each other through the center. Thus in octahedral complexes, the transitions are parity-forbidden while in tetrahedral complexes, the transitions are parity-allowed. **The optical density (A) of parity-allowed transitions in tetrahedral complexes is (10 to 100)times stronger than that of parity-forbidden transitions in octahedral complexes.**

The following section, I make the detail calculation of determining parity-allowed transitions of a Cr^{4+}doped tetrahedral complex using the group theory formalism.

2.8.2.2.1 Determination of parity allowed and parity forbidden transitions in Cr^{4+}ion in tetrahedral complex (T_d symmetry) By using the above reasoning and the group theory, the selection rule states as [22]

$$\langle\ \Psi_i|\hat{O}|\Psi_f\rangle = \sum_j a_j\Gamma_j \supset \Gamma_1 \tag{2.17}$$

That means the direct product of the irreducible representations of initial wavefunction, final wavefunction and the electric dipole operator $\hat{O}$ must include the totally symmetric respresentation to allow the electronic transition from intial state to final state.

Let's see the examples to clarify the above statement. If $Cr^{4+}$is located in perfect tetrahedron, its free ion term ^3F term will split into $^3A_2$, $^3T_2$ and $^3T_1$ with $^3A_2$ is the ground term. Please refer to figure(2.13(a)) and table(2.21). What transitions are parity allowed transition in fig.2.13(a)?

The electric dipole operator has basis of x,y,z. Thus it transforms as T_2 in T_d symmetry. See table(2.21). *Here I have to emphasize that the reference coordinate is complex coordinate, NOT crystal coordinate. That means the selection rule is based on the Cartesian coordinate of the tetrahedral complex(T_d symmetry).*

To examine whether the transiton($^3A_2 \rightarrow {}^3T_2$) is allowed, we have to look at the direct product of A_2(irreducible representation of ground state), T_2(representation of electric dipole operator), and T_2 (irreducible representation of first excited state).

Table(2.21) shows the character table of T_d symmetry.

T_d	$\mathcal{E}$	$8C_3$	$3C_2$	$6S_4$	$6\sigma_d$		
A_1	1	1	1	1	1		$x^2+y^2+z^2$
A_2	1	1	1	-1	-1		
E	2	-1	2	0	0		$\frac{1}{\sqrt{6}}[2z^2-x^2-y^2], \frac{1}{\sqrt{2}}[x^2-y^2]$
T_1	3	0	-1	1	-1	(R_x, R_y, R_z)	
T_2	3	0	-1	-1	1	(T_x, T_y, T_z)	$(x,y,z);(xy,yz,zx)$

Table 2.21: T_d character table

Now we need to find the direct product.

$$\Gamma_{A_2\times T_2\times T_2} =? \tag{2.18}$$

STEP(1):

	$\mathcal{E}$	$8C_3$	$3C_2$	$6S_4$	$6\sigma_d$	
$\Gamma_{A_2\times T_2}$	3	0	-1	1	-1	Γ_{T_1}

STEP(2):

	$\mathcal{E}$	$8C_3$	$3C_2$	$6S_4$	$6\sigma_d$	
$\Gamma_{T_1\times T_2}$	9	0	1	-1	-1	Γ_{total}

Γ_{total} is the reducible respresentation. Thus we must have to decompose to get irreducible representation. As described in section(ref. 2.4.2.2.1), we can decompose Γ_{total} as follows.

For T_d symmetry,

$$\Gamma_{total} = a_1A_1 + a_2A_2 + a_3E + a_4T_1 + a_5T_2 \tag{2.19}$$

From eq.2.14,

$$a_1 = 0; \qquad a_2 = 1; \qquad a_3 = 1; \qquad a_4 = 1; \qquad a_5 = 1 \tag{2.20}$$

Thus $\Gamma_{T_1\times T_2}$ is decomposed as follows.

$$\Gamma_{total} = \Gamma_{T_1\times T_2} = A_2 + E + T_1 + T_2 \tag{2.21}$$

Now we can see that there is no totally symmetric representation coming out from decomposing the direct product $\Gamma_{A_2\times T_2\times T_2}$. Thus *the electronic transition* $^3A_2 \rightarrow {}^3T_2$ *is forbidden in* T_d *symmetry.*

Now Let's examine the transition $^3A_2 \rightarrow {}^3T_1$. By using the similar calculation as

above,

$$\Gamma_{A_2\times T_2\times T_1} = \Gamma_{T_1\times T_1} = \mathbf{A_1} + E + T_1 + T_2 \tag{2.22}$$

The totally symmetric representation A_1 appears this time when $\Gamma_{A_2\times T_2\times T_1}$ reducible representation is decomposed. Thus *the electronic transition* $^3A_2 \rightarrow {}^3T_1$ *is allowed in* T_d *symmetry.*

When Cr substitues Ge in GeO_4^{4-} , its site symmetry is reduced from T_d to C_s . C_s site symmetry is sometime estimated with the more symmetric C_{3v} site symmetry. Figure 2.14 shows the energy splitting of Cr^{4+}located at different symmetric complex. Now we'll examine the allowed and forbidden transition of Cr^{4+}in C_{3v} and C_s site symmetry.

Cr^{4+}in C_{3v} site

C_{3v}	E	$2C_3$	$3\sigma_v$		
A_1	1	1	1	T_z	$x;\ z^2;\ x^2+y^2$
A_2	1	1	-1	R_z	
E	2	-1	0	(T_x, T_y)	$(y,z);(zx,yz);(xy, \frac{1}{\sqrt{2}}[x^2-y^2])$

Table 2.22: C_{3v} character table

In C_{3v} symmetry, if the polarization of excitation is along the crystallographic axis "x", the electric dipole operator transforms as "A_1"

$^3A_2 \rightarrow {}^3E$**:**

$$\Gamma_{A_2\times A_1\times E} = \Gamma_{A_2\times E} = E \tag{2.23}$$

Since the resultant representation is not A_1, transition is forbidden.

$^3A_2 \rightarrow {}^3A_1$**:**

$$\Gamma_{A_2 \times A_1 \times A_1} = \Gamma_{A_2 \times A_1} = A_2 \tag{2.24}$$

Since A_2, transition is forbidden.

$^3A_2 \rightarrow {}^3A_2$**:**

$$\Gamma_{A_2 \times A_1 \times A_2} = \Gamma_{A_2 \times A_2} = A_1 \tag{2.25}$$

Since the resultant representation is A_1 (totally symmetric), *transition is allowed.*

In C_{3v} symmetry, if the polarization of excitation is along the crystallographic axis "y and z", the electric dipole operator transforms as "E"

$^3A_2 \rightarrow {}^3E$**:**

$$\Gamma_{A_2 \times E \times E} = \Gamma_{E \times E} = \mathbf{A_1} + A_2 + E \tag{2.26}$$

Since A_1 appears,*transition is allowed.*

$^3A_2 \rightarrow {}^3A_1$**:**

$$\Gamma_{A_2 \times E \times A_1} = \Gamma_{E \times A_1} = E \tag{2.27}$$

Thus transition is forbidden.

$^3A_2 \rightarrow {}^3A_2$**:**

$$\Gamma_{A_2 \times E \times A_2} = \Gamma_{E \times A_2} = E \tag{2.28}$$

Thus transition is forbidden.

Cr^{4+}in C_s site

C_s	E	σ		
$A^{'}$	1	1	$R_z;\ T_x; T_y$	$x, y;\ z^2, y^2, x^2;\ xy$
$A^{''}$	1	-1	$T_z;\ R_x; R_y$	$z;\ yz, zx$

Table 2.23: C_s character table

In C_s symmetry, if the polarization of excitation is along the crystallographic axis "x and y", the electric dipole operator transforms as A'.

$^3A'' \rightarrow {}^3A'$**:**

$$\Gamma_{A''\times A'\times A'} = \Gamma_{A''\times A'} = A'' \tag{2.29}$$

Since the resultant representation is A'' (nontotally symmetric), transition is forbidden.

$^3A'' \rightarrow {}^3A''$**:**

$$\Gamma_{A''\times A'\times A''} = \Gamma_{A''\times A''} = A' \tag{2.30}$$

Since the final representation is A' (totally symmetric),*transition is allowed.*

In C_s symmetry, if the polarization of excitation is along the crystallographic axis "z", the electric dipole operator transforms as A''.

$^3A'' \rightarrow {}^3A'$**:**

$$\Gamma_{A''\times A''\times A'} = \Gamma_{A'\times A'} = A' \tag{2.31}$$

Thus *transition is allowed.*

$^3A'' \rightarrow {}^3A''$**:**

$$\Gamma_{A''\times A''\times A''} = \Gamma_{A'\times A''} = A'' \tag{2.32}$$

Thus transition is forbidden.

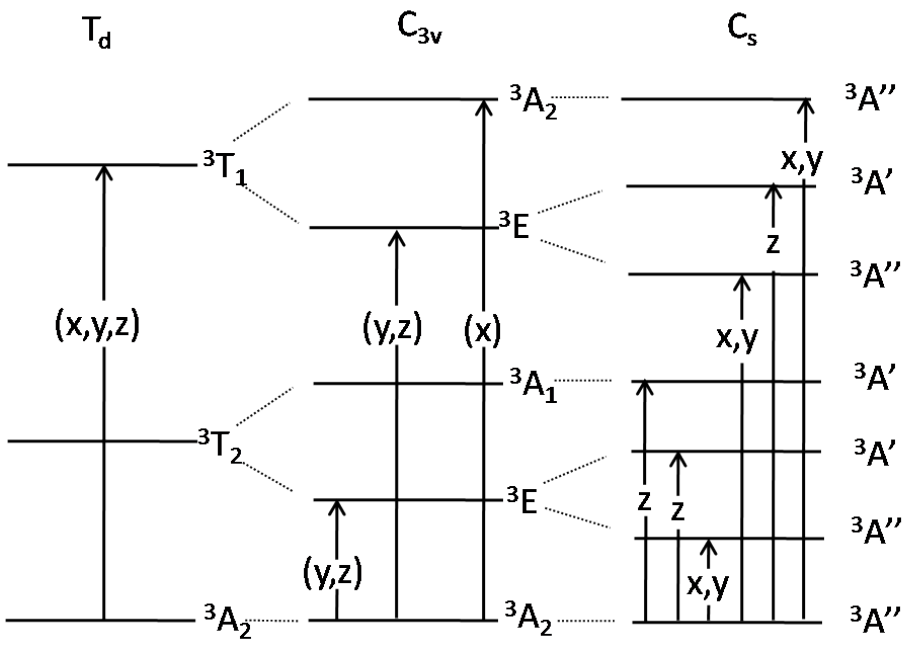

Figure 2.14: The energy level diagram of Cr^{4+}in tetrahedral site when the site symmetry is lowered from T_d through C_{3v} to C_s .The figure also shows the allowed electronic transition of Cr^{4+}in different site symmetry.

All the allowed and forbidden transitions for each polarization direction are summarized in figure(2.14).

2.8.3 Mechanisms which can relax the spin selection rule and the parity selection rule

2.8.3.1 Spin-Orbit Coupling and Fano-Antiresonance

Up until now, we just only consider the d-orbital splitting because of inter-electronic repulsion and crystal field. For the first row transition metal complexes, the effect of spin-orbit coupling is weaker than inter-electronic or crystal field. But for rare-earth ions, the effect of spin-orbital coupling is much stronger than the crystal field. For transition metal complexes, we need the spin-orbit coupling to relax the spin-selection rule. For Ruby crystal, the lasing occurs from ^2E excited state to $^4A_2$ ground state. What is the mechanism to occur such spin-forbidden transition? The mechanisms is as follows:

- From the spin-selection rule, $\langle\psi_{^2E}|\mathbf{r}|\psi_{^4A_2}\rangle$ =0.
- But, ^2E and $^4T_2$ excited states are very close in energy. With the help of the spin-coupling operator, these two states can mix because the mixing coefficient is inversely proportional to the energy difference between these two states, about $1500cm^{-1}$.
- The mixing coefficient c is given by c = $\langle\psi_{^2E}|\lambda\mathbf{L}\cdot\mathbf{S}|\psi_{^4T_2}\rangle/(E_{^4T_2}-E_{^2E})$.
- Because of mixing, transition moment integral for ($^4A_2\rightarrow{}^2E$) transition is now allowed because $\langle\psi_{^2E}|\mathbf{r}|\psi_{^4A_2}\rangle^2 \propto [\langle\psi_{^2E}|\lambda\mathbf{L}\cdot\mathbf{S}|\psi_{^4T_2}\rangle/(E_{^4T_2}-E_{^2E})]^2$.

Two important things to note here is:

- *the spin-forbidden transition must borrow the intensity from the spin-allowed transition. Because of this, the intensity of spin-allowed transition is reduced.*
- *The intensity of spin-forbidden transition depends on the energy difference between two excited states(one excited state is the same multiplicity as the ground*

state while another one has different multiplicity from the ground state). Let's say if the two energy states (for example ^2E and $^4T_2$) closer and closer for some ligands, the intensity of spin-forbidden transition ($^4A_2 \rightarrow ^2E$) is comparable to spin-allowed transition ($^4A_2 \rightarrow ^4T_2$) because spin-allowed transition has to lend the intensity to spin-forbidden transition. Because of this reason, there is a DIP between the peaks of the two transitions and the mechanism occurring such a dip is called Fano-antiresonance.

2.8.3.2 Vibronic transition

To relax the parity-selection rule, we need 'u' vibration to couple the electronic transition. Let me remind that the wavefunction with 'u' character is antisymmetric to the inversion through the center of complex while the wavefunction with 'g' character is symmetric to to the inversion.Since the group theory state that the transition moment integral must be totally symmetric representation of a group a complex belongs. But the d-d transition of centrosymmetric complex such as octahedral one is parity-forbidden since the direct product ($\Gamma(\psi_d) \cdot \Gamma(\mathbf{r}) \cdot \Gamma(\psi_d) = T_{1u}$) has 'u'character. 'u' vibration mixes the 'u' character excited state (usually charge transfer transition) with 'g' character excited state and relaxes the parity-selection rule. For parity-forbidden transition, the vibrational selection rule states that $\Delta\nu$ must be ± 1. At low temperature, the ground state only populate $\nu = 0$ level and the parity-forbidden transition occurs at ($E_{0-0}(electronic) + E_{\nu_0 \rightarrow \nu_1}(`u' vibration)$). Thus the transition occurs at one 'u' vibration frequency higher than where the zero-phonon line of parity-forbidden transition supposes to be. At room temperature ($200cm^{-1}$), the upper vibrational level of ground state is populated. Let's say the ground state has two vibrational states (0 & 1).Now according to vibrational selection rule, $\nu_g(0) \rightarrow \nu_e(1)$ and $\nu_g(1) \rightarrow \nu_e(0)$ transitions are possible. There will be two parity-forbidden bands appear either side of zero-phonon line. Low energy side band ($\nu_g(1) \rightarrow \nu_e(0)$) is

called the *hot band* because this band can only appear if there is thermally populated vibrational energy at ground state.

2.8.4 Why do we need to measured low-temperature spectrum?:Vibrational Progression

Wherever the new crystal is synthesized, we have to measure the low-temperature absorption and emission spectrum. The question is why do we need to measure them? The answer to the question is since the thermally populated vibration bands distorted the transition band-shape, band-intensity and band-width and cover the vital information about pure electronic transition and zero-phonon line. For parity-allowed transition, the bandwidth of transition is broaden with temperature and for parity-forbidden transition, the intensity and shape of transition bands is effected with temperature.

2.8.4.1 Parity-allowed transition and Coth rule

For parity-allowed transition, vibration which transforms the totally symmetric representation of T_d or O_h group where a molecule belongs can couple the electronic transition because of the group theory formalism ($\Gamma(\psi_1) \cdot \Gamma(\mathbf{r}) \cdot \Gamma(\psi_2) = A_{1g}$).

At 77K,

- The ground state populate only $\nu = 0$ vibrational level. The vibrational progression of totally symmetric mode can be observed in the absorption and emission spectrum only if the excited state equilibrium position is shifted relative to that of the ground state. For example, there is not vibronic progression in transition ($^4A_2 \rightarrow {}^2E$) while there is progression of totally symmetric mode in transition ($^4A_2 \rightarrow {}^4T_2$) of Cr^{3+}ions in octahedral coordination. Since in the first transition, the equilibrium position of ground state and excited state align while in the

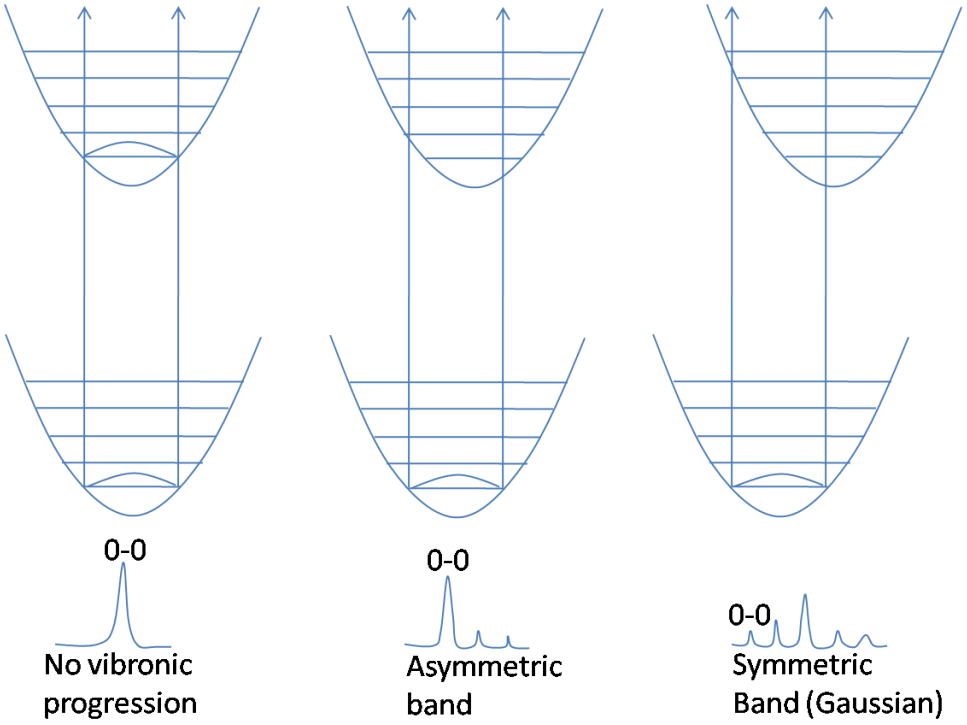

Figure 2.15: Ilustration of vibronic progression for various excited state geometry

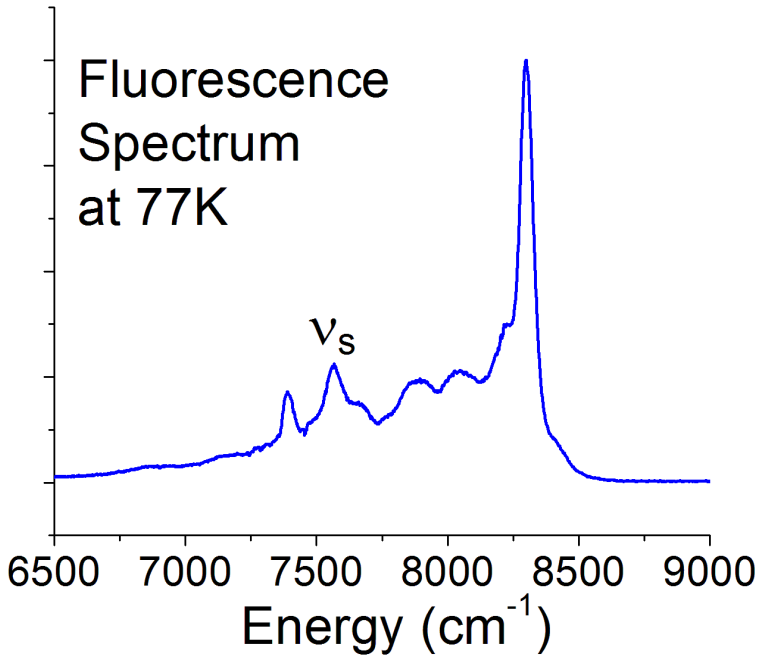

Figure 2.16: Emission spectrum of Cunyite crystal at 77K

latter transition, the equilibrium position of excited state is shifted relative to ground state. As shown in the figure.2.16 & 2.17(b), the vibrational progression of totally symmetric mode having frequency of $700cm^{-1}$ is clearly visible in absorption and emission spectum of cunyite crystal measured at 77K. These are really beautiful pictures illustrating the vibronic progression and asymmetric band formation. Actually, $700cm^{-1}$ frequency vibration is CrO_4^{4-} tetrahedral breathing mode of cunyite crystal and this mode is also observed with Raman spectroscopy.

- Asymmetric band formation: If the excited state geometry slightly changes relative to that of ground state, the asymmetric band shape is resulted, see figure.2.15. This is because the intensity of the vibrations component depends on the overlap integral between the ground and excited state vibrational wavefunctions. If the equilibrium position of excited state is slightly shifted relative to ground state, the ground state vibrational wavefunction overlap largely with the excited state $\nu = 0$ vibrational state and the strongest intensity is observed at zero phonon line.

- Symmetric(Gaussian) band formation: If the bond length of excited state geometry changes significantly relative to the ground state, the symmetric band formation is observed. This is because the ground state wavefunction now overlap with more with higher quantum number vibrational modes and only weak intensity is observed at zero-phonon line. Accordingly the symmetric band is observed. These effects are clearly illustrated in fig.2.15.

At 300K,

- At room temperature, the upper vibrational levels of ground state are populated. Thus the wavefunctions of upper vibrational levels of ground state have a good chance to overlap with those of vibrational levels of the excited states.

As a result, compared to 77K transition, the bandwidth is broadened and the intensity is greatly reduced because the area of transition band have to be the same as the area measured at 77K. But the peak position is the same as the position occur at 77K.

- We can use the so-called coth rule to calculate the transition bandwidth changes with the temperature.

$$BW(T) = BW(0K)\coth(\nu/2kT) \tag{2.33}$$

where, ν is the totally symmetric A_1 mode, k is Boltzmann constant = $1.38 \times 10^{-23} J/K$ and T is temperature.

2.8.4.2 Parity-forbidden transition and Coth rule

As mention in section.2.8.3.2, to allow parity-forbidden transition, we need asymmetric vibration. At 77K, thermally populated vibration is reduced and consequently the intensity of parity-forbidden transition is very weak at low temperature. When temperature is increased, vibrational quantum number is increased and accordingly the intensity is increased. Thus the parity-forbidden transition are sensitive to temperature variation than the parity-allowed transition. We can also use the coth rule here to estimate the transition intensity variation with temperature.

$$I_{parity-forbidden}(T) = I(0K)\coth(\nu/2kT) \tag{2.34}$$

where, ν is the asymmetric mode. When the temperature is increased, the hot bands also appear in the spectrum and the band-shape is distorted and the peak of the band tends to move to the lower energy side.

2.8.5 Polarized absorption spectrum

The transition moment integral is defined as $Q =< \psi_1|\mathbf{r}|\psi_2 >$. The reference coordinates of orbital waves function is the tetrahedral (or) octahedral axes while the reference frame of electric dipole operator is crystal axes. Since the integrand is the dot product and $\psi\cos(\theta)$ is the scaler projection on the electric dipole operator $\mathbf{r}$, the transition strength is strong if the complex's axes align with the crystal axes. Accordingly, the transition strength is strongly polarized.

In olivine crystal structure, there are one tetrahedral site and two octahedral sites. One axis of tetrahedron is align with the crystallographic short axis. The angle between the ligands in tetrahedral complexes is $109.5^{\cdot}$, which is also close to $90^{\cdot}$. Because of this reason the transition strength of tetrahedral sites is strongly polarized.

But in the octahedral site, since the z-axis of octahedron is inclined $62^{\cdot}$ with the crystallographic short axis, the transition strength is about the same regardless of direction of electric field because the scalar projection of orbital wave functions on the electric dipole operator is about the same for any crystal direction the electric field applies. Accordingly, the transition strength of octahedral site in olivine crystal structure is weakly polarized.

It is really fascinating to see the polarized color of cunyite and forsterite crystals with sheet polarizer. Figure.2.17 shows the complementary color wheel and the polarized absorption spectrum of cunyite. The absorption of the transition metal complex can be known by using complementary color wheel. For example, cunyite and forsterite crystals has green color appearance. Since the complementary color of green is red, these crystals have strong absorption in red region. Since the absorption of these crytals are strongly polarized. we can use the sheet polarizer to determine the crystal axes. We got absorption spectrum in one hand and complementary color wheel in another, we'll distinguish the crystal axes by using the color.

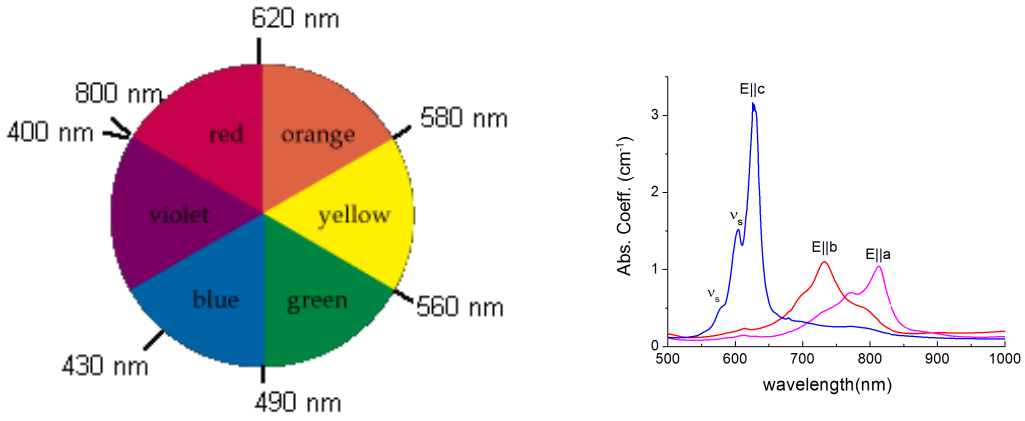

Figure 2.17: (a) Complementary color wheel and (b) Polarized Absorption spectrum of cunyite crystal

c-axis: If the polarizer sheet is align the crystallographic short axis (c-axis) of cunyite crystal, the dark blue color is observed. The complementary color of blue is orange (580-620nm),which agree with the $E \parallel c$ absorption spectrum.

b-axis: If the polarizer sheet is align the crystallographic medium axis (b-axis) of cunyite crystal, the green color is observed. The complementary color of green is red (620-800nm),which agree with the $E \parallel b$ absorption spectrum.

a-axis: If the polarizer sheet is align the crystallographic long axis (a-axis) of cunyite crystal, the yellow color is observed. The complementary color of yellow is violet (<400nm). Since $E \parallel a$ absorption spectrum is out of visible range, the yellow appearance is coming from Cr^{3+}ions absorptions (around 450nm) or the shoulder absorption of charge transfer transition.

2.8.5.1 Tetrahedral site and Octahedral site of olivine crystal structure

Figure.2.18 shows the comparison of crystal coordinates and the complex (tetrahedral or octahedral) coordinates. The group theory states that the irreducible representation of transition moment integral must be totally symmetric representation of a group a molecule belongs. These selection rule is based on the complex coordinate

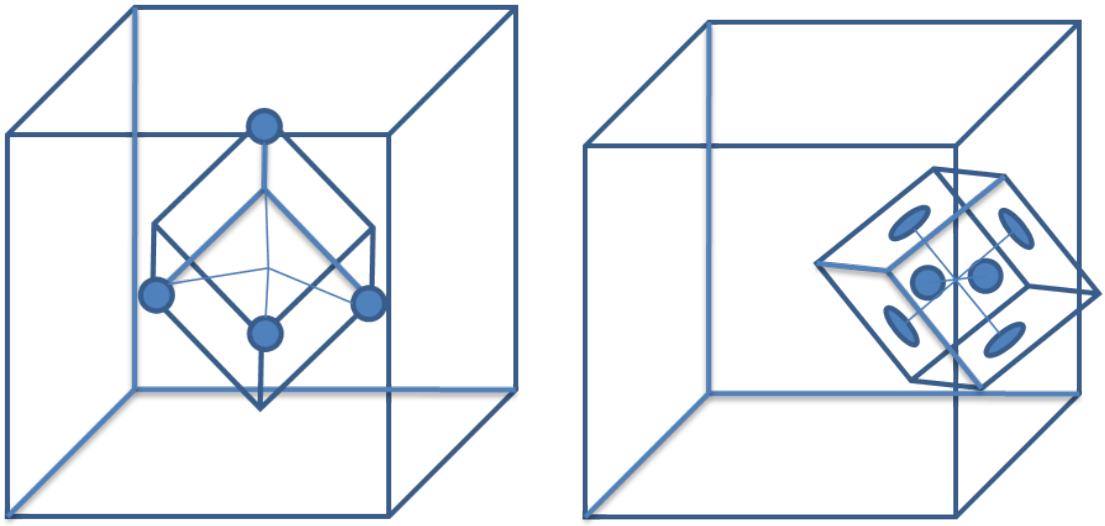

(a) strongly polarized (b) weakly polarized

Figure 2.18: (a) Tetrahedral site position relative to cubic crystal and (b) Octahedral site position relative to cubic crystal in olivine crystal strcture to illustrate site dependent polarized transitions.

and not based on the crystal coordinate. For the tetrahedral site in olivine crystal structure, z-axis of tetrahedron is align with z-axis of crystal. Because of that, there are three polarized sites in tetrahedral complex. In contrast to to the tetrahedral site, any axis of octahedron doesn't align with any crystal axis. If we excite the complex using crystal axis, the complex only see the projection of electric field on the complex axis. Because of this reason, the transition moment integral is weakly polarized if the electric field aligns crystal X,Y, and Z axis.

2.9 Calculating the energy levels of Cr^{4+} and Cr^{3+} ions in $Cr : LiScGeO_4$ using Angular Overlap Model

In section.2.2, the theory of angular overlap model is explained in detail. The reason I have to determine the energy levels of $Cr^{3+}$and Cr^{4+}ions is I'll use this data in next chapter.In ref.[12], the calculation of the energy level of Cr^{4+}ions in tetrahedral site and Cr^{3+}ions in octahedral site in Cr:LiScGeO4 is done using angular overlap model.

2.9.1 Cr^{4+} ions in $Cr : LiScGeO_4$

In d^2 system in tetrahedral coordination, the total of orbital wave functions which can exist under arbitrary crystal field is 45. How we calculate the eigenvalues of 45 wave functions is as follows.The strong field model is a model of choice to calculate the energy levels using angular geometry of complex. First we have to know the geometry of tetrahedral complex. In section.2.9.1.1, the four ligand positions of tetrahedral complex is described with the angle position θ and ϕ. The definition of θ and ϕ is illustrated in fig.2.6. By using these angular values, we need to build the angular overlap matrix for 5 d orbitals, $d_{xy}, d_{xz}, d_{yz}, d_{z^2}$ and $d_{x^2-y^2}$. By diagonalizing AOM matrix, we got the eiganvalues(energy) of split 5 d orbitals. By using these eigenvalues, the 5 eigenfunctions can be determined. As a reminder, in undistorted tetrahedral complex, 3 eigenfunctions have the same energy and form t_2 orbital group (degeneracy is 3) while other 2 eigenfunctions also have the same energy and form e orbital group (degeneracy is 2). If the complex (here, CrO_4^{4-}) is distorted tetrahedron, the symmetry is lower from T_d to C_s symmetry. In C_s symmetry, all degeneracies are lifted.

Now we have to find the split energy levels because of inter-electronic repulsions

by placing the two electrons in 5 d orbitals in possible ways by obeying Pauli exclusion principle. The split energy levels of each electronic configuration can be calculated by doing the direct product of two d wave functions. For example, energy levels of t_2^2 configuration can be described by finding the direct product of two t_2 wave functions. Ideally, (45×45) complex matrix is built using the inter-electronic repulsion potential. By diagonalizing the matrix, it may possibly be determined the eiganvalues if there is no mixing between orbitals because of inter-electronic potential. If there is mixing between orbitals, the calculation of finding eigenvalues and eigenvectors is difficult. If there is degeneracy, we will get the orbitals with the same energy. By collecting the degeneracy orbitals, the final orbital counts will be lower than 45. Up until now, since we don't consider splitting because of the spin-orbit coupling potential, the spin degenerate terms will appear as the crystal field and inter-electronic transition doesn't lift the spin degeneracy.

In the following section, I summarize the calculated energy levels and experimental measure values of Cr^{4+}ions in tetrahedral complex in $LiScGeO_4$ crystal. I have to stress that we always need the absorption spectrum and/or sometimes excitation spectrum to calculate the ligand field parameters e_σ and e_π by using the experimental data because ab initio calculation is not possible with normal computing power. Using the fitting e_σ and e_π values, all energy levels can be calculated including the levels which cannot be observed experimentally. Also the crystal field parameter $10Dq$ and Racha parameters B can be determined from these two parameters.

2.9.1.1 Energy levels of Cr^{4+}ions in $LiScGeO_4$ single crystal: Tetrahedral complex

Geometry of ligands			Ligand parameters	
Atom	θ	ϕ	$\frac{e_\sigma}{e_\pi}$	$= \frac{1}{6}$(fixed)
1	2.5	0	e_σ	$= 9578\ cm^{-1}$
2	114.8	180	e_π	$= 1596\ cm^{-1}$
3	116.8	56.1	$10Dq$	$= 9933\ cm^{-1}$
4	116.8	-56.1	B	$= 526\ cm^{-1}$

Transition	Calculated (cm^{-1})	Experiment (cm^{-1})
$^3A''(^3T_1(P))$	23637	
$^3A''(^3T_1(P))$	23102	
$^3A'(^3T_1(P))$	21622	
$^3A''(^3T_1)$	17338	16900
$^3A'(^3T_1)$	13842	14900
$^3A''(^3T_1)$	13000	12700
$^3A'(^3T_2)$	10271	10400
$^3A'(^3T_2)$	9192	9400
$^3A''(^3T_2)$	9125	8500

2.9.2 Cr^{3+} ions in $Cr : LiScGeO_4$

In Cr^{3+}ions, there are total of three d electrons. Because of that there are total of 120 wave functions we possibly can get from the octahedral crystal field, inter-electronic repulsions and spin-orbit coupling. Since there are more than 100 wave functions, the calculation is more complex than Cr^{4+}ions in tetrahedral sites. The geometry of distorted octahedraon in Cr:$LiScGeO_4$ single crystal can be found in structural studies of this crystal[33]. The same method described in section(2.9.1) can be used

to calculate the energy value of Cr^{3+}ions in $Cr : LiScGeO_4$ crystal.

2.9.2.1 Energy levels of Cr^{3+}ions in $LiScGeO_4$ single crystal: Octahedral complex

The energy level of Cr^{3+}ions in octahedral site in $LiScGeO_4$ crystal is summarized as follows.

Geometry of ligands			Ligand parameters	
Atom	θ	ϕ	$\frac{e_\sigma}{e_\pi}$	$= \frac{1}{6}$(fixed)
1	0	0	e_σ	$= 6670\ cm^{-1}$
2	179	0	e_π	$= 1110\ cm^{-1}$
3	89.6	53.8	$10Dq$	$= 15570\ cm^{-1}$
4	89.6	-53.8	B	$= 738\ cm^{-1}$
5	97.0	-142.8		
6	97.0	142.8		

Transition	Calculated (cm^{-1})	Experiment (cm^{-1})
$^4A''(^4T_1)$	21400	20800
$^4A'(^4T_1)$	21020	20800
$^4A''(^4T_1)$	21000	21200
$^4A''(^4T_2)$	14980	14500
$^4A'(^4T_2)$	14900	13900
$^4A''(^4T_2)$	12830	13420

Figure.2.19(a) shows the absorption spectrum of $Cr : LiScGeO_4$ single crystal and Figure.2.19(b) shows the comparison among the energy values of first and second spin-allowed transition levels $^3T_1$, $^3T_2$ of Cr^{4+}ions in tetrahedral site and these of first and second spin-allowed transition levels $^4T_1$,$^4T_2$ of Cr^{3+}ions in octahedral site. If

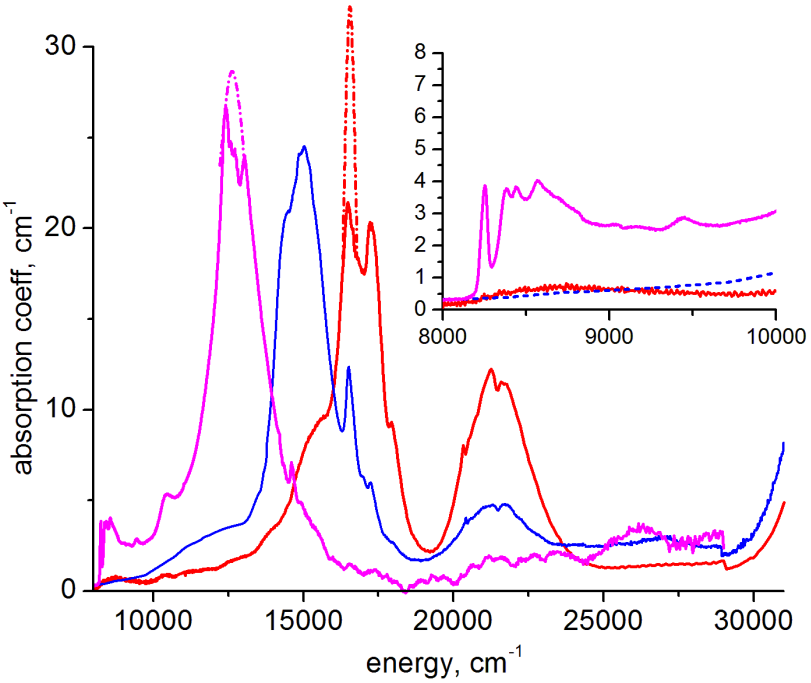

(a) Absorption spectrum of $LiScGeO_4$ crystal

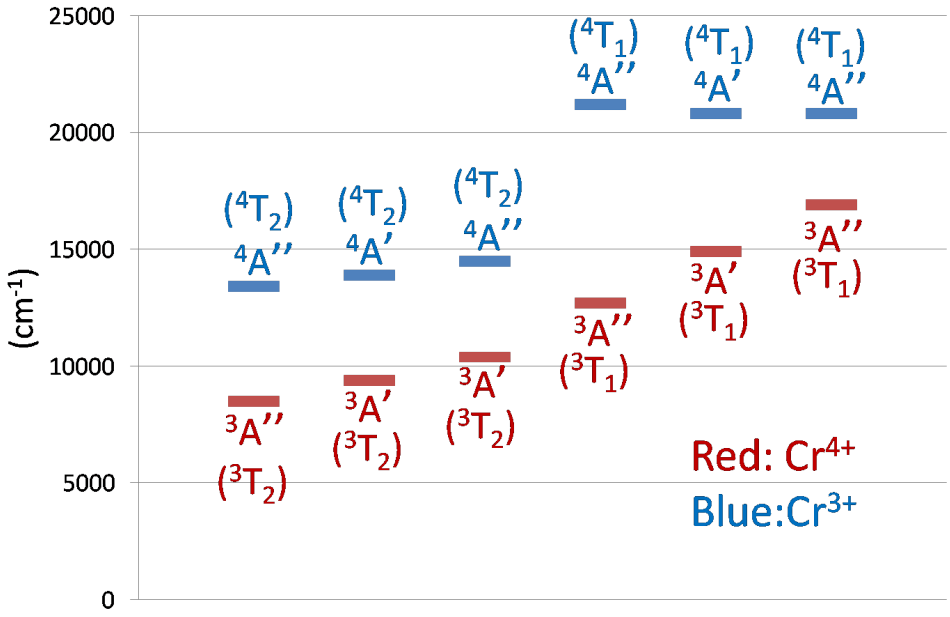

(b) Comparison of $Cr^{3+}$and Cr^{4+}ions

Figure 2.19: Comparison of ${}^3T_1$ & ${}^3T_2(Cr^{3+})$ energy levels and ${}^4T_1$ & ${}^4T_2$ (Cr^{4+}) energy levels

the crystal has the multicenters, the knowledge of energy level of first spin-allowed transitions of different centers is important in distinguishing the optical centers. As shown in figure.2.19(b), first excited state ($^4T_2$) of Cr^{3+}ions is about $5000cm^{-1}$ higher than the first excited state ($^3T_2$) of Cr^{4+}ions. The second spin-allowed transition of Cr^{3+}ions is in ultra-violet region and that of Cr^{4+}ions is in visible range. Since the energy of $^3T_1$ and $^4T_2$ is about the same, the absorption spectrum shows the combined absorption of $Cr^{3+}$and Cr^{4+}ions in visible range. Since the color of $Cr : LiScGeO_4$ is reddish color and the complementary color of red is blue, the absorption of $^4T_1$ transition of Cr^{3+}ions in octahedral site is stronger in this crystal.

Chapter 3

Measurement of relaxation dynamics of Cr^{4+}tetrahedral centers in Cr:$LiScGeO_4$ crystal

In this chapter, the excitation relaxation time of metastable level of Cr^{4+}ions in Cr:$LiScGeO_4$ single crystal is presented using time-resolved pump-probe spectroscopy and streak camera technique.

The discovery of Cr^{4+}:Mg_2SiO_4 laser crystal by Alfano's group[20, 19] has fueled the search for the new laser materials activated with Cr^{4+}ions since 1988. Since the electronic properties of Cr ions is strongly dependent on the local environment, its optical properties vary widely from one host crystal to another. Most crystal hosts don't have the favorable surrounding for chromium ions to decay radiatively. It is well known that Cr^{4+}ions doped optical crystals suffer from multiphonon non-radiative relaxation and excited state absorption. Only a few crystal hosts show proven laser properties. Forsterite(Mg_2SiO_4) host is one of them and it has olivine crystal structure. After Cr:Mg_2SiO_4 crystal, IUSL developed another Cr^{4+}activated laser crystal in 1994, namely Cr^{4+}:Ca_2GeO_4 . It has better quantum efficiency than Cr:Mg_2SiO_4 and the emission peak is shifted to the telecom operating region (1.55 μm). Thus it is possible to engineer the emission range of chromium doped laser crystal by choosing the proper host crystal composition. Because of that reason, research on Cr^{4+}laser goes on with the hope of finding good optical quality crystal

which covers both telecommunication windows (1.33 μm and 1.55 μm). Since both Mg_2SiO_4 and Ca_2GeO_4 host crystals have olivine crystal structure, the host having olivine structure is the material of choice to develop new Cr^{4+}tunable near-infrared lasers.

In olivine crystal structure, there are two octahedral sites for Cr^{3+}ions substitution and one tetrahedral site for Cr^{4+}ions substitution. IUSL developed all laser crystals such as Cr:Mg_2SiO_4 , Cr:Ca_2GeO_4 have the olivine crystal structure. In Cr doped Mg_2SiO_4 crystal, both trivalent and tetravalent chromium ions coexist together and the emission peak of Cr^{3+}ions is around 900nm and of Cr^{4+}ions is around 1100nm. But in Ca_2GeO_4 crystal, only tetravalent chromium ions can exist because Cr^{3+}substitution in place of Ca^{2+} is very unlikely in crystallographic point of view as the ionic size of Ca^{2+}(0.1nm) is larger than that of Cr^{3+}(0.0615nm) [14].

Tables(3.1 & 3.2) shows the broadest tuning range obtained with some $Cr^{4+}$and Cr^{3+}lasers. When we compare the two tables, the tuning range of Cr^{4+}lasers around 1100-1600 while the tuning range of Cr^{3+}lasers is around visible region (700-900nm). Because the emission range of well known Cr^{3+}lasers such as ruby, emerald and alexandrite is around the visible range and the emission range of well known Cr^{4+}lasers such as forsterite, YAG is around near-infrared region, it becomes a trend that only $Cr^{4+}$is the only valence state which produce the near-infrared emission.

Cr^{4+}laser	Tuning range(nm)
Cr^{4+}:forsterite	1130-1367
Cr^{4+}:YAG	1309-1596
Cr^{4+}:$Y_3Sc_{0.5}Al_{4.5}O_{12}$	1394-1628
Cr^{4+}:$Y_3ScAl_4O_{12}$	1464-1604
Cr^{4+}:Ca_2GeO_4	1340-1490

Table 3.1: Broadest tuning ranges obtained with some Cr^{4+}lasers

Cr^{3+}laser	Tuning range (nm)
Cr^{3+}:$LiSrAlF_6$	780-1010
Cr^{3+}:$LiCaAlF_6$	720-840
Cr^{3+}:$Be_3Al_2(SiO_3)_6$(emerald)	695-835
Cr^{3+}:$BeAl_2O_4$(alexandrite)	701-818

Table 3.2: Tuning range of some Cr^{3+}lasers

3.1 Spectroscopic evidences which point to the near-infrared emission center of Cr:$LiScGeO_4$ crystal is Cr^{3+}ions, not Cr^{4+}ions

Since the near-infrared tunable lasers have a lot of applications such as medical imaging, optical remote sensing and especially in optical communications, IUSL constantly looking for the new laser crystals which can give better quantum efficiency and wider tuning range. Because of this efforts, in 1997, the near-infrared laser action from Cr:$LiScGeO_4$ single crystal is achieved and the emission center is assigned to Cr^{4+}ions[27].

Since $LiScGeO_4$ host has the olivine crystal structure, Sc^{3+} and Li^{1+} ions house in octahedral site with mirror symmetry and in octahedral site with inversion symmetry respectively while Ge^{4+} house in tetrahedral site. In this crystal composition, lithium ions are used for the charge compensation purpose. When chromium is doped to the crystal, Cr^{3+}substitute Sc^{3+} and Cr^{4+}substitute Ge^{4+}. Having Cr^{3+}ions in Cr:$LiScGeO_4$ crystal is confirmed by EPR measurement[33].

Starting from 2005, Alfano's group published a series of papers [28, 12, 29, 30] proving that the active center in this crystal is not Cr^{4+}ions and the actual lasing center is Cr^{3+}ions. This claiming is based on the meticulous attention to detail in spectroscopic measurements and analysis. There are four red flags pointing that the

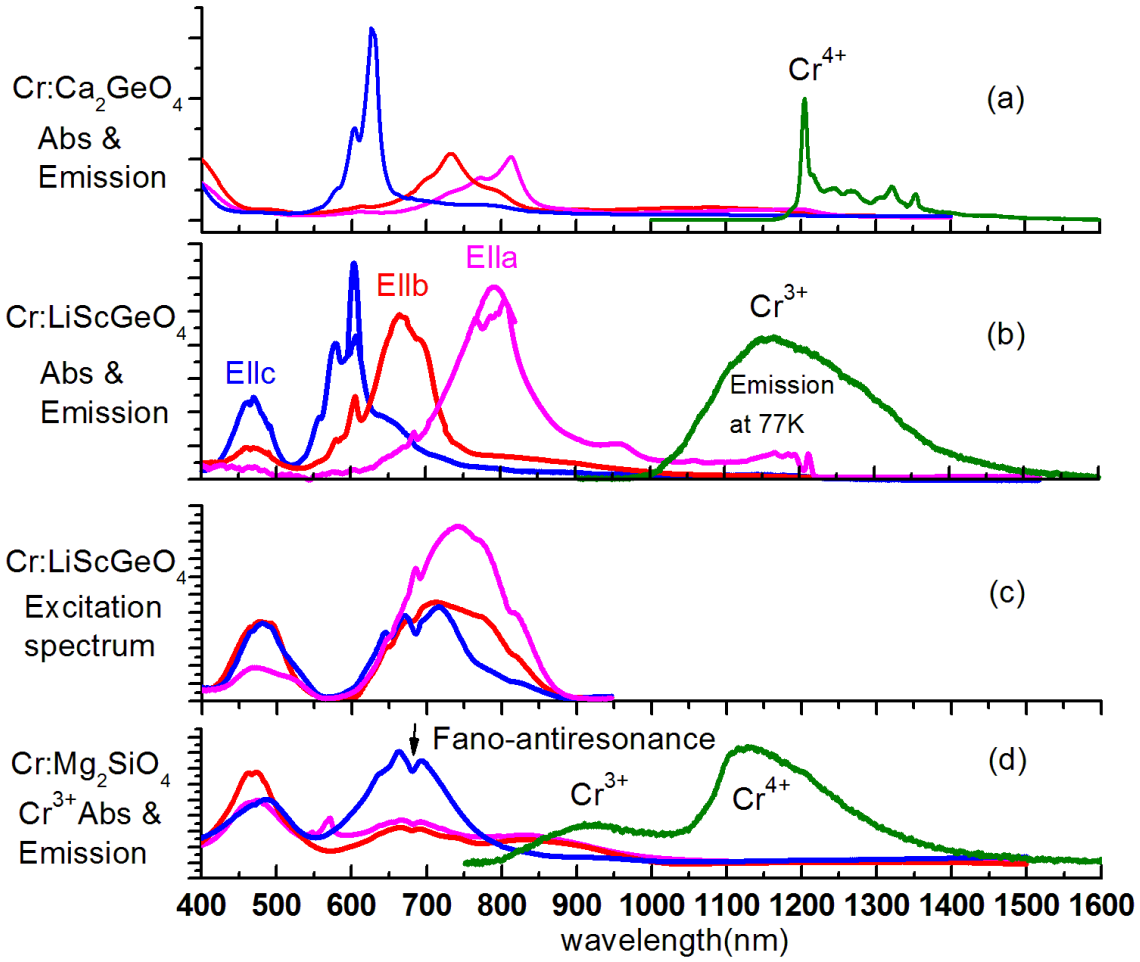

Figure 3.1: (a) The polarized absorption and emission spectrum of Cr:Ca_2GeO_4 .
(b) The polarized absorption and emission spectrum of Cr:$LiScGeO_4$.
(c) The excitation spectrum of Cr:$LiScGeO_4$.
(d) The polarized absorption spectrum of Cr^{3+}ions in Cr:Mg_2SiO_4 and the emission spectrum of forsterite glass ceramic which shows the combined emission of $Cr^{3+}$and Cr^{4+}ions in forsterite crystal.
All measurements were done at low temperature.

emission center is Cr^{3+}in Cr:$LiScGeO_4$ is as follows.

1. Figure. 3.1(a) shows the emission spectrum together with the polarized absorption spectrum of Cr:Ca_2GeO_4 measured at liquid nitrogen temperature. In Cr:Ca_2GeO_4 , only Cr^{4+}ions can exist. Thus the absorption and emission spectrum represents pure Cr^{4+}ion's spectrum. Figure.3.1(b) shows the polarized absorption and emission spectrum of Cr:$LiScGeO_4$ single crystal. The zero-phonon line of metastable level ($^3T_2$) of Cr^{4+}ions is clearly visible in absorption spectrum when the polarization direction is along a-axis of the crystal. The zero-phonon line is located at 1200nm, the same position as Cr:Ca_2GeO_4 crystal. As shown in figure.3.1(b), the near-infrared emission of Cr:$LiScGeO_4$ starts way above the zero-phonon line of Cr^{4+}ions. Since the emission starts way above the metastable level of Cr^{4+}ions, the emission center of this crystal cannot be Cr^{4+}ions.

2. Figure. 3.1(c) shows the excitation spectrum of Cr:$LiScGeO_4$ with monitored emission wavelength of 1200nm. By comparing fig. 3.1(b)& (c) the shape of polarized excitation spectrum is different from that of the polarized absorption spectrum for each polarized excitation direction. This clearly indicates that there are more than one centers exist in the crystal. Fig. 3.1(a)& (d) shows the pure absorption spectrum of $Cr^{4+}$and Cr^{3+}ions respectively. In Cr doped forsterite crystal, Cr^{3+}ions in octahedral site with mirror symmetry have absorption bands peak around 470nm and 670nm, which are similar to two distinct bands of excitation spectrum of Cr:$LiScGeO_4$ crystal. The fact that the different bands appeared in absorption and excitation spectrum of Cr:$LiScGeO_4$ crystal and similarity of excitation spectrum of Cr^{3+}ions in forsterite and the excitation spectrum of Cr doped $LiScGeO_4$ give the clue that the emission center is Cr^{3+}ions in $LiScGeO_4$ crystal.

3. In the excitation spectrum of Cr:$LiScGeO_4$ crystal, Fano-antiresonance dip is clearly visible. The Fano-antiresonance is resulted from the interaction between $^4T_2$ and ^2E through spin-orbit coupling and it always present near 690nm in every well-known Cr^{3+}doped laser crystals such as emerald, alexandrite and forsterite. Having the Fano-antiresonance dip strengthens the claim that $Cr^{3+}$is emission center in Cr:$LiScGeO_4$ crystal.

4. As shown in fig. 3.1(b), the absorption of $LiScGeO_4$ is highly polarization dependent while the excitation spectrum has weakly dependent on the polarization. In olivine crystal structure, there are one octahedral site with mirror symmetry and one tetrahedral site. If Cr is doped in crystal host having olivine structure, Cr^{3+}ions substitute Sc^{3+} ions in octahedral site and Cr^{4+}ions replaced Ge^{4+} ions in tetrahedral site. One axis of tetrahedron aligns with the crystallographic z axis and accordingly the strong dependent on the polarization direction of excitation is observed. Thus the absorption cross-section of Cr^{4+}ions housed in tetrahedral site is strongly dependent on the polarization.In the case of octahedral site, any of octahedral axes do not align with crystallographic axes and only projection of polarized excitation is seen by the active Cr^{3+}ions in octahedral site. Because of this reason, the absorption cross-section is weakly dependent on the polarization direction and consequently the absorption bands of Cr^{3+}ions in $LiScGeO_4$ crystal is weakly polarization dependent. As shown in fig. 3.1(c), the excitation spectra of $LiScGeO_4$ crystal is weakly polarization dependent and this fact shows that the active center is housed in octahedral site of the crystal. This gives us another clue that the near-infrared emission center of $LiScGeO_4$ crystal is Cr^{3+}ions housed in octahedral sites with mirror symmetry.

This discovery raises one serious question. If the near-infrared emission of this crystal is Cr^{3+}ions, where is emission from Cr^{4+}ions which typically is the near-infrared emission center in olivine crystal structure?

If there is no emission from Cr^{4+}ions in tetrahedral coordination in this crystal, excited Cr^{4+}ions must decay non-radiatively. Since the absorption cross-section of Cr:$LiScGeO_4$ and Cr:Ca_2GeO_4 is about the same, the emission cross-section of the two crystals must be about the same. Since the radiative decay rate is independent of temperature in spin-allowed transition, the radiative decay rate of Cr:$LiScGeO_4$ is the same as that of Cr:Ca_2GeO_4 crystal. Since there is no emission from Cr:$LiScGeO_4$ crystal, the non-radiative decay rate must be really fast and the lifetime of excited state is extremely short. There must be some non-radiative decay channels in Cr:$LiScGeO_4$ crystal. In this research, we would like to find out this decay time. If we can show that the decay time is in the order of picosecond or nanosecond, this is another proof that the emission center of this crystal is Cr^{3+}ion.

3.2 Energy level of Cr^{4+}ions in tetrahedral surrounding

Figure.3.2(a) shows the energy level diagram of Cr^{4+}ions in tetrahedral site in Ca_2GeO_4 single crystal. Before Cr doping, $(GeO_4)^{4-}$ tetrahedron has T_d point symmetry. When Cr ions substitute Ge ions, tetrahedron is distorted and its symmetry is reduced from T_d to C_s . At low symmetry, the degeneracy of energy level is lifted and the energy level is split as shown in the figure(3.2(a)). Sometimes C_s symmetry is estimated with C_{3v} symmetry to simplify the energy level calculation. The energy level of Cr^{3+}ions in octahedral surrounding is also shown in the figure as a comparison.

Since Cr:$LiScGeO_4$ crystal is anisotropic crystal, the absorption transition are strongly polarized along certain excitation direction. When the symmetry of tetrahedron is reduced from T_d to C_s symmetry, the degeneracy of $^3T_1$ state is lifted and $^3T_1$ level is split into three. These three transitions are as shown in the fig.3.2(b) as 600nm, 700nm and 800nm. 600nm absorption band is strongly polarized along short

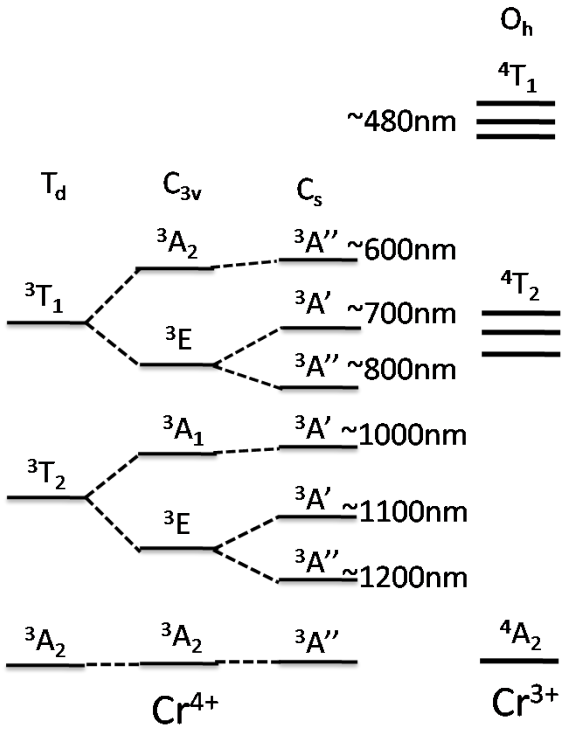

(a) Energy level diagram of Cr^{4+}ions in tetrahedral surrounding with T_d -C_{3v} -C_s symmetry and of Cr^{3+}ions in octahedral surrounding

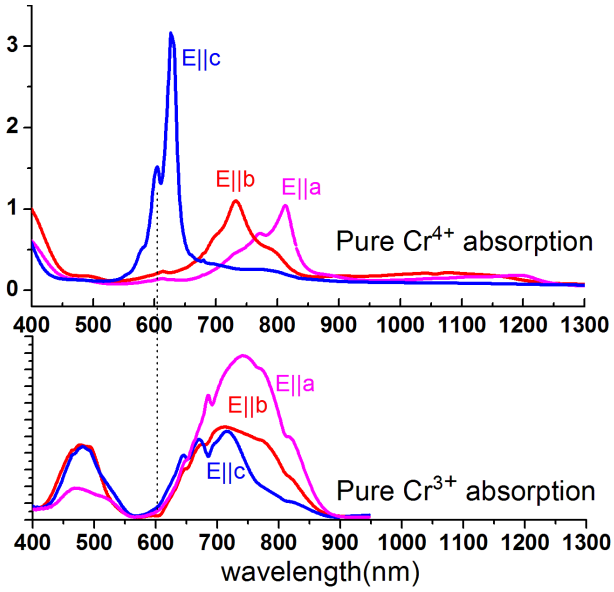

(b) Absorption spectrum of $Cr^{4+}$and Cr^{3+}ions

Figure 3.2: Typical Energy level diagram and absorption spectra of $Cr^{4+}$and Cr^{3+}ions in olivine crystal structure

axis of the crystal, 700nm band is polarized along medium axis while 800nm band is along the long axis of the crystal. Both 700nm and 800nm absorption bands are level with the split states of $^4T_2$ energy level of Cr^{3+}ions while 600 nm band is only associated with tetravalent chromium ions. Since there is no energy states of trivalent chromium ions leveled with $^3T_2$ state of Cr^{4+}ions, 1000, 1100 and 1200nm bands are also only associated with tetravalent chromium ions. The excitation spectrum of Cr:$LiScGeO_4$ also shows that there is almost no near-infrared emission at 600nm excitation, see fig.3.1(c).

Measurable near-infrared emission from Cr:$LiScGeO_4$ crystal is observed when the sample is excited with Argon laser (488nm), 670nm laser diode and Ti:Sapphire laser (800nm line) while there is no emission observed even at 77K when excited with Nd:YAG (1060nm) and 600nm dye laser line. In contrast, the proven Cr^{4+}activated laser crystals such as Cr:Ca_2GeO_4 and Cr:Mg_2SiO_4 show strong near-infrared emission while excited with 1060nm and 600nm laser lines at room temperature. In Cr:Ca_2GeO_4 single crystal, only tetravalent chromium ions can exist because of the size mismatch between Ca^{2+} and Cr^{3+}ions. Thus Nd:YAG 1060nm laser line and Dye 600nm laser line are the best choice to selectively excite tetravalent chromium ions in Cr:$LiScGeO_4$ crystal.

Since Cr:$LiScGeO_4$ single crystal doesn't show any emission with 50MHz bandwidth (10ns) InGaAs detector while excited with either 1060nm line or 600nm line, pump-probe excited state absorption spectroscopy will be used to measure the lifetime of metastable level of Cr^{4+}ions in this crystal.

3.3 Selective Excitation of Cr^{4+}ions in Cr:$LiScGeO_4$

The main objective in this chapter is to measure the decay time of metastable level of Cr^{4+}ions in $LiScGeO_4$ crystal. Before I go to explain the decay dynamic of Cr^{4+}ions,

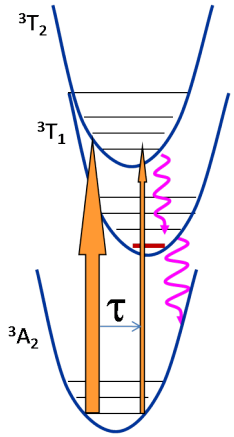

Figure 3.3: Decay dynamics of Cr^{4+}ions in Cr:$LiScGeO_4$ crystal

I have to remind that there are both $Cr^{3+}$and Cr^{4+}ions in this crystal. We know that the emission center is Cr^{3+}ions. Since we're interested in Cr^{4+}ions decay dynamics because of the lack of emission from this valence state, we have to made the site selective excitation. The easiest one is to use 1064nm excitation source. As shown in the figure.3.2, there is no Cr^{3+}ions absorption transition at this wavelength range. But we don't have the 1064nm femtosecond laser source. With the help of the absorption and excitation spectra of Cr:$LiScGeO_4$,fig.3.1 and fig.3.2(b), we choose 600nm excitation line. As you can see in the figure.3.2(b), there is almost zero Cr^{3+}absorption at this wavelength and Cr^{4+}absorption is strong if the crystal is excited along the short (c) axis of the crystal.

3.4 Decay dynamics of excited Cr ions

The decay dynamic of Cr^{4+}ions in Cr:$LiScGeO_4$ crystal is shown in the figure. 3.3. Figure shows only spin-allowed states of Cr^{4+}ions in tetrahedral coordination. Ground state is $^3A_2$, first excited state is $^3T_2$, pumped stated is $^3T_1$ (F). Since the excitation wavelength is 600nm (16500), Cr^{4+}ions are excited to $^3T_1$ (F) state. Since the lifetime of this pumped state is in the order of a few picosecond, the excited ions immediately relax nonraditively to the first excited state ($^3T_2$). Since the $^3T_2$ state is a metastable

state, the ions are populated there. It is quite possible that subsequent pumping place the ions to another excited state $^3T_1$ (P). But compared to the absorption transition ($^3A_2 \rightarrow {}^3T_1$), the absorption to this state requires two photons. Consequently the transition to this state is very weak.

Pump-probe measurement of lifetime of excited state of Cr^{4+} ions in Cr:$LiScGeO_4$ single was done as follows. At the time of pump arrival, most of Cr^{4+} ions at ground state are placed at ($^3T_2$) metastable level through ($^3T_1$) state. Because of strong pumping, the sample transparency is highest at that moment. At the lifetime of excited state, the excited ions decay back to the ground state non-radiatively. Because of repopulation of ground state, the sample transparency is greatly reduced. By measuring the sample transparency by playing the delay between the pump and probe pulses, we can determine the decay time of excited state of Cr^{4+} ions in Cr:$LiScGeO_4$ crystal.

As explained in section3.3, I'll use 600nm femtosecond strong pulses to place the Cr^{4+}ions at the metastable level. Since the absorption cross section of Cr^{4+}ions is strongly dependent on the polarization direction of excited electric field, the propagation direction of excitation beam must be along the long axis of the crystal ([100] direction). With this direction of propagation, the polarization direction of pump beam set along the short axis since the absorption cross-section of Cr^{4+}ions in E$\|$c is maximum while the polarization direction of probe beam is set along the medium axis as there is significant absorption of 600nm line along E$\|$b polarization direction, see fig.(3.1) and fig.(3.2).

3.5 Laser system

Laser system for the pump-probe experiment is as shown in the figure. 3.4. Since the output of the laser system is 500-femtosecond 600nm amplified laser pulse with repetition rate of 10Hz, the laser system comprises the oscillator and the amplifier.

Both the oscillator and the amplifier need the associated pump laser. Synchronization is also needed between the oscillator and amplifier. Thus There are five major components in the system. I would like to describe the important detail about these components as follows.

3.5.1 Diode-pumped Nd:YVO_4 High Q laser

It is used to pump the Rhodamine-6G dye laser. Specifications related to the experiment are

Recommended pump	
laser diode current:	22 A
Maximum pump	
laser diode current:	28 A
Pulse width, FWHM:	7 picosecond
Cooling water	
set temperature:	21 ^{o}C
Average output	
power (after exit):	1064 nm: 4 Watt (at 22 A)
	532 nm: 2.2 Watt (at 22 A)

3.5.2 Synchronous pumped Rhodamine-640 dye laser

Here I would like to document how to prepare the dye solution for the laser.

3.5.2.1 Dye Preparation

The dye used in the dye oscillator is Rhodamine 640. The emission peak of Rh-640 is located at about 603nm. The tunable range is between 598nm to 626nm. The followings are step by step to change the new dye in the laser.

1. Weight 1.44g of the Rh-640 dye power by using the precision scale.

2. Dissolve the dye power with 30ml methanol. Methanol is very good solvent for the dye power.

3. Stir the dye solution by using the magnetic stirrer for about an hour. Mix the resultant dye solution with 1.47 L of viscous ethylene glycol.

4. Clean the reservoir with methanol to clean undissolved old dye at the bottom.

5. Then fill the reservoir with the 50-50 mixture of methanol and ionized water and open the pump about 20 minutes to clean the whole drainage dye's following through.

6. Open the filter housing and drain the dye inside and change the new filter.

7. Fill the new dye with the prepared new dye solution.

Note: If you don't change the filter and you want to change the dye only, you only need to prepare the dye solution for about 1 Litre because the reservoir is enough for 1 Liter. If you did change the filter, you need to prepare 1.5L solution because the new filter sucks approximately 0.5L of dye solution.

3.5.3 Quanta-Ray GCR-3 Q-switched pulsed Nd:YAG laser

It is used to pump the PDA(Pulsed Dye Amplifier). The important specification of GCR-3 is as follows.

Wavelength(nm)	Pulse Width(ns)	Pulse Energy(mJ)/Peak Power (mW)	
		10pps	30pps
1064	7-9	850/105	750/95
532	5-7	400/65	330/50

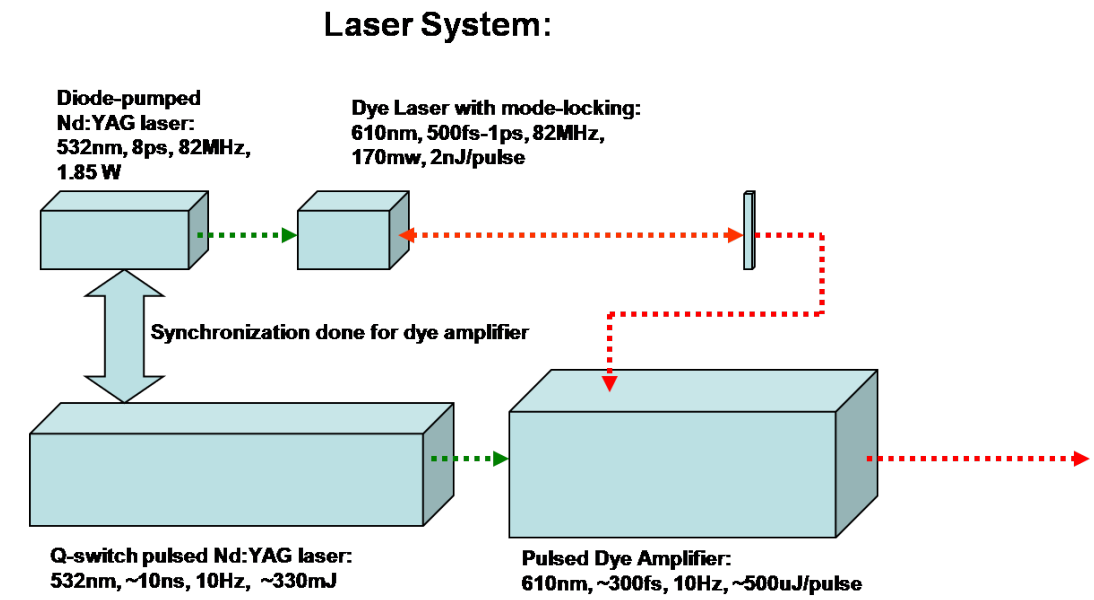

Figure 3.4: Laser system for excitation

3.5.4 Synchronization module

As explain in the above, there is a need to synchronize between Nd:YVO_4, which pumps the dye oscillator and Q-switched Nd:YAG lasers, which pumps the dye amplifier. Synchronization is done in the following figure.

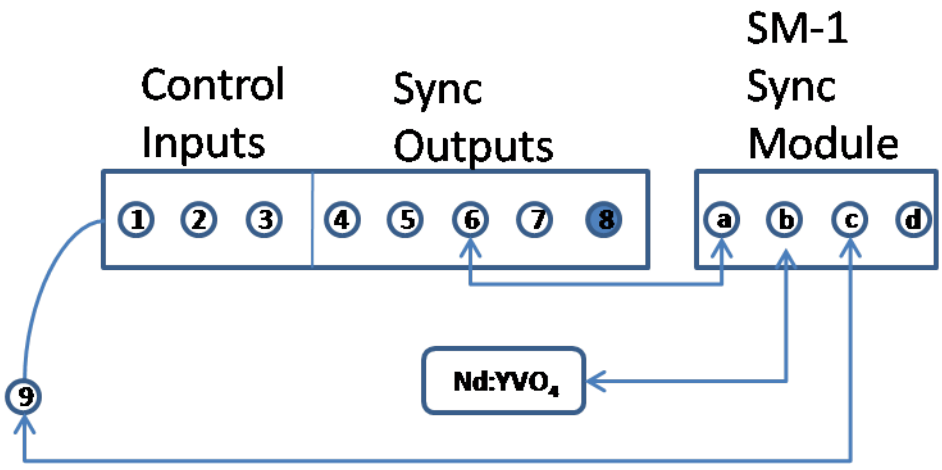

Control Inputs:

1 External oscillator trigger

2 Blank trigger

3 Lamp trigger

9 Q-switch input

Sync Outputs:

4 Oscillator trigger output

5 lamp trigger output

6 Q-switch output

7 Variable trigger

8 Variable trigger adjustment notch

SM-1 Sync Module:

a Q-switch sync signal

b Sync Input (signal from Nd:YVO_4)

c Q-switch out (trigger signal to drive Q-switch laser)

d Sync output (to drive the oscilloscope)

The figure shows the connection diagram between the Q-switched laser and the SM-1 sync module. The function is SM-1 sync module acts like a phase locked loop. It takes the input from the sync pulses from Nd:YVO_4 and the sync pulses from Q-switch laser as the feedback. The main function of SM-1 sync module is to drive Q-switch laser to sync with the Nd:YVO_4 laser pulses.

One problem encountered during this setup is the sync signal from Nd:YVO_4 laser is very weak to drive SM-1 sync module. Since the sync module requires the pure sinusoidal wave and the peak to peak signal of 200mW. As shown in the figure. 3.5b, the sync output of Nd:YVO_4 is distorted square wave and the peak to peak intensity of 4mV. The buffered circuit to amplified the signal is as shown in the figure. 3.5a. The output signal of this buffered circuit is also shown in the figure. 3.5b. The signal is Sine shape and the peak-peak signal intensity is about 400mV, which is more than enough to drive SM-1 sync module.

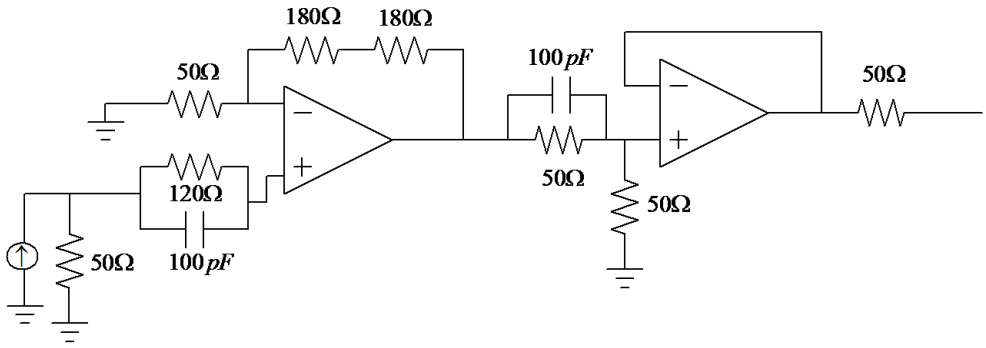

(a) Circuit Diagram of Synchronization Box

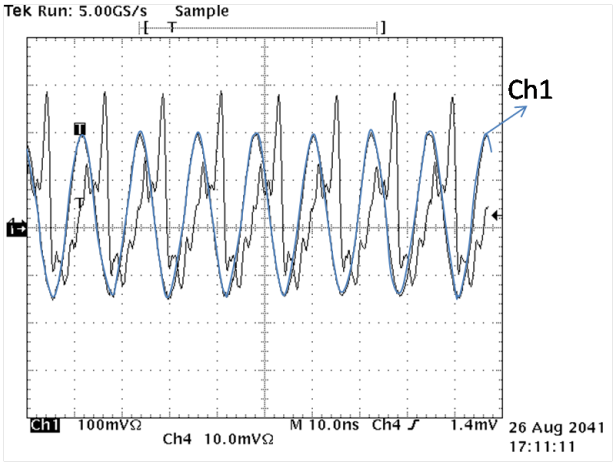

(b) Output Siganal of Sync Circuit Box

Figure 3.5: Required synchronization circuit between two pump lasers

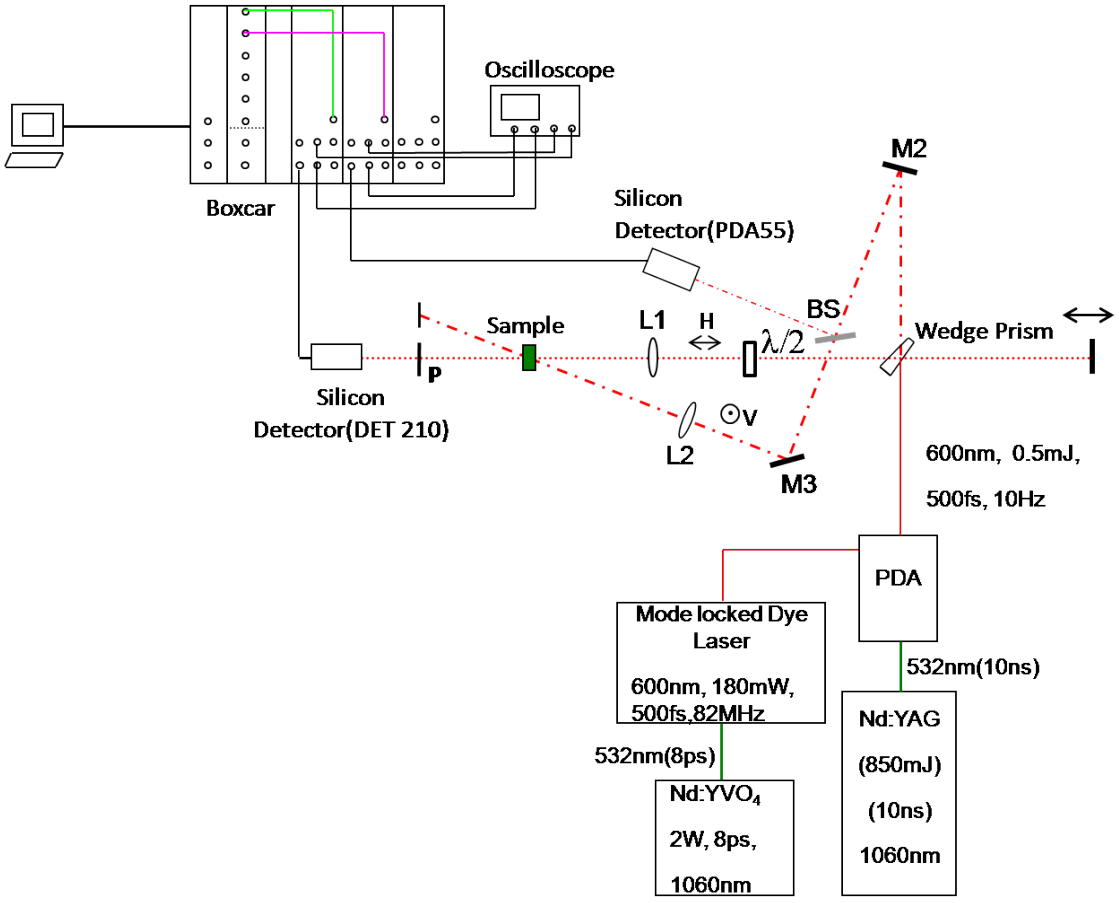

Figure 3.6: Experimental Setup to measure the ultrafast decay time of $LiScGeO_4$

3.6 Picosecond Detection System

The complete experimental setup is shown in figure. 3.6. Major segments of the experiment are the laser system, mechanical delay line, boxcar averager and data acquisition system. The laser system is already explained in the above sections. The following subsections will explain each major segments in detail.

3.6.1 Unidex 11

The mechanical delay is Unidex 11 model from Aerotech Company. Because the useable delay line is about 20cm, we can measure the delay time of a little more than 1ns with this mechanical delay line.

Figure 3.7: SRS 250 - Gated Integrator & Boxcar Averager

3.6.2 SRS 250 - Gated Integrator & Boxcar Averager

There are three instruments for recovering the weak signal from noise. They are

1. SRS(Standford Research Systems) gated integrator and boxcar averager
2. the lock-in amplifier with optical chopper
3. the photon counter (PMT - Photomultiplier Tube)

In this setup we will use the SRS 250 (Stranford Research Systems) gated integrator, boxcar averager and SRS 245 computer interface to recover the noisy signal. Before we go any farther, I would like to explain about the functions of SRS 250 (gated integrator and boxcar averager). As shown in the figure.3.7, SRS 250 have five functional partitions. They are

1. Trigger

   In short, we can use the internal trigger or the external trigger. We use the external trigger from Q-switch. If you use the internal trigger, you can adjust different repetition rate (range: 0.5Hz to 20KHz).

2. Delay

   The delay of the sample gate from the trigger is controlled with these delay controls (range: 1ns - 100ms).

3. Width

   The width of the sampling gate. These controls are the most important setting in our setup (ranges: 2ns - 15μs). With the help of the oscilloscope, the gate is carefully chosen to catch 500-femtosecond laser pulses.

4. Signal

   The sensitivity of the instrument (volts out/volts in). The applicable range is from 1V/V to 1V/5mV.

5. Averaging

   Averged output (Averging range: From 1 pulse to 10K-pulses).

6. Inputs

   There are two inputs. (1) Trigger input from Q-switch and (2) Signal input from the detector. (input impedance: 1MΩ and maximum input voltate: 100volt).

7. Outputs

   There are four outputs.

Gate 50Ω: The gate output shows exactly which portion of the input signal is being sample.

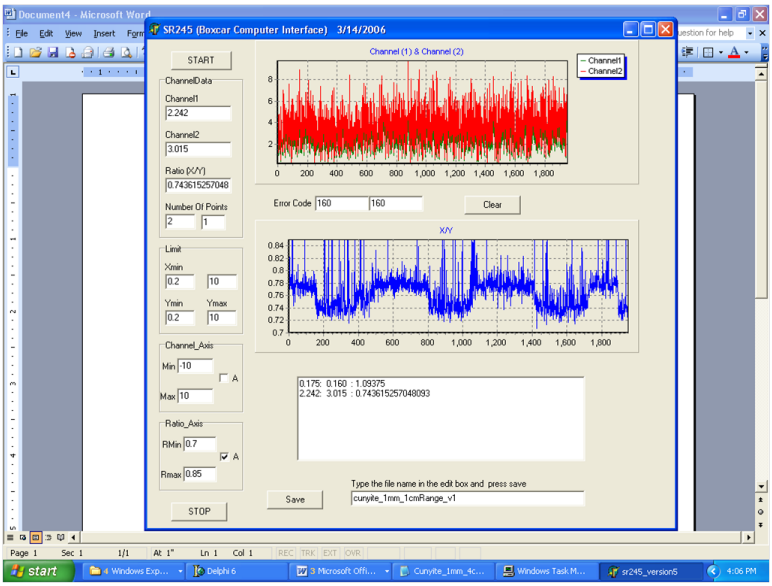

Figure 3.8: SR245-program

Busy 50Ω: The busy output provides a TTL synchronizing pulse when the unit is triggered.

Signal Output: The signal same as the signal input to the unit.

Last Sample: The Last Sample output provides a voltage proportional to the latest input signal averged over the sampling gate.

3.6.3 SRS 245 - Computer Interface and Acquisition Software

SRS 245 computer interface application has been written using Delphi. User interface screen is shown in the figure. 3.8. Code is described in Appendix(B) section.

3.6.4 Detailed Experimental Measurements

As shown in fig.3.6, the 500-fs, 0.5mJ per pulse, 10Hz amplified output pulses from PDA amplifier is splitted using the wedge prism. The wedge prism split the input beam into two with the initial deflection angle of 2^o. One beam has more than 90%

of input beam intensity and the other beam has the rest. High intensity beam is used as the pump beam and the low intensity beam is used as the probe beam. Half wave plate is placed along probe beam path to change the polarization of the probe from vertical to horizontal. By placing the horizontal polarizer at the input of detector, the vertically polarized strong pump beam is eliminated from reaching the detector input. Because 600nm absorption is strongly polarized along the short axis of the crystal, the polarization of the pump beam must be along the short axis while the polarization of the probe beam is along the medium axis since there still is significant absorption of 600nm excitation along the medium axis.

I have to mention one important fact. In place of the wedge prism, we can use the regular glass plate. But the problem with the glass plate is it has two reflections, one from the output surface and the other from the inner surface. Having two reflections in the probe beam can complicate the signal detection process.

The reference signal is taking out from the pump beam by using the thin glass plate and PDA55 - slow silicon detector is used to detect the signal. The probe signal is detected by using fast silicon detector - DET 210 (rise time - 1ns).

The detail steps to measure the average signal is as follows:

Step1: Using the large bandwidth sampling oscilloscope and fast pin photodiode, the delay line is set at (t=0) (pump and probe pulses arrive the sample at the same time. This position (t=0) is marked on the delay line. The resolution of sampling oscilloscope is 8ps and the rise time of detector is less than (200) picosecond while the FWHM of the input pulses is (500) femtosecond.

Step2: The trigger output from Q switch laser is used to trigger the box car. By using built-in delay line of the box car and using the oscilloscope, the signal and reference pulses are captured within the preset gate width. The gate width used in this experiment is 1 ns.

Step3: Using the half-wave plate, the polarization of the probe is change from vertical to horizontal polarization by placing the fast axis of wave plate at 45-degree from the vertical direction. By using the photodiode and oscilloscope, the position of horizontal polarizer is adjusted in order to reduce the pump signal reaching the detector.

Step4: Using SR-245 computer acquisition program and CUNYite crystal, the whole system is tested by delaying the arrival time of probe pulses with respect to the pump pulses.

Step5: The oscilloscope scope monitors four signals. The signal from DET210 detector (probe pulse passing through the sample), the signal from PDA55 detector (the reference signal), the gate signal to capture the main signal and the gate signal to capture the reference signal. By playing the sensitivity of the box car integrator and the gate width, the visibility of signal is boosted.

Step6: By using boxcar integrator and averager, the main and reference signals are integrated within the gate width and the average DC signal is calculated over the integration time (30 sec, 300 pulses).

Step7: Finally, the normalization is done by dividing the average main signal (DC) to the average reference signal (DC) to eliminate the optical signal fluctuations.

3.6.5 Result

The inset of Fig. 3.9. shows the resolution of the setup and the rise time is around half picosecond, which is agree with the pulse width of dye amplifier. Figure. 3.9 also shows the relative transparency of sample before and after the pump arrival. As shown in the figure, there is insignificant drop in transparency at 300 picosecond after pump arrival. Even though the mechanical delay line is moved to the time scale equal

to 800 picosecond, there is little drop in transparency. Because of this observation, the lifetime of Cr^{4+} must be more than 1ns. The various spectroscopic measurements of Cr:$LiScGeO_4$ gives us a hint that there is high probability that the decay time of Cr^{4+} ions in this crystal may be in the sub-ten-nanosecond range. In order to accurately measure the decay time, streak camera is selected as the instrument on this time scale.

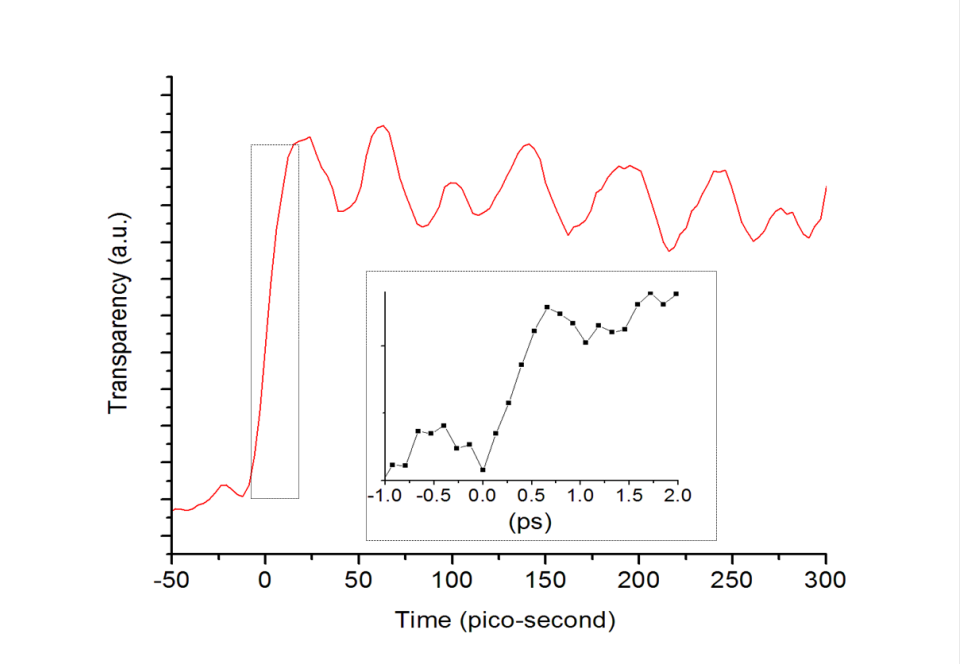

Figure 3.9: Sample transparency before and after pump arrival in the picosecond time scale. The inset shows the rise time of the setup.

3.7 Nano-second detection system

From the femtosecond pump-probe measurement for these crystals, we estimate that the lifetime will be in the range of sub-ten-nanosecond. For this time range, the streak camera with gated photo counting mode is the best for accurate measurement.

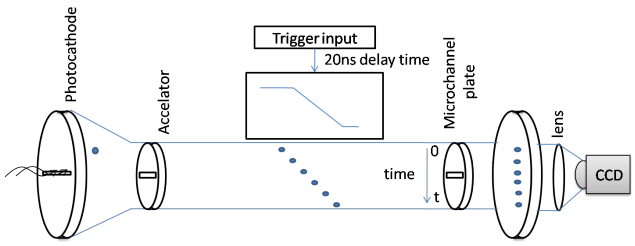

Figure 3.10: Cartoon showing the operating principle of streak camera

3.7.1 Streak Camera

The operating principle of streak camera is shown in fig. 3.10. In short, the streak camera is an oscilloscope with ultrafast time resolution (2 picosecond). The streak camera can be placed after the spectrograph to display the time-variation spectrum image. The phosphor screen is two-directional display; x-axis is used to show the wavelength variation while y-axis is used to show the ultrafast time variation. The time windows in this streak camera is only open for 10ns and the resolution of streak camera itself is 20 picosecond. The operation principle is described as follows. The photons entering the streak camera are transformed into the photoelectrons with the help of photocathode. These electrons are accelerated by using the accelerating electrodes. The only difficulty in using the streak camera is to compensate the intrinsic trigger delay of 20ns. After the streak camera receives trigger pulse from Q-switch laser, its electronic circuitry takes 20ns time to generate the sweep pulse. This trigger delay can be compensated by electronically and optically. Experience tells us that the trigger delay is best compensated by optically to follow the optical jitter. The electrons coming out from the sweeping magnetic field are multiplied by the micro channel plates. These electrons hit the phosphor screen of the streak camera and CCD camera capture the glowing image on the phosphor screen. Actually the streak camera is useful for 3-dimensional measurements; x-axis: wavelength, y-axis: time and z-axis: signal strength (the signal strength is defined as the number of photon

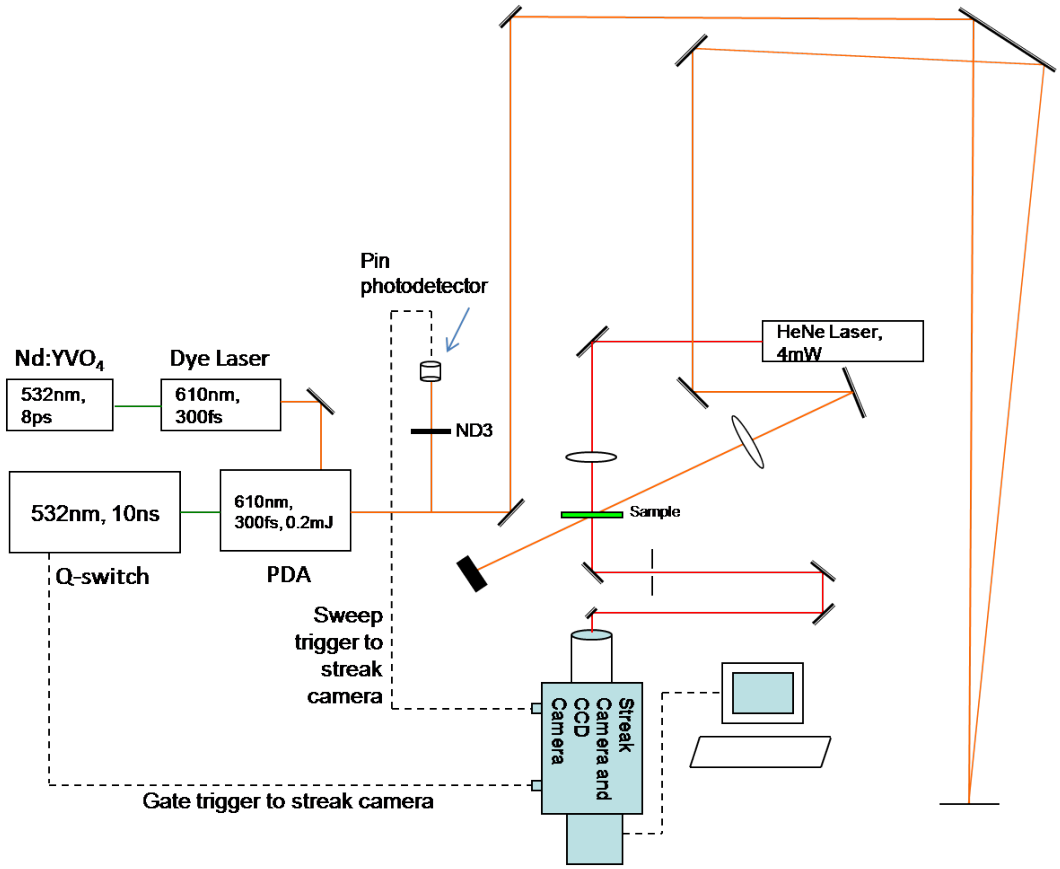

Figure 3.11: Decay mesurement using streak camera and CCD camera

counts at the particular instant in time and space).

3.7.2 Experimental Setup

Fig. 3.11 shows the complete setup of streak camera. The main difficulty in this setup is to compensate the trigger delay of 20ns. We built the electronic to trigger the streak camera 20ns before the arrival of the optical pulses to the streak camera to compensate 20ns streak camera intrinsic delay. Although the electronic works well with the streak camera, it introduces the jitter of about 3ns because it doesn't follow the optical jitter. Since our interested range is within 10ns, we cannot tolerate the jitter of 2ns in this measurement.

Thus, the streak camera is triggered with electrical signal from pin photodetector

to follow the optical jitter. As the streak camera is triggered with the optical pulses, we need to compensate 20ns delay of sweeping circuit. As shown in the figure. 3.11, the pump beam is delay through the optical path length of 25-feet around the optical table. The fine adjustment between trigger and the optical pump beam can be made by using the delay control box.

To eliminate the noises (residual image, reflection from the apparatus), the streak camera with the gated photon counting mode is used. In this mode, the gate is open during the time frame the signal arrive to the streak camera. As shown in the figure. 3.11, the gate circuit is triggered from the Q-switch on/off electrical pulses. In the current streak camera, as shown in fig. 3.12, the usable area in the phosphor screen is about 10ns. With the gated mode, the screen is only open for 7ns. As a result, the ghost image and the reflection is eliminated.

The streak camera image is captured with the CCD camera from the photometric Co. for the data storage.

3.7.3 Result

The objective of the measurement is the same as the femtosecond measurement, which is to measure the lifetime of the excited state ($^3T_2$) of Cr^{4+}ions in Cr:Cr^{3+}:$LiScGeO_4$. The ions in the ground state is depleted with 600nm (Dye Laser) high energy pump beam. The excited ions immediately decay to the metastable state right after excitation. We measured the repopulation time of the ground state with 633nm (HeNe) probe beam. The *repopulation time* is the lifetime of the excited state ($^3T_2$).

The measurement result is shown in the figure. 3.12. The bottom figure is a measurement of Cr^{4+}:Ca_2GeO_4 crystal and the top figure is the decay measurement of Cr^{3+},Cr^{4+}:$LiScGeO_4$.

The question now is what is the resolution of the streak camera. I would say the actual resolution of the streak camera is less than 50-picosecond. The resolution

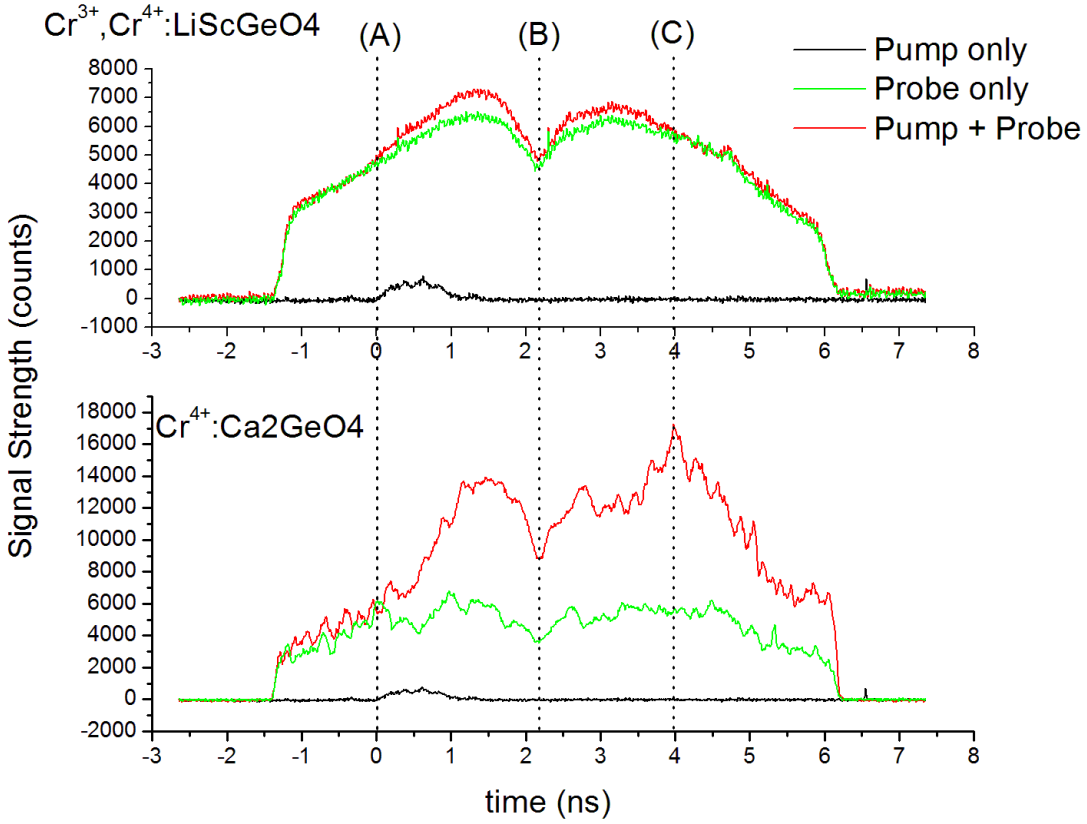

Figure 3.12: Decay time measurement of Cr:Ca_2GeO_4 and Cr:$LiScGeO_4$ single crystals by using streak camera and CCD camera

of the measured signal is (resolution of the streak camera + pulse width + timing jitter). The figure shows the scattered pump signal and the FWHM of the pulse is about 1-nanosecond. Since we know that the FWHM of the pump pulse is about 500-femtosecond, the jitter determines the resolution of the measurement and the jitter is about 800-ps (1-ns). Since our measurement range is about 5ns, we can tolerate 800-ps jitter in our measurement.

In the figure, I marked the three positions to make some explanations of the measurement.

A: "A" position shows the arrival of the pump pulse. It shows the starting point of the dynamical behavior of the examined system.

B: "B" position shows the damage area of the streak camera.

C: "C" position shows the transmission location where Ca_2GeO_4 crystal has highest transmission and where Cr^{3+}:$LiScGeO_4$has the lowest transmission.

Since the excited state lifetime of Cr^{4+}:Ca_2GeO_4 crystal is 15 μs in the room temperature, the transmission should be flat throughout the maximum measurement range of 7-ns. We can use this knowledge as the navigation guide to determine the decay rate of Cr:Cr^{3+}:$LiScGeO_4$single crystal. Some examples of using this knowledge is as follows.

- We determine that "B" position is damaged area because the signal should be flat at about 2ns from excitation.
- At 5.5ns, the signal intensity is reduced. This may be because of the degradation of the phosphor sensitivity because the signal intensity should be the same as the intensity as 2ns.

Let's go back to the figure. 3.12 and I've tried to access the decay time of $LiScGeO_4$ crystal. At the position "C", the transmission of $LiScGeO_4$ crystal

goes to zero while the transmission of Ca_2GeO_4 crystal has the maxium value. This clearly indicate that the excited state decay time of $LiScGeO_4$ crystal is less than 4-ns.

The figure. 3.13a shows the subtracted signal from pumped transmission and un-pumped transmission of Cr^{4+},Cr^{3+}:$LiScGeO_4$crystal in semilog scale. As you can see in the figure, excited state has the single-exponential decay time. As shown in the figure. 3.13a, I create the data points by using draw data tool from the origin software. The bottom figure. 3.13b shows the single exponential fitting of the above data drawed. The fitting clearly shows that *the excited state ($^3T_2$) lifetime of Cr^{4+}ions in Cr^{4+},Cr^{3+}:$LiScGeO_4$ single crystal is about $3\pm 1ns$*

3.8 Discussion of Result

The relaxation time of metastable state of Cr^{4+}ions in Cr:$LiScGeO_4$ single crystal is measured as $3\pm 1ns$. The delay rate of Cr^{4+}ions in $LiScGeO_4$ crystal is about 3 order of magnitude times faster than the decay rate of Cr^{4+}ions in Ca_2GeO_4 . In $LiScGeO_4$, we can expect similar radiative decay rate as Ca_2GeO_4 crystal because the oscillator strengths derived from absorption spectra from the two crystals are about the same. Thus the fast relaxation of metastable level of Cr^{4+}ions in $LiScGeO_4$ originates from nonradiative processes which are 3 order of magnitude faster compared to Ca_2GeO_4 . This result is surprising taking into account that local structure of Cr^{4+}center changes only slightly. This unknown behavior is probably coming from crossing point $(^3A'')^3A_2$and $(^3A'')^3T_2$ adiabatic potentials at some point in multidimensional space (vibrational modes). The origin of this phenomenon will be a subject of our future work.

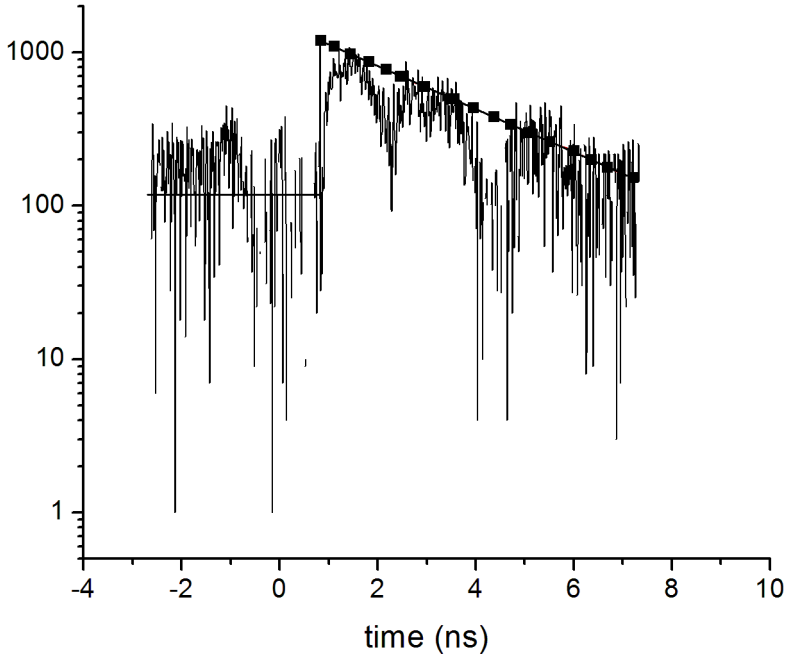

(a) Different signal between pumped and unpumped transmitted signal

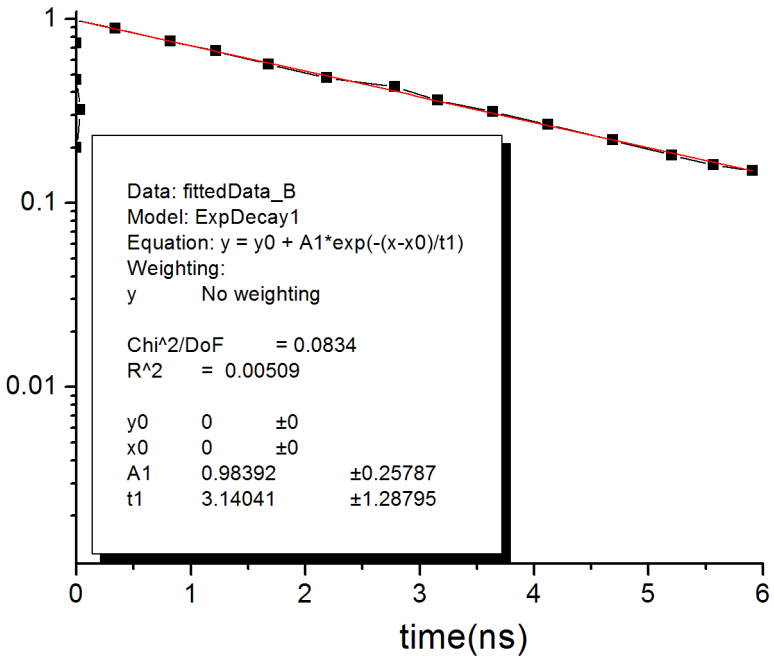

(b) Single-exponential fit

Figure 3.13: Single exponential decay time of ($^3T_2$) of Cr^{4+}ions in Cr:$LiScGeO_4$ single crystal.

Chapter 4

Cr^{4+}doped Ca_2GeO_4 single crystal

4.1 Spectroscopic properties of Cr^{4+}-doped Ca_2GeO_4

Ca_2GeO_4 is a member of olivine family. It is isomorphic with well-known forsterite crystal. Olivine crystal structure is very flexible crystal structure. As shown in the figure.4.1, it has octahedral sites for Cr^{3+}substitution and tetrahedral site for Cr^{4+}substitution. It is an orthorhombic structure with unequal lattice constants. The lattice constants of Ca_2GeO_4 crystal are a(long axis) = 11.4Å, b(medium axis) = 6.79Å and c(short axis) = 5.24Å. Figure.4.2, shows the energy level diagram and spin and parity allowed transitions of Cr^{4+}ions in Cr^{4+}:Ca_2GeO_4 single crystal. In the following sections, the review of spectroscopic properties of Cr:Ca_2GeO_4 are presented. These knowledge are utilized in analyzing the CUNYite glass ceramic materials.

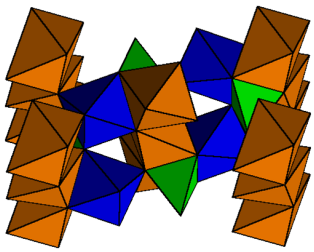

Figure 4.1: Olivine crystal structure.(green = tetrahedral site, orange & blue = octahedral sites)

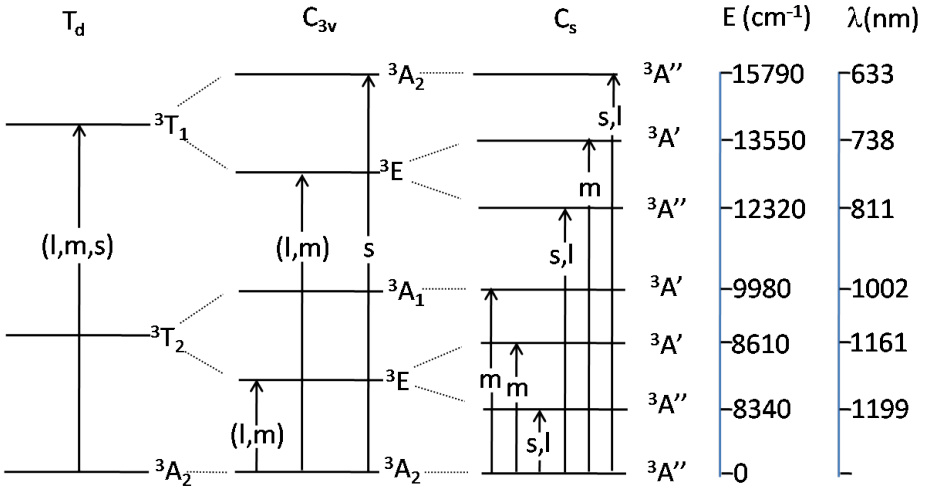

(a) Parity and Spin-allowed transitions of Cr^{4+}ions in Cr:Ca_2GeO_4 crystal(s=short axis, m=medium axis, l=long axis)

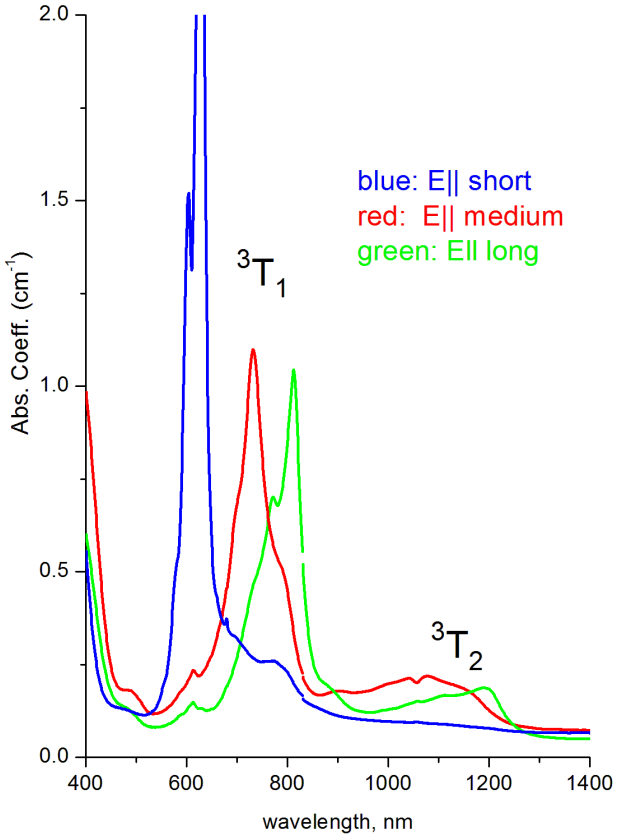

(b) Absorption spectrum of Cr^{4+}ions in tetrahedral surrounding in Cr^{4+}:Ca_2GeO_4 single crystal

Figure 4.2: Energy level diagram and Absorption spectrum of Cr^{4+}ions in Cr^{4+}:Ca_2GeO_4 single crystal

4.1.1 Visible absorption properties of Cr^{4+}:Ca_2GeO_4 crystal

The absorption spectrum of CUNYite(Cr^{4+}:Ca_2GeO_4) in the visible region at 20K is as shown in figure(4.3(a)). The unit cell of Ca_2GeO_4 has an orthorhombic structure. It has three unequal lattice axes. Throughout this thesis, I'll use the notation such as the long axis, medium axis and short axis to clear out ambiguity. The most useable notations in literature is Pmna and Pbmn space group notation. Table. 4.1 shows the correlation between these notations and the notation representing the actual lattice dimension such as long, medium and short axis.

unit cell (orthorhombic)	axis dimension	Pnma	Pbmn
l-long axis	11.397 $\dot{A}$	a	b
m-medium axis	6.787 $\dot{A}$	b	c
s-short axis	5.239 $\dot{A}$	c	a

Table 4.1: Correlation between Pnma, Pbmn space group and lms notation for Cr^{4+}-doped Ca_2GeO_4 single crystal

Absorption spectrum in figure(4.3(a)) clearly shows the zero phonon lines(0-0) and the phonon repetitions($\nu_s, 2\nu_s, 3\nu_s$). The spectrum is asymmetric and most of the absorption intensity falls within zero-phonon transition. This is because Stoke's shift between ground and excited state potential energy surface is small. In other words, the electron-phonon coupling is weak between ground state and ($^3T_1$) state. The illustration of asymmetric band formation and observation of phonon repetitions is as shown in figure(4.3(b)). The crystal is highly anisotropic and the absorption spectrum shows the strong dependency on polarization. As explained in the section(2.7) and shown in Sugano-Tanabe diagram (fig.2.11) of d^2 ions in tetrahedral coordination, the energy level of Cr^{4+}free ion ground term (^3F) splits into $^3A_2$, $^3T_2$, and $^3T_1$ in tetrahedral crystal field. According to the group theoretical calculation, the transition ($^3A_2 \rightarrow {}^3T_2$) is forbidden while the transition ($^3A_2 \rightarrow {}^3T_1$) is allowed. In the selection rule section, section(2.8.2.2.1), the detail calculations are made to determine the allowed and forbidden transitions. The parity allowed transitions for three molecular

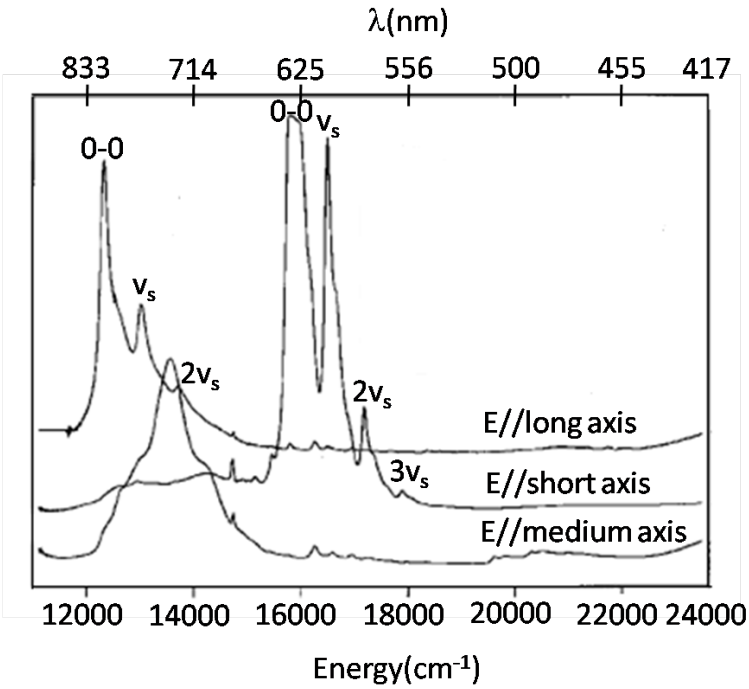

(a) Absorption spectrum of Cr:Ca_2GeO_4 crystal at 20K [10, 9]

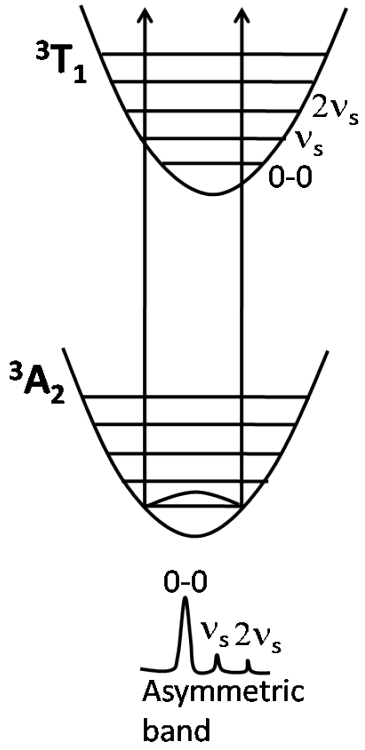

(b) Illustration of energy level diagram of phonon repetitions

Figure 4.3: Polarized absorption spectrum of Cr^{4+}:Ca_2GeO_4 crystal showing zero-phonon line and phonon repetitions.

symmetry (T_d ,C_{3v} and C_s) is shown in fig.(4.2(a)).

When Cr substitutes Ge in Ca_2GeO_4 crystal host, the tetrahedron is distorted due to trigonal elongation along the crystallographic a axis (short axis), leaving the mirror plane, which is composed of long and short axis, as the only symmetric element. That distortion lead to reduction of the symmetry of the tetrahedron from T_d to C_s symmetry. Under Cs symmetry, the degeneracy of the energy term of Cr^{4+}in T_d symmetry is completely lifted. Since the mathematical calculation of energy level of lower symmetry complex is so complex that sometime C_s symmetry is estimated by C_{3v} symmetry. The calculated energy values with C_{3v} site symmetry are within the acceptable range since they are not very far off from the experimental observed values. Very often they are sufficient to quantify the materials. For Cr^{4+}in C_{3v} site symmetry, see fig(4.2(a)) both $^3T_2$ and $^3T_1$ energy terms split into $^3A_1$and ^3E with ^3E is lower in energy than $^3A_1$. The degeneracy of ^3E is lifted when the symmetry is lower from C_{3v} to C_s . The complete splitting and allowed transitions are shown in the figure(4.2(a)) when the site symmetry is reduced from T_d through C_{3v} to C_s . With the help of this figure, the assignments are made for the specific transition.

According to the selection rule for the visible region, when the polarization of excitation is along the short and long axis, we expect to see transitions ($^3A''(^3A_2)$ $\rightarrow$ $^3A''(^3A_2)(^3T_1$)) and ($^3A''(^3A_2)$ $\rightarrow$ $^3A''(^3E$)($^3T_1$)). As shown in the absorption spectrum, fig.4.3(a), when the polarization of the excitation is along the long axis, the zero phonon line is located at around 12 000 cm^{-1}, which is assigned as the transition ($^3A''(^3A_2)$ $\rightarrow$ $^3A''(^3E$)($^3T_1$)) according to references [10, 9]. we also expects to see the transition ($^3A''(^3A_2)$ $\rightarrow$ $^3A''(^3A_2)(^3T_1$)). But the oscillator strength of this transition is so small that we barely see the zero phonon line of the transition. We also clearly see the phonon repetition of the transition ($^3A''(^3A_2)$ $\rightarrow$ $^3A''(^3E$)($^3T_1$)). The energy of the observable phonon is about 700 cm^{-1}. According the ref. [9], the phonon is assigned as the stretching vibration of CrO_4^{4-}tetrahedron which couple to

Excitation direction	Transition	$\lambda_{0\to0}$	Oscillator strength	Pbmn	Pmna
long	$^3A''(^3A_2) \to {}^3A''(^3E\ )[^3T_1\ (et_2)]$	811	9×10^{-4}	b	a
medium	$^3A''(^3A_2) \to {}^3A'(^3E\ )[^3T_1\ (et_2)]$	738	8×10^{-4}	c	b
short	$^3A''(^3A_2) \to {}^3A''(^3A_2)[^3T_1\ (et_2)]$	633	1×10^{-3}	a	c

Table 4.2: Absorption peaks of Cr^{4+}:Ca_2GeO_4 single crystal in visible region

the electronic transition ($^3A''(^3A_2) \to {}^3A''(^3E\ )(^3T_1\ )$). Since this phonon is related to the vibration CrO_4^{4-}tetrahedron, we will use this data when we identify the crystal phase of nanocrystallites in germanate glass ceramics.

When the polarization of the excitation is along the short axis, we should see the two transitions stated above according to the selection rule. But this time, the oscillator strength of the transition ($^3A''(^3A_2) \to {}^3A''(^3A_2)(^3T_1\ )$) is so strong that we could even see the saturation in the absorption spectrum, fig.4.2(b). We can also clearly see the phonon repetitions in this transition with the same phonon frequency of 700 cm^{-1}.

According to the selection rule, we expect to see the transition ($^3A''(^3A_2) \to {}^3A'(^3E\ )(^3T_1\ )$) when the polarization of excitation is along the crystallographic medium axis. We expect to see this transition around 13 000 cm^{-1}according to AOM calculation using observed absorption peaks [10, 9]. The absorption spectrum shows the high oscillator strength of this transition as expected.

We can summarize the above observation of absorption in visible region as follows. I'll use this data to do the assignments of absorption transition in germanate glass ceramics.

4.1.2 Near-infrared absorption spectrum of Cr^{4+}:Ca_2GeO_4 crystal

Compared to the oscillator strength of transitions in visibile region, the strengths of transition in near-infrared region is an order of mangnitude smaller. The reason for this is in Cr^{4+}in T_d symmetry, the transition $^3A_2 \rightarrow {}^3T_2$ is forbidden while the transition $^3A_2 \rightarrow {}^3T_1$ is allowed according to the selection rule . The detail calculation using the group theory to determine whether the transition is allowed or forbidden is shown in the theory section.2.8.2.2.1.

As shown in the near-infrared absorption spectrum, figure. 4.4, when the polarization of excitation is along the crystallographic medium axis, there are one zero phonon line at about 8600 cm^{-1}(ii) and another one at around 1000 cm^{-1}(iii).

According to the selection rule and AOM calculation, the first transition (8600 cm^{-1}) is assigned to $^3A''(^3A_2) \rightarrow {}^3A'(^3E\ )(^3T_2\ )$ and the latter one (10 000 cm^{-1}) is assigned to $^3A''(^3A_2) \rightarrow {}^3A'(^3A_1)(^3T_2\ )$. When the electric field is applied along the crystallographic long axis, the zero phonon appears around 8340 cm^{-1}(i). The same zero phonon line (i) with less oscillator strength appears when the field is applied along short axis. This observations agree very well with the selection rule and this transition is assigned as $^3A''(^3A_2) \rightarrow {}^3A''(^3E\ )(^3T_2\ )$. Compared the oscillator strength of the transitions in E$\|$long and E$\|$medium excitation, the strength in E$\|$short excitation is very low. This can be explained by the allowed and forbidden transitions in C_{3v} symmetry. In C_{3v} symmetry, the transition in near infrared region is forbidden when the excitation is along the short axis. The assignment of the near-infrared absorption spectrum shows the invaluable application of group theory in selection allowed and forbidden transition. The above observation is summarized in the following table and I'll use this data to make the assignment of near-infrared transition in germanate glass ceramics.

In Near-infrared absorption spectrum of Cr^{4+}-doped Ca_2GeO_4 at 20K, we can

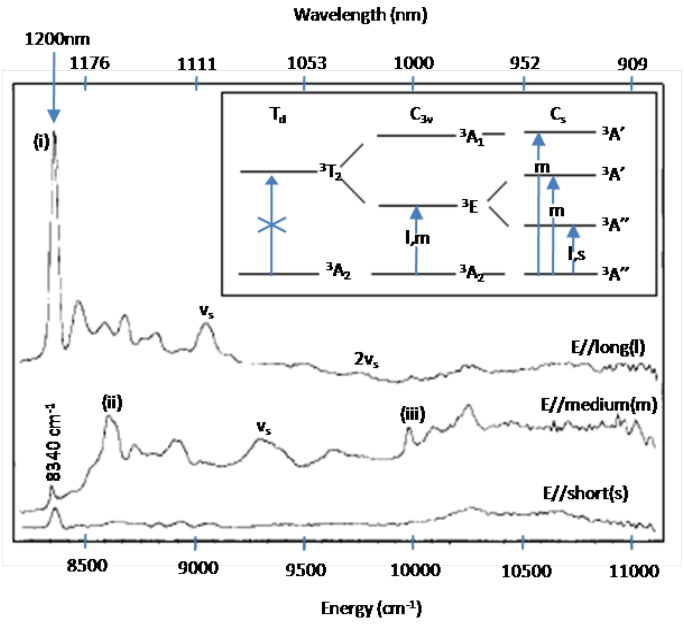

Figure 4.4: Near-infrared absorption spectrum [10] of CUNYite crystal at 28K. (i), (ii), (iii) are zero phonon transitions.ν_s is the vibrational sideband due to coupling with the a_1 streching vibration.

Excitation direction	Transition	$\lambda_{0\to0}$	Oscillator strength	Pbmn	Pmna
long	$^3A''(^3A_2) \to {}^3A''(^3E\ )[^3T_2\ (et_2)]$	1200	6×10^{-5}	b	a
medium	$^3A''(^3A_2) \to {}^3A'(^3E\ )[^3T_2\ (et_2)]$	1161	5×10^{-5}	c	b
	$^3A''(^3A_2) \to {}^3A'(^3A_1)[^3T_2\ (et_2)]$	1002	4×10^{-5}	c	b
short	oscillator strength is too small to mention			a	c

Table 4.3: Absorption peaks of Cr^{4+}:Ca_2GeO_4 single crystal in near-infrared region

also see the phonon repetition coupled to transitions ${}^3A''({}^3A_2) \rightarrow {}^3A''({}^3E\ )({}^3T_2\ )$ and ${}^3A''({}^3A_2) \rightarrow {}^3A'({}^3E\ )({}^3T_2\ )$. The frequency of the vibration for this phone is about 700 cm^{-1}. This coupled phonon is also observable in the transitions of visible region and is assigned as the totally symmetric stretching mode of CrO_4^{4-}tetrahedron.

4.1.3 Emission properties of Cr^{4+}doped Ca_2GeO_4

The unpolarized emission spectrum of CUNYite(Cr^{4+}:Ca_2GeO_4) at 77K and room temperature is shown in fig.(4.5).

The emission is strongly polarized along the long axis of the crystal. The emission spectrum at 15K is very sharp and it also shows the phonon repetition with the frequency of 700 cm^{-1}. The zero phonon line of emission is located at 8340 cm^{-1}, the same energy level position observed in the near-infrared absorption spectrum at 77K. The same zero phonon line and same vibrational frequency clearly indicate that the same active center involved in the absorption and luminescence transition.

The very sharp emission spectrum makes a stir in assignment of the first excited state of Cr^{4+}-doped Ca_2GeO_4 and Mg_2SiO_4 crystals. As shown in the figure. 4.9, the crystal field strength of Ca_2GeO_4 and Mg_2SiO_4 is near the cross point of ${}^3T_2$ and ${}^1E$ excited states. Transition (${}^3A_2 \rightarrow {}^3T_2\ $) is spin-allowed and inter-configurational transition (${}^3A_2(e^2) \rightarrow {}^3T_2\ (et_2)$). Because of the inter-configurational transition, the excited state parabola is shifted related to the ground state parabola, which result in the broader absorption and emission spectrum because of coupling of the vibration and electronic transition. On the other hand, the transition (${}^3A_2 \rightarrow {}^1E\ $) is spin-forbidden and intra-configurational transition (${}^3A_2(e^2) \rightarrow {}^1E\ (e^2)$). Because of intra-configurational transition, the excited state and the ground state parabola aligns, resulting in the sharp absorption and luminescence spectra.

According to the ligand-field analysis of Cr^{4+}-doped Ca_2GeO_4 and Mg_2SiO_4 , their Dq/B value is below the crossing point value. Thus the first excited state

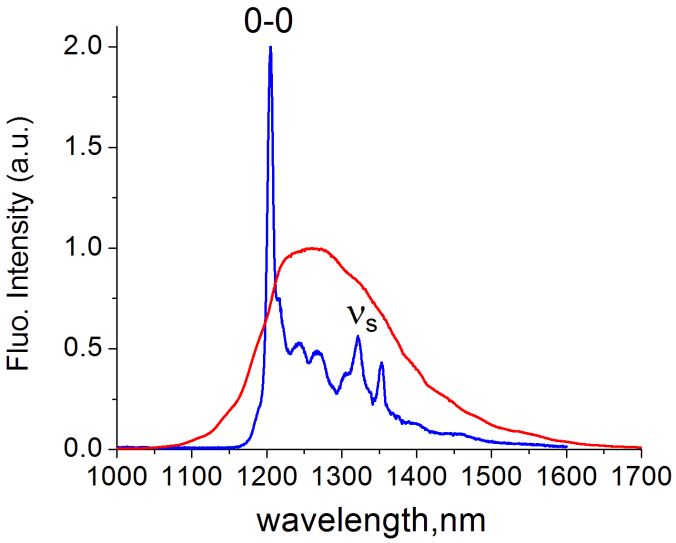

(a) Fluorescence signal strength Vs. Wavelength, nm

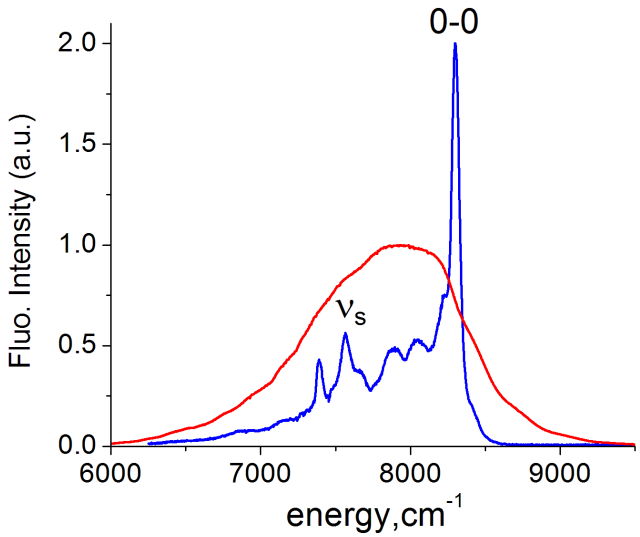

(b) Fluorescence signal strength Vs. Energy, cm^{-1}

Figure 4.5: Emission spectrum of Cr:Ca_2GeO_4 crystal at 77K and 300K

of these materials is assigned as $^3T_2$. Unlike other materials such as Cr^{4+}-doped Zn_2SiO_4 , $Ca_2Al_2SiO_7$, or $LiNbGeO_5$ which consist of broad, structureless bands at all temperatures, the very sharp zero phonon line of Cr^{4+}-doped Ca_2GeO_4 and Mg_2SiO_4 makes wonder whether the first excited state may be intra-configurational ^1E state. But the assignment of the first excited state as $^3T_2$ is confirmed by the piezospectroscopic measurements [34, 35, 36]. In piezospectroscopic measurement, the pressure is applied along one crystallographic axis to tailor the crystal field strength acted on Cr^{4+}ion. By varying the crystal field strength, we expect to see large position change of luminescence peak if the first excited state is $^3T_2$ and negligible change if the first excited state is ^1E . Another way to use the piezospectroscopy is to push the crystal field strength beyond the cross point to see the change of emission band from broad (weak field side) to sharp (strong field side). Because we can change the emission peak with pressure by changing the crystal field strength, Ruby crystals are used to calibrate in DAC (Diamond Anvil Cell) system.

As shown in the fig. 4.5, the luminescence band at room temperature is broadband as expected. The dip in emission spectrum reflects the reabsorption of the emission energy. This reabsorption pushes the lasing peak of the Cr^{4+}:Ca_2GeO_4 laser crystal around 1400 nm.

4.1.4 Decay time of metastable state of Cr^{4+}:Ca_2GeO_4 crystal

Figure. 4.6 shows the temperature dependent decay time of first excited state of Cr^{4+}ions in tetrahedral surrounding of Ca_2GeO_4 crystal host. The figure also compare the temperature dependent decay times between Cr^{4+}:Ca_2GeO_4 and Cr^{4+}:Mg_2SiO_4 laser crystals. For Cr^{4+}:Mg_2SiO_4 laser crystal, it is really interesting to see how fast the lifetime is dropped from 10K to room temperature. At 10K, the lifetime is about 30μs while the decay time is dropped to 3μs at room temperature. This give us the quantum efficiency ($\eta = \tau$ (300K)/τ(10K)) of about 10%. Compared to

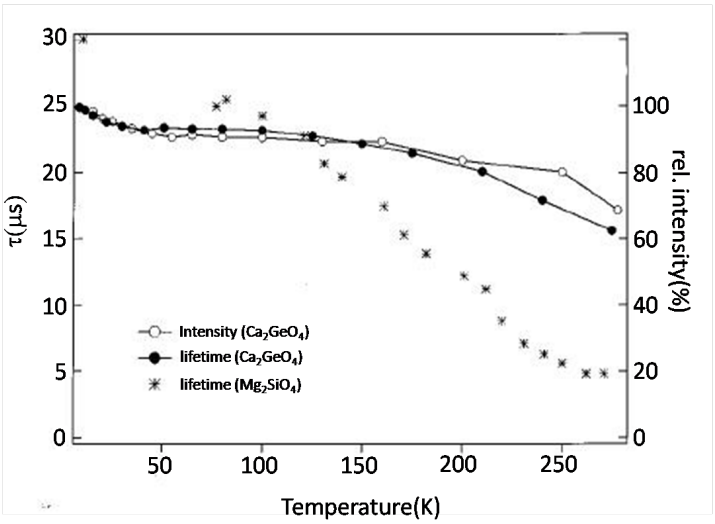

Figure 4.6: Temperature dependent decay time of first excited state of Cr^{4+}-doped Ca_2GeO_4 and Mg_2SiO_4 single crystals[9]

Cr^{4+}:Mg_2SiO_4 laser crystal, the quantum efficiency of Cr^{4+}:Ca_2GeO_4 is about 60% ($\eta = \tau$ (300K)/τ(10K) = 16μs /25μs). Such a huge different in quantum efficiency create a puzzle to the researchers because the two materials are isomorphic and their absorption and emission spectra are very similar.

One major different is in Cr^{4+}:Ca_2GeO_4 , only Cr^{4+}valence state can exist because the large different in atomic radii of Ca^{2+} ion (0.1nm) and Cr^{3+}ion (0.0615nm) makes the substitution difficult [14]. The advantage of having one valence state in Cr^{4+}:Ca_2GeO_4 laser crystal is it is possible to make the microchip lasers because of high Cr^{4+}ion concentration. In contrast to Cr^{4+}:Ca_2GeO_4 , $Cr^{3+}$and Cr^{4+}ions coexist in Cr^{4+}:Mg_2SiO_4 laser crystal. Since we're only interested in near-infrared emission, having Cr^{3+}ion, which emits around 900nm, can reduce the pumping efficiency and Cr^{4+}ion concentration. But having Cr^{3+}ions doesn't increase the non-radiative relaxation because the energy level of the first excited state of Cr^{3+}ion is larger than the emission energy of Cr^{4+}ion. Thus the energy transfer from excited Cr^{4+}ion to Cr^{3+}ion is very unlikely.

Cr^{4+}:Ca_2GeO_4 also defy the energy gap law, which is valid for weakly-coupled

systems such as Cr^{4+}:Ca_2GeO_4 crystal. The energy gap law states that the quenching temperature scale with (1-ϵ^p), where ϵ is the empirical parameter with a value of 0 and 1 and p is the number of phonon bridging the energy gap between the ground state and the first excited state. That means that the quenching temperature is lower for the lower number of p value, which in term means that the smaller the energy gap, the higher the nonradiative relaxation will be. When we compare the energy gap between the the ground state and the first excited state between the two materials (Ca_2GeO_4 and Mg_2SiO_4), the energy gap (8340 cm^{-1}) of Ca_2GeO_4 is smaller than that (9150 cm^{-1}) of Mg_2SiO_4 crystal. According to energy gap rule, the non-radiative relaxation rate of Ca_2GeO_4 should be higher than that of Mg_2SiO_4 . But the experiment shows the reverse result.

I would like to define the quenching temperature. The quenching temperture means the temperature at which the measured lifetime of the metastable state is reduced to 20% of the radiative lifetime, which is measured at 10K (or) liquid nitrogen temperature. From fig. 4.6, the quenching temperature of forsterite is T_q(6 μs) = 240K. Since we cannot measure the quenching temperture of Ca_2GeO_4 from fig. 4.6, we make the decay time measurement of Ca_2GeO_4 between 300K and 500K. The measured result is shown in figure(4.7). From fig. 4.7, the quenching temperature of Ca_2GeO_4 is T_q(5 μs) = 350K. The different in temperture between the two materials is about 100K. Accordingly, Luminescence of Ca_2GeO_4 is less quenched than forsterite crystal.

It is widely believe that the resonance between the local modes (vibration modes of CrO_4^{4-}tetrahedron) and the lattice modes enhance the non-radiative relaxation[22, 21]. Ca_2GeO_4 defies also this conventional belief because even though it has the local mode resonance with the lattice mode, it has higher quantum efficiency than Cr^{4+}:Mg_2SiO_4 , which doesn't have the resonant local mode. Reference [26] claims that the reason for this deviation from the conventional believe is that Ca_2GeO_4 have

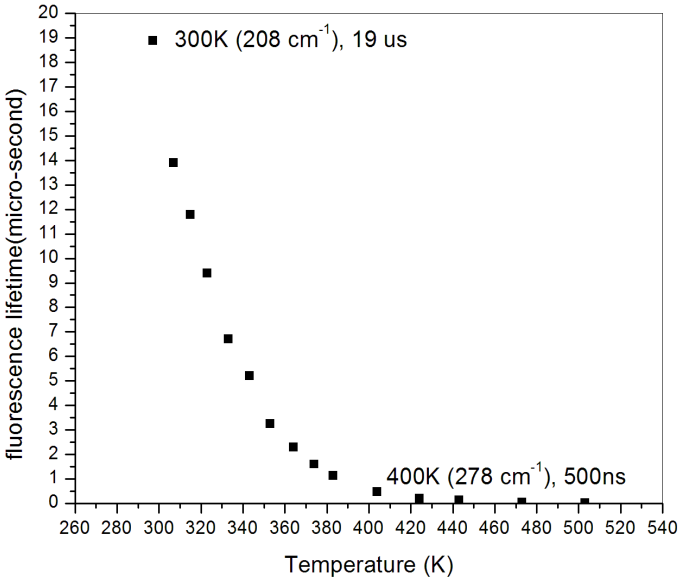

Figure 4.7: Lifetime of CUNYite at 300K and above

the fewer phonon modes than Mg_2SiO_4 , which in turn compensate the resonance effect.

To determine the non-radiative parameters, figure(4.7) is fitted with Struck-Fonger model. The fitting is shown in figure. 4.8. The theory of Struck and Fonger model is fully described in section.A.7. Fitting parameters are non-radiative relaxation rate constant R_{nr}, the effective phonon energy $\hbar\omega$, Huang-Rhys parameter $\mathcal{S}(\hbar\omega)$ and the total number of phonons bridging the energy gap p. The fitting values are shown in the following table.

E_{0-0}	R_{nr}	$\hbar\omega$	$\mathcal{S}(\hbar\omega)$	p
8340 cm^{-1}	1×10^{-14}	347 cm^{-1}	3.74	24

Nevertheless, having higher quantum efficiency and only one valence state in the crystal make Cr^{4+}-doped Ca_2GeO_4 the material of choice in synthesizing the glass ceramic material.

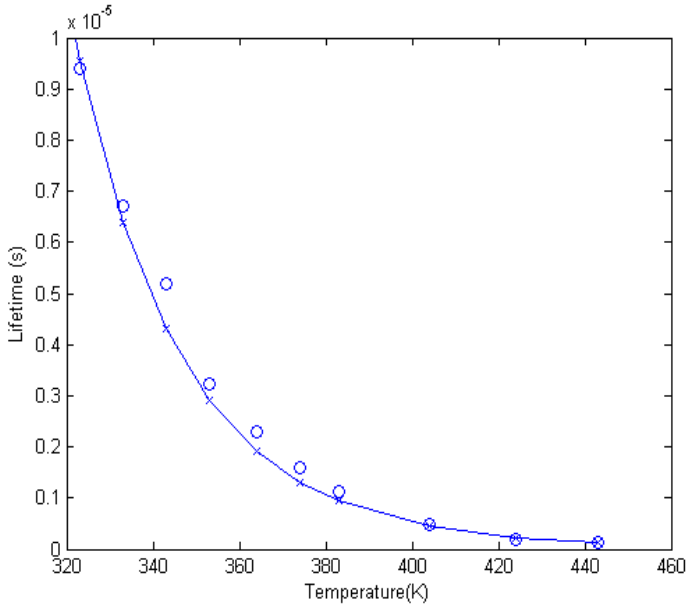

Figure 4.8: Calculated and experimental measured lifetime of Cr^{4+}-doped Ca_2GeO_4 to determine R_{nr}, $\mathcal{S}$ and $\hbar\omega$ values

4.1.5 Ligand field analysis of Cr^{4+}-doped Ca_2GeO_4

In Reference [10], Ligand field parameters ($10Dq$, B, $e_\sigma$and e_π) of Cr^{4+}:Ca_2GeO_4 are calculated by angular overlap model(AOM).The theory of angular overlap mode is presented in theory section.2.2. The ligand field parameters of Cr^{4+}ions in forsterite crystal are also described in the followings for comparison.

Ligand field parameters:

C/B ratio is fixed to 4.2 and $e_\pi/e_\sigma = \frac{1}{6}$

$\mathbf{Ca_2GeO_4}$:	e_σ	8629 cm^{-1}
	e_π	1438 cm^{-1}
	$10Dq = \frac{4}{9}(3e_\sigma - 4e_\pi)$	8950 cm^{-1}
	Dq	895 cm^{-1}
	B	540 cm^{-1}
	Dq/B	1.657
$\mathbf{Mg_2SiO_4}$:	e_σ	9735 cm^{-1}
	e_π	1623 cm^{-1}
	$10Dq = \frac{4}{9}(3e_\sigma - 4e_\pi)$	10100 cm^{-1}
	Dq	1010 cm^{-1}
	B	560 cm^{-1}
	Dq/B	1.8

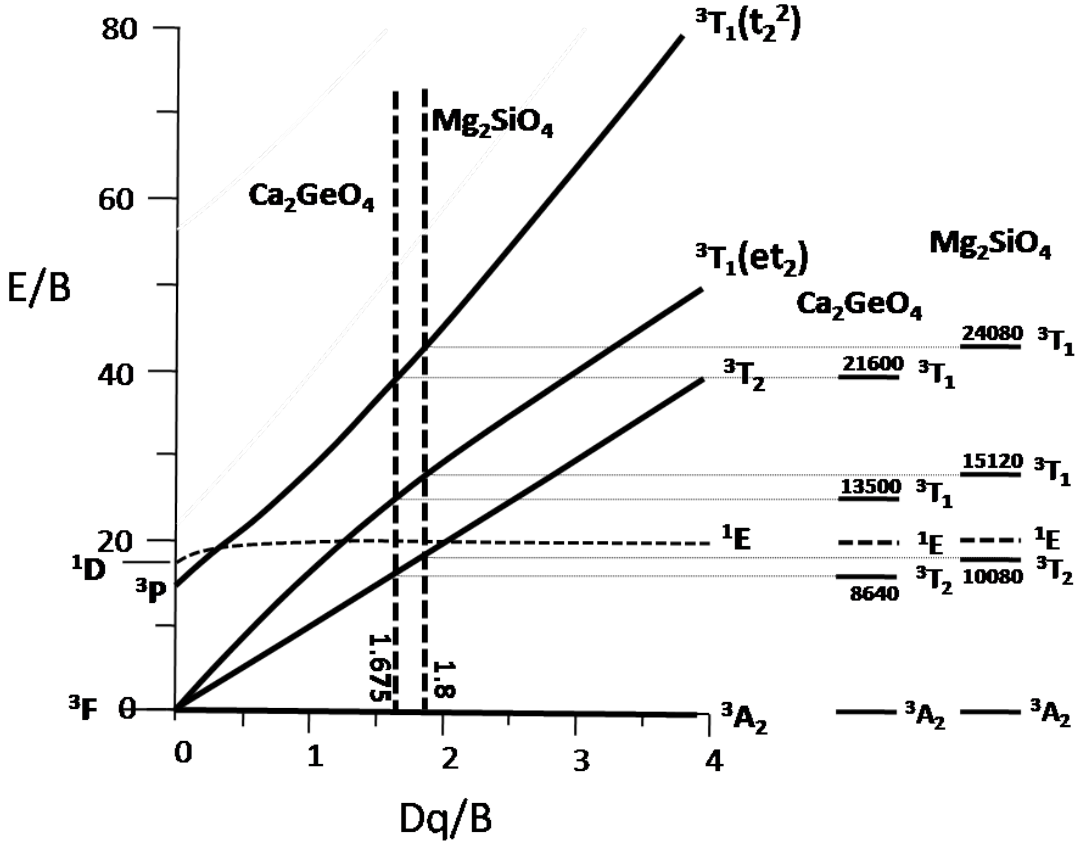

Figure 4.9: Sugano-Tanabe-Diagram showing only the spin-allowed transition for $3d^2$ ions in T_d symmetry

4.2 Cr^{3+}absorption and emission bands in Cr^{4+}:Mg_2SiO_4 single crystal

When we examine the absorption and emission spectrum of glass ceramics, we need to have the sound knowledge of the absorption and emission regions of $Cr^{3+}$and Cr^{4+}ions in olivine crystal strcture. Our objective in synthesizing the glass ceramics is to grow Cr^{4+}:Ca_2GeO_4 nanocrystals inside the glass matrix. As explain in the spectroscopic properties of Cr^{4+}:Ca_2GeO_4 , only Cr^{4+}valence state stabilize in the CUNYite single crystal. But in the germanate glass ceramics, it is quite possible that other valence state can stablize inside the glass matrix. In this section, the absorption and emission properties of Cr^{3+}in olivine crystal structure is described by using the spectroscopic properties of Cr:Mg_2SiO_4 single crystal.

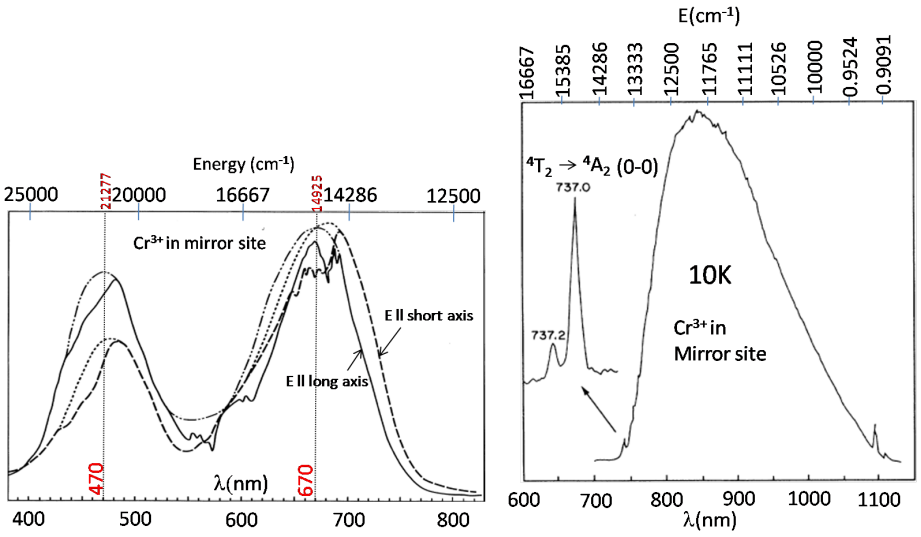

(a) Absorption Spectrum (b) Emission Spectrum

Figure 4.10: Site-selective absorption and emission spectrum of Cr^{3+}ions in mirror-site [13].

In the olivine crystal structure, Cr^{3+}stablize in two sites. One has the mirror symmetry and the other has the inversion symmetry. In Ref. [13], the authors metic-

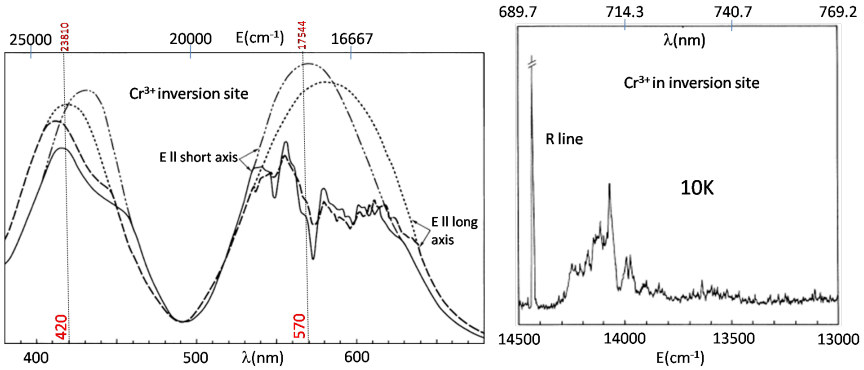

(a) Absorption Spectrum (b) Emission Spectrum

Figure 4.11: Site-selective absorption and emission spectrum of Cr^{3+}ions in inversion-site [13].

ulously examine the absorption and emission properties of Cr^{3+}in $Cr:Mg_2SiO_4$ single crystal. Figure. 4.10a shows the absorption peaks of Cr^{3+}in mirror site. As shown in the figure, one peak is located at 470nm and another one at 670nm. I'll use these peaks as the reference to the absorption peaks of Cr^{3+}in morror site when I examine the absorption spectrum of germanate glass ceramics.

Compared to Cr^{3+}in mirror site, the absorption peak of Cr^{4+}in inversion site is blue shifted about 50nm. As shown in the figure. 4.11a, the absorption peaks is located at 420nm and at 570nm. From these two figures, we can conclude that the absorption peaks of Cr^{3+}in olivine crystal structure is more or less around 450nm and 620nm.

Figure. 4.10b and 4.11b shows the emission spectrum of Cr^{3+}in mirror site and in inversion site respectively. Compared to the crystal field strength in mirror site, the crystal field strength in inversion site is stronger. This difference in crystal field strength in two sites is clearly evident because the shape of emission spectrum of Cr^{3+}in inversion site is very sharp while that of the emission spectum of Cr^{3+}in mirror site is broad and the emission peak is shifted to near-infrared region. Since we're interested in near-infrared region, Cr^{3+}in mirror site is more important than

Cr^{3+}in inversion site.

Chapter 5

Cr doped Glass Ceramics

Glass ceramics is a polycrystalline material. It is a two-phase system; nano-crystals phase and residual glass phase. The first step in manufacturing glass ceramics is making the glass by fast cooling the melt. After the glass is shaped into the desired form, the controlled crystallization is done with the proper heat treatment. During the heat treatment, the nanocrystals are precipitated in the glass matrix. The quality of glass ceramics is strongly dependent on the formation of crystal nuclei during the nucleation process [15]. With nuclei formation, the number of crystals precipitated, the crystal growth rate and thus the final crystallite size are able to control with the proper heat treatment. The objective of manufacturing glass ceramics is to create the material with desired properties. These desired properties are usually coming from the nanocrystals precipitated in the glass matrix. In addition to the desired properties of nanocrystals, we also want to retain the good mechanical properties of glass and its transparency. Another important fact is as the glass-ceramics contain the arbitrary oriented crystals inside the residual glass matrix, their properties are independent of the direction in which they are measured. This is an important fact for this thesis project because in this project, we've tried to grow the laser nanocrystals inside the glass matrix. Since the single proven laser crystals such as Cr^{4+}:Ca_2GeO_4 , Cr^{4+}:Mg_2SiO_4 are dichroic crystals, their optical properties depend on the direction in which they are measured. When the laser nanocrystals are grown in the glass,

directional dependency is weaker and its optical properties are average of optical properties of each direction of the crystal.

In this thesis project, we synthesized the glass ceramics with embedded Cr doped laser nanocrystals in order to use as fiber lasers and fiber amplifiers in optical communications. Specifically, we tried to grow Cr^{4+}:Ca_2GeO_4 proven laser nanocrystals inside the glass matrix. Even though the research on the rear-earth ions doped glass ceramics is mature and the useful information is widely available in literature [37, 16], the research on Cr^{4+}doped glass ceramics is relatively new [38, 39, 40, 41]. Since Cr is very sensitive to local environment, in order to realize the commercial applications of Cr doped glass ceramics as fiber gain medium just like the rear-earth doped glasses, we need to press more research on Cr doped glass and glass ceramics in order to extend the boundary of understanding of the nature of these materials. This is the primary reason for this thesis project.

5.1 Synthesizing process of glass ceramics

The main objective in synthesizing Cr doped glass ceramics is to grow the nano-crystal which has the smiliar phase and optical properties of Ca_2GeO_4 single crystal inside the glass matrix. With this objective in mind, the composition must include CaO and GeO_2 with the ratio of Ca to Ge contents has to be 2 or greater according to Ca_2GeO_4 formula. With CaO and GeO_2, even though it is possible to form the germanate glass with quick quenching, the literatures point out that the upper limit of calcium content must be less than 30% in order to form the germanate glass. The condition for forming the germanate glass and the condition for growing Ca_2GeO_4 crystal phase is contradict to each other. Because of this fact, the boron oxide is included as the primary glass former. Lithium oxide is used as the network modifier oxide to reduce the dangling oxygen bond. As a network modifier oxide, Li_2O promotes the volume crystallization, which is the essential requirement in synthesizing the glass ceramics. By including a few moles of Al_2O_3 in the composition gives transparent sample. Al_2O_3 also helps to form the tetrahedral network in the glass matrix. Tetrahedral sites are essential for Cr^{4+}substitution. Cr_2O_3 is also added to the composition to form Cr^{4+}optical centers.

As stated in Table.5.1, the ratio of mole contents of CaO and GeO_2 is 2, which is fixed throughout searching the right composition to synthesize the germanate glass ceramics. The right composition must give the following properties.

1. having glass forming ability
2. having volume crystallization after devitrification
3. having transparency after devitrification
4. having only Cr^{4+}emission

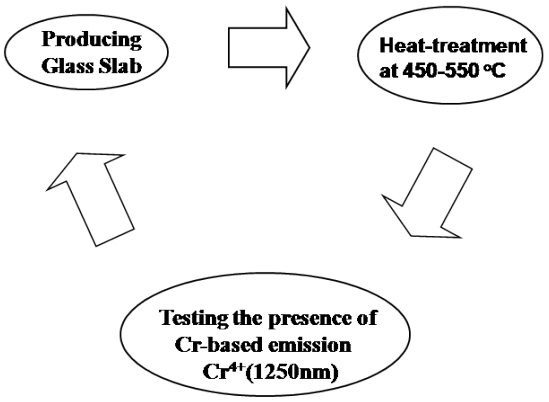

Figure 5.1: Searching the right glass composition which can give Cr^{4+}emission in near-infrared region and have the glass forming ability.

Exp.#	CaO Mol.	GeO_2 Mol.	Li_2O Mol.	B_2O_3 Mol.	Al_2O_3 Mol.	As-quenched	Heat treated	Fluorescence			
								Parent Cr^{3+}	Glass Cr^{4+}	Glass-ceramics Cr^{3+}	Glass-ceramics Cr^{4+}
1	2.00	1.00	0.50	0.50	-	G	S/N	Yes	No	Yes	Yes
2	2.00	1.00	1.00	0.50	-	G/P	V/O	No	No	No	Yes
3	2.00	1.00	1.00	0.78	-	G	V/O	Yes	No	No	No
4	2.00	1.00	0.70	0.50	-	G	V/O	No	No	No	Yes
5	2.00	1.00	0.70	0.34	-	P	-	-	-	-	-
6	2.00	1.00	1.00	0.50	0.10	G	V/O	No	No	No	Yes
7	2.00	1.00	1.00	0.50	0.20	G	V/T	No	No	No	Yes
8	2.00	1.00	0.85	0.50	0.20	G	V/T	No	No	No	Yes
9	2.00	1.00	0.92	0.50	0.20	G	V/T	No	No	No	Yes

Table 5.1: Glass compositions in CaO-GeO_2-Li_2O_3-B_2O_3(Al_2O_3) system

Figure. 5.1 shows the searching procedure to find the right composition in synthesizing the glass ceramics with the desired optical properties. Starting materials $CaCO_3$-GeO_2-B_2O_3-Li_2CO_3-Al_2O_3 are mixed in the appropriate quantities and melted at 1400^{o}C in the platinum crucible. The melt is then quenched in the copper mold and is annealed at 350-400^{o}C to release the thermal stress. The "as quenched" glass slab is then heat-treated at 450-550 ^{o}C to grow the nanocrystallites inside the glass matrix. The devitrificated glass ceramics is then tested for near-infrared emission of Cr^{4+}ions. If the composition doesn't have the desired properties as mention above, the mole contents of Li_2O, B_2O_3 and Al_2O_3 have been changed and the searching circle restarts according to figure. 5.1.

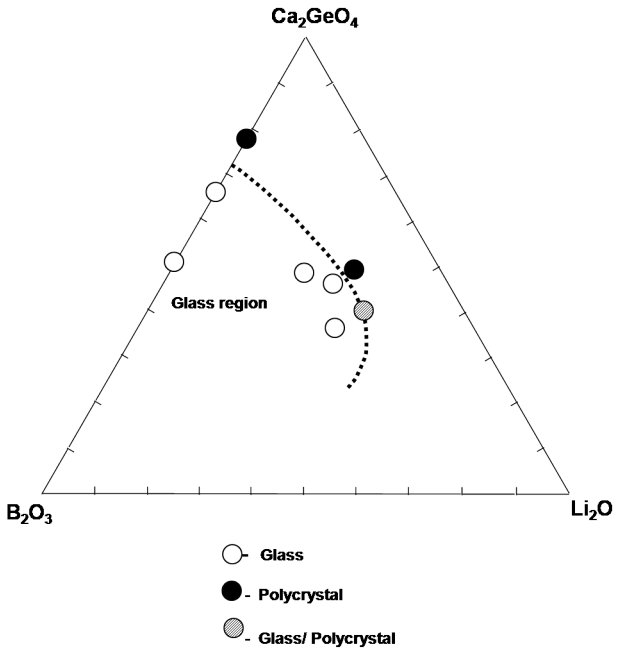

Figure 5.2: Phase diagram of Cr-doped CaO-GeO_2-Li_2O-B_2O_3-Al_2O_3 glass system

According to the table.5.1, some oberservations can be made.

1. Small Li_2O (composition #1) contents give the surface crystallization. Li_2O content must be greater than 0.50 mol to promote the volume crystallization.

2. If the composition has B_2O_3 content of less than 0.50 mol (composition #5), the glass forming ability becomes very poor. On the other hand, If B_2O_3 content of more than 0.78 mol eliminates Cr^{4+}emission (composition #3).

3. Having Al_2O_3 content of 0.20 mol in the composition promotes sample transparency (composition #7,8,9).

The phase-diagram (fig. 5.2) for pseudo-ternary system (Ca_2GeO_4-B_2O_3-Li_2O) shows experimentally tested glass forming region. We used the composition #7 for further experiments such DTA, X-ray diffraction, and spectroscopic measurements.

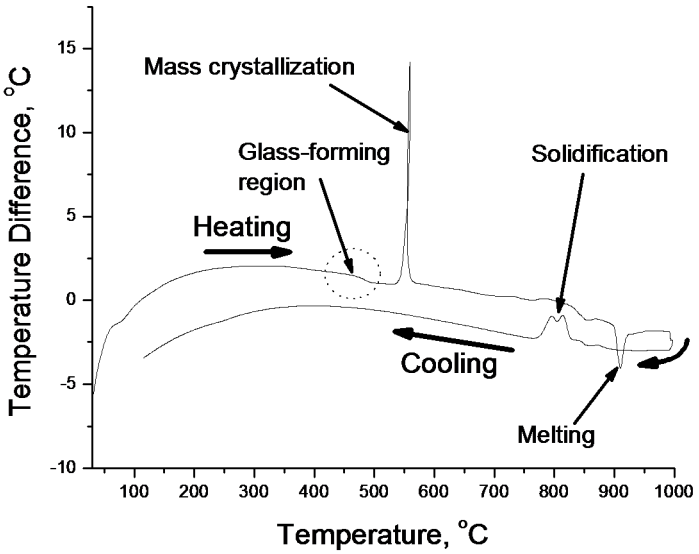

Figure 5.3: Differential Thermal Analysis of Cr^{4+}-doped CaO-GeO_2 glass ceramic

5.1.1 Differential Thermal Analysis of glass composition

Figure. 5.3 shows the differential thermal analysis of composition #7 (2CaO-1GeO_2-Li_2O-0.5B_2O_3-0.2Al_2O_3). Heating range is from 30^{o}C to 1000^{o}C with the heating step of 10 ^{o}C /min. DTA curve is typical for the phase-separated glass. As shown in the figure, the slope change occurs between 450 and 500 ^{o}C indicating the glass formation region. This is the region where we used to grow nucleation and crystallization in glass ceramics. The exothermic maximum at 560 ^{o}C corresponds to crystal phase separation temperature. Melting of crystal phase occur at 900 ^{o}C . When the melt is cooled down without quenching, the melt turns to the crystal at 800 ^{o}C .

According to DTA curve, we have to use the temperature below 560 ^{o}C for devitrification process without inducing mass crystallization.

5.1.2 Glass ceramic model and synthesized samples

Figure. 5.4 shows the "as quenched" glass model and glass ceramic model. As shown in the figure, in "as quenched" glass, several Cr valence states can stable in the glass

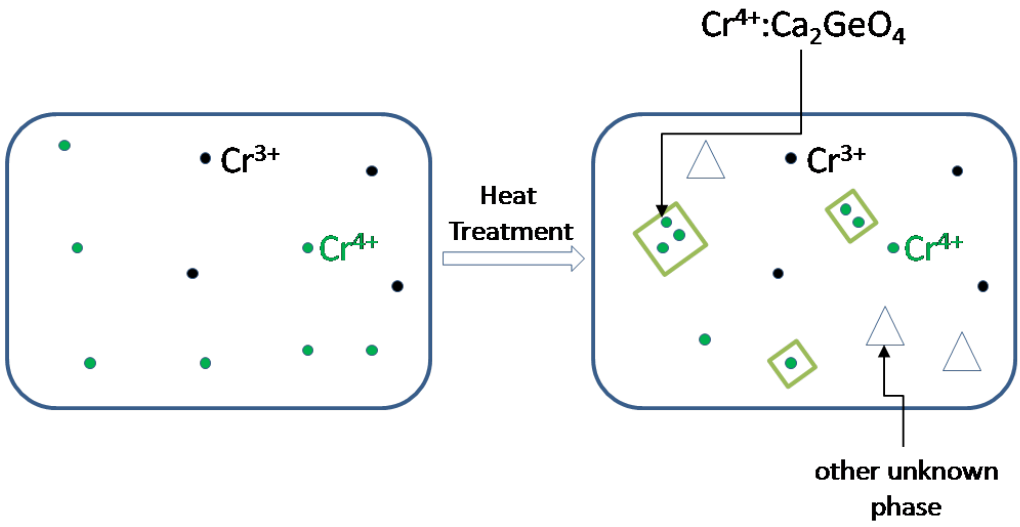

Figure 5.4: Model of Cr -doped "as-quenched" glass and of glass-ceramics

matrix. After heat treatment, the separation of Cr^{4+}:Ca_2GeO_4 like crystal phase and unknown crystal phase may occur. As shown in devitrificated glass model, it is possible that some Cr ions do not participate in crystallization and they can stable in glass matrix. Since stablization of $Cr^{3+}$and Cr^{4+}ions in glass and crystalline phase requires the octahedral and tetrahedral network respectively, we believed that the glass provides the required networks for these ions stablization. Later, I'll verify having these networks in glass with absorption spectroscopy.

Figure.5.5 shows the synthesized as-quenched glass and glass ceramics samples. As shown in the figure, the samples are highly transparent because the nanocrystals grown inside the glass matrix is so small(100nm) that the scattering loss is minimal.

5.1.3 X-ray Diffraction Patterns of Glass Ceramics

Figure. 5.6 shows the X-ray diffraction patterns of Cr-doped germanate glass ceramics at different heat treatment procedure.

- Figure. 5.6(a) shows the reflection pattern of devitrificated glass treated at 460 ^{o}C for one hour. At this heating temperature, the crystallization process is very

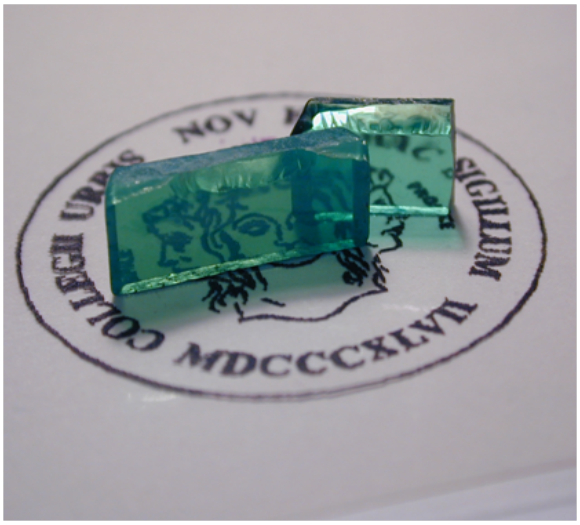

Figure 5.5: Photographs of as-quenched glass and glass ceramics samples

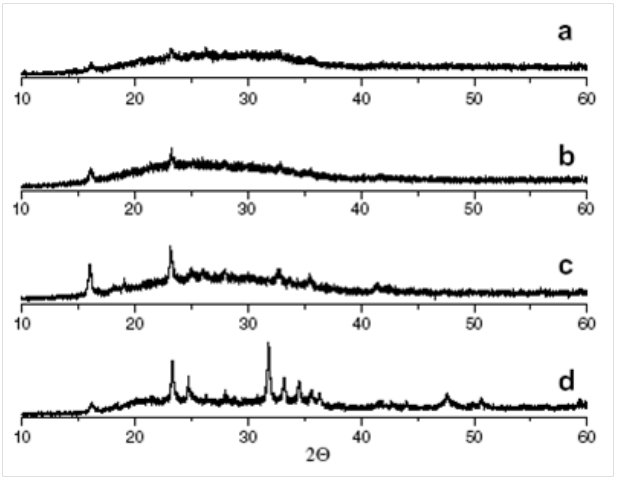

Figure 5.6: The X-ray diffraction patterns of Cr -doped CaO-Ge_2 glass ceramics at different heat treatment procedure (a)460^{o}C (1 hr); (b)475^{o}C (1 hr); (c)490^{o}C (15 min); (d)490^{o}C (1.5 hr).

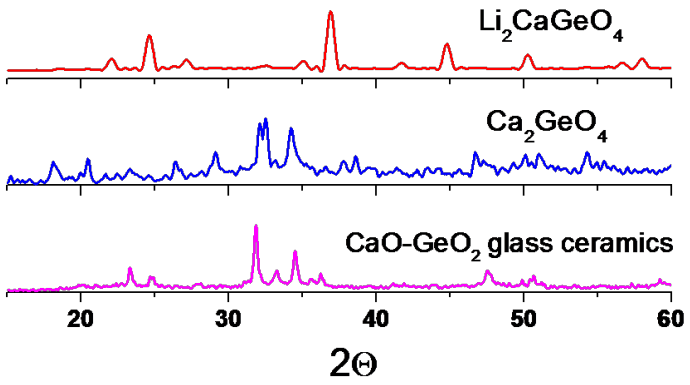

Figure 5.7: X-ray-diffraction patterns of Li_2CaGeO_4 single crystal, of Ca_2GeO_4 single crystal and of CaO-GeO_4 glass ceramics heat treated at 490^{o}C for (30 minutes)

slow and the reflection pattern shows only broadband structrue typical for "as quenched" glass.

- When the glass is heat treated at 475 ^{o}C for 1 hr, the reflection lines are more pronounced than before. But since the strength of reflection lines in Figure. 5.6(a) and(b) are almost the same, the crystallization process is also slow at 475 ^{o}C .

- Figure. 5.6(c) shows the reflections of the glass ceramics sample heat treated at 490 ^{o}C for 15min. At this heat treatment temperature, the crystallization process is strong and the reflections from the crystal phase is clearly seen in the figure. 5.6(d) when the duration of heat treament is increased to 1.5hr.

The X-ray diffraction patterns of glass ceramics clearly shows that the nano-crystallites are formed inside the glass matrix. Now the question is what is the phase of these crystallites?

Figure. 5.7 shows the comparison X-ray diffraction patterns of germanate glass ceramics, Cr^{4+}:Ca_2GeO_4 single crystal and Cr^{4+}:Li_2CaGeO_4 single crystal. As shown in the figure, most of the reflection peaks of glass ceramics are coincide with the

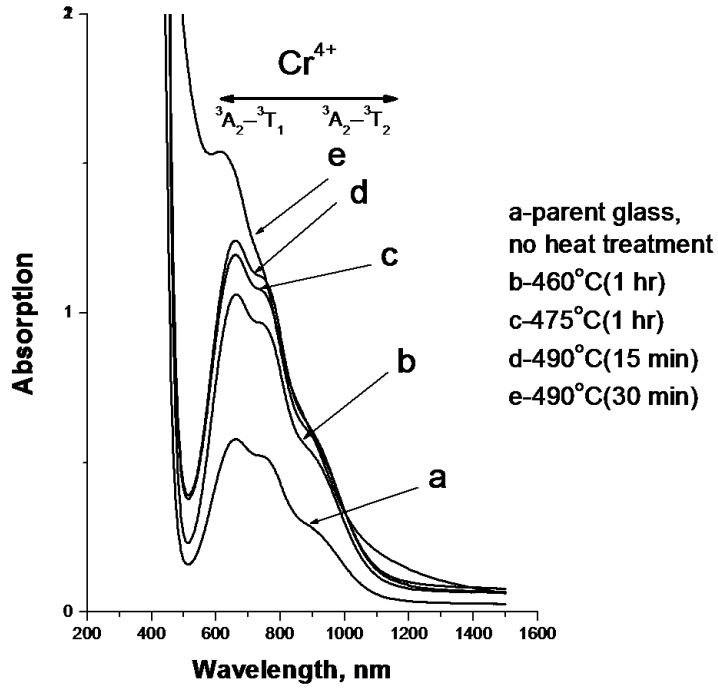

Figure 5.8: Absorption spectra of Cr -doped CaO-GeO_2 glass ceramics Vs heating temperature

reflection peaks of the Cr^{4+}:Ca_2GeO_4 single crystal. From the glass composition we used to synthesize the glass ceramics, there are three possible crystal phases which can be formed after devitrification. There are Ca_2GeO_4 , Li_2CaGeO_4 and $LiAlGeO_4$ crystal phase. We can rule out the possiblity of growing $LiAlGeO_4$ crystal phase because the same diffraction pattern results from the glass composition without Al_2O_3 modifier. The figure also shows that the position of reflection from glass ceramics is not conincide with the X-ray reflections from Li_2CaGeO_4 single crystal. This measurement give us the proof that the nano-crystals grown in the glass matrix is more or less similar to the Ca_2GeO_4 single crystal phase.

5.1.4 Absorption spectra vs. Heat treatment

Figure. 5.8 shows the absorption spectrum of "as quenched" glass and glass ceramics at different heating temperature and duration. The observations can be made as

follows.

- Figure. 5.8(a) shows the absorption spectrum of "as quenched" glass. As shown in the figure, there are three peaks around 600, 800, and 900 in visible region and there is a weak absorption tail near near-infrared region. These absorption ranges are similar to Cr^{4+}ions regions in single crystal. The absorption in ultraviolet region is very strong and it corresponds to the charge transfer transition.

- When the glass sample is heat treated (Figure. 5.8(b)(c)(d)), the absorption shape doesn't change indicating that the absorption of glass host overwhelms nano-crystallites absorption.

- As shown in the figure. 5.8(e), when the glass sample is heat treated at 490 ^{o}C for 30 minutes duration, the absorption wing in the ultraviolet region increases sharply indicating that the scattering increases due to increase in size of nano-crystals with heat treatment.

5.1.5 Emission spectrum vs. Heat treatment

Figure. 5.9 shows the emission spectra of glass ceramics at different heat treatment temperature. As shown in the figure, there is little or no emission from the samples heat treated at 440 ^{o}C for different temperature durations. Since the glass transformation temperature is around 485 ^{o}C , the crystallization is very slow at 440 ^{o}C . Only the nuclei will be formed in this temperature. As shown in Figure. 1.2, since the optical properties of Cr ions is strongly dependent on the local environment, the soft surrounding of the host glass makes the distribution of electronic and vibrational states of Cr ions wider. Even though the glass supply the required tetrahedral and octahedral networks for $Cr^{4+}$and Cr^{3+}stabilization, this inhomogeneity in the electronic transitions in glass surrounding promotes the non-radiative relaxation of the

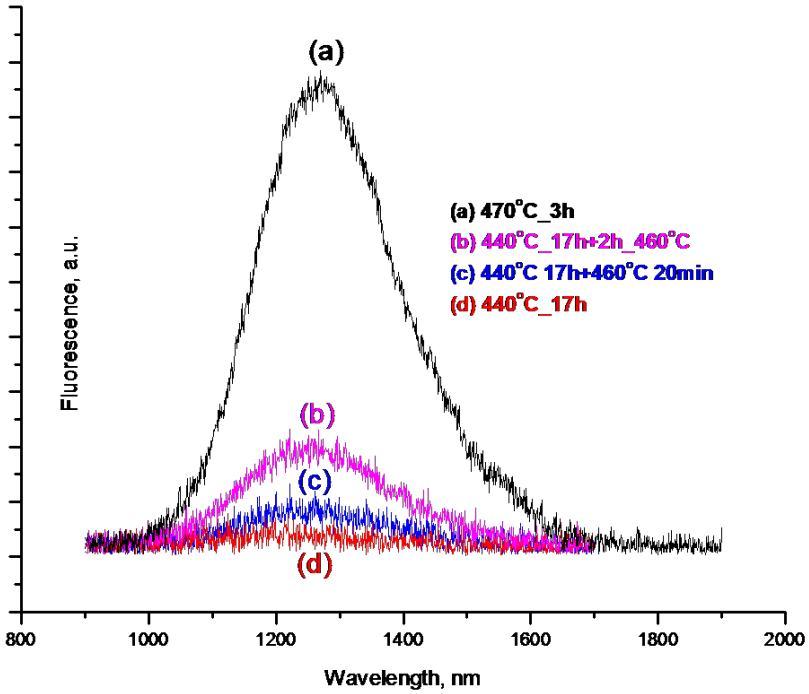

Figure 5.9: Figure showing formation of nanocrystallites by using the emission as the probe to detect the nanocrystals precipitations in glass matrix.

excited energy. This is the reason that there is little or no emission from Cr ions in the glass. At devitrification temperature of 470 ^{o}C , the emission intensity increases dramatically indicating that excited Cr ions has the ordered crystalline surrounding to decay radiatively because the number and size of nano-crystals have been increased at this devitrification temperature.

5.2 Spectroscopic properties of glass ceramics

In this section, the following questions are addressed using the various spectroscopic methods.

1. What is the phase of the nano-crystallites? Is the phase of nano-crystal is Ca_2GeO_4 single crystal phase? What kind of spectroscopic measurements are needed to determine the nano-crystal phase?

   Absorption spectroscopy: Comparing the absorption spectrum of Ca_2GeO_4 single crystal with that of the glass ceramics, we determined the phase of the nano-crystal. With the help of the absorption spectroscopy, we can also determine the valence state of the optical centers because the peak of $Cr^{4+}$and Cr^{3+}in olivine crystal structure is well known.

   Fluorescence spectroscopy: Comparing the emission peak of the Cr^{4+}:Ca_2GeO_4 single crystal with that of the glass ceramics, we can also determine the phase of the nano-crystal.

   Excitation spectroscopy: If we cannot determine the valence state of emission center with the absorption spectroscopy, the excitation spectroscopy can help determine the correct optical center with selective excitation of particular ions.

   Raman spectroscopy: Raman spectroscopy is key to determine the phase of the nano-crystal. Since the phonon spectrum of Ca_2GeO_4 single crystal is well studied in literatures, we can confidently identify the phase of nano-crystals by comparing the phonon spectrum of glass ceramics with that of the single crystal.

2. Are there any valence state other than Cr^{4+}ions? In contract to Mg_2SiO_4 single crystal, only one valence state can exist in Ca_2GeO_4 single crystal.

3. What is the overall performance of Cr -doped germanate glass ceramics (quantum efficiency, lifetime)?

5.2.1 Absorption and Excitation spectrum of germanate glass ceramics

The polarized absorption peaks of Cr^{4+}:Ca_2GeO_4 single crystal in visible and near-infrared regions are described in Table: 4.2 & 4.3. In the germanate glass ceramics, the nano-crystals are not oriented. Consequently, the measured absorption spectrum includes the absorption peaks of all three polarizations. As shown in fig.5.10, in the visible absorption spectrum of Cr^{4+}:Ca_2GeO_4 single crystal, the polarized absorption peaks is located at 811nm for E‖long axis(yellow), at 738nm for E‖medium axis(green), and at 633nm for E‖short axis(blue). In the unpolarized absorption spectrum of germanate glass ceramics, the absorption peaks are located at 650nm, 750nm and 900nm as shown in the figure. 5.10. The absorption peaks of the glass ceramics are not located at the same position as the single crystal. This is because several valence states of chromium ions can coexist in glass ceramics. Also, since chromium ions can stable in glass phase, the absorption of Cr centers in glass matrix may distort the absorption peaks of Cr centers in nano-crystals. Since the volume ratio of nano-crystals is about 30% of total volume, it is possible that the chromium ions content in glass matrix may be more than that in the nano-crystals, which in turn the absorption of Cr ions in glass matrix overwhelm the absorption of Cr ions in nano-crystals. Also, the position of absorption peaks of Cr^{4+}ions in forsterite crystal is shown in fig.5.10. Since the absorption bands of glass ceramic in ultraviolet and visible range overlap with $^4T_1$ and $^4T_2$ energy bands of Cr^{3+}ion, the absorption spectrum of glass ceramics is the combination of the absorption of $Cr^{3+}$and Cr^{4+}ions in glass and crystal phase.

Since the absorption spectrum of glass ceramics has the overlapping bands from different optical centers, the optical centers inside the nano-crystals can be determined by using the site-selective excitation spectrum because Cr^{4+}near-infrared emission only occurs when the nano-crystals are precipitated in the glass matrix.. As shown

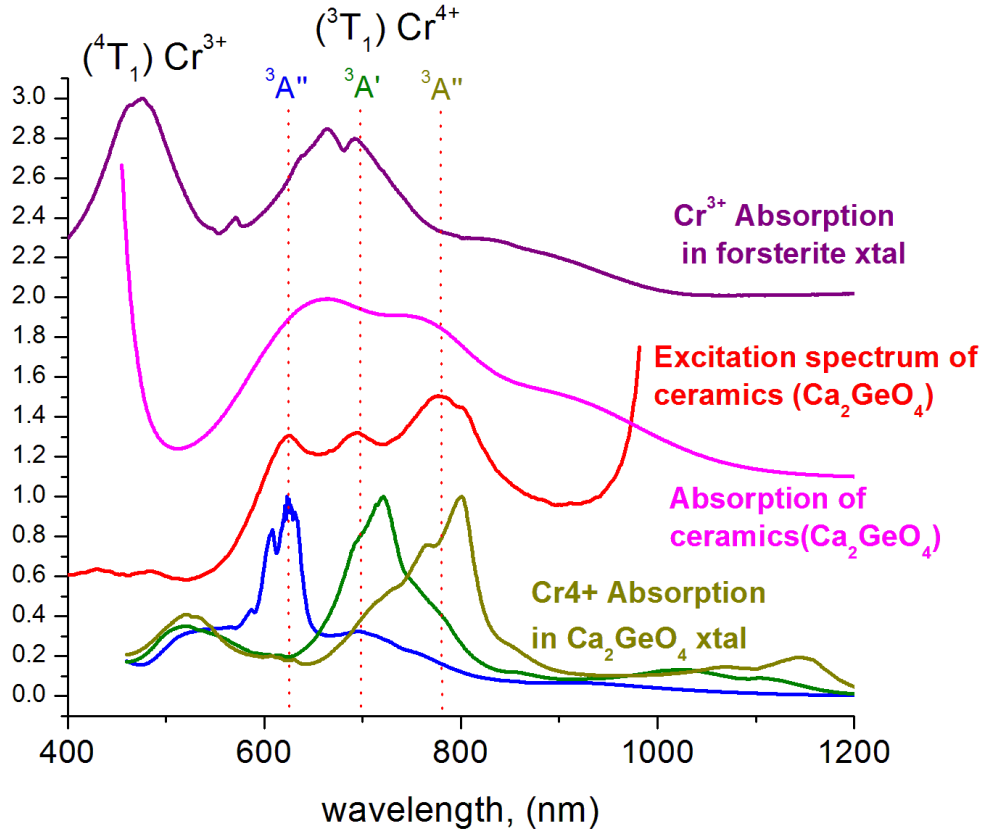

Figure 5.10: Comparison among the absorption spectrum of cunyite single crystal, absorption spectrum of cunyite glass ceramics, excitation spectrum of glass ceramics with monitored emission of 1260nm and excitation spectrum of forsterite single crystal with monitored emission of 900nm

in the figure. 5.9, the intensity of near-infrared emission is stronger with the heat-treatment of the "as quenched" glass sample. By monitoring at the emission peak at 1260nm, the absorption peaks of the active centers in the nano-crystals can be determined. As shown in the figure. 5.10, the absorption peaks of site selective excitation give 633nm, 700nm and 780nm in the visible region. These absorption peaks are very close to the absorption peaks of Cr^{4+}:Ca_2GeO_4 single crystal in the visible region. This clearly indicate that Cr^{4+}valence state is stabilized in the nano-crystals and the phase of nano-crystal is more or less similar to the Cr^{4+}:Ca_2GeO_4 single crystal.

5.2.2 List of possible stabilized valence state of chromium ions in glass ceramics

It is possible that there are several valence states coexist in the material. These valence states contributes the shape of absorption spectrum of glass ceramics. The known stable valence states of Cr ions in the literatures are

- $Cr^{6+}(d^0)$ parity allowed charge-transfer transitions with strong bands located at around 270nm and 380nm.
- $Cr^{4+}(d^2)$centers in tetrahedral environment have three bands (600, 700, and 800nm)caused by the splitting of $^3T_1$ manifold and a weaker bands (800 to 1100nm)caused by the splitting of $^3T_2$ manifold.
- $Cr^{3+}(d^3)$in octahedral environment exhibits two bands at 450nm($^4T_1$) and 620nm($^4T_2$). These absorption bands are clearly shown in the figures. 4.10 and 4.11.
- $Cr^{5+}(d^1)$valence state was detected in sol-gel glasses.
- Cr^{2+} valence state is not detected in the glass host.

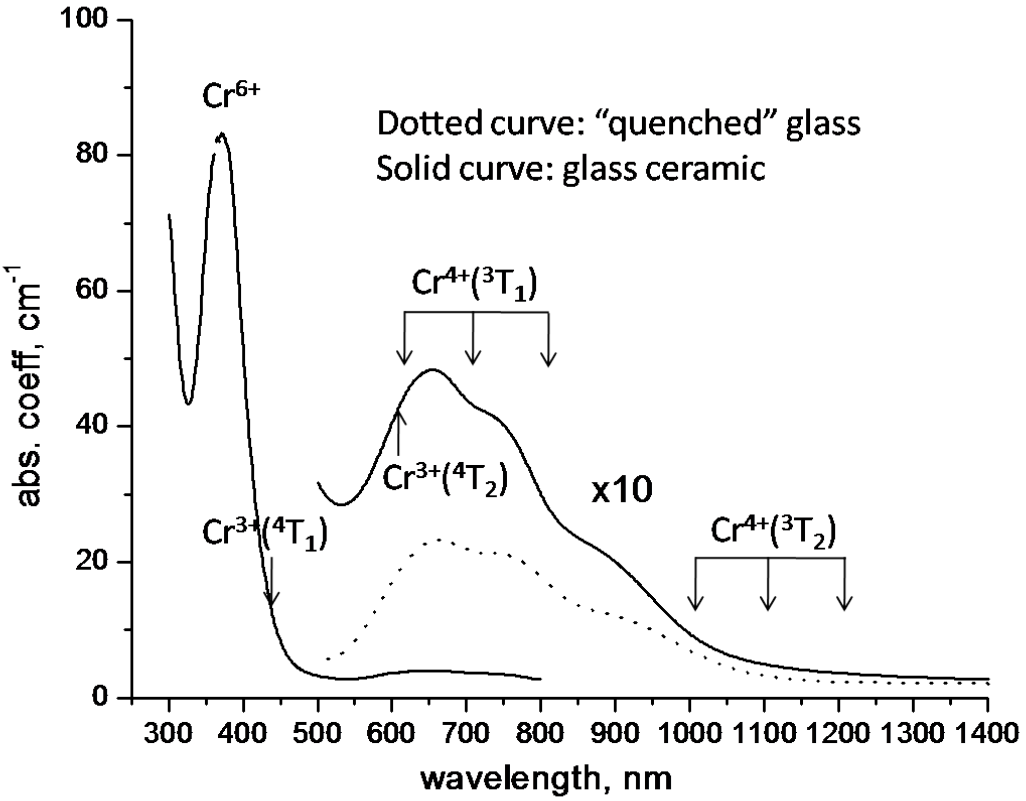

Figure 5.11: The absorption spectrum of the "as quenched" glass and the glass ceramic showing several valence state coexist in the medium

Coexisting several Cr valence states in material makes active center identification difficult because the absorption of different centers will overlap each other. Even if we can identify only Cr^{4+}valence state exist in the material, it is possible that the crystal lattice may be distorted, which in turn the optical properties of Cr centers will be different than that of single crystal because the optical properties of transition metal ions are very much depend on the local surrounding.

5.2.3 Emission spectrum of germanate glass ceramics and single crystal

The emission spectra of glass ceramics and cunyite single crystal measured at 77K are as shown in fig.5.12. The emission spectrum of glass ceramics is broadband even at 77K while the sharp zero-phonon line and phonon repetition are observed in cunyite single crystal. The possible reason of broadband emission of glass ceramic when compared to single crystal is the distortion of crystal lattice and the difference in distortion from site to site, which in turn causes the broadening of the first excited state ($^3T_2$) in the assemble of ions. In other word, the inhomogeneous broadening is much larger in the glass ceramics than the single crystal.

With the help of Sugano-Tanabe diagram 5.13(b), we can explain the broadband emission at 77K as a result of distribution of crystal field strength of Cr^{4+}ions local environment. As shown in the figure, the cunyite single crystal has narrow distribution while the glass ceramics has the wide distribution of crystal field strength because of inequivalent Cr^{4+}ion sites. This is electronic contribution to the broadening of emission band of glass ceramics. Another contribution is lattice vibration. As shown in fig.5.13(a), in single crystal, the vibrational levels are quantized because of order structure of single crystal. In glass, the soft surrounding creates the phonon bath and accordingly the continuum of vibrational levels are observed. But in glass ceramics, we expect that the vibrational structure is neither quantized or continuum. Because of this reason, the continuum of phonon repetition contributes the broadening of emission bands and it is impossible to see the phonon repetition in glass ceramics at 77K.

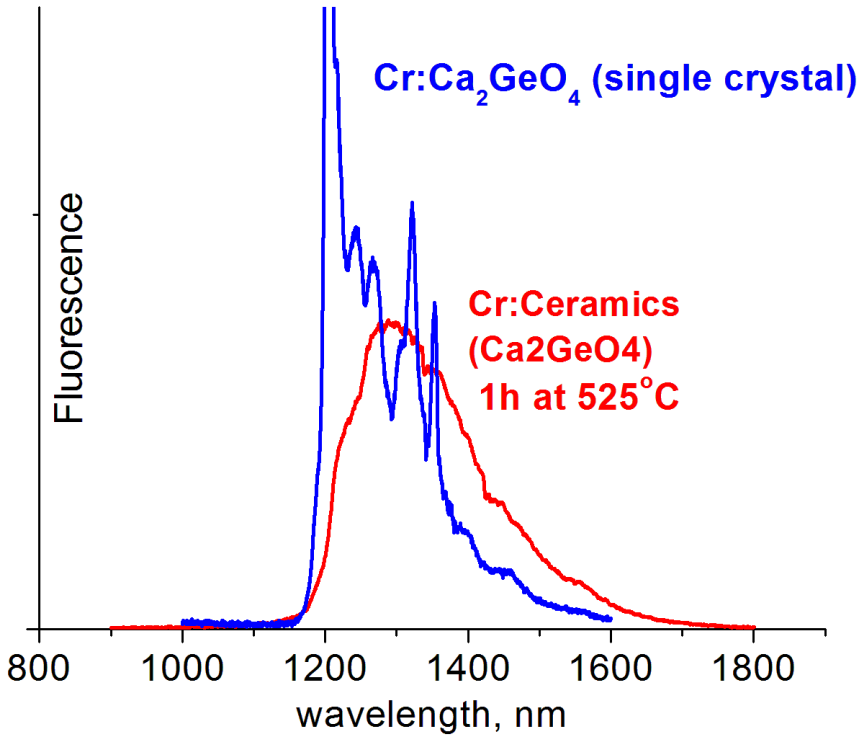

Figure 5.12: The emission spectrum of cunyite single crystal and glass ceramics at 77K

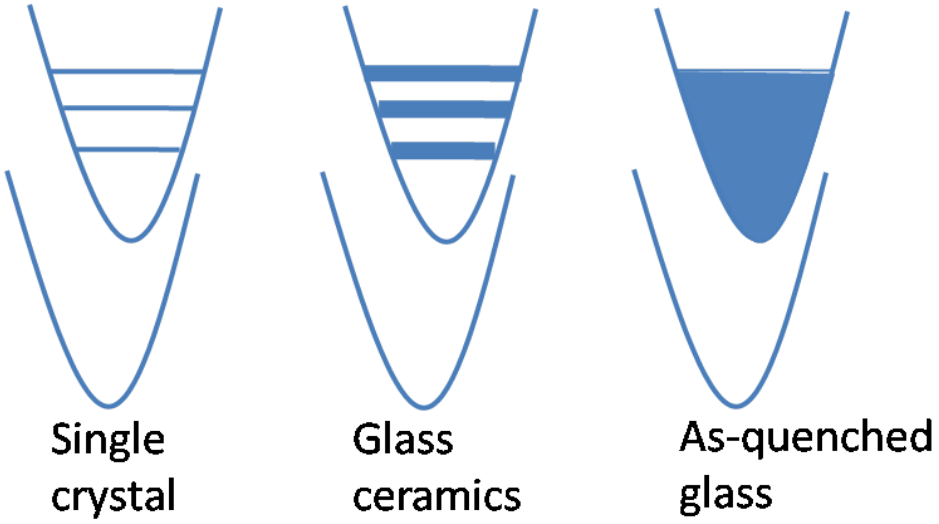

(a) Illustration of distribution of vibrational energy level in glass ceramics

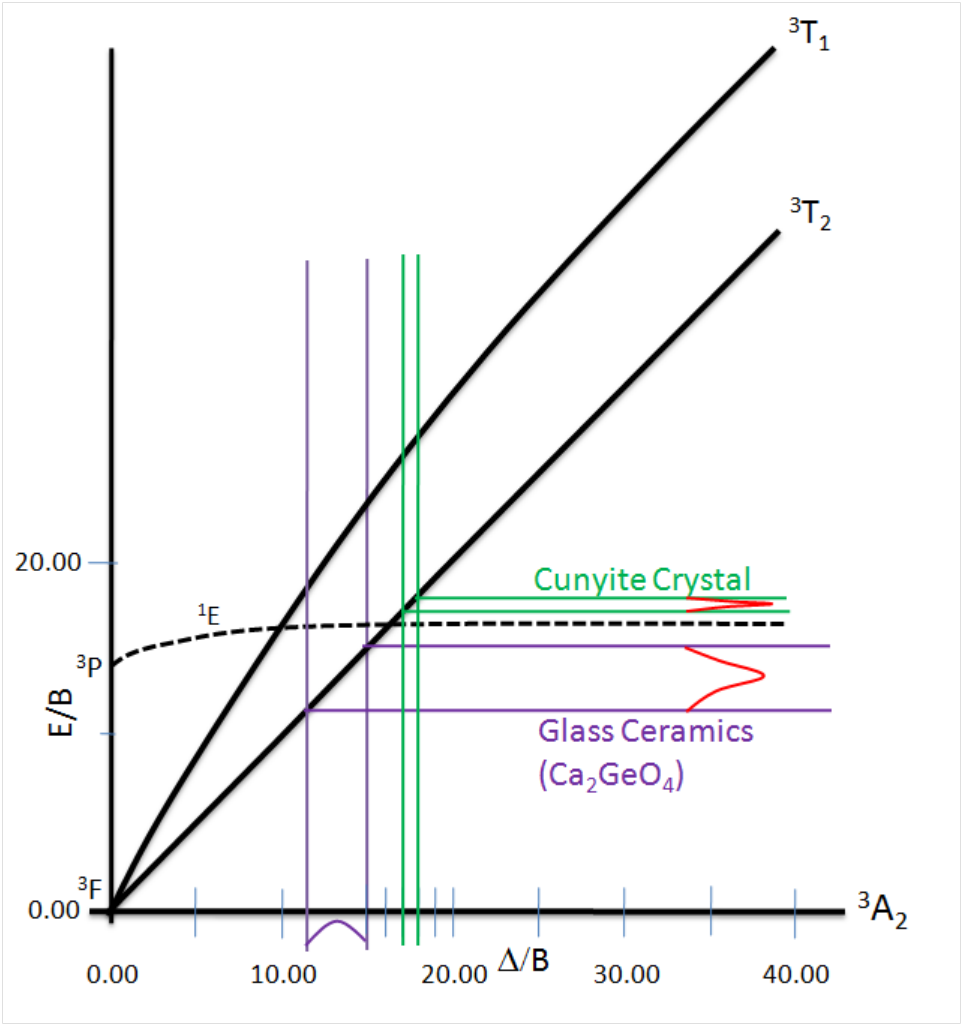

(b) Illustration of distribution of electronic energy level in glass ceramics

Figure 5.13: Illustration of the causes of broadband emission of glass ceramics and sharp emission of single crystal at 77K

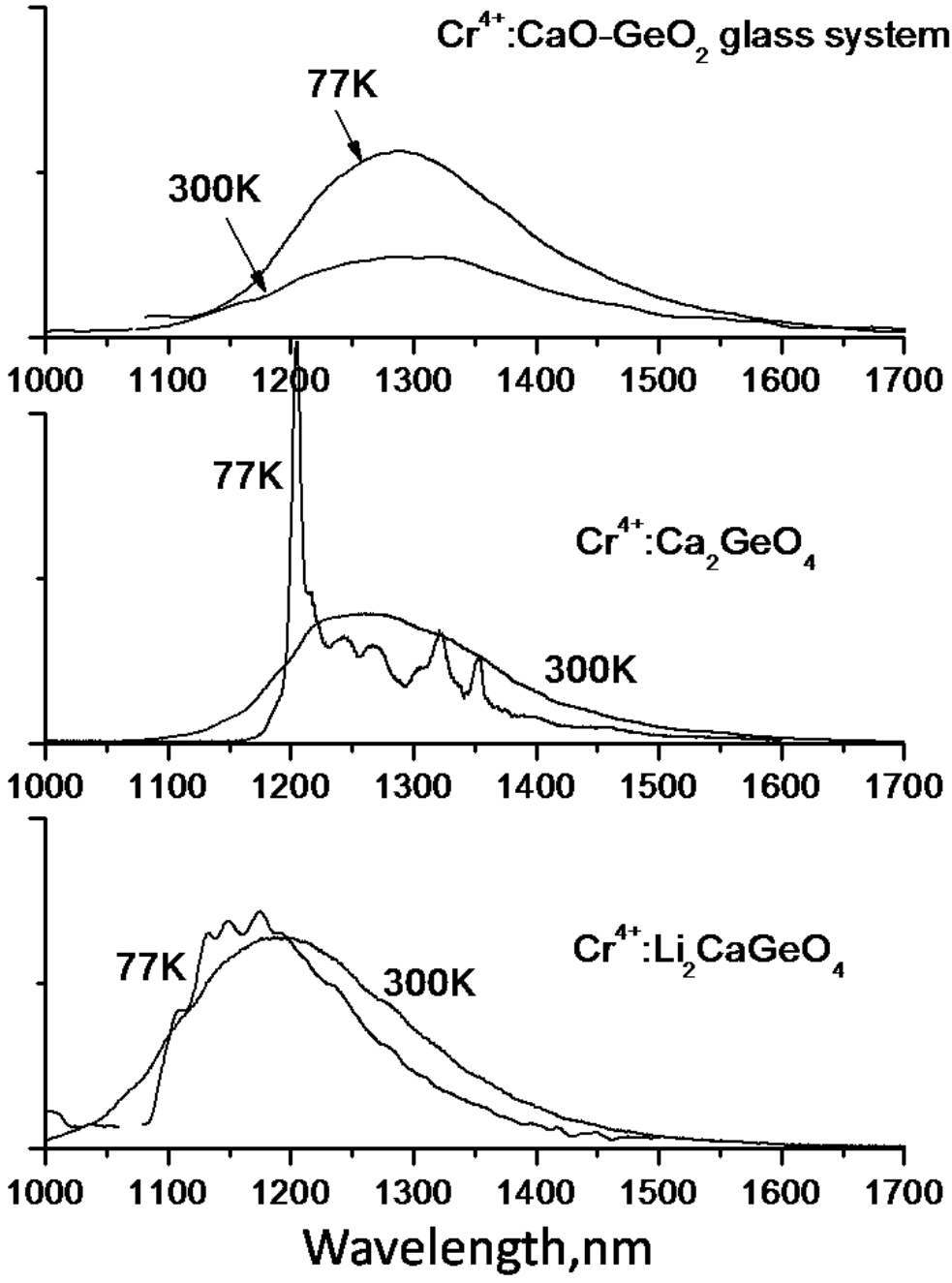

Figure 5.14: Emission spectra of Cr^{4+}-doped CaO-GeO_2 glass ceramics, Ca_2GeO_4 and Li_2CaGeO_4 single crystals

5.2.4 Crystal phase identification using fluorescence spectrum

Since the transition metal ions such as Cr ions are very sensitive to local surrounding, the stored (or) excited energy of these ions decay non-radiatively in most of the crystal host. Some crystal structure such as the olivine crystal structure can have the favorable crystalline surrounding to decay the excited energy radiatively. To identify the phase of the nano-crystal, we need to look what kind of crystal phases, which have the favorable condition for excited Cr ions to decay radiatively, can be formed from this glass composition. From this composition, the two types of crystal phases having the favorable conditions for Cr ions, Cr^{4+}:Ca_2GeO_4 and Cr^{4+}:Li_2CaGeO_4 can be formed. As shown in the figure. 5.14, when we compared the emission peak of the glass ceramics with the emission peaks of Cr^{4+}:Ca_2GeO_4 and Cr^{4+}:Li_2CaGeO_4 single crystals, the emission peak of the glass ceramics is more or less similar position at the emission of Cr^{4+}:Ca_2GeO_4 single crystal at room temperature. When compared with the emission peak of the glass ceramics, the peak of Cr^{4+}:Li_2CaGeO_4 single crystal is blue shifted about 100nm. Because of this observation, the nano-crystal phase is similar to that of Cr^{4+}:Ca_2GeO_4 bulk crystal phase.

5.2.5 Raman Spectroscopy

Raman spectroscopy is a very powerful method to identify the phase of materials by measuring the vibrational frequency of molecular complex. The question here is how many normal modes can exist in a particular molecular complex. Let's look at the unit cell in the olivine crystal structure of Ca_2GeO_4 . In a unit cell, there are four formula units composed with 28 atoms. In a single formula unit, each atoms are bounded to each other partly covalent and partly ionic. We can imagine that the ions are interconnected to each other with spring.

In 3D crystal, each ion can move in X-, Y- and Z-direction. In other words, each ions has 3-degree freedom of movement. If the solid has N atoms, the whole solid has 3N degree of movements. These movements involve translational, rotational and vibrational movements. Since the crystal is built with the stack unit cells along X, Y and Z direction, we only need to considered the translational, rotational and vibrational movement of one unit cells.

In the unit cell of Ca_2GeO_4 crystal, there are 28 atoms and they have 84-degree of movements. Any movement needs energy. The energy is created through heat transfer through the solid and the surrounding environment. Let's introduce the phonon. The phonon is one quanta of energy required to excited these movements. There are two kinds of phonons. One is optical phonon having frequency in optical range and another is acoustic phonon having frequency in microwave range. Because of 3D solid, there are 3 translational and 3 rotational movements. They have the frequency in microwave region. Because of these movements, the acoustic phonons are created and annihilated.

We're interested in optical phonons which are created and annihilated through vibrational movements since these optical phonons are measurable through Raman and Infrared spectroscopy. As explained in above, each crystal structure have their characteristic movements because every crystal have different bonding strength and

different masses of constituents atoms. We'll take advantage of this fact. Raman signal is the finger print of specific crystal structure.

In synthesizing the glass ceramics, our main goal is to synthesize Cr^{4+}:Ca_2GeO_4 nano-crystals inside the glass matrix. First we synthesize the "as quenched" glass and then the nucleation and the crystallization processes are followed. Even though we choose the glass composition carefully to have high probability of Ca_2GeO_4 crystal phase separation, there is the possibility that other crystal phases can be grown during the devitrification procedure. Because of this reason, identification of the crystal phase inside the glass matrix must be made through a series of spectroscopic measurements. Among the spectroscopic techniques, Raman spectroscopy is key to identify the particular crystal phase.

5.2.5.1 Theory of resonance Raman spectroscopy

If the excitation wavelength is tuned into an excited electronic energy level of the fluorescing ions, the creation and annihilation of the vibration modes coupled to the electronic transition is greatly enhanced. Consequently, the Raman scattering intensity of this specific mode is enhanced *six orders of magnitude* more than the intensity of off-resonance Raman scattering. This happens because the polarizability and its dependent on the molecular vibration, is enhanced through the electronic transition. These modes are called *local modes* because these modes are strongly coupled to the electronic transition of specific ions.

Raman scattering intensity is proportional to the square of the polarization transition moment of a specific mode, $I_{Raman} \propto \alpha_k^2$. To enhance scattering intensity of a certain vibration mode k, we need to increase the value of polarization transition moment, α_k.

There are two enhancing mechanisms for resonant Raman scattering, which can

be described by *Albrecht's* $\mathcal{A}$ *and* $\mathcal{B}$ *terms.*

$$\alpha_k = \mathcal{A} + \mathcal{B} \tag{5.1}$$

5.2.5.1.1 Albrecht's $\mathcal{A}$ term enhancement or Franck-Condon scattering

Franck-Condon scattering involves the displacement of the potential minima of the ground state and the excited state along a vibrational normal coordinate, $\mathcal{Q}_k$.

$$\mathcal{A} = K \sum_v \frac{\mathcal{F}_v}{\nu_{vi} - \nu_0 + i\Gamma_v} \tag{5.2}$$

where,

$$\begin{aligned} \mathcal{F}_v &= \langle j|v\rangle\langle v|i\rangle \\ |i\rangle &= |g, i\rangle \text{(initial state)} \\ |j\rangle &= |g, j\rangle \text{(final state)} \\ |v\rangle &= |e, v\rangle \text{(intermediate state)} \end{aligned}$$

K**:** the electronic transition

$\mathcal{F}_v$**:** the overlap integral of the vibrational wavefunctions

ν_0**:** the excitation frequency

This mechanism is strong for electric dipole allowed electronic transition and enhances the totally symmetric modes.

There must be a shift between the potential minima of the ground state and the excited state for $\mathcal{A}$ term to become non-zero. Among the three factors in $\mathcal{A}$ term; the denominator describes the resonant enhancement factor. If the excitation frequency ν_0 is tuned near ν_{vi}, the denominator becomes minimum and consequently $\mathcal{A}$ term is greatly enhanced.

5.2.5.1.2 Albrecht's $\mathcal{B}$ term enhancement or Herzberg-Teller vibronic coupling

Herzberg-Teller vibronic coupling involves a transfer of transition moment between different excited states induced by a vibrational excitation. This coupling is described by Albrecht's $\mathcal{B}$ term.

$$\mathcal{B} = C \sum_{v} \frac{\mathcal{F}'_v}{\nu_{vi} - \nu_0 + i\Gamma_v} \tag{5.3}$$

$$\begin{aligned}
\mathcal{F}'_v &= \langle j|\mathcal{Q}_k|v\rangle\langle v|i\rangle + \langle j|v\rangle\langle v|\mathcal{Q}_k|i\rangle \\
|i\rangle &= |g,i\rangle(\text{initial state}) \\
|j\rangle &= |g,j\rangle(\text{final state}) \\
|v\rangle &= |e,v\rangle(\text{intermediate state})
\end{aligned}$$

For the electric-dipole electronic transition, resonance enhancement occurs through this mechanism via *totally symmetric mode*(T) or *non-totally symmetric modes*(NTS). There is a need to have the second excited states very close the first excited state to become this mechanism active. Even though either TS or NTS vibration modes couples these two excited states, this mechanism is usually good for enhancing the non-totally symmetric modes. There is not necessary to have a shift between potential minima to become this mechanism active.

5.2.5.2 Reasons why we should use Raman spectroscopy to identify the phase of nano-crystals

1. Let's look at the practical experimental point of view. The sample is excited with available excitation source, let's say 532nm or 632nm, which are ubiquitous sources. Most of the photon scatter the same wavelength through Rayleigh scattering. 1 in 10^6 incident photon scatter with the wavelength higher or lower the incident wavelength. That's mean that a quanta or several quantum of energy is added to the excited energy. Where is this energy coming from? The energy

from room temperature is 208.5cm^{-1}($E = kT = 0.695 \times 300$). Let's say if a single vibrational movement requires 800 cm^{-1}energy, it will absorb 4 quantum of phonon to create this movement at room temperature. When the sample is cooled down, the vibrational movement cools down and these 4 quantum of phonon is annihilated through heat emission. Every movement has the characteristic frequency. According to the harmonic approximation, this frequency is associated with the masses of constituent atoms and the bond strength between them. According to this, every molecular structure has vibration movement with characteristic frequency. This so-called finger print vibrational frequency will make material identification process easier.

2. The phonon spectrum of Ca_2GeO_4 single crystal is well studied in our lab. To identify the phase of nano-crystallites is Ca_2GeO_4 single crystal phase, we need find these phonon modes from the nano-crystallites. To identify the lattice modes of Ca_2GeO_4 , we can use the off-resonance Raman spectroscopy.

3. When Cr substitute Ge ions in Ca_2GeO_4 crystal structure, the additional modes occurs because of disorder effect caused by Cr substitution. These modes are called local modes. These local modes of Cr^{4+}:Ca_2GeO_4 single crystals are well known in the literature. If Raman spectrum of the glass ceramics has these local modes, we can confirm that Cr^{4+}ions are stable in non-crystallites.

5.2.5.3 On and Off-Resonance Raman Spectrum of Cunyite single crystal

Here, I would like to be clear about the definition of lattice and local modes of chromium doped Ca_2GeO_4 experimentally. The lattice modes are Raman lines we measure before chromium doped into the crystal host. When chromium (1 wt%) is doped into Ca_2GeO_4, the additional modes appear because of changes in bond

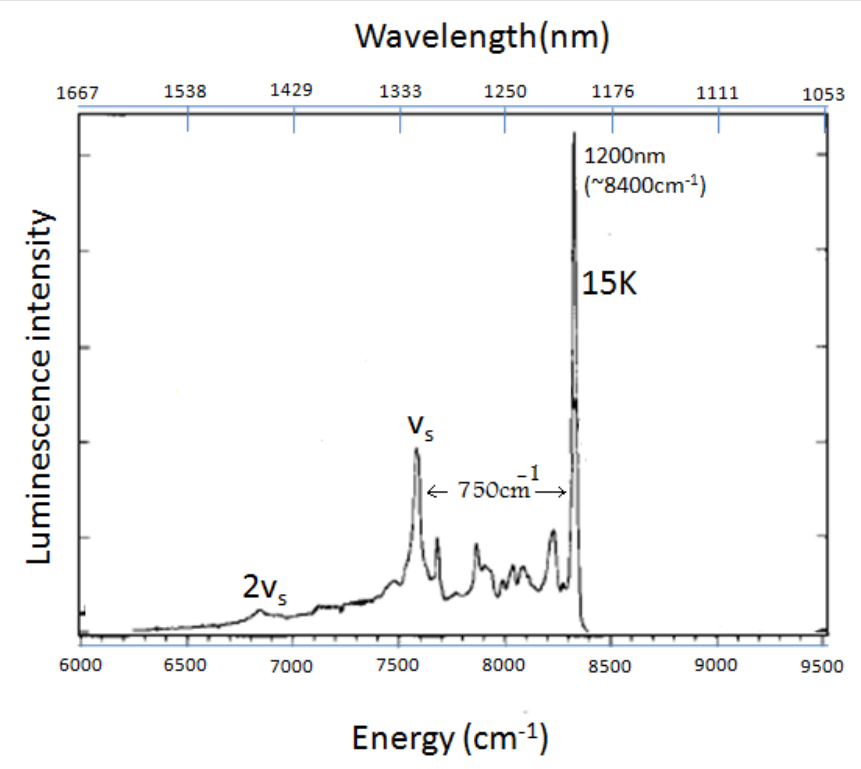

(a) Emission spectrum of cunyite crystal at 77K showing the totally symmetric breathing mode of CrO_4^{4-} tetrahedron

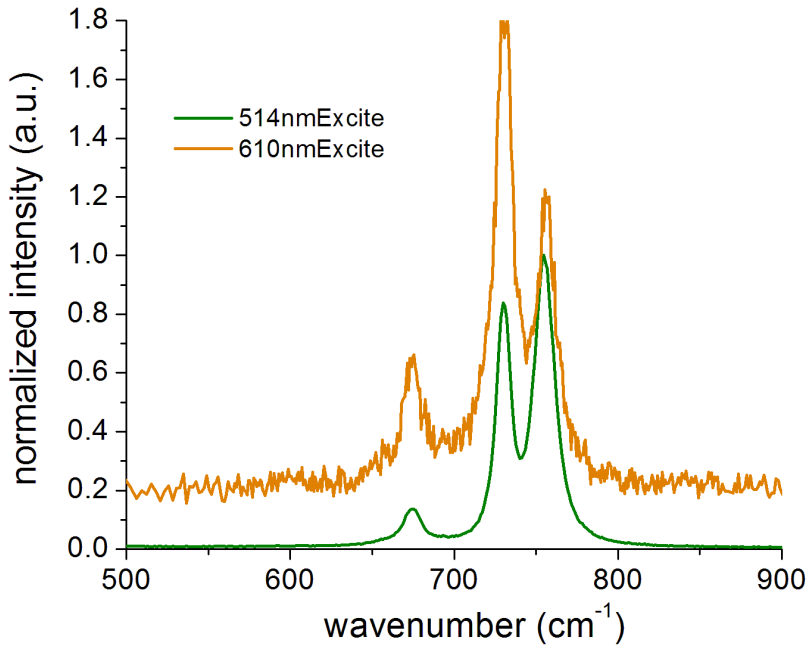

(b) On(610nm excitation) and off-resonance(514nm excitation) Raman spectrum of single crystal.

Figure 5.15: Totally symmetric vibrational mode of cunyite crystal

strength and atomic masses. But the chromium doping is so small that these local modes are swamped by the abundance intensity of lattice modes. But as explained in the theory section 5.2.5.1, the intensity of the local modes can be enhanced by *6 order of magnitude (1000,000times)* by choosing the excitation line near the peak absorption of chromium ions. Thus because of this enhancing mechanism, the local modes are quite stand out among lattice modes in Raman spectrum. The question here is why the local modes are so important in analyzing the laser crystal. The obvious answers are

- The local modes appear because of chromium doping. Because of this reason, it does associated with chromium ions and its electronic structure.
- The local modes are finger print of each chromium doped crystal. By using this, we can identify the phase of nano-crystals without doubt.
- It is a believe that these local modes are the first in line in a series of energy dissipation through vibration modes because it does associate with the electronic transition of chromium ions. Because of this reason, knowledge of these local modes is very important to understand the non-radiative relaxation mechanism in chromium doped laser crystal. The detailed analysis of how the local modes participate in non-radiative relaxation of forsterite crystals, please refer to Dr. Dana Calistru's thesis .[22].

Figure.5.15(a) shows the fluorescence spectrum of cunyite single crystal measured at 77K. The picture shows beautifully the vibronic progression of totally symmetric mode of $750cm^{-1}$. Since this is a fluorescence transition, the ground(^3A) and excited state(^3T) have the same multiplicity. Thus only the totally symmetric mode can couple to the electronic transition. This totally symmetric mode could be the local mode because it does couple to the electronic transition.

Unlike the forsterite crystal, the cunyite crystal has very few local modes. They are [26],

On-Resonance Raman modes (cm^{-1})	Scattering Geometry $k_i(p_i p_s)k_s$
344	x(zy)x
374	y(zx)y
730	y(zz)y

Among these three modes, $730cm^{-1}$ mode is the most noticeable of all and the wavenumber agrees with the one observed from the fluorescence and absorption spectrum of cunyite crystal measured at 77K. Figure.5.15(b) shows on and off-resonance Raman measurement of cunyite crystal using off-resonance argon laser line (514nm) and on-resonance dye laser line (609nm). We use this local mode to identify the phase of nano-crystals and to prove that Cr^{4+}ions is active centers in glass ceramics.

5.2.5.4 On and Off-Resonance Raman Spectrum of Cunyite glass ceramics

In impurity doped crystal, the off-resonance Raman spectroscopy is used to measure the lattice modes of the crystal host. Before using the on and off term, the question is what resonances to what? The former "what" means the excitation energy and the latter "what" means the absorbing energy of impurity ions. The concentration of impurity ions in crystal host is very small, the local modes introduced by disorder substitution is overwhelmed by the lattice modes if the excitation wavelength is not resonance with absorption transition of impurity ions. In theory section 5.2.5.1, the detailed explanation of scattering enhancement through on-resonance excitation is made. On the other hand, if the undoped sample is not available, the off-resonance Raman measurement is necessary to measure the lattice modes of the host crystal. As

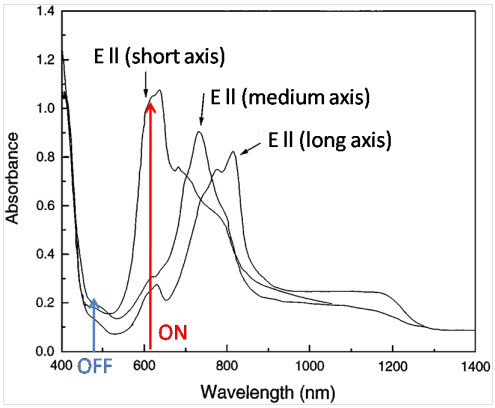

(a) Figure showing the excitation position for Raman measurements in Polarized absorption spectrum of Cr^{4+}:Ca_2GeO_4

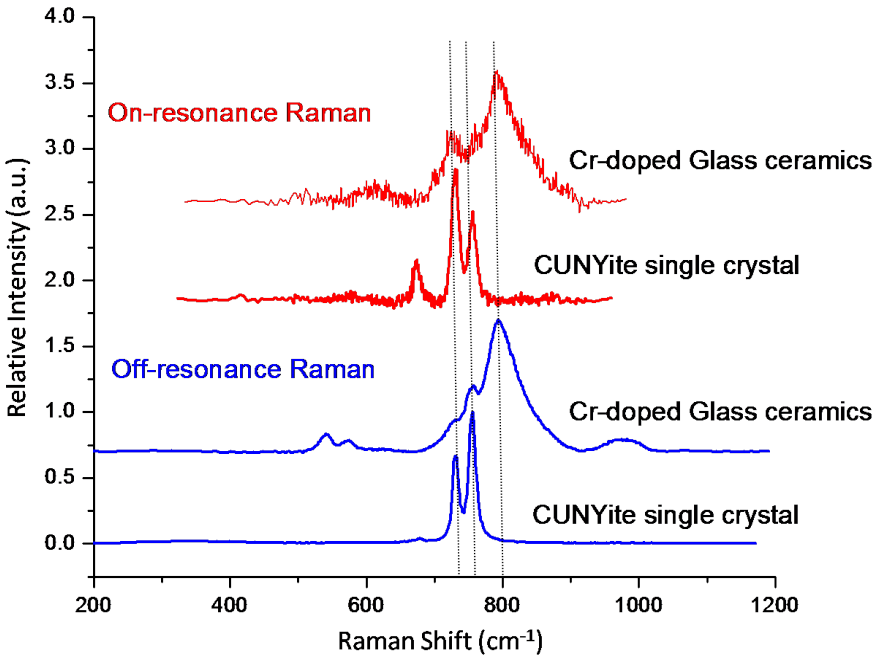

(b) On and Off-Resonance Raman spectra

Figure 5.16: (a) Polarized absorption spectrum [14] of Cr^{4+}-doped Ca_2GeO_4 single crystal and (b) On and Off-Resoance Raman spectra of Cr^{4+}:Ca_2GeO_4 single crystal and Cr^{4+}-doped CaO-GeO_2 glass ceramic

the name implied, the off-resonance Raman measurement uses the excitation source outside the absorption transition of the impurity ions.

Figure. 5.16a shows the polarized absorption spectrum of Cr^{4+}:Ca_2GeO_4 single crystal. The transitions corresponds to the low symmetry components of electronic transition($^3A_2 \rightarrow {}^3T_1$) of Cr^{4+}ions. The absorption peaks are located at 600, 700 and 800 nm. We will use this polarized absorption spectrum as a guidance to measure the on and off-resonance Raman measurement of single crystal and glass ceramics.

Before we go any farther, the main objective is to find the finger print lattice modes of Ca_2GeO_4 crystal structure to identify the host structure of nano-crystals and to find the finger print local modes to identify Cr^{4+}ions substitution in nano-crystals. As shown in fig.5.15(b), the lattice mode of cunyite is 760 cm^{-1} and the local mode of cunyite is 730 cm^{-1} if the scattering geometry is y(zz)y. Using this scattering geometry, I'll search these modes in Raman spectrum of cunyite glass ceramics to prove that the phase of nano-crystals is cunyite crystal phase.

For off-resonance Raman measurement, as shown in the figure. 5.16a, we used the CW argon 488nm laser line, which is well outside the absorption regions of impurity Cr^{4+}ions. For on-resonance Raman measurement, we used the dye laser pumped by the second-harmonic of Nd:YVO_4 laser. Since the dye laser is used Rhodamine 6G as the amplified medium, it can be tunable from 575 to 620nm. We use the narrow band filter of 609 nm to filter out the narrow band excitation line near absorption peak region. Since 609nm is the absorption peak only for excitation parallel to the crystallographic short axis. the crystal must be excited along the short axis in order to get on-resonance local modes. In the case of glass ceramics, excitation direction is not important because the nano-crystals are oriented randomly inside the glass matrix. The enhanced scattering signal will come only from Cr^{4+}ions in the nano-crystals which have the considerable projection of excitation on the short axis of the nano-crystals. Because of this reason, it is understandable that the signal strength of

local mode will be quite low from the glass ceramics.

Figure. 5.16b shows the on and off-resonance Raman measurement of CUNYite single crystal and glass ceramics. In Off-resonance Raman measurement of single crystal, there are two phonon lines representing the vibration movements of GeO_4^{4-}tetrahedron. In Off-resonance Raman spectrum of glass ceramics, the broad phonon band of the glass matrix overlap with the lattice modes from nano-crystals because of structural similarities of the two phases. Even though the phonon modes are overlapped, we can clearly see that the lattice modes of nano-crystallites coincide with those of the cunyite bulk crystal. This clearly indicates that the phase of nano-crystal is Ca_2GeO_4 crystal phase.

When Cr doped into Ca_2GeO_4 crystal host, the so-called "local modes" are created. These local modes are usually hidden under the host phonon modes. By tuning the excitation wavelength around the absorption transition of Cr^{4+}ions, the intensity of these local modes can be increased 6 order of magnitude more than the off-resonance scattering intensity. Again, on-resonance Raman measurement is done using 609nm dye laser line, which is the peak absorption band of Cr^{4+}ions along the short axis of the crystal. Scattering geometry is y(zz)y for single crystal.

On-resonance Raman measurement of single crystal and glass ceramics as shown in the figure. 5.16b. In the single crystal measurement, the scattering intensity of 730 cm^{-1}increase three times more than the off-resonance measurement. As shown in the figure.5.15(b), this local mode resonances with the lattice mode of crystal host. Because $Cr^{4+}$and Ge^{4+}have the same valence and very similar ionic radii (0.041nm versus 0.039nm), substitutional distortion may be minimal, which in turn the energy difference between the local mode and the lattice mode is very close. In on-resonance Raman measurement of glass ceramics, only 730 cm^{-1} is clearly visible while 750 cm^{-1} mode disappears because of on-resonance enhancement. Observing the local mode in glass ceramics clearly indicates that Cr^{4+}substitute Ge^{4+}in GeO_4^{4-}tetrahedron and

gives us the proof that the phase of nano-crystals is very similar to cunyite bulk crystal.

5.2.6 Cr^{4+}Fluorescence Dynamics in Cunyite glass ceramics

As shown in figure.5.11, different valence state of chromium ions coexist in chromium doped glass ceramics. If we assume that the near-infrared emission mostly comes from Cr^{4+}ions in tetrahedral coordination, we can the study the fluorescence dynamics of Cr^{4+}ions in glass ceramics. Even if the near-infrared emission comes form only one valence state, here Cr^{4+}ions, the local environment of each ions may be different in glass ceramics because of stress and interface between different phases. To visualize, Cr^{4+}ions may be doped in glass phase, in interface between glass and crystal and in nano-crystal phase. Since Cr^{4+}ions have different local environment, according to the ligand field theory, there will be distribution of excited state energy. If the Cr^{4+}ions localize in two significantly different sites, their excited state lifetime will be different depending on state of tunneling between potential energy surface of ground state and excited state. Because of this reason, by analyzing the measured lifetime of glass ceramics of near-infrared fluorescence, we can study the fluorescence dynamics of different near-infrared emission centers coexist in glass ceramics. As shown in fig.5.17, compared to the decay curve of cunyite single crystal, the decay curves of glass ceramics is not single-exponential decay in every temperature range indicating that more than one centers contribute to the decay measurement. This is an expected result because there is a distribution of inequivalent sites in glass ceramics.

To recover the decay distribution, we can use the continuous function decay analysis(CFDA). The theory of CFDA [42, 43] is described detail in next section. The main idea of using CFDA is to identify how many distinct centers contribute to the decay measurement.

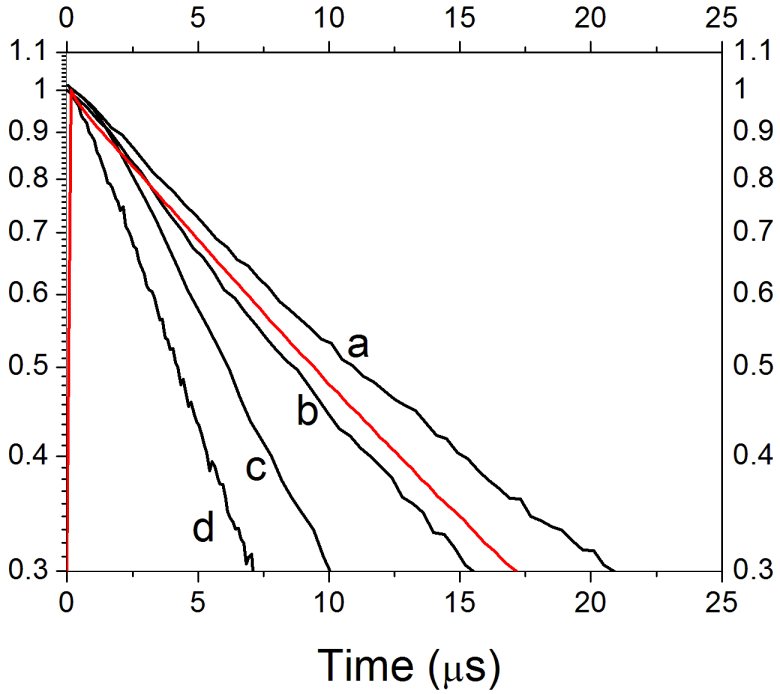

(a) Picture showing the non-single exponential decay in glass ceramics and single exponential decay (straight line) in single crystal (red:cunyite single crystal and black: glass ceramics)

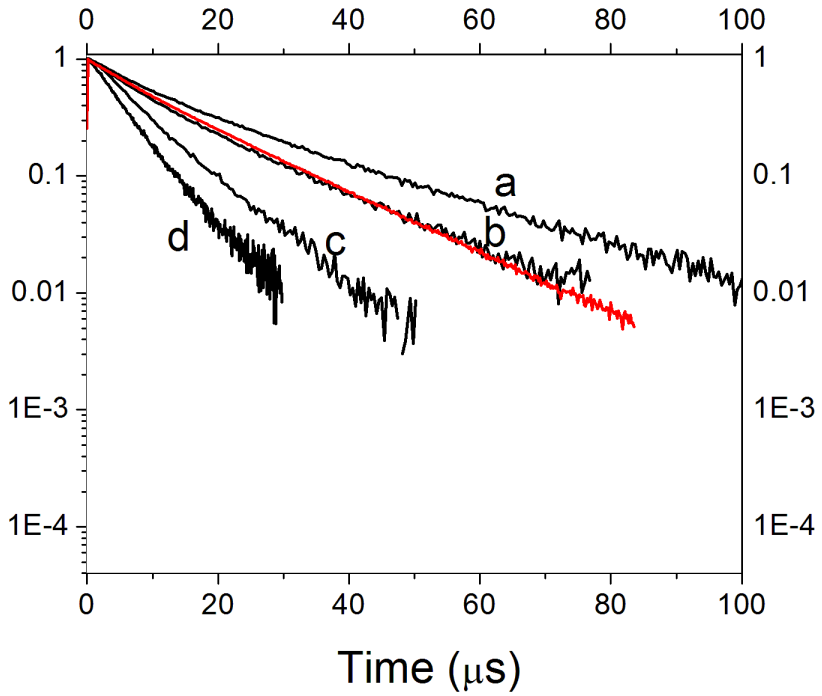

(b) Lifetime in glass ceramics. Black (a:100K, b:180K, c:240K and d:300K). Red line is lifetime of cunyite single crystal measured at 300K

Figure 5.17: Excited state lifetime in glass ceramics

5.2.6.1 Continuous function decay analysis of fluorescence dynamics

The intensity of luminescence from each individual site, i, excited at time t is given by:

$$I_i(t) = \frac{P_i(t)}{\tau_{i,rad}} \tag{5.4}$$

where,

$P_i(t)$**:** probability of finding i^{th} center in the excited state at time t

$\tau_{i,rad}$**:** radiative lifetime of i^{th} center

$P_i(t)$ can be found from the rate equation:

$$\frac{dP_i(t)}{dt} = -\sum_{k\neq i} W_{i\to k}P_i(t) - W_{i\to i}P_i(t) + \sum_{k\neq i} W_{k\to i}P_k(t) - \frac{P_i(t)}{\tau_{i,rad}} \tag{5.5}$$

where,

$W_{i\to k}$**:** nonradiative transfer rate from i^{th} center to k^{th} center

$W_{k\to i}$**:** nonradiative transfer rate from k^{th} center to i^{th} center

$W_{i\to i}$**:** intracenter nonradiative transfer rate

If the emission and absorption bands are not overlapped, we can ignore the inter-center nonradiative transfer. Thus Eq. 5.5 becomes

$$\begin{aligned}\frac{dP_i(t)}{dt} &= -W_{i\to i}P_i(t) - \frac{P_i(t)}{\tau_{i,rad}} \\ &= -P_i(t)\left(\frac{1}{\tau_{i,nr}} + \frac{1}{\tau_{i,rad}}\right) \\ &= -\frac{P_i(t)}{\tau_{i,eff}}\end{aligned} \tag{5.6}$$

From Eq. 5.6, the solution of $P_i(t)$ becomes

$$P_i(t) = \mathcal{A}_i \exp(-\frac{t}{\tau_{i,eff}}) \; ; \qquad \mathcal{A}_i = \frac{N_{i_{excited}}}{N_{i_{total}}} \tag{5.7}$$

where,

$N_{i_{excited}}$**:** number of initially excited i^{th} centers characterized by decay time, $\tau_{i,eff}$

$N_{i_{total}}$**:** total number of i^{th} centers in the sample

Thus, $\mathcal{A}_i = \frac{N_{i_{excited}}}{N_{i_{total}}}$ will vary with the excitation wavelength.

By using Eq. 5.7, Eq. 5.4 becomes

$$I_i(t) = \frac{\mathcal{A}_i(\tau_{i,eff})}{\tau_{i,rad}} \exp(-\frac{t}{\tau_{i,eff}}) \tag{5.8}$$

where,

$\mathcal{A}_i(\tau_{i,eff})$: normalized excited i^{th} centers characterized by $\tau_{i,eff}$

In all cases, the starting point for luminescence decay analysis is the assumption that each individual site decays with *single exponential function*. This results in the following relationship between time dependent total luminescence $I(t)$ and site distribution function $\mathcal{A}$.

$$I(t) = \sum_i \frac{\mathcal{A}_i(\tau_{i,eff})}{\tau_{i,rad}} \exp(-\frac{t}{\tau_{i,eff}}) \tag{5.9}$$

The main challenge is to recover $\mathcal{A}_i(\tau_{i,eff})$, the distribution of decay constants, from experimentally measured decay curves.

In glasses and internally disordered crystals, a continuous distribution of local crystal field is expected. Thus the summation in Eq. 5.9 represents a continuous distribution of decay constants. If we assume $\tau = \tau_{i,eff} = \tau_{i,rad}$,

$$\begin{aligned} I(t) &= \int \frac{\mathcal{A}(\tau)}{\tau} \exp(-\frac{t}{\tau}) d\tau \\ &= \int \mathcal{A}(\tau) \exp(-\frac{t}{\tau}) d(ln\tau) \end{aligned} \tag{5.10}$$

Under the assumption that the constant difference $(\tau_i - \tau_{i-1})$ can be replaced by the constant difference $(ln\tau_i - ln\tau_{i-1})$, E.q. 5.9 can be expressed as,

$$I(t) = \sum_i \mathcal{A}_i(ln\tau_i) \exp(-\frac{t}{\tau_i}) \tag{5.11}$$

where, $\tau_i = \tau_{i,eff} = \tau_{i,rad}$

In more general cases, when the radiative decay is not the only process to de-excite the excited centers, the quantities discovered are not the distribution $\mathcal{A}_i$. In this case, E.q. 5.11 becomes

$$I(t) = \sum_i \mathcal{A}_i(ln\tau_i) \frac{\tau_{i,eff}}{\tau_{i,rad}} \exp(-\frac{t}{\tau_i}) \tag{5.12}$$

Thus the required quantities $\mathcal{A}_{i,recovery}$ becomes,

$$\begin{aligned} \mathcal{A}_{i,recovery} &= \mathcal{A}_i \frac{\tau_{i,eff}}{\tau_{i,rad}} \\ &= \mathcal{A}_i \frac{W_{i,rad}}{W_{i,eff}} \end{aligned} \tag{5.13}$$

To recover the distribution of decay constants from the experimentally measured luminescence decays, the non-linear least square fitting has been used, whereby the χ^2 value of the luminescence decay profile was minimized.

$$\chi^2 = \sum_k \left[\frac{I^{theory}(t_k) - I^{exp}(t_k)}{\sigma_k} \right]^2 \tag{5.14}$$

where,

$I^{theory}(t_k)$**:** theoretical decay function given by E.q. 5.11

σ_k**:** the weighting factors defined by $\sigma_k = |I^{exp}(t_k) - I^{exp}(t_{k-1})|$

5.2.6.2 Lifetime Analysis of glass ceramics

By using the above theory, I did decay analysis of temperature dependent lifetime of cunyite glass ceramics. Figure.5.18 shows the decay distribution of Cr^{4+}ions in glass ceramics at different temperature. Here, we don't care about the width of distribution because this is a result of having slightly changes in local environment of Cr^{4+}ions. But We do care about different peaks appeared in distribution function. The different peaks indicates that more than one near-infrared emission center exists in glass ceramics. As shown in fig.5.18, there are two distinct peaks appeared in CFDA analysis of decay measurement at 100K. One peaks has the lifetime of $5\mu s$ while the stronger peak has the lifetime of $20\mu s$. At 140K, the stronger peak is shifted to the left ($15\mu s$) while the weak peak stays in the same position. The same thing applies for the analysis of decay measurement at 180K. These observation tells us that there are two distinct near-infrared emission centers. The lifetime of one center depends on temperature while the lifetime of another center doesn't depend on temperature. This is because the two centers may have the different excited state.

Without thinking any possible emission centers, the possible explanation for having two centers with different lifetimes is illustrated in fig.5.19b.

Spin-allowed transition: If the excited state have the same multiplicity as that of the ground state, the excited state geometry changes in order to reduce the overall system energy. Accordingly the coupling between the electronic and vibrational transition is strong and there is crossing between the potential energy surface of excited and ground state. Since there is a crossing between the two states, the excited energy can decay non-radiatively through this crossing point. As the temperature is getting higher and higher, the available vibration quantum number is also higher. Because of this reason, the possibility of non-radiative relaxation through tunneling is getting higher and consequently the lifetime of excite state is shorter with higher surrounding temperature.

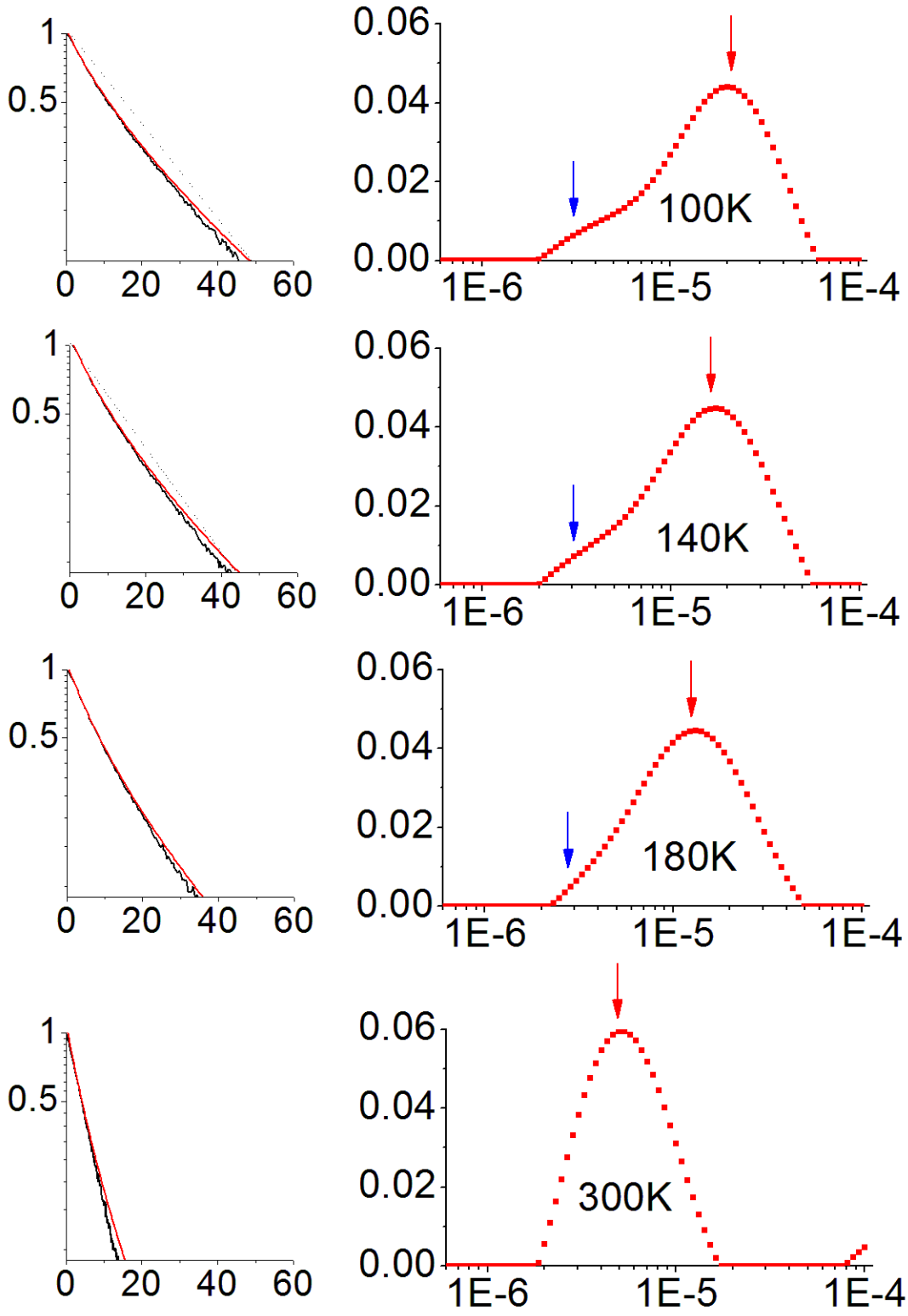

Figure 5.18: Continuous function decay analysis of excited state lifetime

Spin-flip transition: If the ground and excited state have different multiplicity, their geometry is about the same and accordingly their equilibrium position is the same and there is no crossing between the states. Since the geometry of the two states is the same, any available thermal vibrations doesn't help to change back to the ground state geometry. Because of this reason, the lifetime of excited state doesn't depend on temperature.

By consulting Sugano-Tanabe diagram of d^2 ion in tetrahedral coordination, the excited state of Cr^{4+}ions can be $^3A_2$ or ^1E depending on the crystal field strength. According to the above discussion, the excited state of emission center with temperature dependent lifetime can be $^3A_2$ while the excited state of active center with temperature-independent lifetime can be ^1E. We can all agree that the excited state of active center of strong peak is $^3A_2$. But in Cr^{4+}activated single crystals, ^1E level is never observed experimentally. Only split-flip $^1A_1$ is observed in visible range and this is not a metastable level in Cr^{4+}ions in weak field crystal.

Another possible explanation can be the the near-infrared emission center with temperature-independent lifetime can be Cr^{3+}ions in distorted octahedral site. Since active center of other olivine crystals (LIGO, LISO) is Cr^{3+}ions, it could be that Cr^{3+}ions in distorted site contribute to the decay curve measurement if there is a small trace of Cr^{3+}near-infrared emission center in glass ceramics. The first excited state of Cr^{3+}will be ^2E and its lifetime doesn't not depend on temperature. But the energy of ^2E state is in visible range and it doesn't change with the local symmetry. This fact can rule out the possibility of having Cr^{3+}near-infrared emission center.

One good explanation can be that if Cr^{4+}ions interacts with the strong field, the excited state can be $^1A_1$ spin-flip state if we can forget about ^1E level. The energy level arrangement of Cr^{4+}ions in strong field is $^3A_2 < {}^1E < {}^1A_1 < {}^3T_1 < {}^3T_2$. Please refer to the correlation figure of d^2 configuration in theory section. Since we do observe $^1A_1$ state experimentally in weak field crystal, the excited state of emission

center of weak peak in lifetime distribution function could be $^1A_1$. One flaw in this explanation is that all known Cr^{4+}activated crystals are all weak field crystals. The impurity ion is another candidate to explain the emission center with temperature independent lifetime.

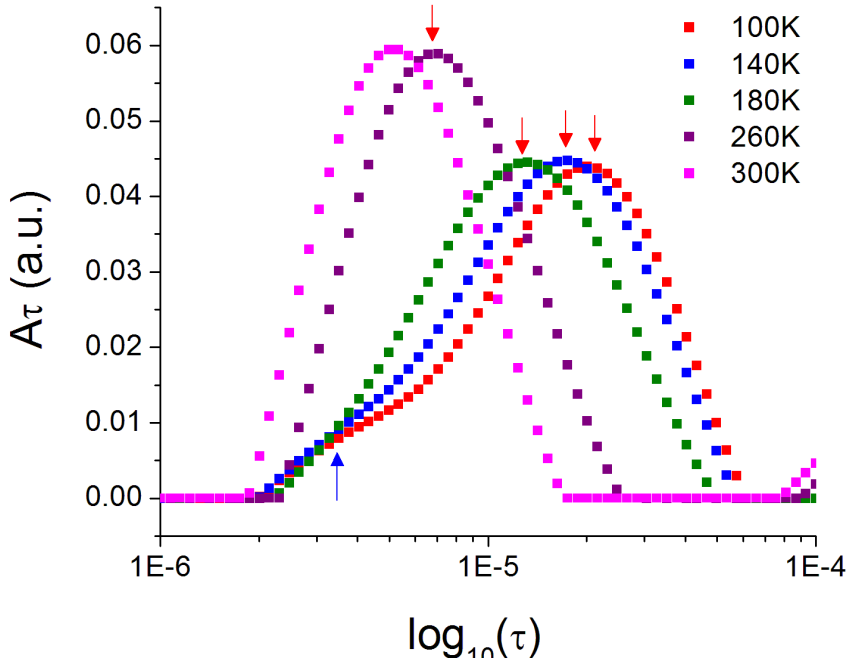

(a) Decay distribution Vs. logarithmic lifetime

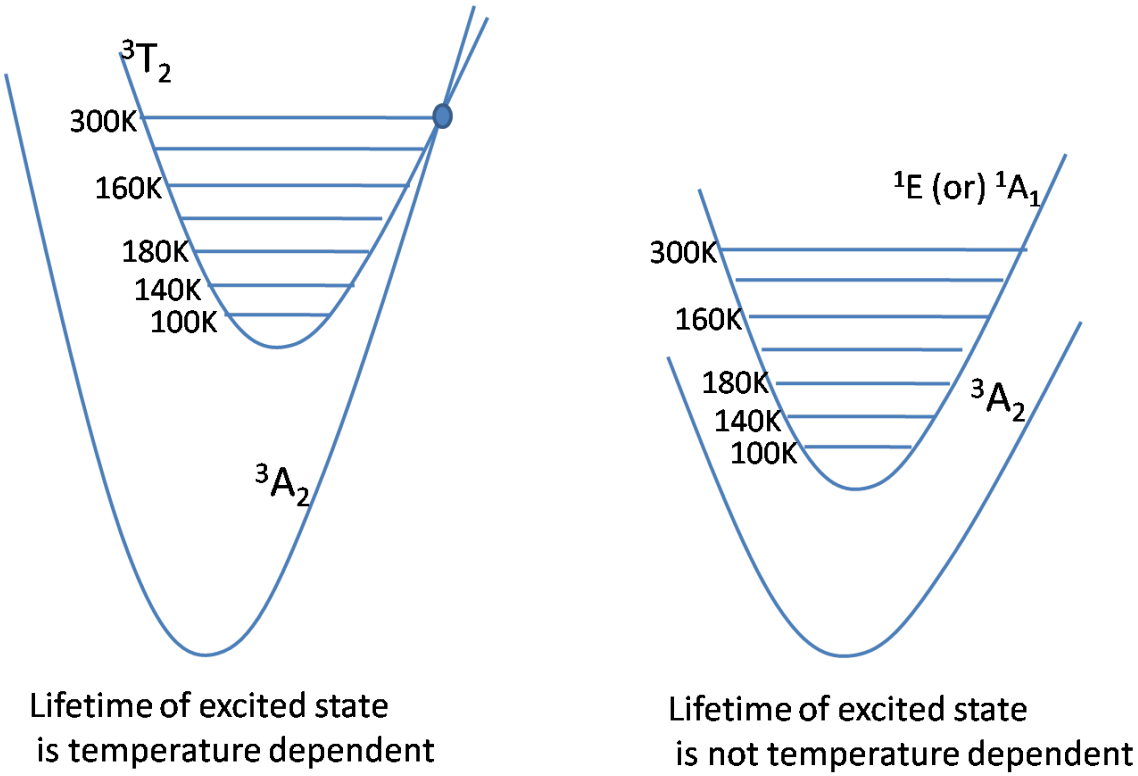

(b) Energy-level illustration of temperature-dependent and temperature-independent lifetime

Figure 5.19: Temperature dependent excited state lifetime in glass ceramics

5.2.7 Phase separation mechanism of glass

Understanding the phase separation mechanism in glass is very important in glass preparation. Although the glass doesn't have the long range order, it did have the short range order. Like the immiscibility presents in the water-oil mixture, the various components of a molten glass mixture (in germanate glass composition: B_2O_3 - CaO - GeO_2 - Li_2O - Al_2O_3 - Cr_2O_3) may display liquid-liquid immiscibility during cooling; that is, the component may separate into two or more disordered glassy phases that eventually are quenched in as glass inside glass when the substance becomes rigid. There are two kinds of phase separation can be exist in glass; the nucleated droplet phase separation and the spinodal phase separation.

The flow chart as shown in Fig. 5.20 shows the process of new phase formation in glass ceramics. Depending on the glass composition and melting temperature, different kinds of liquid phase separation mechanism occur. In each phase separation mechanism, the two phases with different compositions are formed during melting. When the melt is quenched into the hot steel plate, these two phases separate into two glassy phases. The composition difference between the two phases may be small or may be sharp. If the two phases have small composition difference, spinodal decomposition occurs in the "as-quenched" glass. On the other hand, if one composition is sharply different from the other one, droplets of one composition are formed in another composition matrix (see Fig. 5.21).

When the "as-quenched" glass are heated at or just above the glass transformation temperature, the nuclei are formed in the glass having the nucleated droplet decomposition while the nuclei formation rarely occurs in the glass with the spinodal decomposition. Since the main project of this research is to grow the nano-crystallites with CUNYite(Cr^{4+}:Ca_2GeO_4) single crystal phase, homogeneous nuclei formation is highly desired in growing CUNYite glass ceramics.

Fig. 5.21 shows the difference between the microstructure of the glass samples

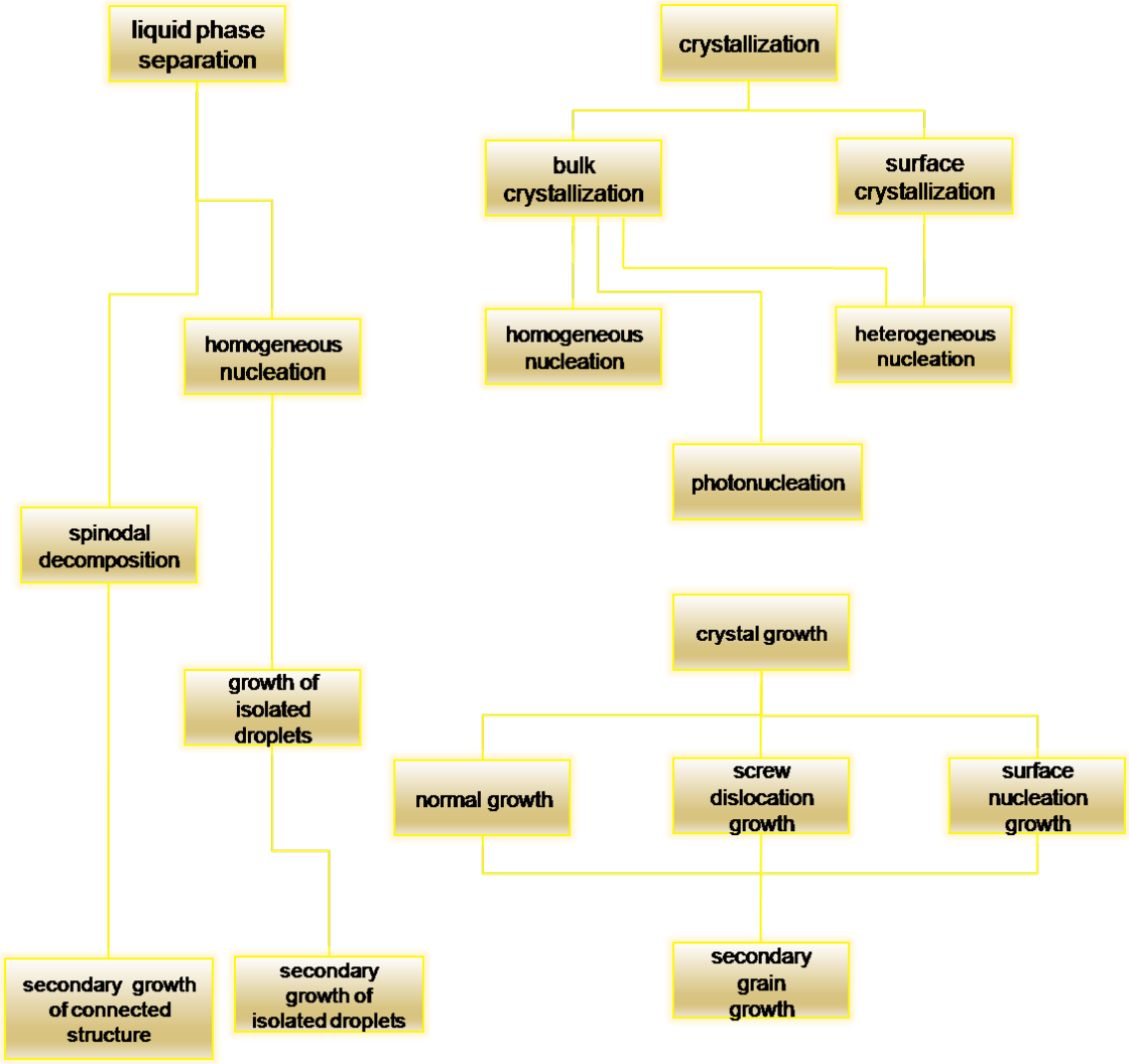

Figure 5.20: Flow chart showing the synthesizing process of glass ceramics [15]

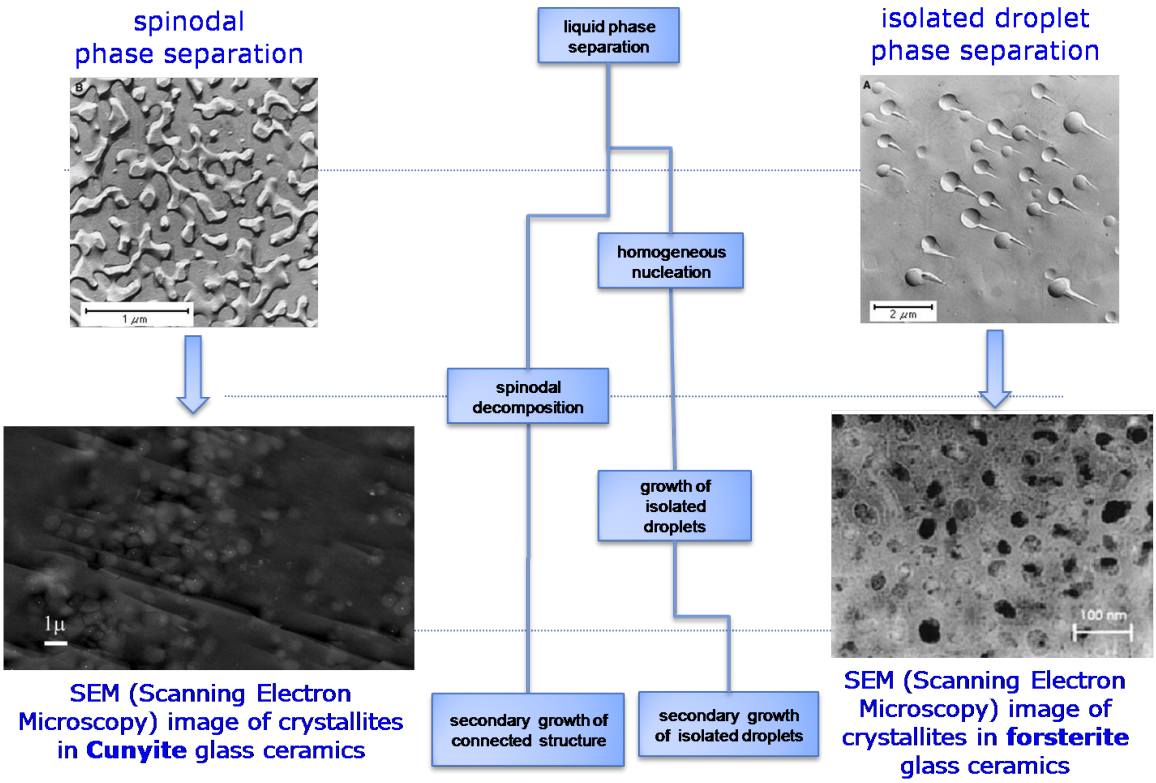

Figure 5.21: phase separation mechanisms

with the nucleated phase separation and with the spinodal phase separation. In the nucleated phase separation, the composition changes from one phase to another is a step-like manner; very sharp changes occur. But in the spinodal phase separation, the composition changes in sine wave like manner; very smooth changes occur. In other words, in spinodal phase separation, there is minor fluctuation in composition.

In synthesizing the host glass of forsterite glass ceramics, TiO_2 is added to the glass mixture as a nucleation agent. Thus the nuclei prestates exist in the "as-quenched" glass. With the help of TiO_2 nucleation agent, probably the intrinsic structure of the glass favors the formation of the nucleated droplet phase separation after cooling the molten glass mixture. With the prestate nuclei in the droplet having composition similar to forsterite structure, it is possible to control the size of nano-crystallites growth inside the glass matrix after the heat treatment.

Fig. 5.21 also shows the microstructure of the forsterite glass ceramics. The quick observation of figure tells us that the crystallites are not cluster; they are homogeneously dispersed through the glass matrix. The size of nano-crystallites is more or less the same (about 20 to 30nm in size).

In contrast to forsterite glass ceramics, the germanate glass ceramics is formed the glass having spinodal decomposition. Using the nucleation agents such as TiO_2 or ZrO_2 doesn't help to form nuclei prestate in germanate glass. Thus not having the nuclei prestate may prevent the nucleated phase separation after cooling the molten glass mixture.

The conclusion on phase separation mechanism cannot be done from conventional methods such as absorption and emission spectroscopies or be observed with high-resolution microscope. Even for TEM images special preparation of samples is needed to see such separation. But with the help of Raman spectroscopy, we can extract some clues about phase separation mechanism in glass ceramics. The Raman spectrum of as-quenched germanate glass and of cunyite single crytal is shown in fig.5.22(a). As

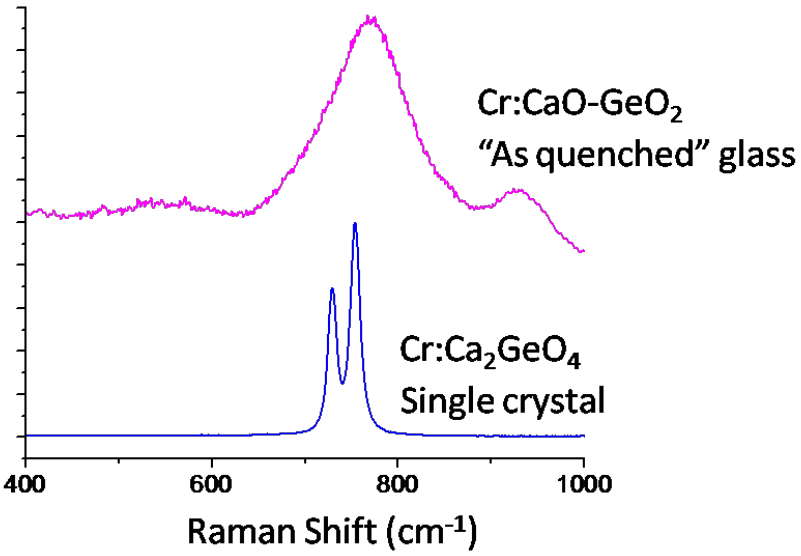

(a) Raman spectra of Cr:CaO-GeO_2 "as quenched" glass and Cr^{4+}:Ca_2GeO_4 single crystal

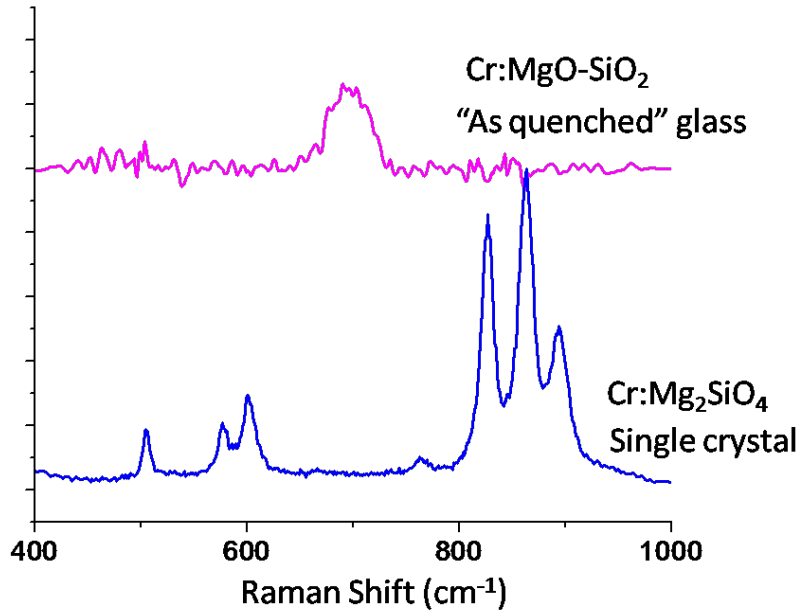

(b) Raman spectra of Cr-doped MgO-SiO_2 "as quenched" glass and Cr^{4+}:Mg_2SiO_4 single crystal

Figure 5.22: Determination of liquid phase separation mechanism using Raman Spectroscopy

shown in fig, the phonon band of glass overlaps with Raman lines of cunyite single crystals indicating that the intrinsic structure of glass similar to that of single crystal because some molecular vibration of the two phases have the same frequency. From this observation, we deduce that the phase separation mechanism of germanate glass ceramics is spinodal phase separation mechanism because of structural similarity of two phases. In contrast to germanate glass, as shown in fig.5.22(b), the phonon band of the silicate as-quenched glass used to synthesize forsterite glass ceramics doesn't overlap with Raman line of forsterite single crystal. This clearly indicates that the intrinsic structure of silicate glass is different from that of forsterite single crystal phase. From this observation, we deduce that the as-quenched silicate glass has nucleated droplet phase separation mechanism because of structural difference between the two phases. This conclusion is supported by SEM image of two glass ceramics, see fig.5.20. The size of nano-crystal of cunyite glass ceramics is $500nm$ because of spinodal phase separation while the size of nano-crystal of forsterite glass ceramics is about $40nm$ because of isolated droplet phase separation. The reason for having larger nano-crystal in cunyite glass ceramics is if the glass have the spinodal phase separation, it is not possible to form the nuclei in the glass matrix. Without nuclei formation, it is very hard to control the size of the nano-crystals with heat treatment.

Chapter 6

Porous glass impregnated with active ion doped nanocrystals

In glass-ceramics, research was performed to grow the Cr^{4+}:Ca_2GeO_4 nano-crystals inside the glass matrix. It was shown that controlling the size of nano-crystals is highly dependent on the phase separation mechanism, the glass composition and the devitrification procedure. It is the foremost importance to obtain the good quality optical material with high transparency. Transparent sample must have the nano-crystals with size of less than the wavelength of visible light. In this research, an attempt was made to grow the nanocrystals with a few lattice parameters in size inside the glass matrix by using the porous glass.

6.1 Porous Glass

Porous glass is sometimes called the reconstructed glass. The trade name by Corning is Thirsty glass. Synthesizing process is similar to that of the glass ceramics. As shown in the Table. 6.1, the main constituents are silicate, boric and alkali oxide, and alumina. These constituents are melted in the crucible and the melt is quenched to form the glass. The resulted akali-borosilicate glass is heated to separate two intermingle-phases. The main phase separation mechanism used to synthesize the porous glass is the spinodal phase separation mechanism. Of the two phases, one

	Composition, wt%			
System	SiO_2	B_2O_3	Na_2O	Al_2O_3
Quaternary	62.7	26.9	6.6	3.5
Ternary	65.0	26.0	9.0	

Table 6.1: Typical compositions for leachable porous alkali-borosilicate glasses [18]

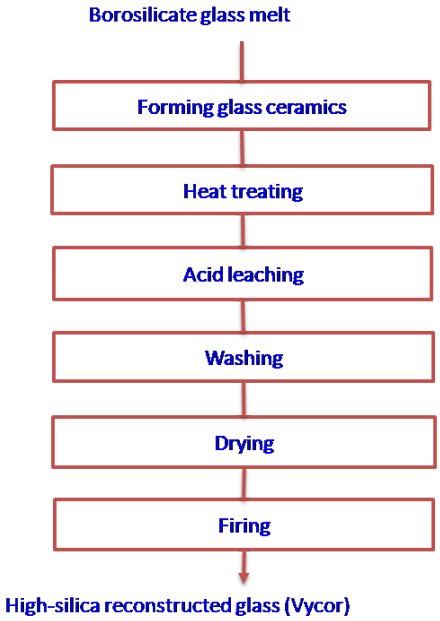

Figure 6.1: Flow chart showing production process for reconstructed glass

phase is rich in silica and insoluble in acid bath while the other phase is rich in alkali and boric oxide and it is soluble in HCl acid bath. A few portion of alumina is added to the composition to prevent the deformation during devitrification. The flow chart showing the production procedure of the porous glass is shown in the figure. 6.1.

Porous glass has many desired properties to synthesize as a composite material. Notable properties are

1. It has the pore network of 4nm in diameter with narrow distribution of the diameter.

2. The porous sample is highly transparent since the pore size is much smaller

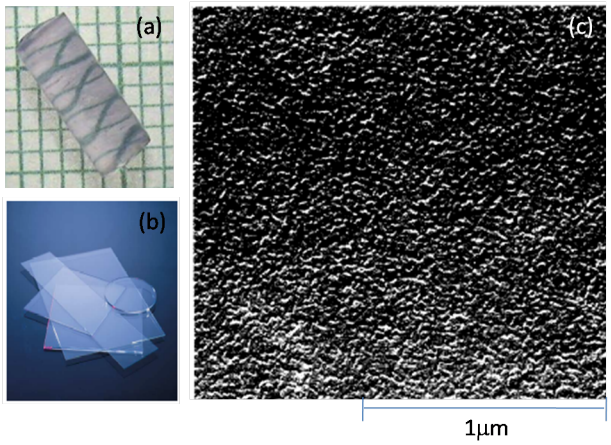

Figure 6.2: (a)Porous glass with impregnated NdOCl nano-crystals (b)Porous disk glass from Corning and (c)Interconnected pore network of the porous glass

than the wavelength of visible light.

3. Pores take up to 30% of total volume.

4. Porous glass are easily manufactured inexpensively.

5. Since its mechanical and optical properties are close to silica, it is possible use the impregnated porous glass in the optical communications.

6. Since it is possible to grow different optical nanocrystals inside the pore network, the optical material with unique properties are able to synthesize by using the porous glass.

Corning offers the porous glass for sale. The porous glass Vycor 7930 from Corning Inc was used in part of this research effort. The pore size distribution is very narrow with about 96% of the pores in the glass being ±0.3nm from the average pore size. **The average pore size of Vycor 7930 is about 4nm (40$\dot{A}$).**

Our goal in using the porous glass is to grow the active ions doped nano-crystals in the nanometer pore network. Consequently it is possible to grow the nano-crystals of lattice-parameter in size since the average pore size is about 4nm. Since using the porous glass as the optical material is a new area in research at this point, there is

no literature backing that the nano-crystals can be grown in the pore network. It is conventionally believe that the optical properties of the doped porous glass comes from the active ions attached to the pore wall or active ions diffused in the glass matrix. Our first task in using the porous glass is to determine whether the nano-crystals can be grown inside the pore network. There are two main tasks we need to accomplish in this part of the research:

1. The sample must be transparent in the visible and near-infrared region. We have to find the mechanism to synthesize the transparent sample

2. There is no proof that the nano-crystals can be grown inside 4nm pore size. We have to find a way to proof that it is possible to grow the nano-crystals of lattice parameter in size.

The porous glass from Corning is know as the thirsty glass. If you leave the porous glass in the air, it absorbs the moisture from the surrounding air. Because of this property, the porous glasses are used moisture absorber in some application. If the crystal grown in the pore netwrok is highly hydroscopic, the optical properties of nano-crystals can be changed dramatically by surrounding water vapor in the pore network. Thus special care has to be taken after synthesizing the impregnated porous glass with self-activated crystals. I'll show changes in the optical properties in the impregnated porous glass in the latter section because of thirstiness of the porous glass.

6.2 Mechanism to grow the transparent sample

During the study on the synthesizing process of the porous glass with salt solution, we have found out that the porous sample becomes more transparent when the sample is impregnated in the water solution. The reason the wet sample is more transparent

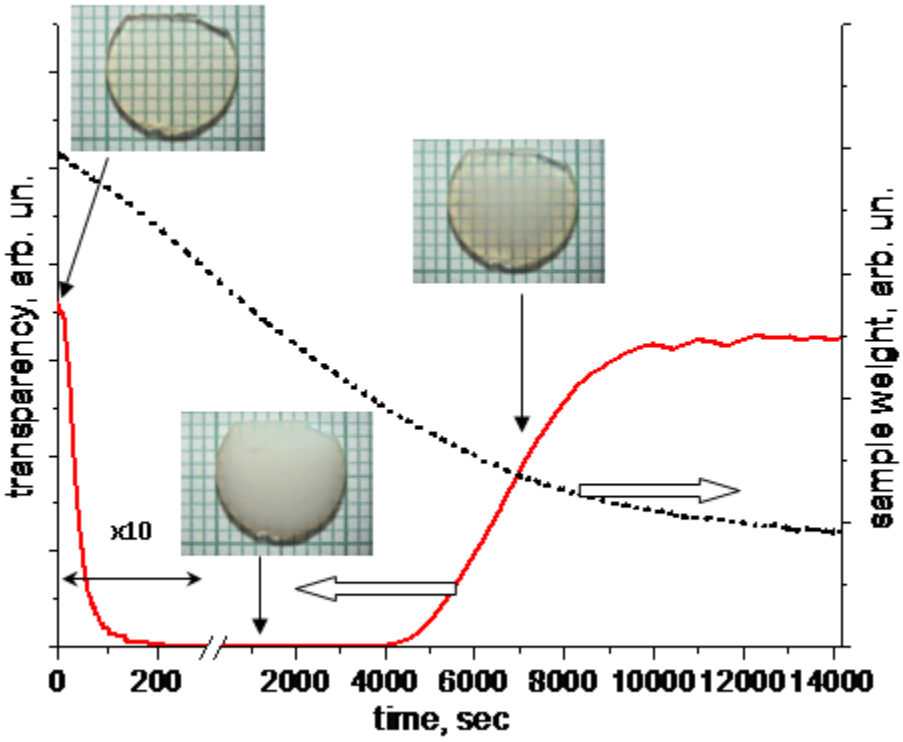

Figure 6.3: Transparency (red) and weight-loss (black) curves of the impregnated porous sample

than the dry sample is the refractive index between the glass and the water is closer than between the glass and the air. If the impregnated sample is left in air to dry for a few minute, the sample becomes opaque and it looks like the white ceramics. When the sample is dry completely, the sample becomes transparent gain. This process is highly reproducible and shown in the figure. 6.3.

Because of the reproducible nature of this process, the pore network is not altered because of impregnation. The question now is why the sample is opaque during the drying process. This process can be explained as follows. In the porous glass, the pore size is 4nm and the pores are interconnected to each other to form the capillary tube like nature. The air and moisture are stored in the pore network because of the

capillary force. When the sample impregnated inside the water bath, because of the capillary sucking force, the water comes in the pore network through the surface and the two facets if the sample shape is cylindrical. The air inside the pore network are trapped in the network and completely dissolved in the network in the form of air bubble.

When the sample is left to dry in the air, the air bubble has a chance to grow and has the positive pushing force because of evaporation of water. Since the pore network is interconnected, the air bubble has a chance to grow near the wavelength of the visible light. Consequently, Mie scattering kicks in and the sample becomes opaque. When the sample becomes dry, the bubbles burst and the air fills the pore network and the sample is transparent again.

According to the above explanation, the air inside the pore network may become the problem in getting the transparent sample. With this process in mind, the sample is vacuumed for about 4hr to evacuate the air from the pore network. After evacuating the air from the pore network, the solution is injected into the evacuated housing where the sample resides. With this mechanism, we can avoid the air bubble formation in the pore network. As shown in the figure.6.2(a), the NdOCl nano-crystals doped porous sample is highly transparent.

6.3 Using Nd^{3+}ions as the probe

Our goal in using the porous glass is to synthesize the wide-array of composite materials with unique properties of their own by using array of optically active ions such as rare-earth and transition metal ions. Our main goal is we want to grow Cr^{3+}or Cr^{4+}activated nanocrystals inside the porous network. Since Cr is very sensitive to the local environment, it must reside in the known phase to retain its good optical properties. But research on the active ions doped porous glass to be used as the

optical materials is relatively new. Our experience tells us that it is very hard to grow the desired crystal phase inside 4nm pore network because there is no literature addressing that even the crystal phase can be grown inside the 4nm size. For example, the long axis of unit cell of Ca_2GeO_4 crystal is about 1 nanometer. Inside the pore network, there is a place to grow only 4 unit cells or 4 monolayer crystal. There is no literature directly addressing that the optical properties of the impregnated porous glass comes from the crystal phase. There is a strong belief that if the active ions are doped into the porous glass, the optical properties of doped glass comes from the individual ions attached to the pore network, not from the crystal phase. Because of this reason, we cannot use Cr doped crystal in the first phase of the research. We need to address the following question if we want to use the porous glass as a glass composite material. The question is "Can we synthesize the nanocrystals with a few lattice parameter in size in the porous network? If so, the optical properties of impregnated porous glass comes from which active ions; from the ion localized in crystal phase or from the individual ion attached to the pore network?"

To try to answer the above research questions, we synthesized the porous glass with so-called self-activated salt crystals in order to utilize the 100% concentration of active ions. Please notice that there is no active ion doping required. Crystal itself is self-activated. Among the known array of ions, we choose Nd^{3+}ions as the ions of choice to test the possibility of growing the nanocrystals inside the pore network. The main reason of choosing this ion are as follows.

1. The absorption and emission line of Nd^{3+}ions is well known and easily detectable.

2. By using the so-called self-activated Nd cystals, we can probe the size effect of nano-crystals by monitoring the decay process of the excited Nd^{3+}ions. Crystals have strong quenching of fluorescence.

3. Nd crystals can easily be synthesized at low temperature from salt solution.

4. Optical properties of such crystals can vary in a wide range in dependence on crystal composition.

6.4 Synthesizing process of porous glass

The first try we make is to grow the NdOCl nano-crystals inside the pore network. To synthesize the NdOCl nanocrystals, the $NdCl_3$ powder is diluted in water solution and heated on the oven and stirred about a few hours. The resulted solution is collidal and a few drop of HCl acid is added to the solution to become transparent. The solution is heated until the purple crystals are formed inside the solution. The crystallized deposit gives the indication that the solution is highly concentrated. By using these crystals, we will play the crystal concentration impregnated in the pore network.

The 5 or 6 mm length of porous sample is placed in the plastic cylindrical container having the size of 1cm in diameter. This plastic container is connected to the vacuumed tube and the air is evacuated for about 4 hrs. After the porous sample is vacuumed, the salt solution is injected into the plastic container and let the porous sucks the salt solution and wait about 15 to 20 minutes before taking out the porous sample from the salt solution. In the meantime, the furnace is preheated at 50 ^{o}C .

Right after impregnation of the porous glass, the porous glass and a few drops of salt solution are placed on the platinum plate to begin the heat treatment procedure. Heat treatment procedure is as shown in the figure.6.4. The maximum heating temperature is kept below 1000 ^{o}C , at which temperture the glass soften and the deformation will occur.

Addition to NdOCl crystal, we tried to grow the different crystal structure by using the above synthesizing process. It is well known that the optical properties of

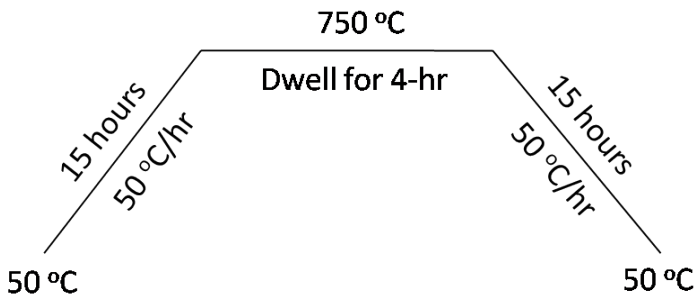

Figure 6.4: Heating procedure for impregnated porous glass

Nd^{3+}ions are not strongly effected by changing the surrounding ligands because of shielding effect of 5s and 6s orbitals. But the weak crystal field acting on the Nd^{3+}ions still can change the fine structure of the states already splitted by the spin-orbit coupling. The difference in fine structure can differentiate the crystal structure where Nd^{3+}ions resides. By monitoring these fine structure and comparing with the optical properties of the bulk crystal, we can tell that the optical properties of Nd^{3+}ions comes from individual Nd^{3+}ions in pore wall or Nd^{3+}ions in crystal structure.

Because of the above reason, we have tried to grow two more crystal structure inside the pore network. one is Cs-Na-NdOCl crystal and another is NdP_5O_{14} crystal. One question can come out is why we choose these two crystals among others. The reason is as follows.

1. Cs-Na-NdOCl crystal can be grown from the salt solution and transparent sample can be produced. The lifetime of Nd^{3+}ions is slighly longer than NdOCl crystal.

2. Nd^{3+}-doped self-activated crystals are known for high fluorescence quenching with concentration. There are a few self-activated crystals which do not follow the trends. They maintain the long lifetime even though we used 100% Nd concentration. NdP_5O_{14} is one of those crystals. NdP_5O_{14} crytal is very important for our experiment. If we can show that the lifetime of the porous glass impregnated with NdP_5O_{14} crystal is much longer than the one impregnated

with NdOCl crystal, we can make the conclusion that the optical properties are coming from Nd^{3+}ions in crystalline environment, not from individual Nd^{3+}ions attached on or diffused into the glass matrix.

6.5 Spectroscopy of nano-crystalline porous glass

6.5.1 NdOCl crystal phase

Our first intention is to grow $NdCl_3$ crystals inside the pore network. But $NdCl_3$ is not stable in air atmoshpere and instead NdOCl crystals are deposited. This fact is confirmed by the X-ray reflection spectrum as shown in the figure. 6.5. X-ray diffraction pattern is obtained by using the powder sample prepared together with the porous glass. Even though we have tried to obtain the X-ray diffraction pattern from ground porous glass, the resulted spectrum is broadband typical for the glass sample.

The synthesized porous glass impregnated with nano-crystals is shown in the figure. 6.2(a). The sample is highly transparent indicating that the grown nano-crystals are smaller than the wavelength of light.

Since the sample is transparent, the absorption spectrum is possible to obtain with the spectophotometer. The resulting spectrum is as shown in the figure. 6.6.

As shown in the figure. 6.6, the absorption line of the impregnated porous glass coincides with the known absorption line of Nd^{3+}ions which clearly indicates that the existent of Nd^{3+}ions inside the porous glass.

The next spectroscopic measurement we did on the porous glass is the fluorescence spectrum of the porous glass. The energy level diagram of Nd^{3+}ions is described in the figure. 6.7. As shown in figure, the metastable level of Nd^{3+}ions is $^4F_{3/2}$. The spin-orbit split ground levels are $^4I_{15-9/2}$. The well-known emission lines are 1.06 μm ($^4F_{3/2} \rightarrow {}^4I_{11/2}$) and 1.33 μm ($^4F_{3/2} \rightarrow {}^4I_{13/2}$). The emission from the transition ($^4F_{3/2}$

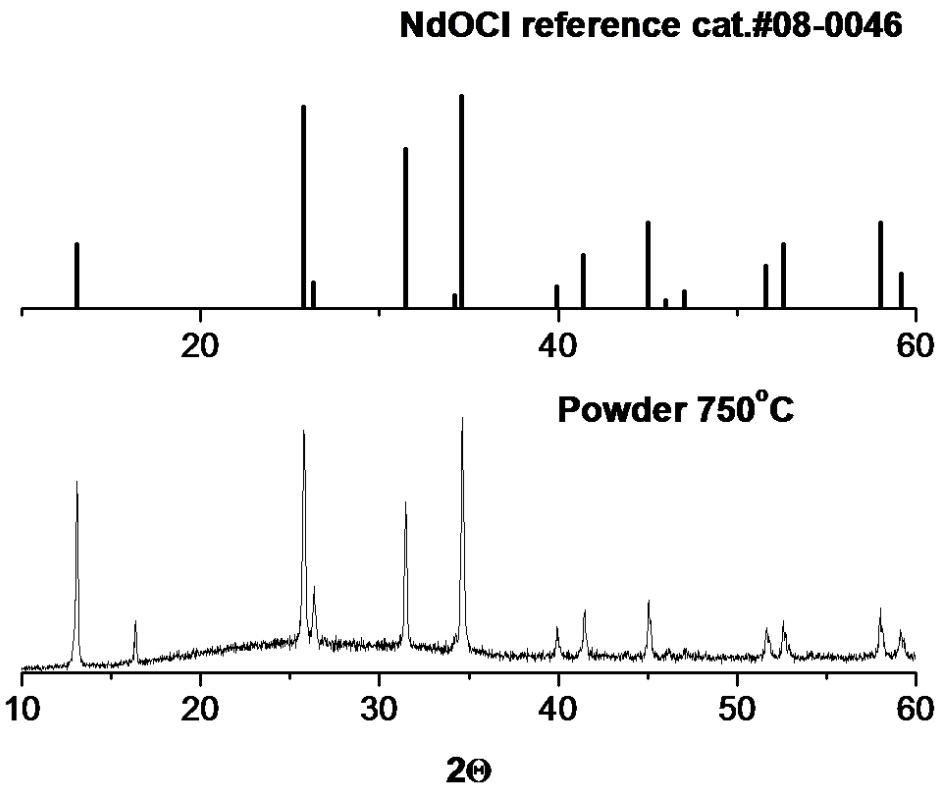

Figure 6.5: X-diffraction pattern of NdOCl crystal from catalog and of NdOCl powder obtained from H_2O solution of $NdCl_3$

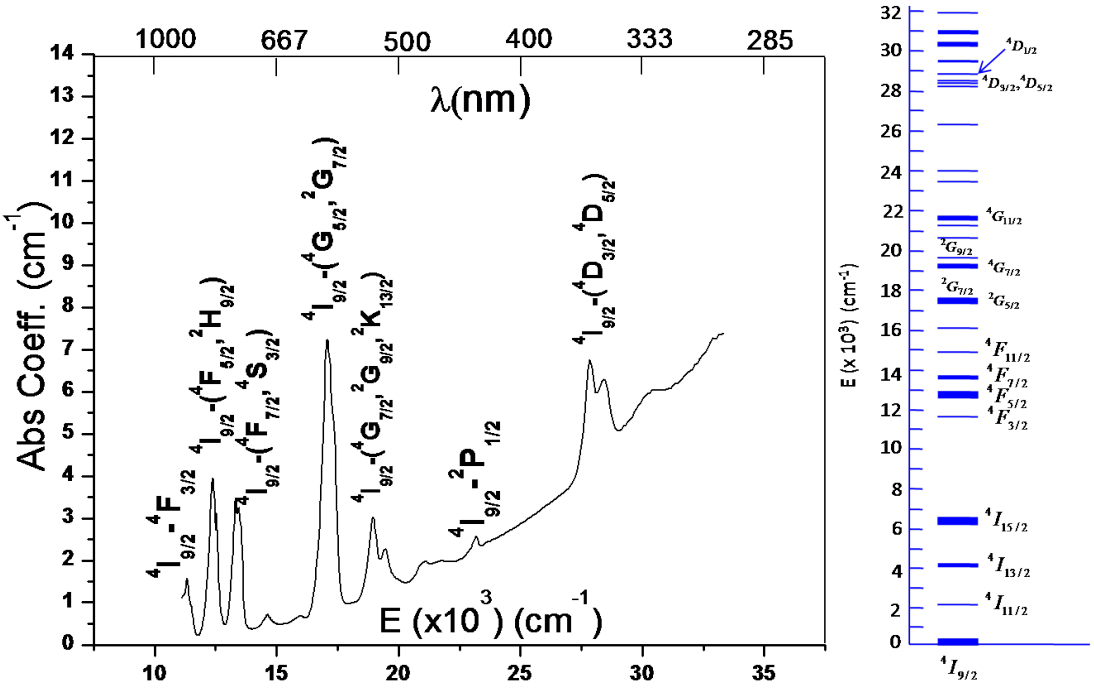

Figure 6.6: The absorption spectrum of NdOCl nanocrystals grown in the pores of Vycor glass (left) and the known Nd absorption lines (right)

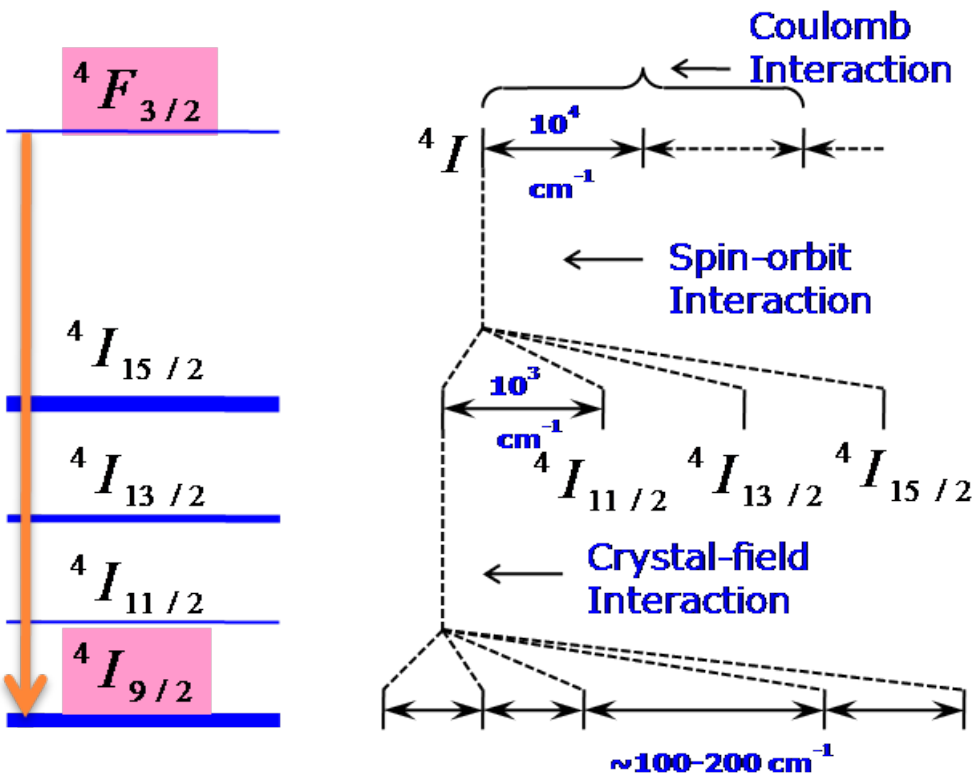

Figure 6.7: Left: First excited state and ground state stark levels of Nd ions. Right: Illustration of crystal field split energy levels

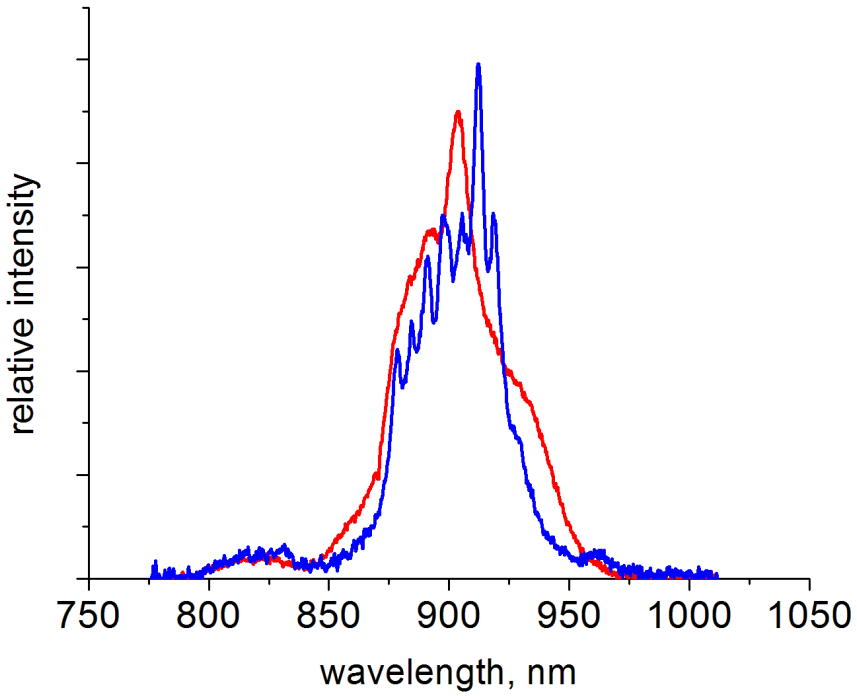

Figure 6.8: The fluorescence spectrum of NdOCl crystals grown in porous glass (smooth structrue) (red) and NdOCl powder (fine structure) (blue)

$\rightarrow {}^4I_{15/2}$) is reabsorbed by the transition (${}^4I_{9/2} \rightarrow {}^4I_{15/2}$) through cross-relaxation process. It is pretty obvious that the emission from the transition (${}^4F_{3/2} \rightarrow {}^4I_{9/2}$) is reabsorbed to ${}^4F_{3/2}$ state through resonant process.

As illustrated in Figure. 6.7, the optical properties of Nd^{3+}ions is weakly effected by the surrounding ligands. Their effect is only visible as the fine structure on the terms splitted by the spin-orbit coupling. Since Nd^{3+}ions in different crystal structure will give the unique fine structure of their own, it doesn't matter which transition we use to monitor the fine structure. We chose to monitor the transition (${}^4F_{3/2} \rightarrow {}^4I_{9/2}$) because we can use the portable Raman spectrum analyzer with the excitation beam of 680nm.

The recorded fluorescence spectrum of impregnated porous glass and powder sample is shown in the figure.6.8. The fluorescence spectrum of powder sample have fine

structure indicating the well-ordered crystalline surrounding while that of the porous glass has the smooth structure. It is well known in the literature that the smooth structure is resulted because of specific size effect. This size effect can be explained as follows.

1. The size of the nano-crystals is in the order of lattice parameters. Compared to the bulk crystal, the nano-crystals have larger surface to volume ions ratio.

2. Compared to the bulk crystal, the optical properties of surface ions is not negligible in mono or double-layer nanocrystals. The measured optical properties is average of the properties of the surface and volume ions.

3. Compared to the ions in bulk crystal which has the very narrow site distribution, the site distribution in the nano-crystals is large.

Because of above three factors, the optical properties are deviated from ions to ions in the assemble. What we're measuring is the averaging of these deviations. That's why the smoothing effects occur in the fluorescence spectrum of the porous glass. As shown in the figure. 6.8 the center of gravity of the two spectra is located more or less at the same position indicating that the same crystal phase in powder and in porous glass.

6.5.2 Decay process of Nd^{3+}ions in NdOCl nanocrystals impregnated in the porous glass

Ti:Sapphire pulse laser with pulse energy of 5mJ is used to excite the porous sample and powder prepared together. Since the crystal in the powder is much larger than the nano-crystals impregnated in the porous glass, we can assume the powder sample as the bulk single crystal. The recorded decay traces are shown in the figure. 6.10. As shown in the figure, the lifetime of Nd^{3+}ions in the bulk crystal is shorter than

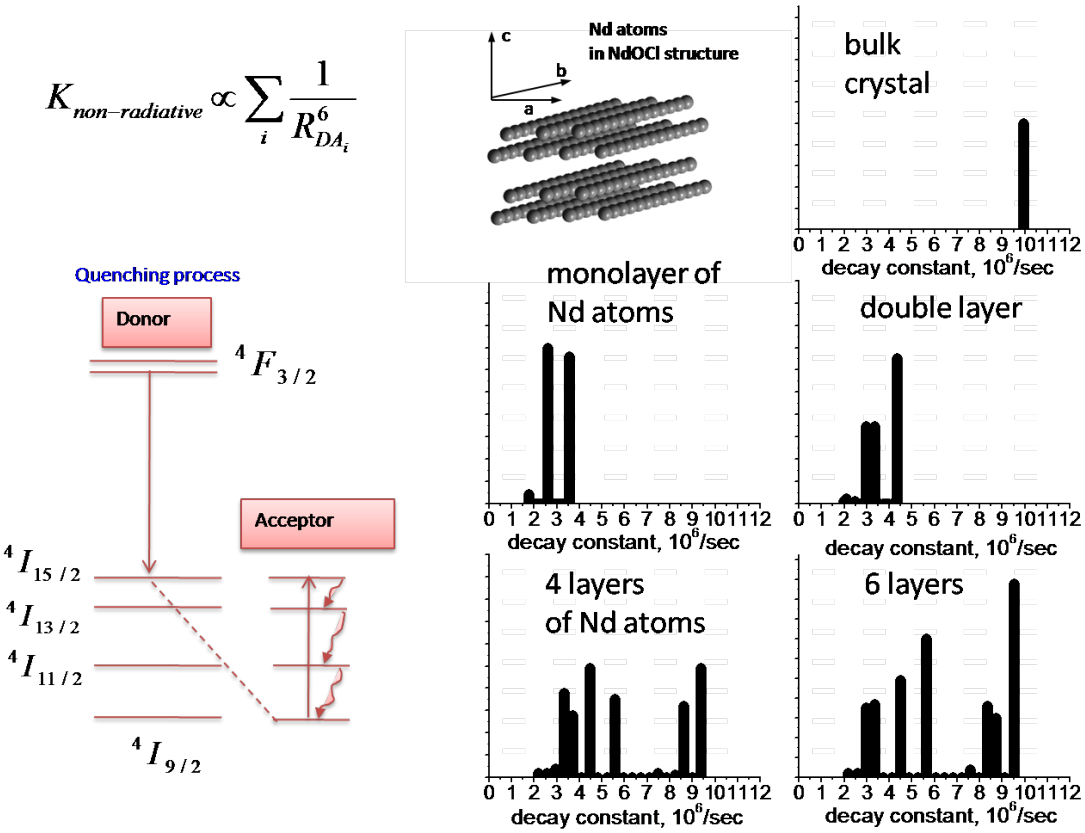

Figure 6.9: Simulation of lifetime distribution of Nd^{3+} ions for monolayer, double-layer, etc. of NdOCl crystal

that of Nd^{3+}ions in nano-crystals. The lifetime of bulk crystal is around 100ns while that of the porous glass is around 250ns. To understand the difference in lifetime between the two samples, we need to examine the non-radiative decay process in the self-activated Nd crystals.

For self-activated bulk crystals, where Nd^{3+}ions separation is short, the decay of fluorescence is single-exponential and can be described by the following equation.

$$I = I(0) \exp\left(-W_{rad}t - W_{quench}t\right) \tag{6.1}$$

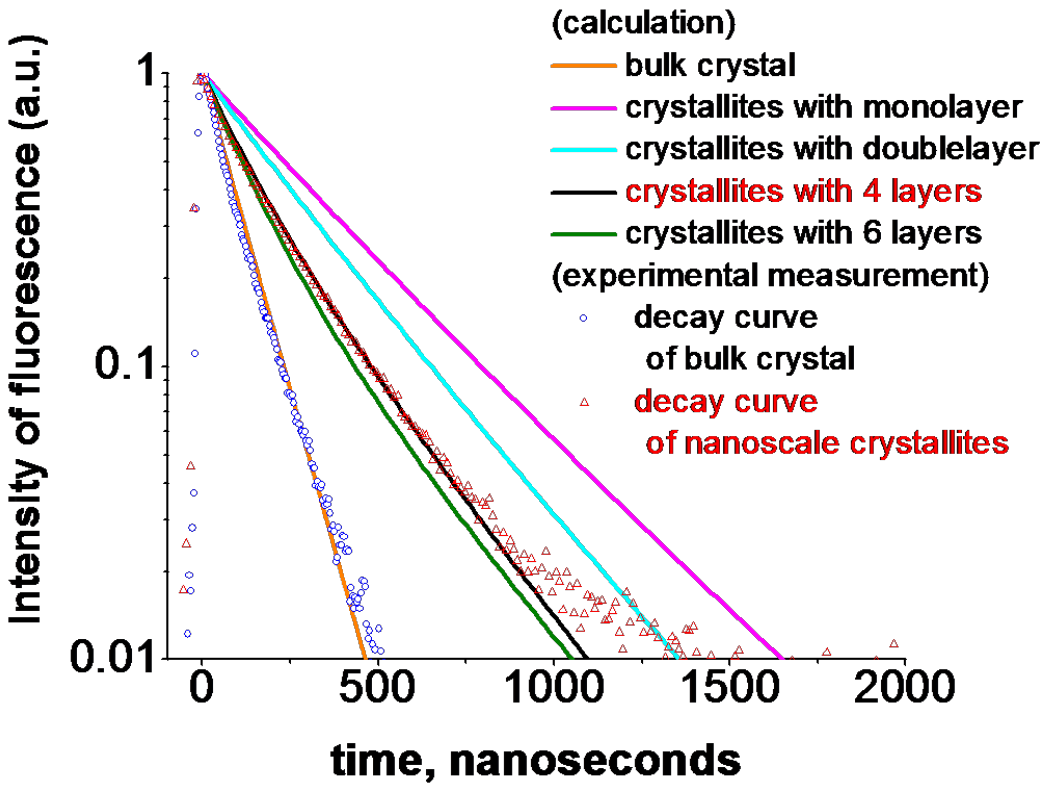

Figure 6.10: calculated and experimental lifetime of Nd^{3+} ions in NdOCl nanocrystals impregnated in the pore network

Where, W_{rad} is radiative rate and W_{quench} is quenching rate.

For the self-activated crystals, the radiative rate is too slow and the above equation is approximated by

$$I = I(0)\exp\left(-W_{quench}t\right) \tag{6.2}$$

The non-radiative process in Nd ions is illustrated in the figure. 6.9. The main loss channel is the cross-relaxation process. The emitted energy from the transition ($^4F_{3/2}$ $\rightarrow$ $^4I_{15/2}$) is resonant with the absorbed energy for the transition($^4I_{9/2} \rightarrow {}^4I_{15/2}$). The excited energy at the state ($^4I_{15/2}$) decays non-radiatively through multiphonon relaxation because the energy difference between spin-orbit split energy states ($^4I_{15-9/2}$) is about 2000 cm^{-1}. If we assume Nd sites are equivalent and the interaction between Nd^{3+}ions is dipole-dipole one, W_{quench} can be approximated by the following equation [44, 45, 46].

$$W_{quench} = K \times \sum_i \frac{1}{R_i^6} \tag{6.3}$$

K**:** a coefficient characterizing the interaction strength.

$\sum_i \frac{1}{R_i^6}$**:** a sum over all lattice sites accessible for Nd atoms.

As described in Eq. 6.3, the more unexcited Nd ions surrounds the excited Nd ions, the higher the concentration quenching rate will be. By using this equation, we can explain the difference in lifetime between the bulk crystals and the nano-crystals as follows.

- The ions in the bulk crystal are mostly volume ions, which means they have more Nd ions surrounding to them. The more Nd ions accessible to the excited ions means that the more chances that the excited ions will decay non-radiatively.

- The pore size in the porous glass 4nm. We can imagine the pore network as the connected long capillary tubes with diameter of 4nm. If we try to grow the nano-crystals inside these tubes, you can visualize that there will be more surface Nd ions in the nano-crystals. More surface ions means less surrounding Nd ions. Accordingly the fluorescence quenching rate will be lower in the nano-crystals.

6.5.3 Estimating the size of nano-crystals grown in the porous glass

There are evidences that the nano-crystals have been grown in the pore network. These evidences are clearly seen in the absorption spectrum, Fig. 6.6, the fluorescence spectrum, Fig. 6.8 and the decay traces, Fig. 6.10. Now the question is what is the size of nano-crystals since the pore size is 4nm? From the literature [47, 48], the longest axis of unit cell in NdOCl crystal is around 1nm, which means that the maximum crystal size it will fit in the pore network is bout 4 atomic layers.

To investigate the size of the nano-crystals, the simulation on the crystal-like model is made by using the fluorescence quenching effect of the self-activated Nd crystals. The main equations used in the calculation is Eq. 6.2 and 6.3.

By using the Matlab, we start building a unit cell with lattice dimension from the literature [47, 48]. Since our porous sample is cylindrical in shape, we start to built the crystal in X-direction by spanning 40 unit cells. Since the pore size in Y-direction and Z-direction is only 4nm, we span the crystal in Y-direction with 4 unit cells. We fixed the crystal dimension in X and Y-axis and we varied the dimension in Z-axis. By using the lattice sum (eq. 6.3), we calculate the decay of fluorescence versus the crystal dimension in Z-axis.

Figure.6.9 shows the histogram of decay rate distribution of Nd^{3+}ions in bulk single crystal, monolayer, doublelayer, 4-layer and 6-layer of NdOCl unit cell in Z-

direction.

As shown in the figure, the non-radiative decay rate of Nd^{3+}ions in bulk crystal is converged to a single value, which means it has the single exponential decay rate. When we looks at the monolayer crystal, the decay rate is much smaller and the decay distribution is larger than the bulk single crystal.

These calculated decay values are plotted in semilog graph as shown in the figure. 6.10. When these semi-log curves are compared with these experimentally measured values for single crystal and nano-crystal in that same figure. The figure clear shows that the calculated decay rate of bulk single crystal perfectly agree with the measured decay rate of the powder sample. The figure also shows the measured decay curve of the porous glass agree with the calculated decay curve of the nano-crystal with the dimension (40 X 4 X 4). From this agreement, we can tentatively draw the conclusion that the crystal size in Z & Y-direction is less than 4nm in size.

6.5.4 Lifetime of Nd^{3+}ions in porous glass

It is understandable that some individual ions are not participate in crystallization and they attach to the pore walls and they can diffuse to the glass matrix. For these Nd atom or ions, the separation between Nd atoms is quite large and accordingly the concentration quenching is lower than Nd^{3+}ions in the nano-crystals.

It is conventionally believed that if you tried to dope Nd ions in the porous glass, the optical properties are primary coming from the individual ions attached to the pore wall and diffused to the glass matrix. We would like to show that the optical properties comes from Nd ions in the crystalline surrounding. To test the above hypothesis, we prepare three $NdCl_3$ solution with different Nd ions concentration and measure the decay constant from the three porous samples.

From figure. 6.11, there are two decay constants representing the two centers. One center has the lifetime of ns while the other one has the lifetime of μs. The

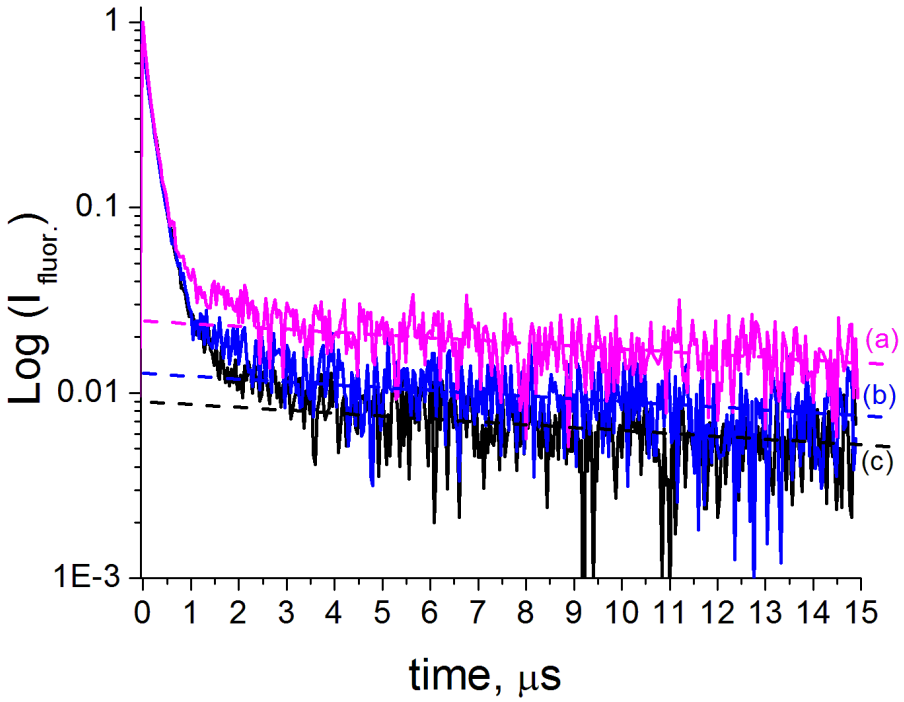

Figure 6.11: Lifetime of NdOCl crystals grown in porous glass Vs. Concentration of $NdCl_3$ impregnated solution. (a)1 mol/l (b)2 mol/l (c)4 mol/l

fluorescence intensity of the center with short lifetime is 99% of total intensity while the center with long lifetime has only 1%. This number tells us that most of Nd ions are in crystalline surrounding while only 1% of total ions are individual ions attached to the pore walls. The above conclusion is drawn from the fact that because the Nd^{3+}ions in crystalline surrounding have more neighbor than individual Nd ions, the fluorescence quenching is higher than individual Nd ions.

Figure.6.11 also shows that the lifetime doesn't change in the short component of decay curve with the variation of Nd concentration. This give us another proof that the crystallization occurs in the pore network because Nd^{3+}ions in nano-crystals are already quenched by surrounding neighbor in any concentration because of size of nano-crystals. When we look at the long component, the lifetime changes with the Nd concentration. Lower concentration gives longer lifetime while the higher concentration gives shorter lifetime, which means that individual Nd separation is shorter with the higher Nd concentration. This observation agrees well with our expectation and give us a proof that the nano-crystals can be grown in the pore network.

6.5.5 Cs-Na-NdOCl nanocrystal

We synthesized another Nd crystal, namely Cs-Na-NdOCl, inside the pore network in order to prove that the optical properties of the porous glass come from Nd^{3+}ions in the crystalline surrounding. As shown in the figure. 6.12a, the shape of fluorescence spectrum of porous glass follows the shape of the bulk single crystal. This is another indication that most of Nd^{3+}ions are stabilized in the nano-crystals.

Figure. 6.12b shows the decay measurement of porous glass and the powder sample prepared together. As shown in the figure, the lifetime of porous sample is about 500ns while that of the bulk single crystal is 250ns. Compared to the lifetime of NdOCl nanocrystals, the lifetime of Cs-Na-NdOCl nanocrystal is twice longer. As

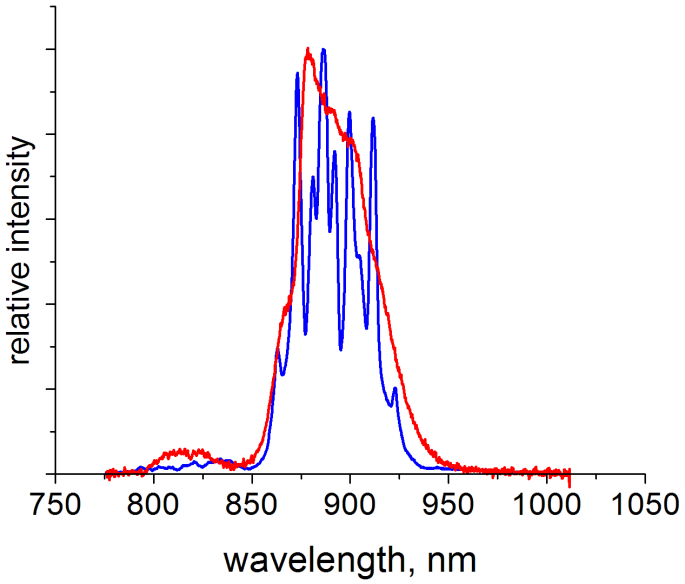

(a) emission spectrum of single crystal (red) and nano-crystals inside pore network (blue)

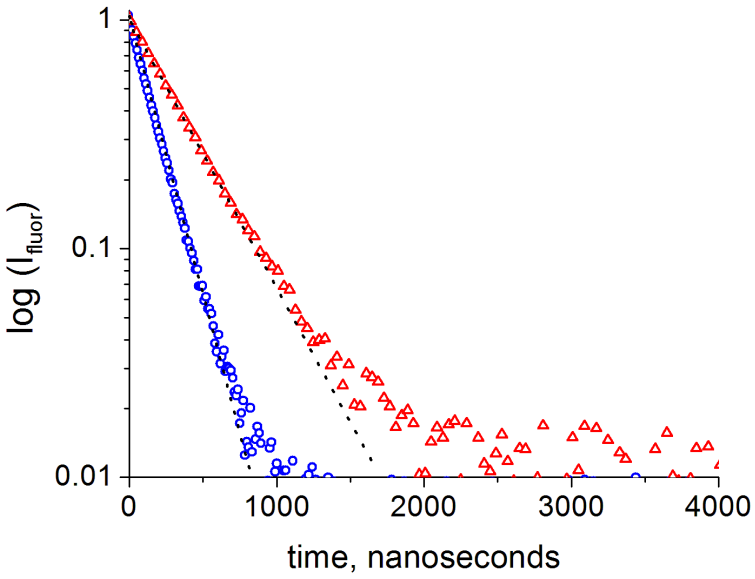

(b) Lifetime measurement of single crystal (red) and nano-crystals inside the pore network

Figure 6.12: Cs-Na-NdOCl nano-crystals impregnated in the pore network

shown in figure.6.10 for NdOCl porous glass & 6.12b for Cs-Na-NdOCl porous glass, the lifetime of porous follows the lifetime trend of bulk single crystal. If the optical properties are determined by isolated Nd ions, the fluorescence quenching should be the same because we kept the Nd concentration about the same. This also is the another indication that the nano-crystals are grown in the pore network.

6.5.6 NdP_5O_{14} nanocrystals

One exceptional self-activated Nd crystal is NdP_5O_{14} crystal. What makes this crystal structure exceptional is that the lifetime of excited Nd^{3+}ions is in the order of μs. If we can show that the long lifetime in the impregnated porous glass, this truly will prove that the optical properties of the porous glass comes from active Nd^{3+}ion centers in crystalline surrounding. Only this type of crystal structure can give the long metastable level lifetime.

Figure. 6.13a shows the emission spectrum of NdP_5O_{14} porous glass and that of the bulk single crystal. The shape of emission of NdP_5O_{14} porous glass also follows the shape of emission of bulk single crystal. In this research we used the three crystal structures NdOCl, Cs-Na-NdOCl and NdP_5O_{14} to test feasibility of crystallization in the pore network. As shown in the figures. 6.8, 6.12a and 6.13a, the three different emission spectra of the respective porous sample follows the shape of the respective bulk single crystal. From these observations, we can draw the conclusion that the optical properties of the porous glass comes from Nd^{3+}ions in the specific crystal structure.

Figure. 6.13b shows the decay measurements of NdP_5O_{14} porous glass and the bulk single crystal. The decay of fluorescence of bulk single crystal is single-exponential and the lifetime of the metastable level is 100 μs. But the decay of NdP_5O_{14} porous glass is non-single exponential and the lifetime composed of short component and long component. The decay of long component is parallel to the decay trace of the bulk

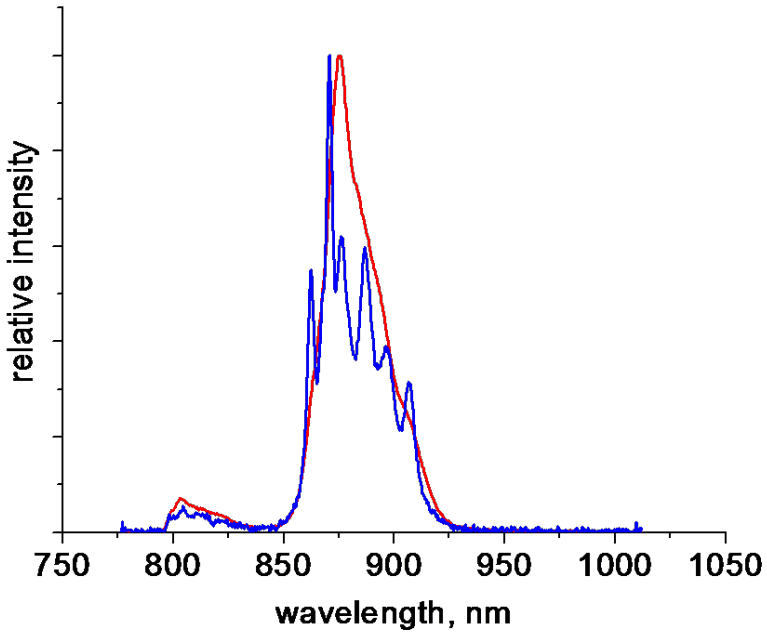

(a) The fluorescence spectrum of NdP_5O_{14} crystals grown in the porous glass (smooth structure)(red) and of NdP_5O_{14} powder (fine structrue)(blue)

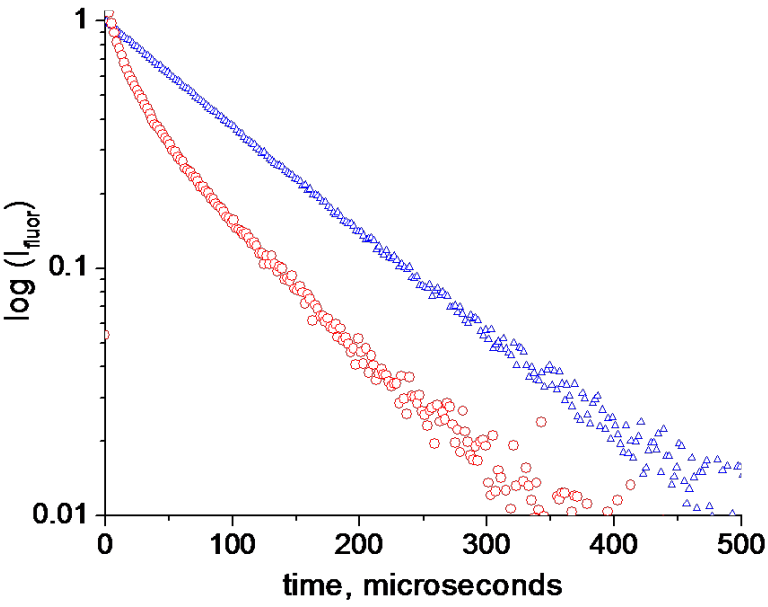

(b) Lifetime of Nd^{3+}ions in NdP_5O_{14}single crystal (blue) and in NdP_5O_{14} nano-crystals impregnated in the pore network (red)

Figure 6.13: NdP_5O_{14} nano-crystals impregnated in the pore network

single crystal. Accordingly its lifetime is 100 μs. The lifetime of short component is 40 μs. This decay trace clearly shows that there are two centers in the porous glass. One center is located in NdP_5O_{14} crystal structure and another one is located in the unknown cryptal phase.

We are not clearly understand having unknown phase together with NdP_5O_{14} crystal phase. Unlike synthesizing of NdOCl and Cs-Na-NdOCl nano-crystals, it is difficult to synthesize NdP_5O_{14} nano-crystals in the porous glass. One problem is NdP_5O_{14} crystal is not soluble in water. It is only soluble in the acid solution. Even though the prepared aqueous solution is transparent, the sample becomes opaque after the heat treatment. To avoid the leaching effect on the pore wall, the sample is heat treated immediately after the solution fills the sample. Since the silica glass is not soluble in the acid solution, we assume that the leaching effect may be minimum if it ever exits. Sample is opaque can means that the crystallites becomes larger than the pore size or the clustering of crystallites occur in the pore network. Unknown phase can also contribute the opacity of the sample. Since the shape of fluorescence spectrum of NdP_5O_{14} porous glass is smooth structure, this is the indication that NdP_5O_{14} crystals has nanometer in dimension based on the conclusion on the other two crystal structures.

Nevertheless, the measured lifetime of NdP_5O_{14} porous glass is clearly departed from the measured lifetime of NdOCl and Cs-Na-NdOCl porous glass (100μs Vs. 100ns). This result alone gives the proof that the nano-crystals can be grown in the pores of 4 nm in dimension. We have given the proofs that the isolated Nd ions contribute minor role in the overall optical properties of the material.

6.6 Water vapor effect and Porous glass sintering

In this research project, the porous glass is impregnated with the $NdCl_3$ aqueous solution and is heated up to 750 ^oC to grow the Nd^{3+}activated crystallites inside the pore network. These crystallite layers are prone to the external disturbance because of thirsty nature of the porous glass. Just after heating the sample, the sample is free of the water molecules. If we left the sample out in the open air, the water vapor crawl inside the free space of the pore network and it somehow affects the optical properties of the activator ions. This effect also shortens the lifetime of the metastable level of excited Nd^{3+}ions.

With aging of the samples, the shape of fluorescence spectrum, the strength of fluorescence emission and the lifetime of the metastable level are changed. These changes are shown in the figure. 6.14. Thus we reasoned that if we heat up the sample to remove the water vapor, we should get the original fluorescence spectrum and decay time. To test this statement, we prepared the fresh sample and measured the fluorescence spectrum and lifetime just after heating the sample. Then we left the sample in the air for one day and measure them to compare with the ones from the fresh sample. After that we reheated the sample at 750 ^oC to see whether we can restore the original spectrum and lifetime that we got from the fresh sample.

From the figure.6.14(a) and 6.14(b), we can clearly see that the original fluorescence shape and decay time are restored under reheating the sample. From these observations, we can see that the water vapor is the main problem to operate these porous glass in open air.

One way to solve this problem is to collapse the pore network in order to eliminate the capillary sucking force. If the porous glass is heated above 800 ^oC , the glass becomes soften, the pore network collapes and the properties of porous glass is close to regular silica glass.

The heating procedure of sintered porous glass is as shown in the figure. 6.15. The

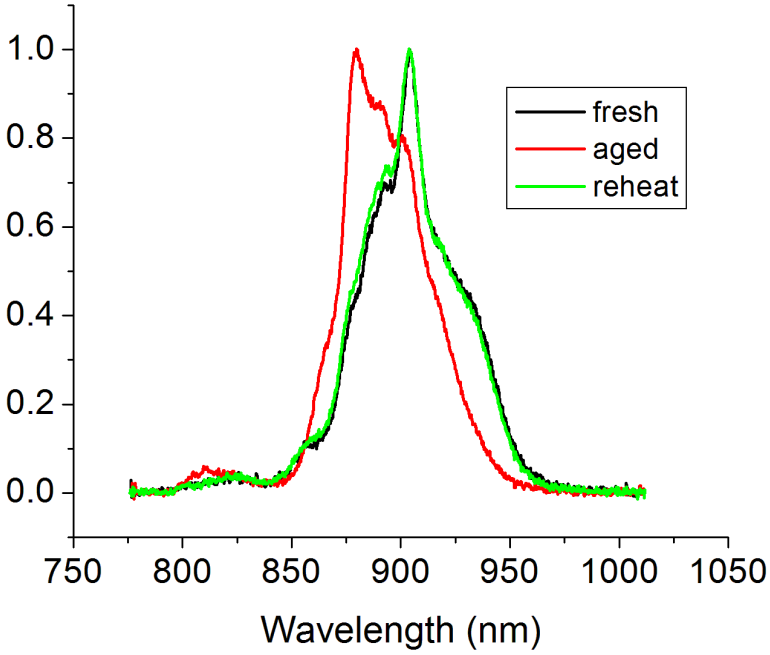

(a) Fluorescence spectrum

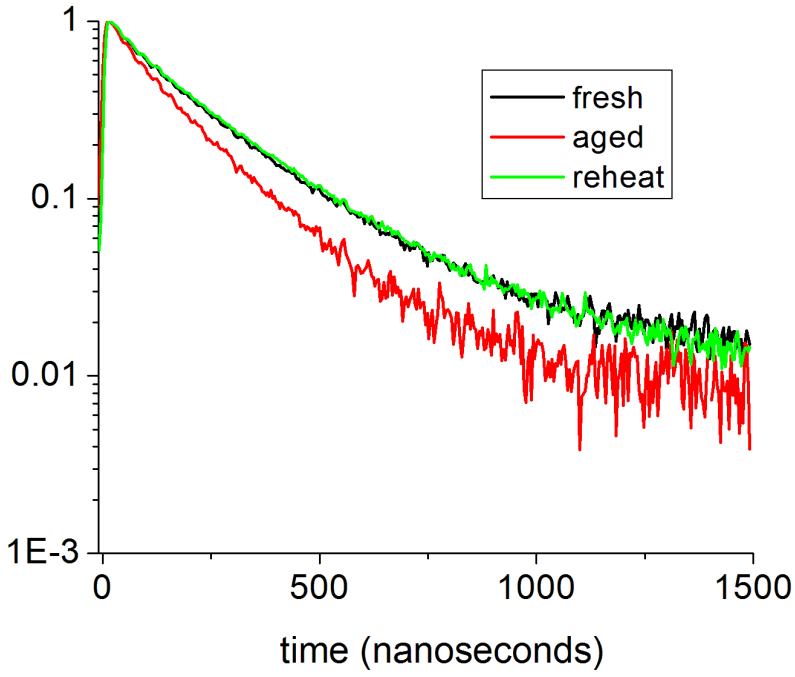

(b) Decay measurement

Figure 6.14: Fluorescence and decay measurement of fresh, aged, reheated impregnated porous sample

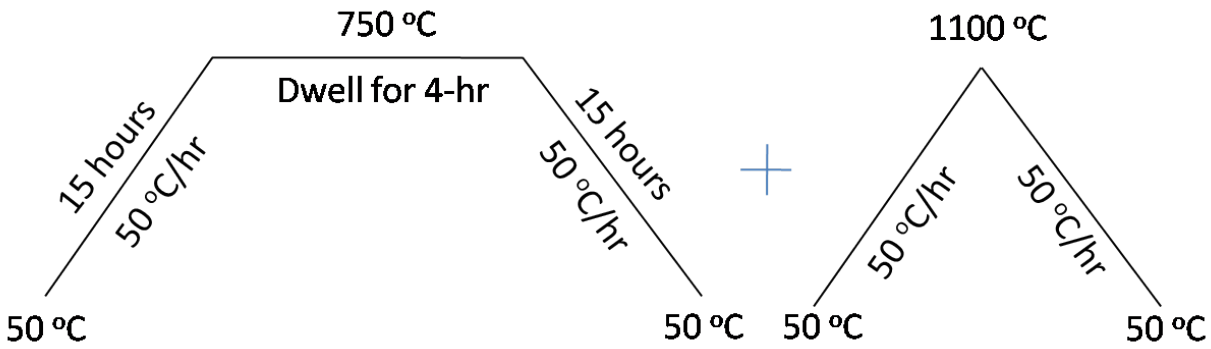

Figure 6.15: Heating procedure for porous glass sintering

optical properties (absorption, fluorescence and lifetime) of unsintered porous glass and sintered porous glass is identical when we compared them except the fact that the sintered porous glass is more transparent than the unsintered one. This is easily understandable that lack of porosity in the sintered porous glass makes the sample more transparent.

6.7 Quantum efficiency of NdP_5O_{14} nanocrystals doped porous glass

In the following section, I tried to calculate the radiative quantum efficiency, the radiative lifetime and the branching ratio of NdP_5O_{14} nanocrystals doped porous glass by using Judd-Ofelt theory. The material design process of rare earth laser host is shown in fig. 6.16. First we have to measure the absorption or reflection spectrum of active ions doped laser crystal, see Fig. 6.17. Using the measured absorption line strength, we can calculate Judd-Ofelt parameters (Ω_t) using a conforming set of reduced matrix elements and Eq.6.6. With the fitted intensity parameters, the spontaneous emission probability of the specific electronic transitions can be calculated using Eq.6.7. By using the spontaneous emission probability, Einstein coefficient "A", we can calculate the radiative lifetime, Eq. 6.8, the quantum efficiency, Eq. 6.9, the branching ratio, Eq. 6.10, and the emission cross-section, Eq. 6.11. If the quantum efficiency is not high enough for the quality laser crystal, we have to change the crystal composition and remeasure the absorption spectrum and recalculate the quantum efficiency for the new sample. This is how we can design the laser glasses in practice.

6.7.1 Judd-Ofelt theory

For the laser crystal activated with Ln^{3+}ions, the intensity parameters Ω_2, Ω_4, and Ω_6 of the Judd-Ofelt theory [45] gives the best fit with the experimentally measured line strength.

Experimental line strength were obtained from absorption spectra using the following equation.

$$S^{ed}_{JJ'} = \frac{\int k(\lambda)d\lambda}{N_0}\frac{3ch(2J+1)}{8\pi^3 e^2 \bar{\lambda}}X \tag{6.4}$$

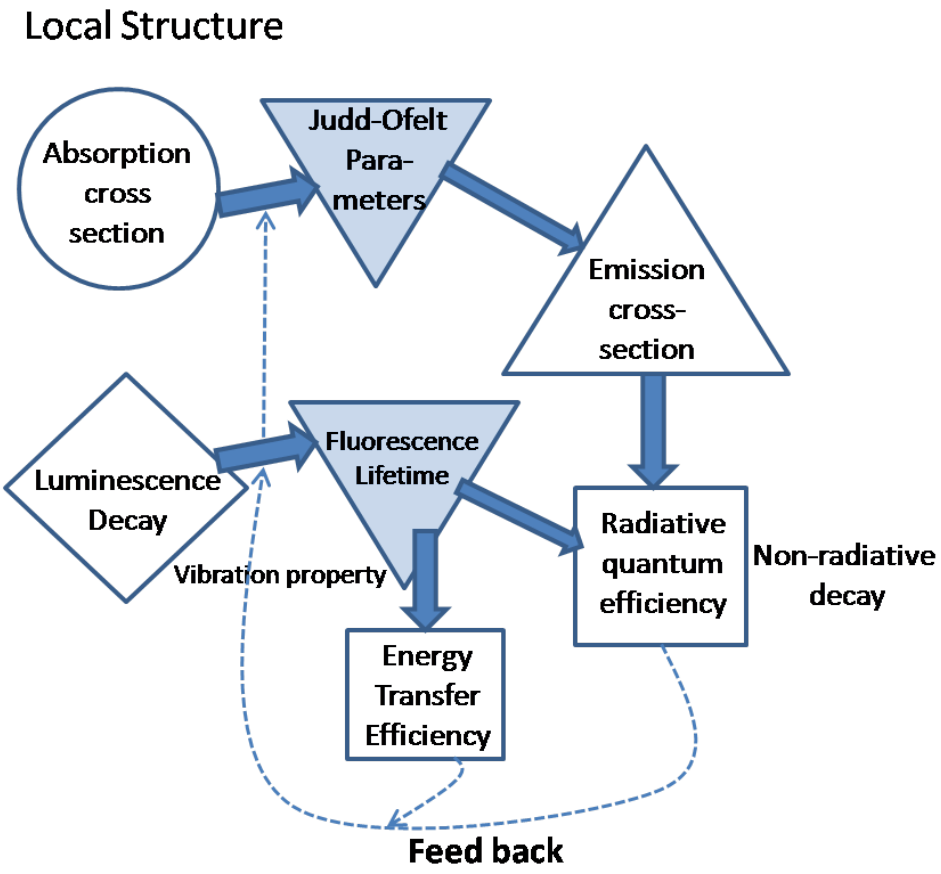

Figure 6.16: Compositional Design of Excellent Laser Host [16]

where,

$\int k(\lambda)d\lambda$ = integrated absorption coefficient

JJ' = intermanifold transition (average of all 3 polarizations)

J = ground state ($^4I_{9/2}$ in Nd^{3+} ions)

$\bar{\lambda}$ = mean wavelength of the transition

c = speed of light

h = Planck's constant

e = electron charge

N_0 = ions concentration

$X = \frac{9\bar{n}}{\bar{n}^2+2^2}$, ($\bar{n}$ = mean refractive index)

The line strength $S^{ed}_{JJ'}$ is related to the intensity parameter Ω_2, Ω_4, and Ω_6 by

$$\vec{S} = \hat{U}\vec{\Omega} \tag{6.5}$$

$\vec{S}$**:** q-dimentional line strength vector (q = # of investigated intermanifold absorption bands)

$\vec{\Omega}$**:** the vector with 3 components that corresponds to intensity parameters Ω_t(Ω_2, Ω_4, and Ω_6)

$\hat{U}$**:** a matrix which represents the conforming set of reduced matrix elements of the tensor operators $U^{(t)}$

From eq 6.5, the following relationship can be derived for Ω:

$$\vec{\Omega} = \left(\hat{U}^T\hat{U}\right)^{-1}\hat{U}^T\vec{S} \tag{6.6}$$

Using the intensity parameters, the spontaneous emission probability of the specific

electronic transitions can be calculated using the following equation

$$A_{JJ'} = \frac{64\pi^4 e^2 n^2}{3h(2J+1)\bar{\lambda}^3} \sum_{t=2,4,6} \Omega_t |\langle 4f^n \alpha[\mathcal{SL}]\mathcal{J} \| U^{(t)} \| 4f^n \alpha'[\mathcal{S'L'}]\mathcal{J'}\rangle|^2 \qquad (6.7)$$

where,

$|\langle 4f^n \alpha[\mathcal{SL}]\mathcal{J} \| U^{(t)} \| 4f^n \alpha'[\mathcal{S'L'}]\mathcal{J'}\rangle|^2$ = Squared-reduced matrix elements for the JJ' transition

$U^{(t)}$ = Unit tensor operator of rank t

J = Lowest excited states ($^4F_{3/2}$ in Nd^{3+} ions)

6.7.2 Spectroscopic parameters

For Nd^{3+} -doped laser materials,

- The *radiative lifetime* of $^4F_{3/2}$ can be calculated from the spontaneous emission probability,

$$\tau_{rad} = \frac{1}{\sum_i A_{^4F_{3/2} \rightarrow {}^4I_{i/2}}} \qquad (6.8)$$

- The *quantum efficiency* (η) can be calculated from the measured fluorescence lifetime and the calculated raditive lifetime as mentioned above.

$$\eta = \frac{\tau_{measured}}{\tau_{rad}} \qquad (6.9)$$

- The *branching ratio* can be calculated by

$$\beta_{^4F_{3/2} \rightarrow {}^4I_{i/2}} = \frac{A_{^4F_{3/2} \rightarrow {}^4I_{i/2}}}{\sum_i A_{^4F_{3/2} \rightarrow {}^4I_{i/2}}} \qquad (6.10)$$

Transitions (from $^4I_{9/2}$)	$E_{JJ'}$ cm^{-1}	$\bar{\lambda}$ (nm)	$[U^{(2)}]^2$	$[U^{(4)}]^2$	$[U^{(6)}]^2$	
$^4F_{5/2}$	12350	810	0.0010	0.2371	0.3972	*
$^2H_{9/2}$	12450	803	0.0092	0.0080	0.1155	
$^4F_{7/2}$	13500	741	0.0010	0.0423	0.4246	*
$^4S_{3/2}$	13500	741	0	0.0027	0.2352	
$^4F_{9/2}$	14650	683	0.0009	0.0092	0.0417	*
$^4G_{5/2}$	17200	581	0.8979	0.4093	0.0359	*
$^2G_{7/2}$	17200	581	0.0757	0.1848	0.0314	
$^2K_{13/2}$	18750	533	0.0069	0.0002	0.0312	*
$^4G_{7/2}$	19000	526	0.0550	0.1571	0.0553	
$^4G_{9/2}$	19450	514	0.0046	0.0609	0.0406	
$^2K_{15/2}$	20900	478	0	0.0052	0.0143	
$^2G_{9/2}$	21050	475	0.0010	0.0148	0.0139	*
$^2D_{3/2}$	21150	473	0	0.0189	0.0002	
$^4G_{11/2}$	21450	466	0	0.0053	0.0080	
$^2P_{1/2}$	23000	435	0	0.0367	0	*
$^4D_{3/2}$	28200	355	0	0.1959	0.0169	*
$^4D_{5/2}$	28350	353	0.0001	0.0567	0.0275	

Table 6.2: Values of reduced matrix elements for the absorption transitions of Nd^{3+} in NdP_5O_{14} nanocrystals in the porous Vycor glass at 300K. "*" indicates the used absorption transition for calculating the intensity parameters.

- The *emission cross-section* can be calculated by

$$\sigma_{^4F_{3/2}\rightarrow{}^4I_{i/2}} = \frac{\lambda_p^4}{8\pi c n_{\lambda_p}^2 \Delta\lambda_{eff}} A_{^4F_{3/2}\rightarrow{}^4I_{i/2}} \tag{6.11}$$

where,

λ_p = wavelength of peak emission

n_{λ_p} = the refractive index at each emission peak wavelength

$\Delta\lambda_{eff} = \frac{\int I(\lambda)d\lambda}{I_{max}}$ = effective line width

6.7.3 Quantum efficiency Calculation

Since NdP_5O_{14} nanocrystals doped porous glass has the quantum efficiency of 86%, Table. 6.6, the nanocrystalline porous glass with NdP_5O_{14} crystal phase can be used

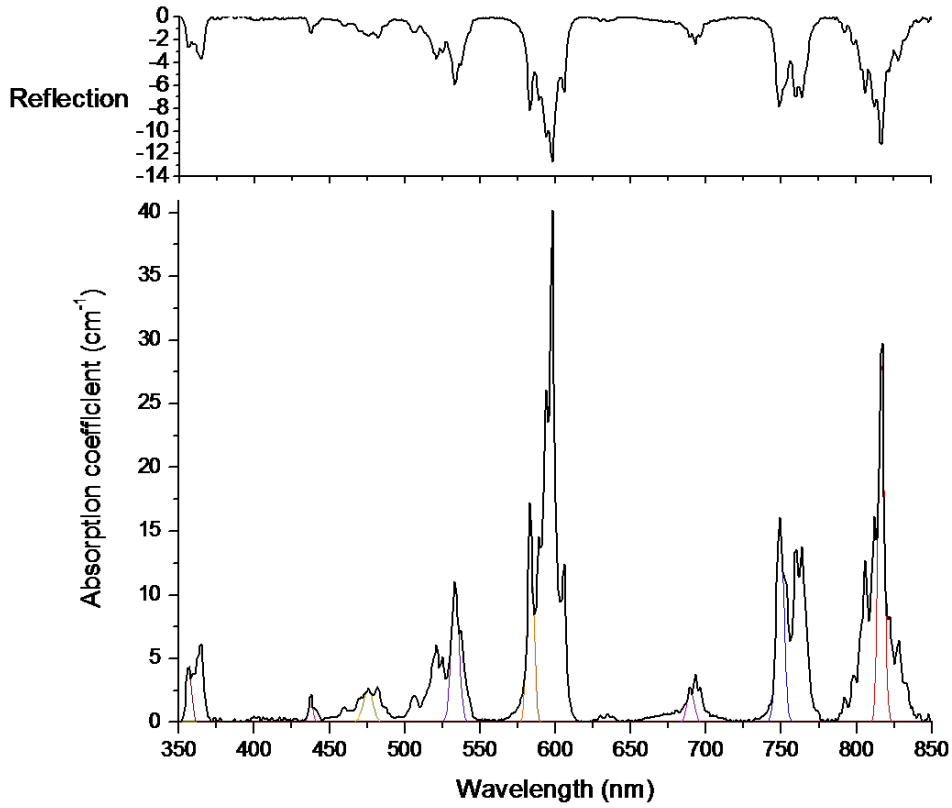

Figure 6.17: Top: The reflection spectrum of ground NdP_5O_{14} - impregnated porous sample. Bottom: Absorption spectrum of Nd^{3+} ion in NdP_5O_{14} nanocrystal impregnated in the pores of the porous Vycor glass. This absorption spectrum is calculated by using reflection data and Beer-Lambert Law. Color graphs are the Gaussian-fitted absorption lines, which are used to calculate Judd-Ofelt parameters.

Transitions (from $^4I_{9/2}$)	$E_{JJ'}$ (cm^{-1})	$\bar{\lambda}$ (nm)	Γ (nm-cm^{-1})	S_{cal} ($10^{-20} cm^2$)
$^4F_{5/2}$	12350	816	139.00	12.31
$^4F_{7/2}$	13500	749	97.21	9.38
$^4F_{9/2}$	14650	689	15.00	1.57
$^4G_{5/2}$	17200	583	81.00	10.04
$^2K_{13/2}$	18750	533	67.26	9.12
$^2G_{9/2}$	21050	476	20.28	3.08
$^2P_{1/2}$	23000	437	7.43	1.23
$^4D_{3/2}$	28200	357	19.47	3.94

Table 6.3: Calculated absorption line strengths S_{cal} of Nd^{3+} in NdP_5O_{14} nanocrystals in the porous Vycor glass at 300K.

N ($\times 10^{20}$) (ions/cm^2)	Ω_2 ($\times 10^{-19}$) (cm^2)	Ω_4 ($\times 10^{-19}$) (cm^2)	Ω_6 ($\times 10^{-19}$) (cm^2)	X_{Nd} $=\Omega_4/\Omega_6$
1	0.265	1.698	2.155	0.788

Table 6.4: Intensity parameters and Nd^{3+} density for NdP_5O_{14} crystals embedded in porous Vycor glass

Transiton (From)	Transition (To)	$E_{JJ'}$ (cm^{-1})	$[U^{(2)}]^2$	$[U^{(4)}]^2$	$[U^{(6)}]^2$
$^4F_{3/2}$	$^4I_{15/2}$	5400	0	0	0.0288
	$^4I_{13/2}$	7500	0	0	0.2085
	$^4I_{11/2}$	9500	0	0.1136	0.4104
	$^4I_{9/2}$	11350	0	0.2293	0.0548

Table 6.5: Squared Reduced-Matrix Elements for intermanifold $^4F_{3/2} \rightarrow {}^4I_{i/2}$ Transitions of Nd^{3+} ions. These values are used for calculating the spontaneous emission rates and branching ratios.

Transiton	τ_0 (μs)	A (s^{-1})	β (%)	$\tau_{^4F_{3/2}} = \tau_{rad}$ $1/\sum_i A(^4F_{3/2} \rightarrow {}^4I_{i/2})$	$\tau_{measured}$ ($\tau_r + \tau_{nr}$)	η (%)
$^4F_{3/2} \rightarrow {}^4I_{15/2}$	22128	45.19	0.005			
$^4F_{3/2} \rightarrow {}^4I_{13/2}$	1140	877.40	10.2	116 μs	100 μs	86 %
$^4F_{3/2} \rightarrow {}^4I_{11/2}$	234	4268	49.5			
$^4F_{3/2} \rightarrow {}^4I_{9/2}$	291	3432	39.8			

Table 6.6: τ_0 (calculated raditive lifetime); A (radiative probability); β (branching ratio) of NdP_5O_{14} -impregnated porous Vycor glass

Host	R=$\beta_{1.06}/\beta_{1.35}$	$X_{Nd}=\Omega_4/\Omega_6$	τ (μs) Measured	JO
YVO_4 [8]	4.15	0.827	90	-
$GdAlO_3$ [8]	4.18	0.853	100	-
$La_2Be_2O_5$(BEL) [8]	4.20	0.870	155	-
present Nd:Vycor	4.90	0.788	100	116
$Gd_3Sc_2Ga_3O_{12}$(GSGG) [8]	5.10	0.728	281	284

Table 6.7: Comparison of spectroscopic properties of some Nd^{3+} -doped laser crystals and present Nd^{3+} -doped porous Vycor glass.

as the fiber lasers and fiber amplifiers.

Chapter 7

Supplemental study

7.1 Spatial Phase Modulation from permanent memory in doped glass

7.1.1 abstract

Diffraction rings are observed from photo-induced permanent memory of doped glass. The permanent memory is created by the high intensity picosecond laser beam. A 1mm spot size of laser beam creates spatially induced refractive index memory, which has nearly Lorentzian beam profile of refractive index variation. When a probe laser beam passes through the memory region, the diffraction rings arisen from spatial self-phase modulation of the transverse phase of the input beam are created. Agreement between the observed and calculated beam pattern using Kirchhoff's diffraction integral is satisfactory.

7.1.2 Introduction

Diffraction rings were first observed by Zolot'ko [49] and Shen and coworkers [50, 51] when the high intensity laser beam passes through the nematic liquid crystal film. Spatial self-phase modulation (SSPM) mechanisms of the spatial profile of the laser beam was attributed as causing the diffracted beam. SSPM is analogous to the

frequency broadening effect caused by the time domain self-phase modulation(SPM) of laser beam. The SSPM effect was observable mostly in liquid crystal medium because of its large non-linear refractive index, $\Delta n = 0.1$. In the highly non-linear film, the nonlinear refractive profile is temporarily created by the high intensity spatial laser beam profile. This index variation causes interesting self-action effects in space and in time such as self-focusing, self-defocusing and self-phase modulation of the input beam. Besides the nonlinear effect in the transparent medium, the laser-induced index profile can occur in the absorbing media due to the temperature gradient induced by the transverse beam profile.

In addition to the nonlinear medium such as liquid crystal, the temporary diffraction rings are also observed in the absorption media such as lead glass [52], solution of saturable absorber (bis-(4-dimethylamino-dithiobenzil)-nickel) [53] and Rhodamine 6G dye solution [54] due to the laser-induced temperature dependent refractive index changes. In these media, the index profile is temporarily created by the input laser beam and the steady state laser diffraction at the far field is measured and reported. The induced index was not permanent.

In this research project, the diffraction rings are observed from the permanent refractive index profile burned into the doped glass by the high intensity picosecond laser pulses. Because of the radial variation in intensity of the laser beam, the temperature gradient following the laser profile is created by the absorption of ions in the doped glass. This temperature in turn creates the permanent memory of refractive index variation profile across the transverse direction of the laser beam. These diffraction rings can be accounted for the spatial self-phase modulation of incoming beam by the presence of memory of the refractive index profile on the surface of the doped glass.

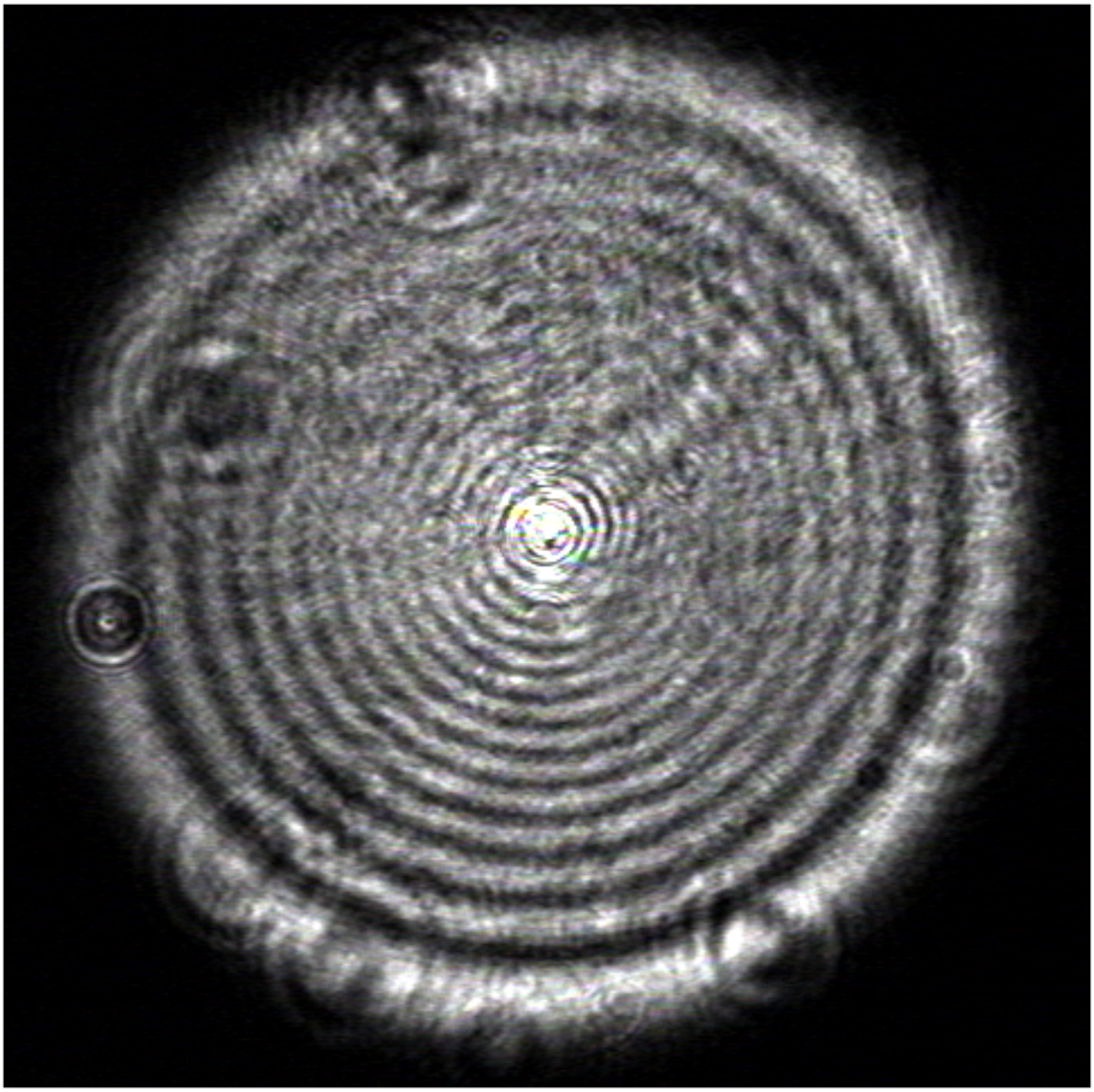

Figure 7.1: Diffraction rings observed at far field when the focused beam of HeNe laser (632nm) shines on the refractive index variation memory produced by picosecond 532nm laser beam

7.1.3 Method

The ultrafast laser beam used to create the induced index profile is second harmonic generation from High-Q picosecond laser primary pulses with 1060nm, 8ps at 82MHz. The spot size of the laser output is about 1mm and the maximum average power is 2W. The laser output beam propagates through the glass and the memory is created without focusing. The diffraction rings shown in fig. 7.1 are observed at the far field when the focused beam of HeNe laser (632nm) passes through the permanent memory created by picosecond 532nm laser beam on the surface of the doped glass.

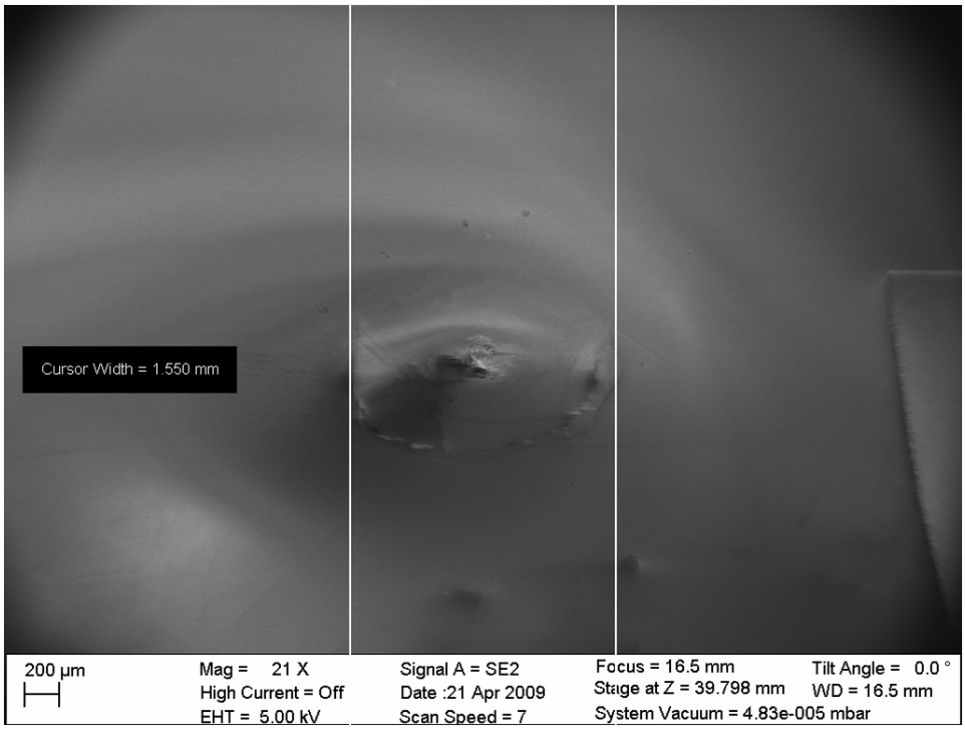

Figure 7.2: SEM image of the memory region

Figure. 7.2 shows the SEM picture of the memory region in the glass. The diameter of the whole memory region is 1.55mm which agrees with the spotsize of the excitation beam and the diameter of central region is 200μm. The shape of memory is very similar to the Lorentzian shape, where the changes in central region (200μm) are very dramatic and smooth changes occur in the peripheral region. The memory is

created by the electronic transition of transition metal ions from Fe, Mn, Co, Ni and Cu ions doped in the glass. Having these transition metal ions in the glass is confirmed by using the mass spectrometry.

7.1.4 Theory

Following Shen [50], Kelly [52] and Khoo [55], the diffraction rings caused by the spatial self-phase modulation can be explained by the application of Kirchchoff diffraction integral. The spatial intensity distribution of the diffraction rings caused by self-phase-modulation of the input beam at the distance Z is given by:

$$I(\rho, Z) = \left(\frac{2\pi}{\lambda Z}\right)^2 I_0 \left| \int_0^\infty r dr J_0\left(\frac{2\pi r \rho}{\lambda Z}\right) \exp\left(-\frac{2r^2}{\omega^2}\right) \exp\left[-i(\phi_D(r) + \Delta\phi(r))\right] \right|^2 \tag{7.1}$$

$$\phi_D(r) = k\left(\frac{r^2}{2Z} + \frac{r^2}{2R}\right)$$

$$\Delta\phi(r) = \frac{2\pi}{\lambda}\int_0^d \Delta n(r,z)dz = \phi_{max}\exp\left(-\frac{2r^2}{\omega^2}\right),$$

where ρ is the transverse position on the observation plane, r is the radial distance from the center of the memory region, Z is the distance from the memory element to the observation plane, R is the radius of curvature of the laser beam, ω is the spread of memory region, ϕ_D is the phase changes due to radius of curvature and longitudinal position of the beam, $\Delta\phi$ is the phase changes due to the refractive index profile $\Delta n(r,z)$ of the memory region.

For the medium having temperature-induced refractive index variation, the induced ϕ_{max} can be defined as [54]:

$$\phi_{max} = k\left(\frac{\partial n}{\partial T}\right)\frac{d(1-\exp^{-\alpha d})}{h\pi\omega^2}I_0 = kn_2dI_0, \tag{7.2}$$

where $\frac{\partial n}{\partial T}$ is the rate of change of refractive index with temperature, $k = \frac{2\pi}{\lambda}$, d is the thickness of the permanent memory, α is the absorption coefficient, h is the convective heat transfer coefficient and n_2 is effective non-linear refractive index. ϕ_{max} can also be estimated from the observed number of diffraction rings [50].

$$\phi_{max} \sim 2\pi N, \tag{7.3}$$

where N is the number of diffraction rings.

In eq. 7.1, there are two phase terms which can be modulated. ϕ_D is the phase shift primarily related to the radius of curvature of the laser beam and $\Delta\phi$ is the phase shift related to the refractive index variation of the medium. The transverse wave vector can be calculated from $\Delta\phi$ and is defined as:

$$k_\perp = \frac{d\Delta\phi}{dr} \tag{7.4}$$

Using the transverse wave vector, the maximum half-cone diffraction angle is approximately given by [50],

$$\theta \sim \frac{k_\perp}{k} \tag{7.5}$$

Figure. 7.3 shows the phase shift profile across the memory region and associated half-cone angle for each point of the memory region. As shown in fig.7.3, every point in the phase shift profile has another point having the same half-cone angle: point A and point B have angle θ_1 while point C and D have angle θ_2. The electric field passing through these two points having the same angle can interfere constructively or destructively depending on both the amount of phase shift each point on the memory

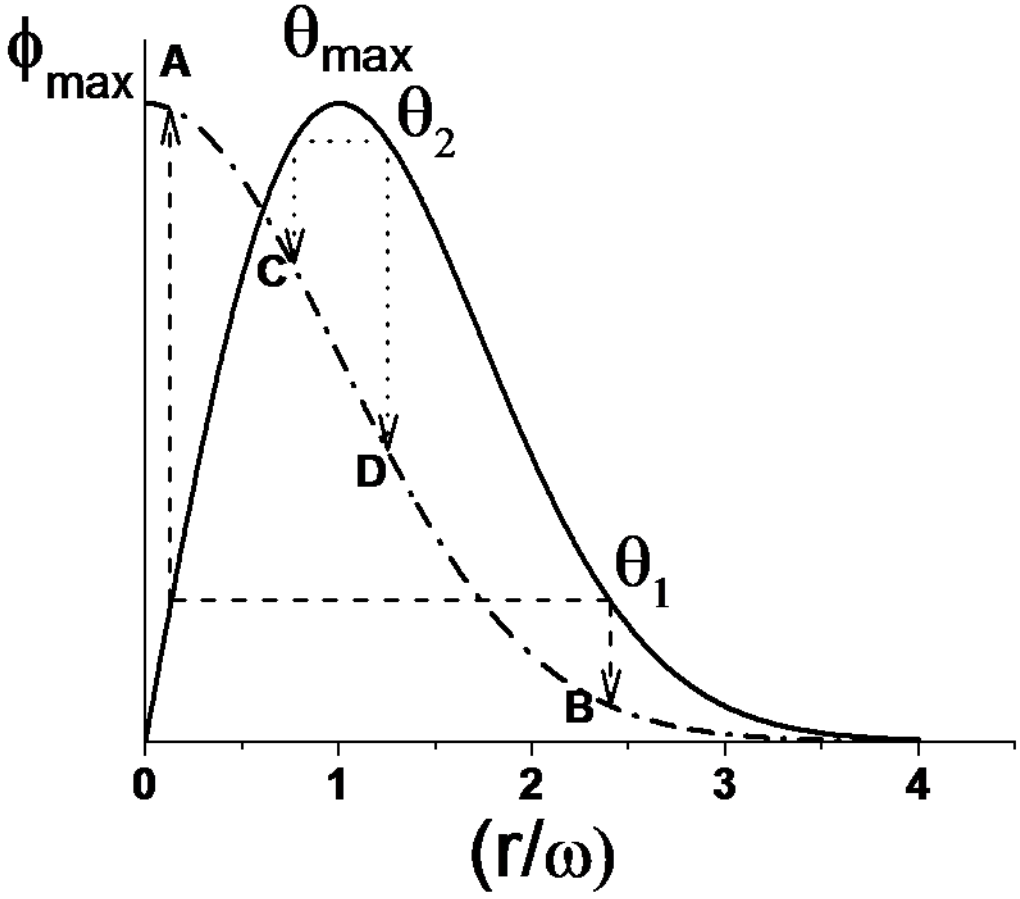

Figure 7.3: Phase shift profile(dotted) on the memory region and associated diffraction angle profile(solid)

region delivers and the phase shift induced by the optical path length difference. As shown in fig. 7.3, the maximum diffraction angle comes from the inflection point of the phase shift profile. Accordingly the outermost ring is thickest, see fig. 7.1. The cause of thick ring at the boundary is, at the inflection points(C,D), there is little phase difference among the electric fields and spatial period of occurrence of maximum intensity is wider.

7.1.5 Result

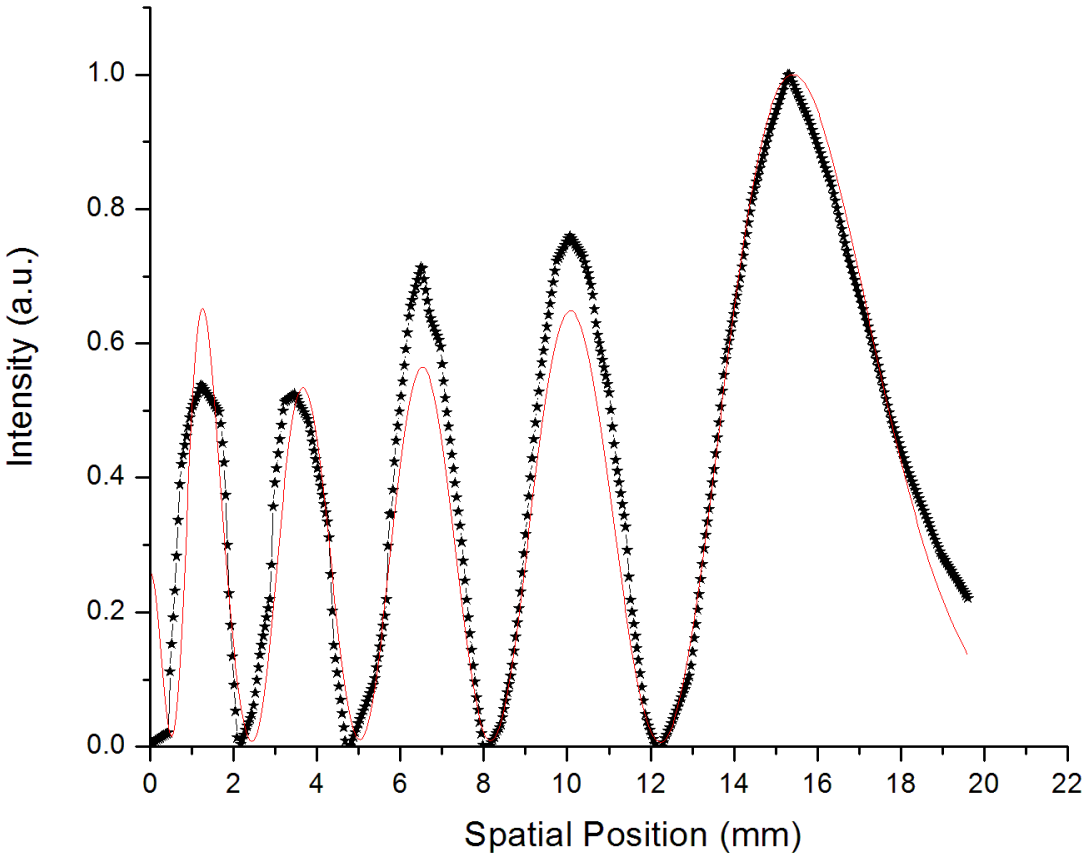

Figure 7.4: Experimental and theoretical fitted data. The solid line is theoretical fit and the dotted line is experimental data

Figure. 7.4 shows the comparison between theoretical fit and experimental data of diffracted waves. The experimental data measured using CCD camera (Marshall V1700) and transition stage. The distance of CCD camera is placed from the memory is 65cm. The number of rings appeared at power density of 113 W/cm^2 is 6. Using the formula, $\phi_{max} \sim 2\pi N$, ϕ_{max} is estimated to be 12π radian. Using this value, the experimental data is fitted with the theoretical values using Kirchoff diffraction integral and parameters $\omega = 100\mu m, I_0 = 113W/cm^2, R = 10^5(atfocus), Z = 65cm$. The experimental data agrees with the theoretical interpretation in fig. 7.4. The fitted (n_2) value is $6.8X10^{-4}cm^2/W$ for the memory thickness of 500 μm. The calculated ($\Delta n = n_2 I_0$) value is 0.077, which is close to the effective refractive index ($\Delta n = 0.1$) of liquid crystal.

7.1.6 Forward and Backward Direction

The self-diffraction pattern at the forward and backward direction of the memory is shown in fig. 7.5. As shown in the figure, the number of diffraction rings at the backward direction is more than twice the number of diffraction rings appeared at the forward direction. According to the relation $\phi_{max} \sim 2\pi N$, the effective nonlinear phase shift at the backward direction is twice more than the phase shift at the forward direction. This is understandable in the sense that, at the backward direction the light has to pass through the memory region twice to reflect backward. Because the longer propagation distance, the light beam experience more nonlinear phase shift at the backward direction. It may be that the maximum phase shift at the backward direction is twice than the phase shift at the forward direction. This is confirmed by counting the number of diffraction rings at each observation plane. But that kind of counting is not quite accurate because the excitation is very bright and the diffraction rings are densely populated at near axis and it is difficult to count at the forward direction.

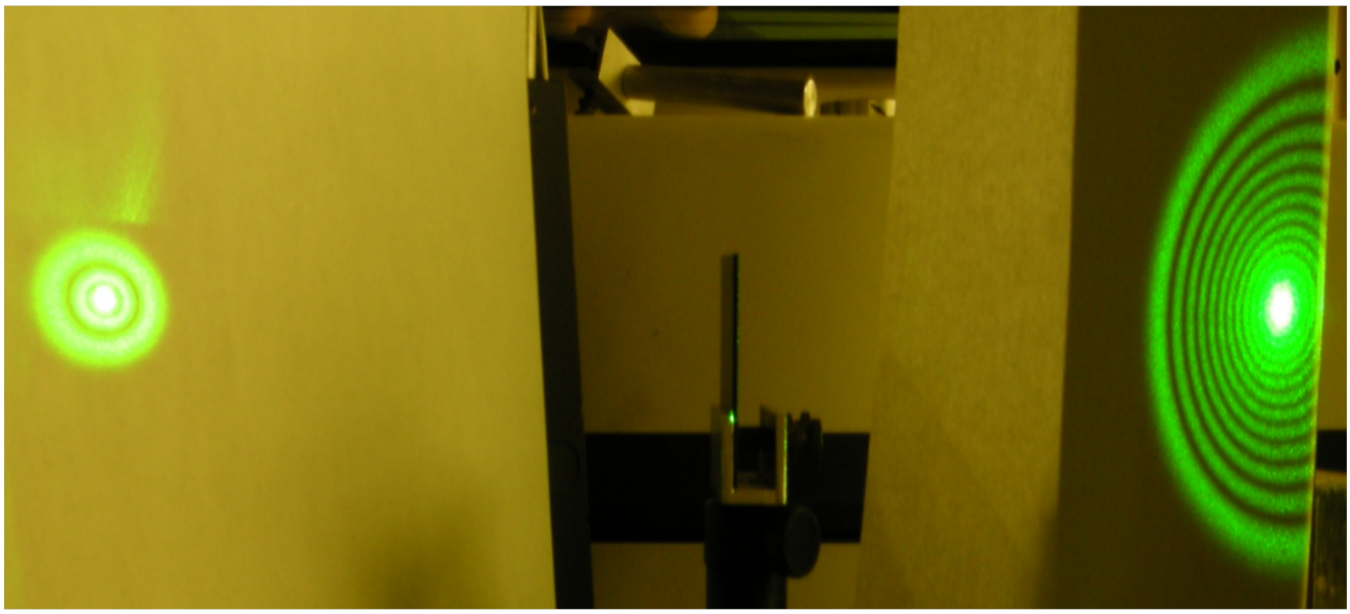

Figure 7.5: Diffraction rings appeared at the forward(left) and backward(right) observation planes

7.1.7 Conclusion

The permanent memory of laser-induced non-linear refractive index profile is created using picosecond 532nm and 1060nm pulses. The permanent memory causes the transverse phase-modulation of the passing beam and consequently the beautiful diffraction rings appear at the far field observation plane. The agreement between the experimental data and theoretical calculated values using Kirchhoff diffraction integral gives the proof that the spatial self-phase modulation mechanism is the major cause of observing the diffraction rings.

Chapter 8

Conclusion

8.1 Conclusion on glass composite materials

This thesis is focused on creating the novel materials which can be used as the amplified media in the fiber lasers and fiber amplifiers. The tunable range of $Cr^{3+}$and Cr^{4+}ions doped olivine laser crystals is well within the optical telecommunication bands. If we can use the optical properties of Cr doped crystal in telecommunications, we can revolutionize the optical communications by reducing the operation cost. But, unlike Nd or Er ions, we cannot doped Cr directly to the glass since Cr is very sensitive to local environment and thus the emission will be quenched because of wide distribution of inequivalent sites in glass. The most logical solution seems to be to synthesize the glass composite materials which have the good mechanical properties of glass and the good optical properties of Cr doped laser crystals. The glass composite is a two-phase system: glass phase and nano-crystal phase embedded in the glass matrix. By synthesizing the phase of nano-crystals as proven laser crystal phase, we can expect that the optical properties of synthesized glass composite materials are very similar to these of proven laser crystals such as Cr:forsterite and CUNYite. In thesis, we synthesized the glass ceramics with embedded nanocrystals. The main objective of this project was the phase of nanocrystals must be very similar to the proven laser crystal Cr:Ca_2GeO_4 (CUNYite) phase. With an array of spectro-

scopic measurements, we conclude that the phase of nanocrystals is very similar to that of the proven laser crystal Cr:$CaGeO_4$ (CUNYite) phase. The following is the summary of observations from spectroscopic measurements[4].

- There is no emission from as-quenched glass. Only after heat-treated to the as-quenched sample, the near-infrared emission appears. This clearly indicates that the emission comes from the nanocrystals.

- *From absorption spectroscopy* of glass ceramics, the absorption spectrum shows that there are several Cr valence states contributing to the spectrum. The main peak of the absorption spectrum does not overlap with the well-known Cr^{4+}ions absorption peaks. Unlike single crystal, the absorption spectrum is unpolarized.

- *From excitation spectroscopy* of glass ceramics, the peaks of excitation spectrum well overlap with the polarized absorption peaks of single crystals. This clearly indicates that the emission center is Cr^{4+}ions in crystal phase.

- *From low temperature fluorescence spectroscopy* of glass ceramics, unlike the sharp emission of the single crystal, the fluorescence spectrum of glass ceramics is broadband. This is because the site distribution resulted from nanocrystal doping to the glass matrix. In single crystal, only the homogeneous broadening contributes to the bandwidth of the spectrum. In glass ceramics, both homogeneous and inhomogeneous broadening contributes to the bandwidth of the spectrum. More or less, the center of gravity of fluorescence spectrum is not very far from the zero-phonon line of single crystal. But the center of gravity of fluorescence spectrum of glass ceramics is red-shifted related to that of the single crystal.

- *From off-resonance Raman spectroscopy* of glass ceramics, in addition of the Raman lines of host glass, the Raman lines of single crystal are clearly visible

in Raman spectrum of glass ceramics. This alone clearly indicates that there is Ca_2GeO_4 single crystal phase in glass ceramics.

- *From on-resonance Raman spectroscopy* of glass ceramics, the so-called local modes of single crystal are strongly enhanced in the Raman spectrum of glass ceramics when the excitation line is tuned within the absorption band of Cr^{4+}ions. This indicates that the nanocrystals phase is Cr:$CaGeO_4$ single crystal phase.

- *From the decay time measurement* of glass ceramics, we identified that there are more than one near-infrared emission centers in glass ceramics. One center has temperature dependent lifetime and we identify this center as Cr^{4+}ions in Cr:Ca_2GeO_4 nanocrystals. The other center has temperature independent lifetime and this center can be Cr^{3+}or other impurity center.

- *From the lifetime* measurement of glass ceramics, the quantum efficiency of the glass ceramic is determined as 35% while the quantum efficiency of single crystal is 50%.

- In synthesizing the glass ceramics, there are two kinds of phase separation mechanisms. One kind is called spinoidal phase separation while another kind is called isolated droplet phase separation mechanism. To determined what kind of phase separation mechanism occurs in glass ceramics is very difficult even under the powerful microscope. In this thesis, we show that by using the Raman spectroscopy, we can determine the phase separation mechanism in glass ceramics.

The above spectroscopic evident clearly points out that the nano-crystal phase is very similar to Cr:Ca_2GeO_4 laser crystal phase. The broadband emission and high quantum efficiency of new glass-ceramics make it the promising medium for fiber lasers and amplifiers.

In synthesizing the glass ceramics, one important issue arises. Sometime it is hard to control the size of nanocrystals if the glass has the spinoidal phase separation mechanism. To solve this problem, we've tried to use the porous glass. The porous glass has pore network with 4nm pore size. Since the size of the pore network is 4nm, the nanocrystals grown in the pore network cannot have the size of more than 4nm. But growing the nanocrystals having a few lattice parameters in size is pretty new research area. There is no strong literature pointing out that the crystallites of that small size can be grown. Thus we have tried to answer this question in this thesis. The question is "can we synthesize the nanocrystals with a few lattice parameters in size in the pore network?". To answer this question, Cr is not the best active ion to probe the size effect because the optical properties of Cr is strongly effected by the surrounding environment. Because of this reason, we've tried to use neodymium ion because the optical properties of Nd ions is well-studied and its sharp absorption lines are easily measurable. Its optical properties also vary with the crystal composition. These so-called self-activated crystals (no doping required) have strong fluorescence quenching effect. By using this effect, we can probe the size effect of nanocrystals. In this investigation, we've grown the three type of self-activated salt crystals inside the pore network and investigate whether the optical properties of porous glass come from the crystal structure or the individual ions attached to the porous network. As described in chapter(6) and in publication([3]), the summary of the research on the porous glass is as follows.

- By clearly understanding the process of nano-air-bubbles formation in the pore network, it is possible to synthesize the transparent sample by proper vacuuming the sample and controlling the crystal concentration.

- In this thesis, three salt crystals (NdOCl, Cs-Na-NdOCl and NdP_5O_{14}) are grown in the pore network. In synthesizing the nanocrystals impregnated porous glass, we synthesize the salt powder using the same experimental condition.

We use these salt powders as bulk crystals. The fine structure of fluorescence spectrum of each salt crystal varies with the crystal composition. Since the fluorescence spectrum of porous glass follows the shape of that of bulk crystal, we deduce that the optical properties are coming from the crystal structure and not from the individual ions. From the lifetime measure of NdOCl and NdP_5O_{14} salt crystals clearly points out that the lifetime changes one order of magnitude by changing one crystal composition to another. Because of these observations, we confidently conclude that the nanocrystals having a few lattice parameters in size can be grown in the pore network.

- These so-called self-activated Nd crystal have strong concentration quenching effect. By using this effect, we can estimate the size of nanocrystals in the pore network. The estimated size of nanocrystals is less than 4nm.

Thus the porous glass gives us the unique way to create the nanocrystals with a few lattice parameter in sizes. Since the pore volume is 30% of total volume and the sample is highly transparent, the nanocrystals impregnated porous glass is a promising medium for fiber lasers and amplifiers.

8.1.1 Proposed future experiments on glass ceramics and porous glasses

As shown in the glass ceramics model 8.1, both $Cr^{3+}$and Cr^{4+}ions can stable even in as-quenched glass. When the glass is heat-treated, the Cr doped nanocrystals are precipitated in the glass matrix. X-ray diffraction measurement also shows there is other unknown phase together with Cr doped crystal. By looking at this model figure(8.1), we can visualize that there are Cr ions in glass matrix, Cr ions in nanocrystals and Cr ions in interface. These Cr ions can be Cr^{3+}, $Cr^{4+}$and Cr^{6+}. The trace of having these ions is observable in absorption spectrum. The decay measurement also points

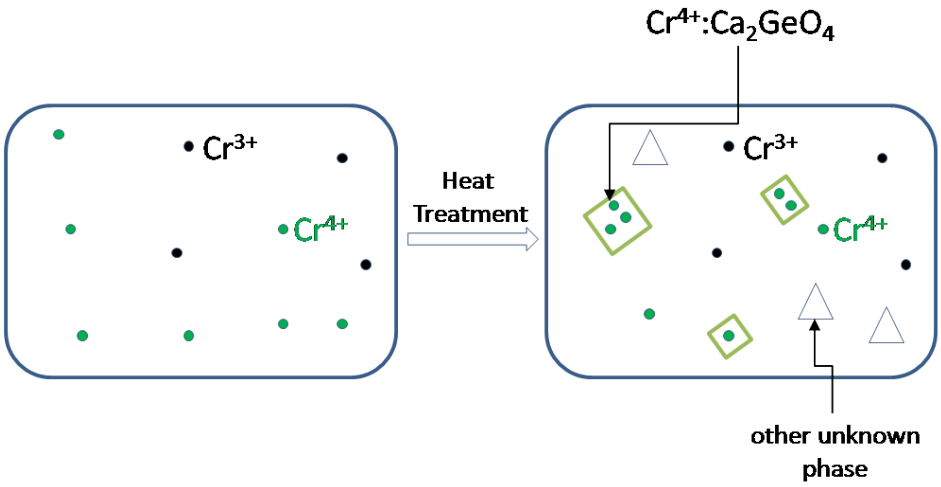

Figure 8.1: Glass ceramics model

out that there are more than one near-infrared emission center in the glass ceramics. All these experimental observations tell us that we need to improve the sample quality. If we can improve the sample quality in order to increase damage threshold and to reduce the losses because of undesired impurities, we can realize making the fiber lasers and amplifiers using these Cr doped glass composite materials. For the future synthesizing process, we should use the Raman spectroscopy to identify the phase separation mechanism in glass. By using the information given by the Raman spectroscopy, we can change the chemical composition in order to get the nucleated droplet phase separation mechanism in Cunyite glass ceramics. If the glass ceramics has the nucleated droplet phase separation mechanism, we can easily control the size of nanocrystals, which in turns we can get high quality transparent sample.

8.2 Conclusion on Decay dynamics of Cr^{4+}ions in $Cr:LiScGeO_4$ crystal

As described in chapter(3), there is no detectable emission from Cr^{4+}ions in $Cr:LiScGeO_4$ crystal. The near-infrared emission center of $Cr:LiScGeO_4$ crystal is Cr^{3+}ions. Even though the structural similarity between $Cr:CaGeO_4$ and $Cr:LiScGeO_4$ crystals, the quantum efficiency of Cr^{4+}ions in $Cr:LiScGeO_4$ single crystal is 0.01%

$$\tau_{300K}/\tau_{77K} = 3ns/30\mu s \tag{8.1}$$

while the quantum efficiency of Cr^{4+}ions in $Cr:CaGeO_4$ single crystal is 50%

$$\tau_{300K}/\tau_{77K} = 15\mu s/30\mu s \tag{8.2}$$

.

The reason for having such a low quantum efficiency in this $Cr:LiScGeO_4$ crystal is the crystal has strong non-radiative relaxation with temperature. According to Mott's activation energy model described in appendix(A), the activation energy must be very low in this crystal. There must be at least one crossing point between the ground state and the excited state adiabatic potential surfaces in multidimensional vibration space.

8.2.1 Proposed future experiment

The proposed future experiment for Cr^{4+}ions $Cr:LiScGeO_4$ single crystal is to test the hypothesis outlined in section(8.2). Maybe we can use the on and off-resonance Raman measurements to describe the specific decay channel in this crystal.

8.3 Conclusion on Spatial Phase Modulation from Permanent Memory in doped glass

The permanent memory of refractive index profile is created on the surface of the doped glass by using strong picosecond mode-locked laser pulses. This permanent memory creates beautiful diffraction rings at the forward and backward observation planes by modulation the phase of passing beam. The number of rings appeared on the forward and backward direction is different because of the optical path length difference between the forward and backward direction.

8.3.1 Proposed future experiment

The effect coming from the permanent memory is quite new. Usually, the diffraction rings appear because of the SELF-phase modulation from the materials having non-linear refractive index. Future investigation should be in the direction of how we can use this permanent memory in real applications. One application can be the limiting of optical input power by placing the aperture at the output side of doped glass. By placing the aperture, we can decrease the input power by diffracting the beam and only using the power contained in axial portion, which are allowed to pass through the aperture.

Appendix A

Important parameters describing spectroscopic characteristics of activated crystals

A.1 Beer-Lambert law

When the light passes through the sample, the intensity of transmitted light will be less than the that of incident one because of sample absorption. Beer-Lambert law states that the intensity of transmitted light will be:

$$I_T = I_0 \cdot 10^{-A} \tag{A.1}$$

Here, A = **Optical Density** = **OD**. Thus eq.A.1 can be rewrite as:

$$\mathbf{OD} = log_{10}\left(\frac{I_0}{I_T}\right) \tag{A.2}$$

If you know the sample length (l), you can find the **Absorption Coefficient**($\alpha(\nu)$) from optical density. Absorption coefficient is:

$$\alpha(\nu) = \frac{A(\nu)}{l} \tag{A.3}$$

The unit of absorption coefficient is cm^{-1}. The absorption coefficient can be

calculated from the absorption spectrum.

A.2 Einstein Coefficient A

If we find the absorption coefficient from the absorption spectrum. we can find he spontaneous emission rate of excited state. The spontaneous emission rate is also called as Einstein Coefficient A and is defined as:

$$A_{21} = \frac{1}{N_1} \frac{8\pi\nu_{21}^2}{c^2} \int_{\nu_1}^{\nu_2} \alpha_\nu d\nu \tag{A.4}$$

where, N_1 = the ions concentration at ground state

ν_{21} = the energy difference between ground and excited state

A.3 Oscillator Strength

From the absorption coefficient, we can also find the oscillator strength of the transition. Oscillator strength is defined as:

$$f_{21} = \frac{1}{N_1} \frac{mc}{\pi e^2} \int_{\nu_1}^{\nu_2} \alpha_\nu d\nu \tag{A.5}$$

A.4 Emission and Absorption cross-section

By using Einstein coefficient A and B and steady state rate equation, we can show that the emission and absorption cross-section is the same.

$$\sigma_{emission} = \sigma_{abs} \tag{A.6}$$

$$\sigma_e(\nu_{21}) = \frac{\lambda_{21}^2 A_{21}}{4\pi^2 n^2 \Delta\nu_{lum}} \tag{A.7}$$

where, $\Delta\nu_{lum}$= the absorption bandwidth of the transtion.

A.5 Lifetime of an excited state

In ideal, pure system, the lifetime of an excited state (let's say level-2) is the reciprocal of the addition of spontaneous emission from level-2 excited state to all stark levels of ground state. Lifetime is defined as:

$$\tau_2 = \frac{1}{\sum_{j=1}^{n} A_{2j}} = \tau_{rad} \tag{A.8}$$

In reality ,in addition to the radiative emission, the lattice phonons can dissipate the excited energy. Because of the vibrational phonons present in system, eq.A.8 can be modified as

$$\tau_2 = \frac{1}{\sum_{j=1}^{n} (A_{2j} + d_{2j})} = \tau_{lum} \tag{A.9}$$

Thus we call eq.A.8 is radiative lifetime and eq.A.9 is luminescence(measured) lifetime. The non-radiative lifetime can be defined as:

$$\tau_{nr} = \frac{1}{\sum_{j=1}^{n} d_{2j}} \tag{A.10}$$

By using eq.A.8, eq.A.9 and eq.A.10, the luminescence lifetime be rewrote as:

$$\frac{1}{\tau_{lum}} = \frac{1}{\tau_{rad}} + \frac{1}{\tau_{nr}} \tag{A.11}$$

A.6 Quantum Efficiency

Quantum efficiency is defined as:

$$\eta = \frac{\text{radiative rate}}{(\text{radiative rate} + \text{non-radiative rate})} \tag{A.12}$$

$$\eta = \frac{\tau_{measured}}{\tau_{rad}} \tag{A.13}$$

Experimentally, the quantum efficiency can be found as:

$$\eta = \frac{\tau_{exp} \text{ at } 300\text{K}}{\tau_{exp} \text{ at } 77\text{K}} \tag{A.14}$$

A.7 Multi-phonon non-radiative relaxation analysis using Stuck and Fonger model

Since the energy difference between the ground state and excited state of transition metal ions is smaller compared to that of the rare-earth ions, these two levels can be bridge by multi-phonons. Thus the multi-phonon nonradiative decay is the major loss channels of the excited energy of chromium ions. These are two basic models to study the non-radiative decay process of transition metal ions doped system. These are Mott's activation-energy model and Struck and Fonger model.

A.7.1 Mott's activation energy model

The heart of Mott's activation energy model is activation energy. Activation energy is defined as the energy difference between the potential energy surface minimum of excited state and the crossing point between the excited state and ground state. Thus the non-radiative relaxation rate is getting faster as activation energy is smaller. The equation describing Mott's activation-energy model is:

$$W_{nr}(T) = A_m \exp\left(-\frac{E_x}{kT}\right) \tag{A.15}$$

where, E_x =Activation energy, $A_m = 1{\times}10^{13}$Hz

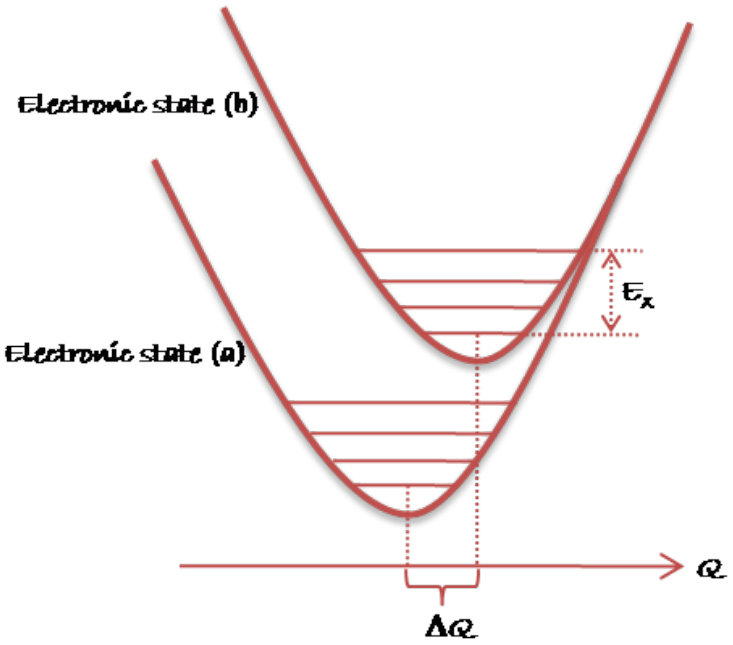

Figure A.1: Mott's activation energy model

A.7.2 Struck and Fonger model

The improved non-radiative relaxation model over Mott's activation energy one is Struck and Fonger. According to Struck and Fonger model, the temperature dependence of non-radiative decay rate can be expressed as follows:

$$W_{nr}(T) = K_{nr}\frac{e^{p-S}}{\sqrt{2\pi p}}\left[\frac{S}{p}\right]^{p}\left[\frac{p}{p^{*}}\right]^{\frac{1}{2}}\left[\frac{2p<1+m>}{p+p^{*}}\right]^{p}\exp^{(p^{*}-p-2mS)} \tag{A.16}$$

$$p^{*} = \sqrt{p^{2}+4S^{2}<1+m><m>}$$

$$<m>=\frac{1}{\exp(\hbar\omega/kT)-1}$$

where,

K_{nr} = Non-radiative decay constant

$p=\frac{E_{zpl}}{\hbar\omega}$ = Number of phonons bridging the energy gap between the ground and excited state

E_{zpl} = Energy of zero-phonon line

$\hbar\omega$ = Energy of effective totally symmetric phonon (g character)

S = Huang-Rhys parameter

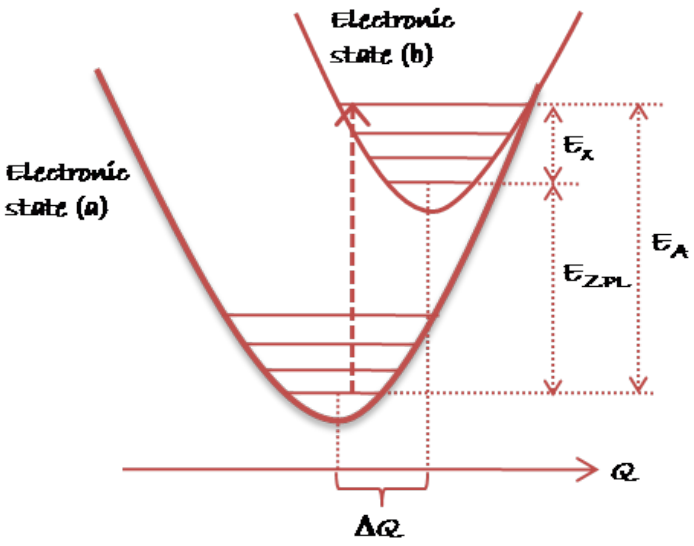

Figure A.2: Single configurational coordinate model

A.7.2.1 Huang-Rhys parameters (S)

Huang-Rhys parameter, S, determines the strength of electron-phonon coupling of the system. Huang-Rhys parameter (S) is defined as:

$$S = \frac{E_A - E_{zpl}}{\hbar\omega} \tag{A.17}$$

$$S = \frac{\omega(\Delta Q)^2}{2\hbar} \tag{A.18}$$

- S corresponds to the *average number of phonons* participating in the absorption and emission process.
- S is a measure of *degree of coupling* between ion and its surrounding.

A.7.2.1.1 Typical S value The typical Huang-Rhys parameters (S) of different active centers are tabulated in table(A.1).

Coupling Strength	Active ion	S value
low	rare-earth ion	0.01∼0.1
medium	transition metal ion	1∼10
high	color center	10∼100

Table A.1: Typical values of Huang-Rhys parameters (S)(Stoke's shift) for different active ions

A.7.2.2 Analyzing the experimental data with Struck and Fonger Model

The measured luminescence decay rate is composed of the radiative and non-radiative rate. Usually the non-radiative decay rate changes with the temperature while the radiative decay rate is insensitive to the temperature variation. To analyze the experimental data, we have to make sure that the temperature dependent of the luminescence decay is only related to the non-radiative process. A hint about the influence of the radiative decay rate on the temperature dependent lifetime can be determined by the ratio(K) of the normalized lifetime(τ) and the normalized intensity(I) of emission. Thus K is defined as:

$$K(T) = \frac{\tau_{rad}(T)}{\tau_{rad}(T = 77K)} \tag{A.19}$$

$$K(T) = \frac{\tau(T)}{\tau(T = 77K)} / \frac{I(T)}{I(T = 77K)} \tag{A.20}$$

If K value is insensitive to the temperature variation, the temperature dependent of the measured luminescence decay rate is only related to the nonradiative decay process. We can fit the measured temperature dependent luminescence decay rate with Struck and Fonger model to determine

- the electron-phonon coupling strength, S
- total number of energy bridging phonons, p
- energy of effective phonon, $\hbar\omega$.

Appendix B

SR245-Boxcar-Data-Aquisition-Program

```
{
unit sr245_v5;

interface

uses
  Windows, Messages, SysUtils, Variants, Classes, Graphics, Controls, Forms,
  Dialogs, StdCtrls, ExtCtrls, TeeProcs, TeEngine, Chart, Series, Spin;

type
  TForm1 = class(TForm)
    Chart1: TChart;
    Button1: TButton;
    Chart2: TChart;
    GroupBox1: TGroupBox;
    Channel1: TLabeledEdit;
    Channel2: TLabeledEdit;
    Limit: TGroupBox;
    Ratio: TLabeledEdit;
    Xmin: TLabeledEdit;
    Ymin: TLabeledEdit;
    Ymax: TLabeledEdit;
    Chart1_Axis: TGroupBox;
    Chart2_Axis: TGroupBox;
    Min: TLabeledEdit;
    Max: TLabeledEdit;
    Channel_Auto: TCheckBox;
    RMin: TLabeledEdit;
    Rmax: TLabeledEdit;
    Ratio_Auto: TCheckBox;
```

```
    NOP: TLabeledEdit;
    Xmax: TEdit;
    Button2: TButton;
    Timer1: TTimer;
    Edit1: TEdit;
    Edit2: TEdit;
    Edit3: TEdit;
    Label1: TLabel;
    Button3: TButton;
    Memo1: TMemo;
    Button4: TButton;
    Edit4: TEdit;
    Label2: TLabel;
    procedure FormCreate(Sender: TObject);
    procedure Button1Click(Sender: TObject);
    procedure Channel_AutoClick(Sender: TObject);
    procedure Ratio_AutoClick(Sender: TObject);
    procedure MinChange(Sender: TObject);
    procedure MaxChange(Sender: TObject);
    procedure RMinChange(Sender: TObject);
    procedure RmaxChange(Sender: TObject);
    procedure Button2Click(Sender: TObject);
    procedure Timer1Timer(Sender: TObject);
    procedure XminChange(Sender: TObject);
    procedure YminChange(Sender: TObject);
    procedure Button3Click(Sender: TObject);
    procedure Button4Click(Sender: TObject);

  private
    { Private declarations }
  public
    { Public declarations }
  end;

const
  (* GPIB status bit definitions.                                    *)
  ERR     = $8000;          (* Error detected                       *)
  TIMO    = $4000;          (* Timeout                              *)
  ENDgpib = $2000;          (* EOI or EOS detected                  *)
  SRQI    = $1000;          (* SRQ detected by CIC                  *)
  RQS     =  $800;          (* Device needs service                 *)
  SPOLL   =  $400;          (* Board has been serially polled       *)
  EVENT   =  $200;          (* An event has occurred                *)
  CMPL    =  $100;          (* I/O completed                        *)
  LOK     =   $80;          (* Local lockout state                  *)
```

```
 REM     =   $40;           (* Remote state                              *)
 CIC     =   $20;           (* Controller-in-charge                      *)
 ATN     =   $10;           (* Attention asserted                        *)
 TACS    =    $8;           (* Talker active                             *)
 LACS    =    $4;           (* Listener active                           *)
 DTAS    =    $2;           (* Device trigger state                      *)
 DCAS    =    $1;           (* Device clear state                        *)

 (* Error messages returned in global variable iberr:                    *)
 EDVR =  0;                 (* System error                              *)
 ECIC =  1;                 (* Function requires GPIB board to be CIC    *)
 ENOL =  2;                 (* Write function detected no Listeners      *)
 EADR =  3;                 (* Interface board not addressed correctly   *)
 EARG =  4;                 (* Invalid argument to function call         *)
 ESAC =  5;                 (* Function requires GPIB board to be SAC    *)
 EABO =  6;                 (* I/O operation aborted                     *)
 ENEB =  7;                 (* Non-existent interface board              *)
 EDMA =  8;                 (* Error performing DMA                      *)
 EOIP = 10;                 (* I/O operation started before previous     *)
             (* operation completed                        *)
 ECAP = 11;                 (* No capability for intended operation      *)
 EFSO = 12;                 (* File system operation error               *)
 EBUS = 14;                 (* Command error during device call          *)
 ESTB = 15;                 (* Serial poll status byte lost              *)
 ESRQ = 16;                 (* SRQ remains asserted                      *)
 ETAB = 20;                 (* The return buffer is full *)

 T10s                  = 13;

 BDINDEX               = 0;     (* Board Index                        *)
 PRIMARY_ADDR_OF_SCOPE = 2;     (* Primary address of device          *)
 NO_SECONDARY_ADDR     = 0;     (* Secondary address of device        *)
 TIMEOUT               = T10s;  (* Timeout value = 10 seconds         *)
 EOTMODE               = 1;     (* Enable the END message             *)
 EOSMODE               = 0;     (* Disable the EOS mode               *)

 ARRAYSIZE             = 550;  (* Size of read buffer               *)

type

 (* Type declarations for exported NI-488.2 Global Variables.         *)
 Tibsta  =  function : integer; stdcall;
 Tiberr  =  function : integer; stdcall;
 Tibcntl = function  : Longint; stdcall;
```

```
  (* Type declarations for exported NI-488.2 functions.             *)
  Tibclr = function (ud : integer) : integer; stdcall;

  Tibdev = function(ud:  integer;
                    pad: integer;
                    sad: integer;
                    tmo: integer;
                    eot: integer;
                    eos: integer) : integer; stdcall;

  Tibonl = function(ud: integer;
                    v:  integer) : integer; stdcall;

  Tibrd  = function (ud:  integer;
                     var  rdbuf;
                     cnt: Longint) : integer; stdcall;

  Tibtrg = function (ud : integer) : integer; stdcall;

  Tibwrt = function (ud:  integer;
                     var  wrtbuf;
                     cnt: longint) : integer; stdcall;

procedure TalkToDevice(Command:String);forward;
var
  Form1: TForm1;

  (* Declaration for the Handle for the GPIB library.               *)
  Gpib32Lib: THandle;

  (* Addresses for NI-488.2 GPIB global status variables.           *)
  AddrIbsta  : Tibsta;
  AddrIberr  : Tiberr;
  AddrIbcntl : Tibcntl;

  (* Pointers to the NI-488.2 GPIB global status variables.         *)
  Pibsta  : ^integer;
  Piberr  : ^integer;
  Pibcntl : ^Longint;


  (* Declarations for the NI-488.2 GPIB calls.                      *)
  ibclr  : Tibclr;
  ibdev  : Tibdev;
  ibonl  : Tibonl;
```

```
  ibrd   : Tibrd;
  ibtrg  : Tibtrg;
  ibwrt  : Tibwrt;
  Dev:integer;
  ReadDev : packed array[0..5] of char;
  RD      : packed array[0..20] of char;
  ReadBuff: packed array[0..20] of char;
  serM1:TFastLineSeries;
  serM2:TFastLineSeries;
  serM3:TFastLineSeries;
  MyThreadExit: Boolean;
  X, Y, R, XT, YT, RT, XA, YA, RA: real;
  Xmini, Xmaxi, Ymini, Ymaxi: real;
  NumOfPoints:longint;
  T:TextFile;
  RDFloat:real;
  RDstring:String;
  fileName:String;

implementation
{$R *.dfm}
procedure loadDLL;
var
  str : string;
  begin
    Gpib32Lib := LoadLibrary('GPIB-32.DLL');
    If Gpib32Lib = 0 Then
      Begin
        str := 'LoadLibrary FAILED!';
        MessageDlg(str, mtError, [mbOK], 0);
        halt;
      End;

  (* Get the addresses of the GPIB Global Variables.                *)
    @AddrIbsta  := GetProcAddress(Gpib32Lib, 'user_ibsta');
    @AddrIberr  := GetProcAddress(Gpib32Lib, 'user_iberr');
    @AddrIbcntl := GetProcAddress(Gpib32Lib, 'user_ibcnt');

  (* Get the addresses of the functions needed for this application. *)
    @ibclr  := GetProcAddress(Gpib32Lib, 'ibclr');
    @ibdev  := GetProcAddress(Gpib32Lib, 'ibdev');
    @ibonl  := GetProcAddress(Gpib32Lib, 'ibonl');
    @ibrd   := GetProcAddress(Gpib32Lib, 'ibrd');
    @ibtrg  := GetProcAddress(Gpib32Lib, 'ibtrg');
    @ibwrt  := GetProcAddress(Gpib32Lib, 'ibwrt');
```

```
  (*
   * Verify that addresses were obtained. If unable to get any one of
   * the addresses, then free the library, display an error message
   * and HALT the program.
   *)
    if (@AddrIbsta  = NIL) Or
       (@AddrIberr  = NIL) Or
       (@AddrIbcntl = NIL) Or
       (@ibclr      = NIL) Or
       (@ibdev      = NIL) Or
       (@ibonl      = NIL) Or
       (@ibrd       = NIL) Or
       (@ibtrg      = NIL) Or
       (@ibwrt      = NIL) Then
       Begin
         str := 'GetProcAddress FAILED!';
         MessageDlg(str, mtError, [mbOK], 0);

         (* Free the GPIB library.                                  *)
         FreeLibrary(Gpib32Lib);
         halt;
       End;

  (* Initialize GPIB global pointers to point to address location.  *)
       Pibsta  := @AddrIbsta;
       Piberr  := @AddrIberr;
       Pibcntl := @AddrIbcntl;
  end;
 (* ======================================================================
 *                       Procedure GPIBCleanup
 *
 * After each GPIB call, the application checks whether the call
 * succeeded. If an NI-488.2 call fails, the GPIB driver sets the
 * corresponding bit in the global status variable. If the call
 * failed, this procedure prints an error message, takes the device
 * offline and exits.
 * ======================================================================
 *)
procedure GPIBCleanup(msg: string);
  var
    str       : string;      (* String used for displaying messages. *)
    ibstaStr  : string;      (* String for converting ibsta.         *)
    iberrStr  : string;      (* String for converting iberr.         *)
    ibcntlStr : string;      (* String for converting ibcntl.        *)
```

```
begin
  ibstaStr := IntToHex(Pibsta^, 4);
  iberrStr := IntToStr(Piberr^);

  str := msg;
  str := Concat(str, #13);  (* Add a line feed character.          *)
  str := Concat(str, 'ibsta = $' + ibstaStr);

  str := Concat(str, '  <');
  if (Pibsta^ and ERR) <> 0 Then
    str := Concat(str, ' ERR ');
  if (Pibsta^ and TIMO) <> 0 Then
    str := Concat(str, ' TMO ');
  if (Pibsta^ and ENDgpib) <> 0 Then
    str := Concat(str, ' END ');
  if (Pibsta^ and SRQI) <> 0 Then
    str := Concat(str, ' SRQI ');
  if (Pibsta^ and RQS) <> 0 Then
    str := Concat(str, ' RQS ');
  if (Pibsta^ and SPOLL) <> 0 Then
    str := Concat(str, ' SPOLL ');
  if (Pibsta^ and EVENT) <> 0 Then
    str := Concat(str, ' EVENT ');
  if (Pibsta^ and CMPL) <> 0 Then
    str := Concat(str, ' CMPL ');
  if (Pibsta^ and LOK) <> 0 Then
    str := Concat(str, ' LOK ');
  if (Pibsta^ and REM) <> 0 Then
    str := Concat(str, ' REM ');
  if (Pibsta^ and CIC) <> 0 Then
    str := Concat(str, ' CIC ');
  if (Pibsta^ and ATN) <> 0 Then
    str := Concat(str, ' ATN ');
  if (Pibsta^ and TACS) <> 0 Then
    str := Concat(str, ' TACS ');
  if (Pibsta^ and LACS) <> 0 Then
    str := Concat(str, ' LACS ');
  if (Pibsta^ and DTAS) <> 0 Then
    str := Concat(str, ' DTAS ');
  if (Pibsta^ and DCAS) <> 0 Then
    str := Concat(str, ' DCAS ');
  str := Concat(str, '>');
  str := Concat(str, #13);  (* Add a line feed character.          *)
```

```
  str := Concat(str, 'iberr = ' + iberrStr);
  str := Concat(str, '  <');
  if Piberr^ = EDVR Then
    str := Concat(str, ' EDVR ');
  if Piberr^ = ECIC Then
    str := Concat(str, ' ECIC ');
  if Piberr^ = ENOL Then
    str := Concat(str, ' ENOL ');
  if Piberr^ = EADR Then
    str := Concat(str, ' EADR ');
  if Piberr^ = EARG Then
    str := Concat(str, ' EARG ');
  if Piberr^ = ESAC Then
    str := Concat(str, ' ESAC ');
  if Piberr^ = EABO Then
    str := Concat(str, ' EABO ');
  if Piberr^ = ENEB Then
    str := Concat(str, ' ENEB ');
  if Piberr^ = EDMA Then
    str := Concat(str, ' EDMA ');
  if Piberr^ = EOIP Then
    str := Concat(str, ' EOIP ');
  if Piberr^ = ECAP Then
    str := Concat(str, ' ECAP ');
  if Piberr^ = EFSO Then
    str := Concat(str, ' EFSO ');
  if Piberr^ = EBUS Then
    str := Concat(str, ' EBUS ');
  if Piberr^ = ESTB Then
    str := Concat(str, ' ESTB ');
  if Piberr^ = ESRQ Then
    str := Concat(str, ' ESRQ ');
  if Piberr^ = ETAB Then
    str := Concat(str, ' ETAB ');
  str := Concat(str, '>');
  str := Concat(str, #13);  (* Add a line feed character.         *)

  ibcntlStr := IntToStr(Pibcntl^);
  str := Concat( str, 'ibcntl = ' + ibcntlStr);

  MessageDlg(str, mtError, [mbOK], 0);

(* The device is taken offline.                                  *)
  ibonl(Dev, 0);
```

```
  (* Free the GPIB library.                                          *)
    FreeLibrary(Gpib32Lib);

    halt;
end;

procedure initializeSeries;
begin
serM1:=TFastLineSeries.Create(Form1);
serM2:=TFastLineSeries.Create(Form1);
serM3:=TFastLineSeries.Create(Form1);
Form1.Chart1.RemoveAllSeries;
Form1.Chart1.AddSeries(serM1);
Form1.Chart1.AddSeries(serM2);
Form1.Chart2.AddSeries(serM3);
Form1.Chart1.LeftAxis.Automatic:=True;
Form1.Chart1.BottomAxis.Automatic:=True;
Form1.Chart2.LeftAxis.Automatic:=True;
Form1.Chart2.BottomAxis.Automatic:=True;
serM1.SeriesColor:=clGreen;
serM2.SeriesColor:=clRed;
serM3.SeriesColor:=clBlue;
serM1.Title:='Channel1';
serM2.Title:='Channel2';
serM3.Title:='Ratio';
end;

procedure TForm1.FormCreate(Sender: TObject);
begin
Form1.Caption := 'SR245 (Boxcar Computer Interface)   ' + DateToStr(Date);
X:=0; Y:=0; XT:=0; YT:=0; XA:=0; YA:=0; RA:=0;
Timer1.Enabled:=False;
loadDLL;
Dev := ibdev(BDINDEX, PRIMARY_ADDR_OF_SCOPE,
       NO_SECONDARY_ADDR, TIMEOUT, EOTMODE, EOSMODE);
       if (Pibsta^ AND ERR) <> 0 Then
       GPIBCleanup('Unable to open device');

     ibclr(Dev);
     if (Pibsta^ AND ERR) <> 0 Then
       GPIBCleanup('Unable to clear device');
InitializeSeries;
TalkToDevice('MS');
//writeln(T,'XA','       ','YA','      ','RA','       ','NumOfPoints','        ','
end;
```

```
procedure TalkToDevice(Command: String);
var RD: packed array [0..20] of char;
    CL,i:integer;
begin
  Command := Command + #13;
  CL := StrLen(PChar(Command));
  for i := 0 to (CL-1) do
  RD[i]:= Command[i+1];
  ibwrt(Dev, RD, CL);
end;

procedure ListenToDevice;
var S:String; S1:PChar;
begin
  ibrd(Dev, ReadBuff, 10);
  S1:=(Pointer(@ReadBuff[0]));
  S:=S1;
  S:=copy(S,1,Pos(#13,S)-1);
  RDString:=S;
  RDFloat:=StrToFloat(S);
end;

procedure TForm1.Button1Click(Sender: TObject);
begin

  Xmini:=StrToFloat(Xmin.Text);
  Ymini:=StrToFloat(Ymin.Text);
  Xmaxi:=StrToFloat(Xmax.Text);
  Ymaxi:=StrToFloat(Ymax.Text);

  Timer1.Enabled:=True;
  TalkToDevice('SC1,2:1000');//Scanning the data
  TalkToDevice('?S');
  ListenToDevice; Edit1.Text:=FloatToStr(RDFloat);
  //Button4.Click;
end;

procedure TForm1.Timer1Timer(Sender: TObject);
var i,j:integer;
    SSS:string;
begin
  Timer1.Enabled := False;
  j:=0;
  TalkToDevice('ES');//End scanning the data
```

```
TalkToDevice('?S');
ListenToDevice; Edit2.Text:=FloatToStr(RDFloat);
TalkToDevice('?N');//Getting # of points scanned
ListenToDevice;//Read data is in ReadBuff global variable
NOP.Text:=RDString;
NumOfPoints:=StrToInt(RDString);
Memo1.Clear;
for i:=1 to NumOfPoints do
begin
  SSS:='';
  TalkToDevice('N');
  ListenToDevice; X:=RDFloat;
  SSS:=RDString;
  TalkToDevice('N');
  ListenToDevice; Y:=RDFloat;
  if Y<>0 then
  SSS:=SSS+':  '+RDString+'  : '+FloatToStr(X/Y)
     else SSS:=SSS+':  '+RDString;

  Memo1.Lines.Add(SSS);
  if ( X > Xmini) and (Y > Ymini ) and ( X < Xmaxi ) and ( Y < Ymaxi ) then
    begin
    XT:=XT+X;
    YT:=YT+Y;
    j:=j+1;
    end;
end;

//Averaging the data
if j<>0 then
begin
  Edit3.Text:=IntToStr(j);
  XA := XT/j; Channel1.Text:=FloatToStr(XA);
  YA := YT/j; Channel2.Text:=FloatToStr(YA);
  if YA<>0 then RA := XA/YA; Ratio.Text:=FloatToStr(RA);

  //writeln(T,RA);
  //Ploting the series
  serM1.AddY(XA,'',clGreen);
  serM2.AddY(YA,'',clRed);
  serM3.AddY(RA,'',clBlue);
  Form1.Chart1.AddSeries(serM1);
  Form1.Chart1.AddSeries(serM2);
  Form1.Chart2.AddSeries(serM3);
  X:=0; Y:=0; XT:=0; YT:=0; XA:=0; YA:=0; RA:=0; NumOfPoints:=0;
```

```
    Channel1.Repaint;
    Channel2.Repaint;
    Ratio.Repaint;
    NOP.Repaint;
    Chart1.Repaint;
    Chart2.Repaint;
    Edit3.Repaint;
  end;
  Button1.Click;
end;


procedure TForm1.Channel_AutoClick(Sender: TObject);
begin
  if Channel_Auto.Checked then
    Form1.Chart1.LeftAxis.Automatic := True
  else
    begin
    Form1.Chart1.LeftAxis.AutomaticMinimum := False;
    Form1.Chart1.LeftAxis.AutomaticMaximum := False;
    try
      Form1.Chart1.LeftAxis.Maximum := StrToFloat(Max.Text);
      Form1.Chart1.LeftAxis.Minimum := StrToFloat(Min.Text);
    except
    end;
    end;
end;

procedure TForm1.Ratio_AutoClick(Sender: TObject);
begin
  if Ratio_Auto.Checked then
    Form1.Chart2.LeftAxis.Automatic := True
  else
    begin
    Form1.Chart2.LeftAxis.AutomaticMinimum := False;
    Form1.Chart2.LeftAxis.AutomaticMaximum := False;
    try
      Form1.Chart2.LeftAxis.Maximum := StrToFloat(Rmax.Text);
      Form1.Chart2.LeftAxis.Minimum := StrToFloat(Rmin.Text);
    except
    end;
    end;
end;
```

```
procedure TForm1.MinChange(Sender: TObject);
begin
  if Channel_Auto.Checked = false then
  begin
     Form1.Chart1.LeftAxis.AutomaticMinimum := False;
     try
     Form1.Chart1.LeftAxis.Minimum := StrToFloat(Min.Text);
     except
     end;
  end;
end;

procedure TForm1.MaxChange(Sender: TObject);
begin
  if Channel_Auto.Checked = false then
  begin
     Form1.Chart1.LeftAxis.AutomaticMaximum := False;
     try
     Form1.Chart1.LeftAxis.Maximum := StrToFloat(Max.Text);
     except
     end;
  end;
end;

procedure TForm1.RMinChange(Sender: TObject);
begin
  if Channel_Auto.Checked = false then
  begin
     Form1.Chart2.LeftAxis.AutomaticMinimum := False;
     try
     Form1.Chart2.LeftAxis.Minimum := StrToFloat(RMin.Text);
     except
     end;
  end;
end;

procedure TForm1.RmaxChange(Sender: TObject);
begin
  if Channel_Auto.Checked = false then
  begin
     Form1.Chart2.LeftAxis.AutomaticMaximum := False;
     try
     Form1.Chart2.LeftAxis.Maximum := StrToFloat(RMax.Text);
     except
     end;
```

```
  end;
end;

procedure TForm1.Button2Click(Sender: TObject);
begin
  Timer1.Enabled:=false;
  Edit1.Text:='Begin Scan';
  Edit2.Text:='After Scan';
  Channel1.Text:='';
  Channel2.Text:='';
  Ratio.Text:='';
  NOP.Text:='';
  edit3.Text:='';
end;

procedure TForm1.XminChange(Sender: TObject);
begin
  try
  Xmini:=StrToFloat(Xmin.Text);
  except
  end;
end;

procedure TForm1.YminChange(Sender: TObject);
begin
  try
  Ymini:=StrToFloat(Ymin.Text);
  except
  end;
end;

procedure TForm1.Button3Click(Sender: TObject);
begin
  serM1.clear;
  serM2.clear;
  serM3.clear;
end;

procedure TForm1.Button4Click(Sender: TObject);
var i:integer;
begin
  fileName:='C:\Thandar\031706\'+edit4.Text+'.txt';
  AssignFile(T,fileName);
  Rewrite(T);
  for i:=0 to serM3.Count - 1 do
```

```
    WriteLn(T,serM3.Yvalues.Value[i]);
end;

end.


}
```

Bibliography

[1] T. Myint, M. Y. Sharonov, A. Bykov, and R. R. Alfano, "Relaxation dynamics of Cr^{4+} tetrahedral centers in Cr:$LiScGeO_4$ single crystal." Optics Letters, submitted, December 2009.

[2] T. Myint, J. Hurwitz, and R. R. Alfano, "Spatial phase modulation from permanent memory in doped glass." Optics Letters, submitted, December 2009.

[3] M. Sharonov, T. Myint, A. Bykov, V. Petričević, and R. Alfano, "Optical properties of neodymium activated crystalline nanostructures grown in transparent porous glass," *J. Opt. Soc. Am. B*, vol. 24, November 2007.

[4] M. Sharonov, A. Bykov, T. Myint, V. Petričević, and R. Alfano, "Spectroscopic study of chromium-doped transparent calcium germanate glass-ceramics," *Optics Communications*, March 2007.

[5] S. K. Zhang, T. Myint, W. B. Wang, B. B. Das, R. R. Alfano, and M. Tamargo, "Optical study of strongly coupled cdse quantum dots." Journal of Vacuum Science and Technology, Accepted, November 2009.

[6] K. Nassau, *The Physics and Chemistry of Color*. Wiley-Interscience, 1983.

[7] B. N. Figgis and M. A. Hitchman, *Ligand Field Theory and Its Applications*. WILEY-VCH, 2000.

[8] R. C. Powell, *Physics of Solid-State Laser Materials*. Springer, 1998.

[9] M. Hazenkamp and H. Güdel, "Optical spectroscopy of Cr^{4+}-doped Ca_2GeO_4 and Mg_2SiO_4 ," *Physical Review B*, vol. 53, February 1996.

[10] M. Hazenkamp, U. Oetliker, H. Güdel, U. Kesper, and D. Reinen, "Absorption and luminescence spectroscopy of Cr^{4+}-doped Ca_2GeO_4 . a potential near infrared laser material," *Chemical Physics Letters*, February 1995.

[11] S. Kück, "Laser-related spectroscopy of ion-doped crystals for tunable solid-state lasers," *Applied Physics B*, vol. 72, 2001.

[12] M. Sharonov, A. Bykov, P. Rojas, V. Petričević, and R. Alfano, "Spectroscopy of chromium centers in $LiScGeO_4$ and $LiInGeO_4$ single crystals," *Physical Review B*, vol. 72, September 2005.

[13] W. Jia, H. Liu, S. Jaffe, and W. Yen, "Spectroscopy of $Cr^{3+}$and Cr^{4+}ions in forsterite," *Physical Review B*, vol. 43, March 1991.

[14] V. Petričević, A. Bykov, J. Evans, and R. Alfano, "Room-temperature near-infrared tunable laser operation of Cr^{4+}:Ca_2GeO_4," *Opitcs Letters*, vol. 21, November 1996.

[15] Z. Strnad, *Glass-Ceramic Materials*. Elsevier, 1986.

[16] S. Tanabe, "Optical transitions of rare earth ions for amplifiers: how the local structure works in glass," *Journal of Non-crystalline Solids*, pp. 1–9, 1999.

[17] E. I. Solomon and A. Lever, *Inorganic Electronic Structure and Spectroscopy*, vol. 1 of *v.1.Methodology & v.2.Applications and Case studies*. John Wiley & Sons, Inc., 1999.

[18] T. H. Elmer, "Porous and reconstructed glasses," in *ENGINEERED MATERIALS HANDBOOK*, vol. 4, pp. 427–432, ASM International, 1987.

[19] V. Petričević, S. Gayen, and R. Alfano, "Laser action in chromium-activated forsterite for near-infrared excitation: Is Cr^{4+} the lasing ion?," *Appl. Phys. Lett.*, vol. 53, December 1988.

[20] V. Petričević, S. Gayen, and R. Alfano, "Laser action in chromium-activated forsterite for near infrared excitation," *Applied Optics*, vol. 27, pp. 4162–4163, October 1988.

[21] S. G. Demos, *Ultrafast Physics behine the nonradiative relaxation process of chromium ions in forsterite crystals*. PhD thesis, The Graduate Center of City College of New York, 1993.

[22] D. M. Calistru, *Role of local modes in nonradiative processes taking place in impurity doped laser crystals*. PhD thesis, The Graduate Center of City College of New York, 1997.

[23] J. Evans, V. Petričević, A. Bykov, A. Delgado, and R. Alfano, "Direct diode-pumped continuous-wave near-infrared tunable laser operation of Cr^{4+}:forsterite and Cr^{4+}:Ca_2GeO_4," *Opitcs Letters*, vol. 22, August 1997.

[24] J. Evans, V. Petričević, and R. Alfano, "Continuous-wave all-solid state laser operation of Cr^{4+}:forsterite and Cr^{4+}:Ca_2GeO_4," *OSA TOPS, Diode Pumped Solid State Lasers: Application and Issues*, vol. 17, 1998.

[25] B. Xu, J. Evans, V. Petričević, S. Guo, O. Maksimov, M. C. Tamargo, and R. Alfano, "Continuous-wave and passively mode-locked operation of a cunyite(Cr^{4+}:Ca_2GeO_4) laser," *Applied Optics*, vol. 39, September 2000.

[26] S. Owen, D. M. Calistru, S. Demos, A. Bykov, V. Petričević, and R. Alfano, "Role of electron-phonon interaction in improved laser performance of the Cr^{4+}:Ca_2GeO_4 laser crystal," in *Conference on Lasers & Electro-Optics(CLEO)*, 1997.

[27] V. Petričević, A. Bykov, J. Evans, A. Seas, A. Delgado, R. Alfano, and G. Kanunnikov, "Laser action of Cr:$LiScGeO_4$ crystals," in *Conference on Lasers & Electro-Optics(CLEO)*, 1997.

[28] M. Sharonov, V. Petričević, A. Bykov, and R. Alfano, "Near-infrared laser operation of Cr^{3+}centers in chromium-doped $LiInGeO_4$ and $LiScGeO_4$ crystals," *Optics Letters*, vol. 30, pp. 851–853, April 2005.

[29] M. Sharonov, V. Petričević, A. Bykov, and R. Alfano, "Ultra-wideband near-infrared laser operation of Cr^{3+}centers in chromium doped Li(In,Sc)GeO_4 olivines," in *Conference on Lasers & Electro-Optics(CLEO)*, 2005.

[30] M. Sharonov, A. Bykov, V. Petričević, and R. Alfano, "Continuous tunable laser operation in both the 1.31 and 1.55 μm telecommunication windows in LiIn(Si/Ge)O_4 olivines doped with trivalent chromium," *Opitcs Letters*, vol. 32, December 2007.

[31] T. H. Maiman, "Stimulated Optical Radiation in Ruby," *Nature*, vol. 187, no. 4736, pp. 493–494, 1960.

[32] J. C. Walling, H. P. Jenssen, R. C. Morris, E. W. ODell, and O. G. Peterson, "Tunable-laser performance in BeAl2O4:Cr^{3+}," *Optics Letters*, vol. 4, pp. 182–183, 1979.

[33] A. Galeev, N. Khasanova, C. Rudowicz, G. Shakurov, A. Bykov, G. Bulka, N. Nizamutdinov, and V. Vinokurov, "Multifrequency EPR study of Cr^{3+}ions in $LiScGeO_4$," *J.Phys.:Condens. Matter*, vol. 12, pp. 4465–4473, 2000.

[34] W. Jia, H. Liu, Y. Wang, U. Hömmerich, H. Eilers, K. Hoffman, and W. M. Yen, "Stress effects on the fluorescence spectra of tetravalent chromium in some crystalline hosts," *Journal of luminescence*, vol. 59, no. 5, pp. 279–287, 1994.

[35] W. Jia and W. M. Yen, "Advances in the spectroscopy of Cr^{4+}-doped laser materials," *Journal of Applied Spectroscopy*, vol. 62, no. 5, p. 966, 1995.

[36] H. Eilers, U. Hömmerich, S. Jacobsen, and W. M. Yen, "Spectroscopy and dynamics of Cr^{4+}:$Y_3Al_5O_{12}$," *Physical Review B*, vol. 49, November 1994.

[37] S. Tanabe, "Development of rare-earth doped fiber amplifier for broad band Wavelength-Division-Multiplexing telecommunication," *IPAP*[1] *Books 2*, pp. 101–112, 2005.

[38] G. H. Beall, "Transparent forsterite glass-ceramics," Tech. Rep. 6632757[2], Corn-

[1] IPAP = Institute of Pure and Applied Physics, Japan

[2] Technical Report means Patent number in this thesis

ing Incorporated, October 2003.

[39] G. Beall and D. Duke, "Transparent glass-ceramics," *Journal of Materials Science*, vol. 4, pp. 340–352, December 1969.

[40] S. Tanabe, "Novel Oxide glass and glass ceramic materials for optical amplifier," *Ceramic transactions*, pp. 1–16, 2005.

[41] M. Grinberg, W. Jaskólski, P. Macfarlane, and K. Holliday, "The influence of substitutional disorder on non-radiative transitions in Cr^{3+}-doped gallogermanate crystals," *J. Phys. Condens. Matter*, pp. 2815–2829, 1997.

[42] M. Grinberg, D. Russell, K. Holliday, K. Wisniewski, and C. Koepke, "Continuous function decay analysis of a multisite impurity activated solid," *Opitcs Communications*, pp. 409–418, 1998.

[43] M. Sharonov, A. Bykov, S. Owen, V. Petričević, and R. Alfano, "Spectroscopic study of transparent forsterite nanocrystalline glass-ceramics doped with chromium," *J. Opt. Soc. Am. B*, vol. 21, November 2004.

[44] A. A. Kaminskii, *Laser Crystals: Their Physics and Properites*. Springer Series in Optical Sciences, 1981.

[45] A. A. Kaminskii, *CRYSTALLINE LASERS: Physical Processes and Operating Shemes*. CRC Press, Inc., 1996.

[46] R. Englman, *Non-Radiative Decay of Ions and Molecules in Solids*. North-Holland, 1979.

[47] R. A. Mayanovic, A. J. Anderson, W. A. Bassett, and I.-M. Chou, "On the formation and structrure of rare-earth element complexes in aqueous solutions under hydrothermal conditions with new data on gadolinium aqua and chloro complexes," *Chem. Geol.*, vol. 239, pp. 266–283, 2007.

[48] G. D. D. Cul, *Luminescence, Raman and Absorption Spectrophotometric Studies of selected lanthanide and actinide compounds in the solid state*. PhD thesis, The University of Tennessee, Knoxville, 1990.

[49] A. Zolot'ko, V. Kitaeva, N. Kroo, N. Sobolev, and L.Chillag, "The effect of an optical field on the nematic phase of the liquid crystal ocbp," *JETP Letter*, vol. 32, p. 158, 1980.

[50] S. Durbin, S. Arakelian, and Y. Shen, "Laser-induced diffraction rings from a nematic-liquid crystal film," *Optics Letters*, pp. 411–413, September 1981.

[51] E. Santamato and Y. Shen, "Field-curvature effect on the diffraction ring pattern of a laser beam dressed by spatial self-phase modulation in a nematic film," *Optics Letters*, pp. 564–566, December 1984.

[52] F. Dabby, T. Gustafson, J. Whinnery, Y. Kohanzadeh, and P. Kelley, "Thermally self-induced phase modulation of laser beams," *Applied Physics Letters*, pp. 362–365, May 1970.

[53] K. Ogusu, Y. Kohtani, and H. Shao, "Laser-induced diffraction rings from absorbing solution," *Optical Review*, pp. 232–234, 1996.

[54] R. Harrison, L. Dambly, D. Yu, and W. Lu, "A new self-diffraction pattern formation in defocusing liquid media," *Optics Communications*, pp. 69–72, June 1997.

[55] I. Khoo, J. Hou, T. Liu, P. Yan, R. Micheal, and G. Finn, "Transverse self-phase modulation and bistability in the transmission of a laser beam through a nonlinear thin film," *J. Opt. Soc. Am. B*, pp. 886–891, June 1987.